

Low-loss TeO₂ devices on Si and Si₃N₄ photonic circuits

LOW-LOSS TELLURIUM OXIDE DEVICES INTEGRATED ON SILICON AND
SILICON NITRIDE PHOTONIC CIRCUIT PLATFORMS

By HENRY C. FRANKIS, B. ENG

A thesis submitted to the School of Graduate Studies in partial fulfillment of the
requirements of the requirements for Degree Ph. D.

McMaster University © Copyright by Henry C. Frankis, July 22 2021

McMaster University

Ph.D. (2021)

Hamilton, Ontario (Department of Engineering Physics)

TITLE: Low-loss tellurium oxide devices integrated on silicon and silicon nitride photonic circuit platforms

AUTHOR: Henry C. Frankis, B. Eng (McMaster University)

SUPERVISOR: Dr. Jonathan D. B. Bradley

NUMBER OF PAGES: xxii, 203

Abstract

Silicon (Si) and silicon nitride (Si_3N_4) have become the dominant photonic integrated circuit (PIC) material platforms, due to their low-cost, wafer-scale production of high-performance circuits. However, novel materials can offer additional functionalities that cannot be easily accessed in Si and Si_3N_4 , such as light emission. Tellurium oxide (TeO_2) is a novel material of interest because of its large linear and non-linear refractive indices, low material losses and large rare-earth dopant solubility, with applications including compact low-loss waveguides and on-chip light sources and amplifiers. This thesis investigates the post-processing integration of TeO_2 devices onto standardized Si and Si_3N_4 chips to incorporate TeO_2 material advantages into high-performance PICs. Chapter 1 introduces the state-of-the-art functionality for various integrated photonic materials as well as methods for integrating multiple materials onto single chips. Chapter 2 presents the development of a high-quality TeO_2 thin film fabrication process by reactive RF sputtering, with material refractive indices of 2.07 and optical propagation losses of <0.1 dB/cm at 1550 nm. Chapter 3 investigates a conformally coated TeO_2 - Si_3N_4 waveguide platform capable of large TeO_2 optical confinement and tight bending radii, characterizing fiber-chip edge couplers down to ~ 5 dB/facet, waveguide propagation losses of <0.5 dB/cm, directional couplers with 100% cross-over ratio, and microresonators with internal Q factors of 7.3×10^5 . In Chapter 4 a spectroscopic study of $\text{TeO}_2:\text{Er}^{3+}$ -coated Si_3N_4 waveguide amplifiers was undertaken, with internal net gains of up to 1.4 dB/cm in a 2.2-cm-long waveguide and 5 dB total in a 6.7-cm-long sample demonstrated, predicted to reach >10 dB could 150 mW of pump power be launched based on a developed rate-equation model. Chapter 5 demonstrates TeO_2 -coated microtrench resonators coupled to silicon waveguides, with internal Q factors of up to 2.1×10^5 and investigates environmental sensing metrics of devices. Chapter 6 summarizes the thesis and provides avenues for future work.

Acknowledgements

Firstly, I would like to thank my supervisor Dr. Jonathan Bradley for trusting me to be the first full-time member of his research group. It has been a unique opportunity which has allowed me to grow in many ways and provided me an excellent experience. I would also like to thank my committee members Dr. Peter Mascher and Dr. Andy Knights, the latter of whom I would also like to thank for providing me the opportunity to work part time in the Centre for Emerging Device Technologies (CEDT) as a CEDT scholar.

Speaking of the CEDT, much of the experimental fabrication and film characterization research described in this thesis was carried out in the CEDT, and made possible thanks to many of the excellent individuals associated with it. I would like to acknowledge the work of the CEDT directors, formerly Dr. Rafael Kleiman, and currently Dr. Andy Knights, for their efforts in organization and equipment procurement, including the new sputtering system that was delivered during my first few months and has been the workhorse of our group's research ever since. Excellent training on how to use the sputtering system and various other CEDT equipment was provided by Doris Stevanovic and Dr. Shahram Tavakoli, the latter of whom was also hugely helpful in system repairs and maintenance throughout the years.

CMC Microsystems has continually been an excellent resource for training, software access and high-quality silicon photonic chip fabrication throughout my PhD. The SiEPIC photonic courses run by Dr. Lukas Chrostowski and follow up chip design aided by Jessica Zhang, Dan Deptuck and Susan Xu of CMC were essential to establishing much of my fundamental knowledge on the theory of integrated photonic devices.

While those previously mentioned have played a large role in the overall work of this project, much of the day-to-day work was made possible thanks to contributions from my fellow research group members, including: Hamidu Mbonde, Renjie Wang, Cameron Naraine, Khadijeh Miarrabas Kiani, Bruno Segat Frare, and summer students: Daniel Su, Caitlyn Smith, Benjamin Jarvis-Frain and Arthur Méndez-Rosales. In particular, original research group members Jeremy Miller, Chenglin Zhang and Dawson Bonneville were critical in establishing many of the fundamental processes and setting up the basic equipment that are now key in our research work. Much of this work was also made easier thanks to the members of our neighboring lab group: David Hagan, Ross Anthony

I would like to thank Yanran Xie, who 'deserves her own paragraph'.

Lastly, I would like to thank my parents for their many years of unending support.

Table of Contents

Abstract	iii
Acknowledgements	iv
List of Figures	viii
List of Tables	xix
List of Acronyms	xx
Declaration of Authorship	xxii
1 Introduction	1
1.1 Integrated Optics	1
1.2 Integrated Optical Functionalities and Materials	3
1.3 Material and Waveguide Integration Schemes.....	11
1.4 Tellurite Glass.....	15
1.5 Thesis Objectives.....	17
1.6 Statement of Thesis Work	18
1.7 Publications.....	18
2. Low-Loss Tellurium Oxide Thin Film Deposition by RF Reactive Sputtering	35
2.1 Introduction.....	36
2.2 Tellurite Film Deposition System and Procedures	37
2.3 Tellurite Film Characterization Methods	40
2.3.1 Ellipsometry	40
2.3.2 Prism Coupling	41
2.3.3 Rutherford Backscattering Spectrometry.....	48
2.4 Optimization of TeO ₂ Deposition Recipe	50
2.5 Co-Sputtering of Erbium Dopants into Tellurite Films	56
2.6 Conclusion	60
3. Passive Tellurium Oxide Coated Silicon Nitride Waveguides and Devices	64
3.1 Introduction.....	65

3.2 Waveguide Fabrication and Structure.....	66
3.3 Simulated Waveguide Properties	70
3.4 Passive Photonic Devices	79
3.4.1 Visible to Infrared Waveguide Loss Characterization	80
3.4.2 Fiber-Chip Edge Couplers	83
3.4.3 Directional Couplers	86
3.4.4 High Q-Factor Microresonators	94
3.5 Conclusion	107

4. Erbium-Doped Tellurium Oxide Coated Silicon Nitride Waveguide Amplifiers . 112

4.1 Introduction.....	113
4.2 Spectroscopic Properties of Erbium-Doped Tellurium Oxide.....	115
4.2.1 Optical Processes and Gain	115
4.2.2 Erbium Energy Diagram	117
4.2.3 Absorption and Emission Cross Sections	120
4.2.4 Excited State Lifetimes	126
4.2.5 Ion Quenching and Energy Transfer	130
4.2.5 Sample Comparison	134
4.3 Internal Net Gain in Erbium-Doped Waveguide Amplifiers.....	135
4.4 Erbium-Doped Waveguide Rate Equation Modelling and Amplifier Optimization...	143
4.4.1 Energy-Level Population Dynamics	144
4.4.2 Change in Optical Power	147
4.4.3 Rate Equation Model.....	150
4.4.4 Amplifier Optimization	152
4.5 Conclusion	154

5. Tellurium Oxide Microcavities Integrated on a Silicon Photonics Platform..... 163

5.1 Introduction.....	164
5.2 Silicon-Integrated TeO ₂ Microcavity Fabrication	166
5.3 TeO ₂ Microcavity Design	170
5.3.1 Microcavity Mode Properties	172
5.3.2 Radiation Loss Minimization.....	174
5.3.3 Optical Coupling Between Silicon Waveguide and TeO ₂ Microcavity.....	175
5.4 TeO ₂ Microcavity Characterization.....	184
5.4.1 Design A Results	184
5.4.2 Design B Results.....	186
5.5 Application of TeO ₂ Microcavity as an Environmental Sensor.....	188
5.6 Conclusion	194

6. Conclusions	200
6.1 Major Results.....	200
6.2 Suggested Future Work.....	201
Appendices	204
Appendix A – List of Silicon Nitride Structures	204
Appendix B – Q Factor Fitting Code.....	208
Appendix C – Rate Equation Solver Code.....	213
Appendix D – Coupled Mode Theory Solver Code	226

List of Figures

Fig. 1.1	Cross section of (a) strip and (b) ridge waveguides for single material system waveguide platforms. Combined materials systems can be categorized as (c) vertical or (d) lateral multilayer platforms with independent waveguide modes, or hybrid waveguides as demonstrated with (e) heteroepitaxy, (f) wafer/die bonding or straightforward (g) planar and (h) conformal coating techniques. ..	13
Fig. 2.1	Picture of Kurt J. Lesker PVD Pro 200 thin film deposition system in the CEDT cleanroom, with control tower on the left and vacuum chamber on the right.	37
Fig. 2.2	Diagram of interior of sputter deposition system, featuring an inverted 6-inch sample holder on a rotating platform backed by a heater and a substrate plasma, with confocal magnetron sputtering guns with metallic tellurium and erbium targets at the bottom of the chamber connected to an RF power supply. Argon gas is inlet through two valves at the bottom of the chamber, while oxygen is inlet through a ring coiled around the substrate holder.	38
Fig. 2.3	A bare silicon, thermally oxidized silicon, and glass slide test piece as well as several chips mounted onto the substrate holder.	39
Fig. 2.4	Diagram of light ray travelling through planar thin film of thickness T , with a refractive index of n_0 and cladding refractive indices of n_1 and n_2	42
Fig. 2.5	Solutions of the interference term versus propagation constant for a TeO_2 thin film on thermal oxide at a wavelength of 638 nm and TE polarization, for TeO_2 film thicknesses of 0.2, 0.4, and 0.6 μm	45
Fig. 2.6	A light ray incident on a prism face at an angle of α to the sidewall normal will refract into the prism and experience an internal reflection from the base of the prism at an angle of σ	45
Fig. 2.7	(a) Red light streak propagating through tellurium oxide thin film in prism coupler. (b) Diagram of how prism coupler collects scattered light for loss measurements.	46
Fig. 2.8	Sample measured intensity of scattered light through the top of a TeO_2 film, versus distance away from coupling point. The data is fit with an exponential equation to estimate a 3.7 dB/cm optical propagation loss.	47
Fig. 2.9	Three particles incident on a scattering center at different relative positions are scattered off the sample at different angles.	48
Fig. 2.10	Example of a measured RBS spectrum showing the number of scattered particles with different energies for a TeO_2 film on a silicon substrate, with scatterings from Te atoms seen near 1500 keV, a broad spectrum of Si scatterings below 800 keV, and small signature of O scatterings around 600 keV.	49

Fig. 2.11	Measured refractive index at 1550 nm and deposition rate versus (a and b) DC bias applied to the Te sputtering target and (c and d) O ₂ flow rate of several fabricated tellurite thin films.	51
Fig. 2.12	(a) A set of tellurite films deposited on glass slides at different O ₂ flow rates, with measured refractive index and optical propagation loss at 633 nm indicated. Measured film loss of samples at 633 and 1310 nm versus (b) refractive index and (c) O/Te ratio of samples. Vertical lines represent the x < 2 stoichiometric limit of TeO _x , beyond which film losses were seen to increase beyond the measurable limit (~25 dB/cm).	53
Fig. 2.13	Loss at 638, 847, 1310, and 1550 nm-wavelengths of 0.4, 0.3, 0.1 and 0.1 dB/cm respectively measured in a high quality 436-nm-thick TeO ₂ film by prism coupling. (b) Scattered intensity versus propagation length for the 638-nm-wavelength light streak.	54
Fig. 2.14	(a) Sellmeier fits from several low loss samples used to obtain an average refractive index dispersion profile (black line), and standard deviation of variation (red zone). (b) Comparison of measured refractive index dispersion profiles from ellipsometry to refractive indices measured at different wavelengths by prism coupling.	55
Fig. 2.15	Map of variation in tellurite film (a) refractive index at 1550 nm and (b) thickness, compared to average value measured over a 3-inch silicon wafer by ellipsometry. The average refractive index and film thickness are 2.048 and 309.4 nm, respectively.	56
Fig. 2.16	Film loss, as measured by prism coupling versus (a) wavelength and (b) Er ³⁺ absorption cross section at each wavelength, used to fit erbium concentrations of 1.4×10 ²⁰ and 2.7×10 ²⁰ ions/cm ³ for two sample TeO ₂ :Er ³⁺ films.	58
Fig. 2.17	Measured erbium ion concentration of thin films versus RF sputtering power applied to the erbium target for two different tellurium targets that are sputtered at different conditions. Trial A sputtered a tellurium target near a 165 V bias with 10.5 sccm of O ₂ flow, while Trial B sputtered a different tellurium target near a 130 V bias with 9.5 sccm of O ₂ flow.	59
Fig. 2.18	Refractive index of films at (a) 633 and (b) 1550 nm wavelength versus erbium ion concentration, showing a decrease in the measured refractive index with increasing erbium dopant concentration.	60
Fig. 3.1	Mask layouts of (a) Chiplet A containing paperclips of various length, (b) Chiplet B containing longer paperclips and (c) Chiplet C containing several passive devices, including directional couplers and ring resonators.	66

Fig. 3.2	Diagram of fabrication process used to form TeO ₂ coated Si ₃ N ₄ waveguides, starting with growth of an 8- μ m-thick wet thermal oxide on a 4-inch silicon wafer (i), followed by the deposition of a 0.2- μ m-thick Si ₃ N ₄ film in an LPCVD process (ii), which is then patterned using stepper lithography and reactive ion etching to form Si ₃ N ₄ strips (iii), after which the wafer is diced into chiplets and transferred from the foundry to the Centre for Emerging Device Technologies (CEDT) at McMaster University (iv), where it is coated in a reactively sputtered TeO ₂ film (v) and, in some cases, top-cladded in a spin-on fluoropolymer layer (vi).	68
Fig. 3.3	SEM cross section of two nearby TeO ₂ coated Si ₃ N ₄ waveguides after a focused ion beam (FIB) cut, showing the SiO ₂ lower cladding, the Si ₃ N ₄ strips and the conformal TeO ₂ coating. (b) Cross-sectional diagram of the TeO ₂ -Si ₃ N ₄ hybrid waveguide structure.	69
Fig. 3.4	Dispersion of materials used in the waveguide structure including TeO ₂ , LPCVD Si ₃ N ₄ , thermal SiO ₂ , and Cytop. The SiO ₂ and Si ₃ N ₄ refractive indices are from reference data [35,36] and the TeO ₂ and Cytop refractive indices are from ellipsometry measurements.	70
Fig. 3.5	Simulated electric-field mode profiles of 1.0 μ m \times 0.2 μ m Si ₃ N ₄ strips coated in (a) 200, (b) 400 and (c) 600-nm-thick TeO ₂ coatings at 1550 nm wavelengths.	70
Fig. 3.6	(a) Simulated effective index of the first three waveguide modes for waveguide widths from 0.5 to 3.0 μ m for a 0.2- μ m-thick silicon nitride strip coated in a 200-nm-thick TeO ₂ film at 1550 nm wavelength. The waveguide is seen to reach the single mode condition at Si ₃ N ₄ strip widths below 1 μ m as the TE ₁ mode begins to radiate into the slab. (b) Simulated effective index of the fundamental TE polarized SiO ₂ -TeO ₂ -Cytop slab mode for different thicknesses of TeO ₂	71
Fig. 3.7	Single mode conditions at wavelengths from 0.6 to 2.0 μ m for (a) 200, 400 and 600-nm-thick tellurium oxide coatings on a 0.2 μ m tall silicon-nitride waveguide and (b) a 400-nm-thick tellurium oxide coating on 0.1, 0.2 and 0.3- μ m-thick silicon nitride strip waveguides.	72
Fig. 3.8	Maps indicating whether the TeO ₂ -Si ₃ N ₄ waveguide supports only a TE polarized mode (green) or both a TE and TM polarized mode (red) under the single mode condition for (a) a 0.2 μ m Si ₃ N ₄ strip height with 200, 400, and 600-nm-thick TeO ₂ coatings and (b) a 400-nm-thick TeO ₂ coating and 0.1, 0.2 and 0.3 μ m Si ₃ N ₄ strip height at 630, 980, 1310, 1550 and 2000 nm wavelengths. Simulated electric-field mode profile of the fundamental (c) TE and (d) TM polarized modes of a 1.0 μ m \times 0.3 μ m Si ₃ N ₄ strip coated in a 400-nm-thick TeO ₂ layer.	73

Fig. 3.9	Simulated TeO ₂ -Si ₃ N ₄ waveguide properties for varying TeO ₂ film thickness, including (a) effective index, (b) optical confinement factor within the silicon nitride strip and tellurite glass coating, (c) effective mode area and (d) minimum bend radius at which the waveguide is able to maintain radiation losses less than 0.01 dB/cm for the fundamental TE mode for a 1.2 μm × 0.2 μm silicon nitride strip waveguide with 200, 400 and 600-nm-thick TeO ₂ coatings at visible to near-infrared wavelengths.	74
Fig. 3.10	Illustration showing (a) difference between evanescent and slab radiation in waveguide structure and (b) how the minimum waveguide bend radius of the hybrid waveguide structure is predominantly affected by radiation from the evanescent field at longer wavelengths (blue line), and radiation into the tellurite slab surrounding the waveguide at shorter wavelengths (red line).	76
Fig. 3.11	Simulated TeO ₂ -Si ₃ N ₄ waveguide properties for varying Si ₃ N ₄ strip width, including (a) effective index (b) optical confinement factor within the silicon nitride strip and tellurium oxide coating, (c) effective mode area and (d) minimum bend radius at which the waveguide is able to maintain radiation losses less than 0.01 dB/cm for the fundamental TE mode for 1.0, 1.2 and 1.4 μm × 0.2 μm silicon nitride strip waveguides with a 400-nm-thick TeO ₂ -coating at visible to near-infrared wavelengths.	77
Fig. 3.12	Simulated TeO ₂ -Si ₃ N ₄ waveguide properties for varying Si ₃ N ₄ strip height, including (a) effective index (b) optical confinement factor within the silicon nitride strip and tellurium oxide coating, (c) effective mode area and (d) minimum bend radius at which the waveguide is able to maintain radiation losses less than 0.01 dB/cm for the fundamental TE mode for 1.2 μm × 0.1, 0.2 and 0.3 μm silicon nitride strip waveguides with a 400-nm-thick TeO ₂ -coating at visible to near-infrared wavelengths.	78
Fig. 3.13	Diagram of fiber-chip coupling setup used in passive device characterization. Signal light is polarized with a set of polarization paddles and launched into then off the chip by aligning fibers to optical facets of waveguide with xyz stage. Intensity of light coupled off chip is measured by a photodetector.	79
Fig. 3.14	Loss of a TeO ₂ thin film on an unpatterned thermally oxidized silicon wafer measured by the prism coupling method at 638, 847, 980, 1310 and 1550 nm wavelengths. Inset: image showing red light propagation in the TeO ₂ film.	80
Fig. 3.15	Insertion loss measured versus waveguide length at 980, 1310, 1550 and 2000 nm, fit to have optical propagation losses of 3.1±0.3, 0.8±0.3, 0.8±0.3, and 0.6±0.2 dB/cm, respectively.	81
Fig. 3.16	(a) Top-down image of red light propagating through a 3.45-cm-long TeO ₂ -Si ₃ N ₄ waveguide. (b) Pixel intensity of image versus propagation length along the waveguide, fit to have an optical propagation loss of 8.4±1.1 dB/cm.	82

Fig. 3.17	Simulated fiber-chip coupling loss at 1550 nm, accounting for Fresnel reflection losses and mode mismatch of a 2.5 μm spot size fiber with TeO_2 - Si_3N_4 waveguides with varying width and TeO_2 layer thickness.	84
Fig. 3.18	Optical facets of uncoated Si_3N_4 waveguides prepared by (a) dicing, (b) etching and (c) focused-ion-beam polishing.	85
Fig. 3.19	Simulated electric field profiles at 1550 nm of the (a) symmetric and (b) antisymmetric modes of 1- μm -wide Si_3N_4 waveguides with a 0.5 μm coupling gap between the interior walls of the two waveguides, coated in a 150-nm-thick TeO_2 film.	87
Fig. 3.20	Calculated coupling rate parameter (\mathcal{C}) between the two waveguides shown in Fig. 3.18 versus coupling gap. The coupling coefficient is proportional to the difference in the effective index of the symmetric mode (n_s) and antisymmetric mode (n_A).	88
Fig. 3.21	Layout of a directional coupler system, with a defined coupler length of l_{Coupling} separated by a minimum coupling gap of G_0 with sine bend transitions with an amplitude of δ for a full period length of S on each side.	89
Fig. 3.22	Diagram showing contributions to loss when measuring directional coupler circuits. Light coupled through Port I will transmit a ratio of $T_{\text{C,I}}$ of the incident light as it is coupled onto the chip, after which it experiences a waveguide propagation loss of $T_{\text{WG,I}}$ while travelling down the arm of Port I. A certain percentage of light is coupled between waveguides in the coupling region, and an output signal can then be measured on either the thru or drop port of the coupler, ports III and IV respectively, each with their own associated coupling and propagation losses.	91
Fig. 3.23	Measured directional coupler cross-over ratio for 1- μm -wide Si_3N_4 strips with a 0.8 μm nominal coupling gap and coupling lengths from 0 to 80 μm coated in a 0.15- μm -thick TeO_2 coating at a 1550 nm wavelength. Also shown are the simulated cross-over ratios for the same structure with 0.8, 0.96 and 1.1 μm nominal coupling gaps, demonstrating better agreement with the simulated results for 0.96 μm gap. (b) Measured and simulated cross-over ratios at 1510, 1570 and 1630 nm wavelengths, compared to the simulated 0.96 μm coupling gap.	93
Fig. 3.24	Measured directional coupler cross-over ratio for 1- μm -wide Si_3N_4 strips with a 0.8 μm nominal coupling gap at a 1570 nm wavelength with (a) a 150-nm-thick TeO_2 -coating, (b) a 300-nm-thick TeO_2 -coating and (c) a Cytop cladding with no TeO_2 -coating, which are best fit to simulated coupling gaps of 0.96, 0.95, and 0.78 μm , respectively.	94
Fig. 3.25	Diagram of a microring resonator. Incident light from Port I of the bus waveguide that is coupled into the ring resonator through Port IV returns via Port II, creating an interference pattern in the transmitted signal power in Port III.	96

Fig. 3.26	Simulated (a) ring build up (T_{Ring}) and (b) ring transmission (B_{Ring}) ratios for a ring resonator versus the phase shift around the ring, for an amplitude attenuation coefficient of $\eta = 0.75$, and coupler transmission coefficients of $t = 0.6, 0.8$ and 0.9	97
Fig. 3.27	(a) Diagram of a microring resonator showing the radius R and coupling gap G , and top view SEM images of (b) a $\text{TeO}_2\text{-Si}_3\text{N}_4$ ring resonator and (c) the bus waveguide to ring coupling section.	99
Fig. 3.28	Measured resonance spectrum of a $\text{TeO}_2\text{-Si}_3\text{N}_4$ ring resonator (a) from 1510–1640 nm and (b) over a shorter wavelength range from 1620–1622 nm.	100
Fig. 3.29	(a) TeO_2 , Si_3N_4 and SiO_2 material dispersion relations from 600 to 1600 nm used to simulate the effective index, n_{Eff} , of a $\text{TeO}_2\text{-Si}_3\text{N}_4$ waveguide with Si_3N_4 strip dimensions of $1.0 \mu\text{m} \times 0.2 \mu\text{m}$ and TeO_2 -coating thickness of 330 nm, which is then used to calculate the group index, n_g . (b) Comparison of the group index calculated based on simulation, with error bars based on a ± 0.03 difference in TeO_2 refractive index, to the measured group index based on the microring resonator FSR.	101
Fig. 3.30	Transmission of 300 μm radius ring resonators with gaps of 0.9, 1.3 and 2.0 μm near 1550 nm wavelengths. The measured data points are fit using the coupled mode theory transmission equation to find loaded Q factors of 1.6×10^5 , 2.8×10^5 and 6.3×10^5 in the undercoupled, critically coupled and undercoupled regimes, respectively. The inset shows a close-up view of the transmission of the undercoupled resonator.	103
Fig. 3.31	(a) Loaded Q factor measured in rings with different coupling gaps, compared with the fitted maximum internal Q factor (Q_i) of 7.3×10^5 , which is used to calculate the external Q factor (Q_c) at each gap. (b) Measured and calculated extinction ratio of rings at different coupling gaps.	104
Fig. 3.32	Measured Q factor of 100, 200, 300 and 400 μm radius ring resonators. Radii of 300 μm and above demonstrate little difference in Q factor and are limited by the waveguide loss of 0.5 dB/cm. The 200 μm radius ring experiences a small drop in Q factor, while the 100 μm radius ring is dominated by radiation and experiences a significant drop in Q factor.	105
Fig. 3.33	Measured loss in 600 μm radii rings with 0.8, 1.0 and 1.2- μm -wide Si_3N_4 strips coated in tellurium-oxide layers of 130, 224, 283, 330, 380, 436 and 515 nm thickness. The data shows that waveguides with TeO_2 -coatings that are close to or thinner than the simulated single-mode TeO_2 thickness for a given Si_3N_4 strip width can maintain low waveguide losses, while thicker TeO_2 -coatings begin to experience a significant increase in waveguide loss.	106
Fig. 4.1	Optical processes in a two-level energy system, including (a) spontaneous emission, (b) optical absorption, and (c) stimulated emission.	115

Fig. 4.2	Energy level diagram of Er^{3+} ions in tellurium oxide and the relevant electron transition processes for an amplifier operating in the C-band, including optical, electrical, and thermal transitions.	118
Fig. 4.3	(a) Diagram of sub-level absorption and emission process between broadened ground and excited state energy bands. (b) Normalized, absorption and emission cross sections between the $^4\text{I}_{15/2}$ and $^4\text{I}_{13/2}$ energy bands of an erbium doped silica fiber [76].	121
Fig. 4.4	Measured transmission loss in a 2.93-cm-long $\text{TeO}_2:\text{Er}^{3+}\text{-Si}_3\text{N}_4$ waveguide from 1510 to 1630 nm, broken down into contributions from fiber losses ($L_{\text{Fiber}}(\lambda)$), fiber-chip coupling losses (L_{Coupling}), background waveguide optical propagation loss (L_{WG}), and erbium absorption loss ($L_{\text{Er}}(\lambda)$).	123
Fig. 4.5	(a) Erbium absorption cross section as estimated from RBS, with a peak cross section of $7.1 \pm 0.6 \times 10^{-21} \text{ cm}^2$ at 1531 nm measured in a $\text{TeO}_2:\text{Er}^{3+}$ waveguide with a concentration of $2.6 \times 10^{20} \text{ ions/cm}^3$. (b) Measured and calculated erbium absorption loss for a $\text{TeO}_2:\text{Er}^{3+}$ waveguide with an Er^{3+} concentration of $1.5 \times 10^{20} \text{ ions/cm}^3$ and 58 % optical confinement in the $\text{TeO}_2:\text{Er}^{3+}$ coating.	124
Fig. 4.6	Estimated erbium absorption cross section around 970 nm, based on 970 nm transmission measurements and the ion concentration of the device found from 1550 nm spectroscopy, with a peak cross section of $2.8 \times 10^{-21} \text{ cm}^2$ at 968 nm.	125
Fig. 4.7	(a) Setup used to measure the emission spectrum. (b) Emission cross section of $\text{TeO}_2:\text{Er}^{3+}$ around 1500 nm based on the back-collected ASE spectrum and scaled to match the measured absorption cross section.	126
Fig. 4.8	Diagram of rare-earth luminescent lifetime measurement setup.	128
Fig. 4.9	Lifetime measurements of the ASE signal intensity versus time (with offset to distinguish between the data sets) carried out on $\text{TeO}_2:\text{Er}^{3+}\text{-Si}_3\text{N}_4$ waveguides with erbium concentrations of 0.6, 0.9, and $1.5 \times 10^{20} \text{ ions/cm}^3$. The data is fit to have $^4\text{I}_{13/2}$ excited state lifetimes of 0.26, 0.31, and 0.21 ms, respectively. ...	128
Fig. 4.10	Measured luminescent lifetimes in several different $\text{TeO}_2:\text{Er}^{3+}$ waveguides with erbium dopant concentrations of between 0.6×10^{20} and $2.8 \times 10^{20} \text{ ions/cm}^3$. Minimal correlation was found between dopant concentration and luminescent lifetime, as was also seen in other $\text{TeO}_2:\text{Er}^{3+}$ work [36], with an average measured lifetime of 200 μs . A sample with a concentration of $2.2 \times 10^{20} \text{ ions/cm}^3$ deposited at a 140 °C temperature was seen to have a significant increase of luminescent lifetime up to 0.48 ms.	129
Fig. 4.11	Absorption saturation measurement setup diagram.	131

Fig. 4.12	(a) Measured erbium absorption loss at 1530 nm in a 2.93-cm-long waveguide coated in a 330-nm-thick $\text{TeO}_2:\text{Er}^{3+}$ film with an erbium concentration of 1.5×10^{20} ion/cm ³ versus launched signal power into the waveguide. The results are compared to calculations based on a three-level rate equation model which assume that 0% and 27% of ions are quenched. (b) Measured erbium absorption loss relative to the peak absorption at 1530 nm versus signal power launched into the waveguide, for three different waveguides fit to have 14, 27 and 38 % ion quenching.	132
Fig. 4.13	Estimated quenching fraction of samples versus (a) erbium dopant concentration, and (b) $^4\text{I}_{13/2}$ luminescent lifetime. In general quenching fractions are larger than those seen in Al_2O_3 samples [86], with the exception of a sample deposited at a 140 °C temperature with a 2.2×10^{20} ions/cm ³ erbium dopant concentration measured to have a 22 % quenching fraction. In general, longer excited state lifetimes are predicted to lead to reduced quenching fractions due to less pathways for quenching through OH^- impurity interactions [36].	133
Fig. 4.14	(a) 1637 nm resonance mode measured on a 1.0- μm -wide, 400- μm -radius silicon nitride ring resonator with a gap of 2.6 μm , coated in the same $\text{TeO}_2:\text{Er}^{3+}$ film as the gain sample, fit to have a Q factor of 1.3×10^6 . (b) Measured erbium absorption losses from 1460 to 1640 nm across 2.2- and 6.7-cm-long waveguides, indicating a peak absorption of approximately 3.2 dB/cm at 1531 nm.	136
Fig. 4.15	(a) ASE intensity versus decay time measured on the sample selected for gain measurements using the luminescent lifetime setup, fit to give a lifetime of 0.48 ms. (b) Relative erbium absorption in a 2.2-cm-long waveguide versus launched signal power, fit to give a quenched ion fraction of 22%.	137
Fig. 4.16	940 nm resonance mode measured in a 1- μm -wide, 300- μm -radius $\text{TeO}_2:\text{Er}^{3+}$ -coated silicon nitride ring resonator with a nominal coupling gap of 1.0 μm . The resonance is fit to have a Q factor of 2.5×10^5 , corresponding to an estimated optical propagation loss of 2.5 dB/cm at this wavelength.	138
Fig. 4.17	(a) Diagram of double-side pump measurement setup used to measure gain in $\text{TeO}_2:\text{Er}^{3+}$ amplifiers. (b) Image of a $\text{TeO}_2:\text{Er}^{3+}$ paperclip amplifier pumped with a 970 nm diode laser exhibiting green luminescence from radiative decays from the $^4\text{F}_{7/2}$ state.	139
Fig. 4.18	Internal net gain measured in a 2.2-cm-long $\text{TeO}_2:\text{Er}^{3+}$ -coated Si_3N_4 waveguide amplifier versus (a) launched pump power at a 1533 nm signal wavelength, and (b) wavelength at maximum available pump power for both 970 and 1470 nm pump wavelengths.	141
Fig. 4.19	Internal net gain measured in a 6.7-cm-long $\text{TeO}_2:\text{Er}^{3+}$ -coated Si_3N_4 waveguide amplifier versus (a) launched pump power at a 1533 nm signal wavelength, and (b) wavelength at maximum available pump power for both 970 and 1470 nm pump wavelengths.	142

Fig. 4.20	Measured and simulated internal net gain at 1558 nm versus launched signal power for the 2.2- and 6.7-cm-long waveguide samples pumped at 1470 nm. Minimal change in net gain is measured up to launched signal powers of -6 and -10 dBm in the 2.2- and 6.7-cm-long waveguides respectively, in agreement with predictions from simulations.	143
Fig. 4.21	Three-energy-level diagram for erbium-doped TeO ₂ and relevant transitions used in device simulations, including: stimulated transitions between the ground state and the second or third energy levels, spontaneous decay of the third and second energy levels, and energy transfer upconversion of two second level electrons to the ground state and third energy level.	144
Fig. 4.22	(a) Optical mode profile determined by an eigenmode simulation, versus, (b) effective optical mode profile with 22 active areal elements representing the relative optical intensity in the gain medium applied in the rate equation solver.	149
Fig. 4.23	(a) Diagram of operation method for rate equation model, where an initial optical power at a z position is broken down into areal elements based on the simulated mode profile. The population rate equations and intensity evolution are solved in each areal element, which then updates the initial power and intensities in the next z step along the length of the waveguide, where the process is repeated. (b) A more detailed logic flow diagram describing the rate equation model's calculation process.	151
Fig. 4.24	Simulation results showing the (a) average inversion ratio versus propagation length, (b) internal net gain versus propagation length and (c) internal net gain at the end of the waveguide versus simulation time of the rate equation model for a launched 1558-nm signal power of -20 dBm and launched 1470-nm pump powers of 1, 5 and 10 mW.	152
Fig. 4.25	Simulated internal net gain versus launched 1470 nm pump power for a 1558 nm signal with 0, 22, and 40% quenched ions compared to measured results, showing good agreement between simulation and measurement for a 22 % quenched ion fraction.	153
Fig. 4.26	Simulated internal net gain versus (a) launched 1470 nm pump power for a 1558 nm signal and (b) signal wavelength for 150 mW of launched pump power, for waveguide lengths of 5, 10, and 15 cm.	154
Fig. 5.1	Diagram of microcavity fabrication procedure. The foundry began fabrication with, [i] a 0.22- μ m thick silicon layer on a 2- μ m BOX [ii] which was patterned and etched to form the bus waveguides, [iii] after which a 3 μ m thick silicon dioxide top cladding is deposited, [iv] which was patterned and etched into a circular microtrench structure. Chips were then sent out of the foundry where [v] a tellurite coating was deposited in post-processing, forming the resonator layer.	166

Fig. 5.2	(a) Layout and dimensions of microtrench mask design, (b) SEM image of fabricated microtrench and (c) dimensions of silicon bus waveguide and width tapers.	168
Fig. 5.3	(a) Relevant dimensions of the fabricated microtrench cross section. (b) Cross sectional SEM image of a microtrench after a focused-ion beam cut. The trench was coated in a polymer to improve image quality.	169
Fig. 5.4	Cross-sectional SEM image of microcavity resonator exposed with a focused-ion-beam cut, showing a microtrench coated in a TeO ₂ film next to a silicon bus waveguide.	170
Fig. 5.5	(a) Cross-sectional profile of TeO ₂ coated microcavity and silicon waveguide, with relevant device dimensions used in simulations. (b) Simulated fundamental TE-polarized electric-field profiles for the fundamental mode of a TeO ₂ cavity with a 900-nm-thick TeO ₂ coating at a 100 μm bend radius, next to the simulated mode of a 0.22×0.30 μm ² silicon waveguide.	172
Fig. 5.6	Simulated electric-field mode profiles for a microcavity coated in a 900-nm-thick TeO ₂ film at bending radii of (a) 40 μm, (b) 100 μm and (c) 200 μm.	172
Fig. 5.7	Simulated (a) mode area and (b) optical confinement of the fundamental TE-polarized mode of microcavity resonator coated in TeO ₂ film thicknesses of 0.5 to 1.1 μm at bending radii of 40, 100, and 200 μm.	173
Fig. 5.8	Simulated radiation limited internal Q factors of microcavities coated in 500-, 700-, 900-, and 1100-nm-thick TeO ₂ coatings considering the effects of (a) bending radiation losses and (c) substrate radiation losses.	175
Fig. 5.9	Simulated (a) effective index of silicon bus waveguide versus waveguide width, and variation in effective index for a ±10 nm waveguide width variation, (b) effective index versus TeO ₂ coating thickness for microcavities with 40, 100 and 200 μm bending radii.	176
Fig. 5.10	Shaded box shows the simulation region for the silicon waveguide and microcavity resonator in (a) cylindrical coordinates and (b) mapped to Cartesian coordinates.	177
Fig. 5.11	Permittivity profile and normalized x polarized electric-field component and y polarized magnetic-field component of the optical mode profiles for the (a-c) microcavity resonator and (d-f) silicon bus waveguide.	178
Fig. 5.12	Cross-over ratio versus propagation length along the coupler for a 700-nm-thick TeO ₂ microcavity with a 0.30-μm-wide silicon bus waveguide at simulated coupling gaps of 0.14, 0.18 and 0.25 μm.	182
Fig. 5.13	Minimum calculated external Q factors between a 0.30-μm-wide silicon bus waveguide and TeO ₂ microtrench cavities with a 100 μm bend radius coated in 500-, 700-, 900- and 1100-nm thick TeO ₂ layers at coupling gaps between 0.10 and 0.45 μm.	183

Fig. 5.14	(a) Transmission spectrum of microtrench cavity from design A, with a 1100-nm-thick TeO ₂ coating. (b) A fundamental mode of the device fit using the Q factor fitting code to have an internal Q factor of 1.6×10^5 at a wavelength of 1597 nm.	185
Fig. 5.15	(a) Transmission spectrum of microtrench cavity from design B, coated in 1115-nm of TeO ₂ , with inset showing a close-up view of two resonant free spectral ranges. (b) A fundamental mode of the device fit using the Q factor fitting code to have an internal Q factor of 0.9×10^5 at a wavelength of 1627 nm.	186
Fig. 5.16	(a) Transmission spectrum of microtrench cavity from design B, with a 100-nm-thick Cytop layer under a 630-nm-thick coating of TeO ₂ , with inset showing a close-up view of two resonant free spectral ranges. (b) A fundamental mode of the device at a wavelength of 1566 nm fit to have an internal Q factor of 2.1×10^5	188
Fig. 5.17	(a) Resonance spectra of a microcavity coated in 1100-nm of TeO ₂ at temperatures from 20 to 40 °C. (b) Thermal shift of resonances versus temperature for 480-, 900- and 1100-nm-thick TeO ₂ coated cavities fit with thermal sensitivities of 28, 47 and 30 pm/°C respectively.	189
Fig. 5.18	Resonance spectra measured for optical microcavities coated in (a) 900- and (b) 1100-nm-thick TeO ₂ films before and after the chips were coated in a layer of DI water.	191
Fig. 5.19	Measured resonance shift versus cladding refractive index for a 900-nm-thick TeO ₂ microcavity coated in solutions with various concentrations of glycerol and DI water.	192
Fig. 5.20	Resonance modes of (a) 900- and (b) 1100-nm-thick TeO ₂ coated optical microcavities before and after being coated in a layer of DI water showing reduced Q factors.	192
Fig. 5.21	Simulated (a) wavelength shift and (b) RIU sensitivity versus evanescent medium refractive index for cavities with 500 to 1100-nm-thick TeO ₂ coatings.	193

List of Tables

Table 1.1	Summary of different optical functionalities and properties demonstrated in several of the most common integrated photonic material systems.	6
Table 1.2	Comparison of selected properties of Si, Si ₃ N ₄ and TeO ₂	16
Table 1.3	Comparison of TeO ₂ waveguide properties ($\lambda = 1.5 \mu\text{m}$, TE polarization).	17
Table 2.1	Deposition parameters and thin film properties over the first several deposition processes for a newly installed Te target at a 125 W forward sputtering power.	54
Table 2.2	Optimized deposition parameters for RF reactive sputtered TeO ₂ thin films. ..	55
Table 3.1	Average and standard deviation of coupling loss per facet measured on diced, etched, and FIB polished TeO ₂ -Si ₃ N ₄ waveguides using tapered fibers	85
Table 4.1	Comparison of TeO ₂ :Er ³⁺ -coated Si ₃ N ₄ waveguide samples' spectroscopic properties.	134
Table 4.2	Default parameters used in the simulation and optimization of waveguide amplifiers.	152
Table 5.1	Layout parameters for microtrench devices in Design A and B.	170
Table 5.2	Measured properties of TeO ₂ coated microcavities characterized on chip design A.	186
Table 5.3	Measured properties of TeO ₂ coated microcavities characterized on chip design B.	187

List of Acronyms

PIC	Photonic Integrated Circuit
CMOS	Complementary metal-oxide-semiconductor
SOI	Silicon-on-insulator
SHG	Second harmonic generation
THG	Third harmonic generation
FWM	Four wave mixing
SCG	Super continuum generation
KCG	Kerr comb generation
SPM	Self phase modulation
TO	Thermo optic
PD	Plasma dispersion
EAM	Electro absorption modulation
SO	Stress optic
R	Raman
CVD	Chemical Vapor Deposition
PVD	Physical Vapor Deposition
CSD	Chemical Solution Deposition
MBE	Molecular Beam Epitaxy
MOVPE	Metal Organic Vapor Phase Epitaxy
TPA	Two-photon absorption
PECVD	Plasma-Enhanced Chemical Vapour Deposition
LNOI	Lithium-niobate-on-insulator
CMP	Chemical mechanical polishing
DBR	Distributed Bragg reflector
DFB	Distributed feedback laser
RF	Radio Frequency
RBS	Rutherford backscattering spectrometry
CEDT	Center for Emerging Device Technologies
RPM	Revolutions per minute

MFC	Mass flow controller
DC	Direct current
VASE	Variable angle spectroscopic ellipsometer
TE	Transverse electric
TM	Transverse magnetic
TIR	Total internal reflection
LPCVD	Low pressure chemical vapor deposition
SEM	Scanning electron microscopy
FIB	Focused-ion-beam
SM	Single mode
SOA	Semiconductor optical amplifier
ALD	Atomic layer deposition
GSA	Ground state absorption
ESA	Excited state absorption
ETU	Energy transfer upconversion
CR	Cross relaxation
OSA	Optical spectrum analyzer
WDM	Wavelength division multiplexor
NSA	Non saturable absorber
EDFA	Erbium doped fiber amplifier
RIU	Refractive index units
CMC	Canadian Microsystems Corporation
BOX	Buried oxide
FDTD	Finite-difference time-domain
DI	Deionized
LOD	Limit of detection

Declaration of Authorship

I, Henry C. Frankis, declare that the thesis, “Low-Loss Tellurium-Oxide Devices Integrated on Silicon and Silicon Nitride Photonic Circuit Platforms” was written by and presents research work lead by myself.

Contributions made by others to this work include:

Chapter 2

- Jeremy W. Miller and Dawson. B. Bonneville assisted with modelling and fitting RBS data.

Chapter 3

- Waveguide design and layouts were made in collaboration with Chenglin Zhang and Dawson B. Bonneville.
- Silicon-nitride photonic chips were fabricated at the LioniX foundry.
- Dawson B. Bonneville, Khadijeh Mirabbis Kiani and Daniel Su assisting in taking optical measurements related to fiber-chip coupling loss, microresonators, and cutback losses.
- Dr. Zhan Su provided the original code for fitting resonance spectrum data.
- Samuel Norris assisted with developing the optical facet FIB milling fabrication process.

Chapter 4

- Hamidu M. Mbonde and Dr. Renjie Wang contributed to developing the excited state lifetime measurement setup.

Chapter 5

- Dawson B. Bonneville assisted in layout design of microcavity resonator circuits.
- Silicon photonic chips were fabricated at the IME/AMF foundry.
- Daniel Su assisted in taking passive and sensing measurements of microcavity devices.

CHAPTER 1

Introduction

1.1 Integrated Optics

The concept of integrated optics, which involves the implementation of photonic integrated circuits (PICs) on a compact substrate, was first devised of and explored in the early 1970's [1], where the potential for small sizes, thermal and mechanical stability, and various applications garnered significant interest. The following years saw the initial development of many basic integrated photonic components and their fundamental theory [2], as well as progress on silicon (Si) as an integrated photonic material (silicon photonics) in the mid 1980's through the 1990's [3]. The anticipated deployment of PICs for high-speed optical interconnects in data centers fueled a surge in the development of integrated photonic devices/systems and processing infrastructure beginning in the early 2000's [4,5]. Currently, the first generation of integrated photonic products have begun entering the data center market, which is experiencing constantly increasing data and power consumption requirements [6] as global data needs continue to grow into the 'Zettabyte Era' [7]. The development of high-performance photonic circuit components as well as the increasing access to low-cost, wafer-scale production has seen integrated photonics more recently proposed for applications branching into light detection and ranging (LiDAR) scanners [8,9], holographic and augmented reality display technology [10-12], biological sensors for medical purposes [13,14], quantum computing [15,16] and free-space wireless communications networks [17,18]. With such a wide range of potential applications integrated optics research is experiencing a push for both improved device performances as well as a more varied library of device functions.

Much like the transition from discrete components to integrated microelectronic devices revolutionized the capabilities of electrical systems [19-21], integrating photonic systems onto chips provides several significant advantages over bulk and fiber-based optical systems. Firstly, the compact size of integrated devices enables a range of applications towards portable systems, from ultra-small form factor pluggable transceivers at data centers [22,23], to handheld biological and environmental sensing products [24]. Additionally, integrated systems that include all the photonic circuit components on a single chip eliminate the need for time-consuming and expensive post-processing alignment between different components, have improved thermal and mechanical stability, and can enable the co-integration of integrated electrical circuitry into the same package [3,25]. Lastly, integration allows photonic circuits to be produced at low costs and high volumes through wafer-scale processing techniques [26,27].

Like electrical circuits, photonic circuits can become increasingly complex with widely varying applications, but much of their functionality can be achieved with only a handful of base components. For example, the simplest schematic of an optical data link circuit [28,29] would require a light source (signal laser), an optical switch that responds to an electrical or environmental input to modify the transmission path or intensity of light (modulator/switch), and a light detection component to convert optical signals to the electrical domain (photodetector), all of which are connected by an optical transmission bus (waveguide). As systems become more complex and designed for specific applications various additional photonic components, such as wavelength multiplexors and filters, power-splitters, time delay elements, and optical amplifiers become necessary additions to the photonic component library.

One of the primary challenges in PIC design is finding a material or combination of material systems that can reliably perform all the necessary functions of an optical circuit, while maintaining low-cost and high-volume production. Because of large variations in optical, electronic, structural and chemical properties, a wide array of materials have been proposed and studied in integrated optical applications. Of particular interest are photonic materials and devices that can be fabricated using the complementary metal-oxide-semiconductor (CMOS) methods used in silicon microelectronics processing, to leverage both the existing knowledge and infrastructure. The use of CMOS fabrication technology enables low-cost, high quality and high-volume manufacturing as well as rapid scaling of performance and functionality in photonic microsystems. Currently integrated optics is in the process of transitioning into a ‘fabless’ industry [30,31], where high-quality, standardized, integrated photonic chip fabrication is made cheaply and easily accessible to researchers and industry alike, while creating an ever-expanding library of tested and verified components that can be ‘dragged and dropped’ into more complex system designs. Thus, integrated photonics has begun to shift predominantly towards silicon-on-insulator (SOI) [26,27], and silicon nitride-on-insulator [32-35] based waveguides due to their CMOS infrastructure compatible processing and well-developed component libraries and will likely continue to merge towards combined multilayer platforms in the future [35,36]. While this standardization process is an important step towards producing high performance PICs in large volumes, one of the trade-offs is the limitation in the ability to introduce novel materials, which can provide some of the functionalities which are missing in standard PICs.

In this introduction we review and compare the strengths and weaknesses of various material systems for integrated photonics, as well as the potential fabrication approaches and waveguide designs for creating combined material system (hybrid) photonic platforms, particularly on silicon and silicon nitride. We then propose tellurium oxide (TeO_2) as material of significant interest for back-end integration with PICs due to its promising linear, nonlinear and active (light-emitting) optical properties. The remainder of the thesis then focuses on the experimental design, realization, and characterization of TeO_2 waveguide structures and devices integrated onto standardized silicon and silicon nitride photonic platforms.

1.2 Integrated Optical Functionalities and Materials

There are many different material systems of interest for integrated optics. Here we aim to provide a summary of the various strengths and weaknesses of several of the most common material systems, in order to place the work of this thesis in context to the larger field of integrated optics and provide the background and motivation for TeO₂, silicon and silicon nitride devices and PIC platforms. To assess and compare the capabilities of the different material systems we have identified the following properties as the primary functions of interest with regard to designing integrated photonic microsystems:

- **Optical transmission:** The transmission of light in a waveguide to transport a signal between various on-chip devices is the most basic function of a PIC. Waveguides also form the basis of most passive circuit elements, such as filters and multiplexors, and active devices such as modulators and detectors. A basic waveguide consists of a core material surrounded by a cladding material with higher and lower refractive index, respectively, such that light is guided along the core by total internal reflection. To minimize signal loss between on-chip elements and create high quality devices, waveguides ideally exhibit minimal optical propagation losses. This is achieved through high-quality materials with low absorption, as well as low sidewall scattering at the core-cladding interface, by using smooth etching recipes and lower refractive-index-contrast waveguide designs. However, it is also important for waveguides to confine light tightly enough to maintain small bending radii, which keeps devices on a scale compatible with integrated systems, where large core-cladding index contrast is preferred, presenting a tradeoff in design.
- **Switching/modulation:** To encode information into the optical domain waveguides must respond to an external, typically electrical, stimulus which modifies the material properties to affect the phase or intensity of light propagating through the device. Optical switching techniques can be amplitude-based, where the stimulus directly changes the loss of the waveguide, or phase-based, where the stimulus results in a change to the speed of light travelling through the waveguide. To operate as a switching element, phase-based switching techniques require an interferometric structure, where the changes to phase can be used to adjust the interference condition. While amplitude modulation can be implemented directly on a simple straight waveguide, to enhance power consumption efficiency and reduce device sizes amplitude modulators are also typically implemented in an interferometric structure. Phase-based tuning can be applied to almost all materials via the thermo-optic effect, where an electrical input to a resistive heating element can be used to change the refractive index of the material and thus the speed of light. However, the slow thermal response time and large energy consumption limits temperature-based phase tuning techniques

to low-speed, or constant offset applications. In order to achieve the high-speed modulation necessary for data-processing applications alternative switching methods are required, such as the electro-optic (Pockels) effect [37] available in non-centrosymmetric crystals, or by controlling the carrier concentrations and bandgaps of semiconductors via the plasma-dispersion [38] and the Franz-Keldysh [39] effects, respectively.

- **Light detection:** To measure the power of an optical signal it must be converted to the electrical domain. Ideal photodetectors maximize responsivity producing a large electrical signal relative to the optical intensity, respond linearly to changes in optical signal power with minimal noise, and can operate at speeds compatible with high-speed optical modulation. Detectors typically require semiconductor materials that can absorb photons of the desired wavelength to promote electrons into the conduction band, which can then be swept into the electrical circuit and collected as photocurrent. Therefore, a significant portion of the optimization and design of photodetectors is geared towards electrical circuit design as well as material and optical properties. Key properties for detector materials include a large absorption coefficient to increase responsivity over small device lengths, large carrier mobility for fast response times, and minimal dark current for low noise operation.
- **Optical gain/light emission:** An optical source, typically a laser, is required in photonic circuits to provide the signal to the system. Due to the current difficulties in fabricating electrically-pumped lasers in most material systems other than III-Vs it is common to use an off-chip laser source that is then coupled onto the chip from a fiber, particularly in silicon photonics. However, there are a growing number of approaches to realize lasers which are integrated directly on the photonic chip. The three primary elements of a laser are the optical gain medium, the pump source, and the optical cavity. The optical gain medium is responsible for photon emission, typically through the stimulated emission process, which requires a majority of the light emitters (electrons) in the medium to enter an excited energy state. The two most common approaches to this are either through electrical carrier injection of electrons into the conduction band of a semiconductor, or optical excitation of dopants such as rare-earth ions in a rare-earth soluble host medium. When an excited optical gain medium is surrounded by an optical cavity, the photon emission has the potential to build up in intensity which can eventually lead to laser emission. Integrated photonic resonant cavities, which can be designed in several ways, most typically use either ‘mirrors’, based on waveguides with periodic features in the Bragg regime, or a closed loop resonator. Without the cavity, the gain medium can be used as an optical signal amplifier to boost signal light as it travels between different components. Amplifiers are expected to become increasingly important circuit elements to

compensate transmission and device insertion losses as the complexity and scale of on-chip photonic systems grows.

- **Nonlinearities:** Optical nonlinearities are a growing domain of interest in integrated photonics. There are many specific nonlinear processes which can occur in materials, but all are generally the response of a material to a high intensity optical input signal that generates light at another wavelength through either an up- or down-conversion process, or a combination thereof. A brief summary of the distinctions between various nonlinear effects [41] is provided here. Upconversion processes such as second (SHG) and third harmonic generation (THG) occur when two or three photons, respectively, of the same wavelength combine to generate a photon at a lower wavelength. Four wave mixing (FWM) is a similar process in which two incident photons, which can be of the same (degenerate) or different wavelengths (nondegenerate) combine to generate a shorter (signal) and a longer (idler) wavelength photon with total energy equal to the two incident photons. If the signal and idler build up enough intensity to generate their own FWM processes cascaded FWM can occur, resulting in supercontinuum generation (SCG) of light over a broad wavelength range from a monochromatic input. An SCG process in an optical cavity can be used to realize frequency combs, referred to as Kerr comb generation (KCG) in microcavities, which have applications in precision spectroscopy and measurement instruments as well as multichannel light sources. Nonlinear optical effects can also alter the refractive index of the medium, which for pulsed light inputs can stretch the signal resulting in a spectral broadening, referred to as self phase modulation (SPM). Raman scattering, where light inelastically scatters from molecules can create either an up or down conversion of the signal and stimulated Raman scattering is applied in amplifiers and lasers. Light scattering from macroscopic scale vibrations of the material can cause similar effects through Brillouin scattering. Efficient nonlinear processes require large nonlinear figures of merit for the specific nonlinear mechanism, as well as low waveguide losses, low nonlinear two-photon absorption and the ability to dispersion engineer waveguides for phase matching and maintaining pulse shapes.

A summary of several common integrated photonics materials and their various mature optical and optoelectronic functionalities is given in Table 1.1. While some of the material systems mentioned might have realized certain functionalities in other platforms, we include only functionalities which are well established in integrated systems. Additionally, to narrow discussions further we predominantly focus on high index contrast waveguides suitable for densely integrated microsystems, which are typically achieved through thin film technologies. The materials are divided into four distinct groups based on their composition and properties: (i) group IV semiconductors, (ii) dielectrics, (iii) wide bandgap crystals, and (iv) III-V semiconductors. In general, group IV and dielectric materials use low-cost wafer scale

processes and can be built on CMOS fabrication infrastructure, while III-V's and other crystalline materials do not.

Table 1.1 Summary of different optical functionalities and properties demonstrated in several of the most common integrated photonic material systems.

	Material system	Waveguide loss and minimum wavelength	Switching/modulation methods	Light detection schemes	Optical gain / light emission	Non-linearities	Fab. methods
Group IV	Si [41-52]	2 – 3 dB/cm >1100 nm	TO, PD	PN junction	–	R, SHG, KCG	Smart cut
	Ge [53-57]	2.5 dB/cm >1700 nm	EAM	PN junction	Carrier injection	–	Epitaxy
	SiC [58-61]	2 – 4 dB/cm >400 nm	TO	–	–	SPM	CVD, Smart cut
Dielectrics	Si ₃ N ₄ [62-66]	0.001 – 0.009 dB/cm >300 nm	TO	–	–	SHG, THG, FWM, SCG, KCG	CVD
	SiO ₂ [67-69]	0.1 dB/cm >300 nm	–	–	–	–	Thermal, CVD
	Al ₂ O ₃ [70-74]	0.2 dB/cm >300 nm	–	–	Rare Earths	FWM	PVD
	TeO ₂ [75-78]	0.1 dB/cm >300 nm	–	–	Rare Earths	SPM	PVD
	AlN [80-84]	0.6 dB/cm >300 nm	Pockels	–	–	THG, FWM, KCG	PVD
	PZT [85-88]	–	SO, Pockels	–	–	–	CSD
Crystal	LiNbO ₃ [89-99]	0.4 dB/cm >400 nm	Pockels	–	Rare Earth	SHG, KCG	SmartCut
III-V	InGaAsP [100-105]	2 – 4 dB/cm >1250 nm	PD, EAM	PN junction	Carrier injection	–	MBE, MOVPE
	AlGaAs [106-110]	0.4 – 2.0 dB/cm >600 nm	–	–	–	SHG, FWM, KCG	MBE, MOVPE

TO – Thermo Optic; PD – Plasma Dispersion; EAM - Electro Absorption Modulation; SO - Stress Optic; R - Raman; SPM – Self Phase Modulation; FWM – Four Wave Mixing; THG – Third Harmonic Generation; SHG – Second Harmonic Generation; CVD – Chemical Vapor Deposition; PVD – Physical Vapor Deposition; CSD – Chemical Solution Deposition; MBE – Molecular Beam Epitaxy; MOVPE – Metal Organic Vapor Phase Epitaxy.

Silicon (Si) is currently one of the most well-established platforms for integrated photonics, largely due to the extensive processing infrastructure that already exists from the microelectronics industry, and the well-developed library of high-performance optoelectronic components. Silicon-on-insulator (SOI) wafers can be fabricated by the SmartCut process [41], whereby a thicker handle substrate is wafer bonded onto the thermally oxidized wafer and cut into a thin film. Si waveguides can achieve moderate optical propagation losses around 1550 nm of typically 2–3 dB/cm [42-44]. However, the ubiquity of the Si waveguide platform arises from its excellent optoelectronic functionality. While the thermo-optic effect can be used for low-speed switching and wavelength trimming [45], high speed modulation can be achieved through the plasma dispersion effect, whereby variations in the refractive index and absorption of the Si waveguide can be controlled by the concentration of free carriers. By forming a PN junction across the waveguide and varying the applied bias, modulation at up to 50 Gb/s [46] has been demonstrated. Additionally, although silicon is nominally transparent at telecom wavelengths, optical absorption through deep traps has been used to demonstrate photodetection in pure silicon waveguides [47], with additional defects added via post-processing used to demonstrate detection up to 2000-nm wavelength [48]. However, the potential for light emission from silicon remains a challenge due to its indirect bandgap. Several years ago, the Raman effect, excited by a high power 1536 nm wavelength source travelling through a silicon waveguide was used to demonstrate the first instance of a laser on an all-silicon platform operating at a wavelength of 1669 nm [49]. However, the techniques required to reduce two-photon absorption (TPA) and nonlinear losses in the silicon waveguide to achieve Raman lasing are complex and the wall-plug efficiencies remain low. The large TPA has also limited the demonstration of other nonlinear functions in Si, such as the demonstration of a Kerr-combs and second harmonic generation, to mid-infrared wavelengths ($>2\ \mu\text{m}$) with specialized processing modifications required to reduce losses [50-52]. Currently there remains no established and effective method for fabricating light emitting devices directly in silicon.

Germanium (Ge) is a group IV semiconductor with a much smaller bandgap than that of silicon of around 0.7 eV, corresponding to a photon wavelength of approximately 1700 nm. This makes germanium an unsuitable material for waveguiding applications in the telecom C-band, as it exhibits significant optical absorption. However, germanium has more recently generated interest as a waveguiding material for mid-infrared devices through the germanium-on-silicon platform, capable of operating at wavelengths of up to 8500 nm with moderate propagation losses of down to 2.5 dB/cm [53]. While the absorption at wavelengths below ~ 1700 nm makes germanium an inappropriate material for C-band waveguides, it does make it an ideal material for photodiodes at telecom wavelengths. The development of high-quality epitaxial growth of germanium on silicon [54] has allowed for the realization of germanium photodetectors on silicon waveguide platforms, achieving responsivities of 0.8 A/W at data rates of up to 40 Gb/s [55]. Although, like silicon, germanium is nominally an indirect bandgap material, its direct band gap of approximately 0.8 eV is only slightly larger than its indirect gap.

Through the use of strain and appropriate doping, carrier injection into the direct band has been observed to allow light emission down to 1576 nm wavelength in germanium/silicon platforms [56]. However, efficiencies are low and extremely high voltages are required. Similarly, electrically stimulated modulation of the absorption coefficient resulting from the direct band-gap of germanium through the Franz-Keldysh effect has been used to demonstrate electro-absorption modulators operating at up to 56 Gb/s at 1610 nm, but the ability to maintain open eyes drops off dramatically at shorter wavelengths [57].

Silicon-carbide (SiC) is nominally a group IV semiconductor, though due to its large bandgap its properties are much closer to that of a dielectric. Recent advances in the deposition of SiC through plasma-enhanced chemical vapor deposition (PECVD) [58] have facilitated the rapid development of SiC as an integrated photonic waveguide material. Its large nonlinear refractive index, comparable to that of silicon, and low multi-photon absorption coefficients and thermal sensitivities makes SiC a material of great interest for nonlinear functions [58]. While self phase modulation [58,59], and tuning by integrated micro heaters [60] have been demonstrated in SiC waveguides, their relatively large propagation losses of 2-4 dB/cm [58, 61] currently limit the realization of higher order nonlinear functions.

Silicon nitride (Si₃N₄) has become an integrated optic material of increasing significance because of its ultra-low waveguide propagation losses and mature, low-cost fabrication methods. Low-loss silicon nitride thin films can be grown on thermally oxidized silicon substrates by a low-pressure chemical vapor deposition process. It can be patterned into thin and wide low-confinement strip waveguide structures designed to minimize sidewall scattering losses, leading to propagation losses as low as 0.1 dB/m for a 40-nm-thick by 6- μ m-wide strip [62]. Thicker Si₃N₄ layers can increase optical confinement but result in a tradeoff of increased losses up to \sim 9 dB/m for 100-nm-thick by 2.8- μ m-wide strip waveguides [63]. These ultra-low optical propagation losses allow silicon nitride to achieve waveguides with very efficient nonlinear optical processes despite its relatively low nonlinear refractive index. Recent advances in processing, which allow for silicon nitride thin films to be grown to large thicknesses without film-cracking, have enabled appropriate dispersion engineering of Si₃N₄ waveguides and numerous demonstrations of FWM, SCG and KCG [64,65]. However, despite its excellent passive and nonlinear optical properties, there currently exists no effective solution to implement optical switching, other than thermal phase tuning [66], or light detection and emission directly in silicon nitride. More complex active and optoelectronic devices in Si₃N₄ therefore typically requires hybrid integration of a secondary material.

Silicon dioxide (SiO₂), or silica, is the primary core material for fiber optic cables. Low index contrast waveguides fabricated in thermal SiO₂ on silicon wafers by implantation [67] or diffusion [68,69] of dopants have demonstrated <0.1 dB/cm losses and maintain some niche applications. However, the large mode size and bending radius requirements of low index contrast waveguides are unsuitable for dense on-chip integration, and high-index-contrast waveguides are difficult to achieve with SiO₂ cores because its relatively low material refractive index (1.44 at 1550 nm), cannot achieve appropriate index contrast with most cladding

materials common in integrated photonics. Therefore, the primary function of SiO_2 in high-index-contrast integrated optics is as a highly stable, low-loss, cladding material used in combination with other waveguide core materials. Thermally oxidized silicon wafers provide an excellent substrate and bottom cladding material with ultra-low losses that can be cheaply and easily grown. SiO_2 deposited by chemical vapor deposition (CVD) is also an appropriate top cladding material for almost all materials, although it has slightly higher material losses than thermal SiO_2 [63].

Many other oxide glasses with larger refractive indices have been investigated as waveguide materials. Oxide-based glass thin films can be deposited onto various substrates using reactive sputtering deposition, whereby a metallic target is sputtered in an oxygen ambient. The oxide glass thin films can then be patterned into waveguides by etching [70]. Al_2O_3 thin film ridge waveguides have demonstrated low waveguide losses of ~ 0.2 dB/cm [71] and have been extensively studied for their potential for rare-earth doped optical amplifiers and lasers. Net gain of up to 20 dB/cm has been measured at 1533 nm in erbium-doped Al_2O_3 waveguides [72] and a variety of rare-earth-doped Al_2O_3 waveguide lasers have been demonstrated [73]. Explorations of nonlinear optical effects in an Al_2O_3 resonator have demonstrated the occurrence of four-wave mixing on integrated platforms [74]. TeO_2 is another oxide glass that has demonstrated waveguide losses of < 0.1 dB/cm [75], as well as net gain of up to 14 dB and lasing in erbium-doped TeO_2 waveguides [76,77]. Furthermore, while TeO_2 has relatively large nonlinear figures of merit for an oxide glass, limited work has been explored for its use in nonlinear applications prior to this thesis. Prior nonlinear results have demonstrated self phase modulation (SPM) in TeO_2 ridge waveguides [75], and the use of erbium doped TeO_2 as a loss compensation mechanism in combination with chalcogenide waveguides [78]. While here we discuss only Al_2O_3 and TeO_2 several other oxide glass materials films have been studied in integrated photonics platforms with various promising properties [79].

Aluminum nitride (AlN) is a thin film material that has been widely used in electromechanical systems, however it also has several unique properties of interest for integrated optics. Polycrystalline AlN thin films can be grown by reactive sputtering [80,81] which exhibit a moderately high electro-optic (Pockels) coefficient of ~ 1 pm/V [80,81]. AlN ridge waveguides have demonstrated reasonably low waveguide losses of 0.6 dB/cm, as well as modulation speeds of up to 5 Gb/s at a 1550 nm [80,81]. Although these speeds are lower than those seen in other material systems, modulation via the Pockels effect does not require multiple masking and dopant implantation steps, thus AlN could potentially provide a low-cost modulation source for moderate speed applications. As well as applications in electro-optic modulation, AlN also has a reasonably large optical nonlinearity, leading to demonstrations of efficient second and third harmonic generation, four-wave mixing and Kerr comb generation demonstrated in ridge waveguides [81-84].

Lead zirconate titanate (PZT) is a material with a large piezo-electric and electro-optic response. PZT thin films are grown by the chemical solution deposition (CSD) method, also referred to as the sol-gel process, where a liquid solution is coated onto a surface and then

densified in a heat treatment [85]. A lack of suitable etch recipes has limited the ability to fabricate waveguides directly in the PZT layer [86], however, PZT coatings on Si_3N_4 waveguides have demonstrated it as a material with great potential for modulation applications. Modulators based on the piezoelectric effect, whereby a voltage applied to a PZT layer stresses the underlying waveguide and creates a phase shift has enabled switching speeds into the high kHz [87], while electro-optic modulators in PZT thin films have demonstrated up to 40 Gb/s modulation on a Si_3N_4 waveguide platform [88].

Lithium-niobate (LiNbO_3) is one of the primary materials used for optoelectronic functionality in fiber communications, due to its large electro-optic response of ~ 33 pm/V and high nonlinear figures of merit. Weakly guided LiNbO_3 waveguides in bulk glass can be defined through methods such as titanium dopant diffusion or proton exchange [89,90]. However, with regard to high-index-contrast devices, lithium-niobate has only more recently made progress through the lithium-niobate-on-insulator (LNOI) platform which is enabled by the development of a lithium niobate SmartCut style process [91]. Ridge style waveguides in the LNOI platform have demonstrated waveguide losses of down to 0.4 dB/cm [92,93], with modulation speeds of up to 100 Gb/s in Mach-Zehnder phase modulators through the Pockels effect [94]. Erbium-doped LiNbO_3 waveguides studied in bulk glass have demonstrated large and narrow absorption and emission cross sections, which is advantageous for highly efficient and stable lasers, but limits applications as an amplification medium in multiplexed wavelength signal systems [95,96]. Erbium-doped devices in LNOI are still in the early stages of development. Recent results have measured up to 5 dB of net gain in a 0.5 cm long erbium doped waveguide at a narrow wavelength range around 1530 nm [97,98]. Similarly, despite its early development LNOI platforms have already demonstrated second harmonic generation and Kerr-combs on integrated platforms [91,99].

III-V semiconductors could be considered the material platform best able to accomplish the diverse range of functionalities desired for integrated photonic technologies. However, the growth of III-V wafers and stack layers is highly expensive, limited to small sizes, and uses non-CMOS compatible materials and processes, resulting in a significant tradeoff regarding their use as integrated photonic materials [100]. The indium gallium arsenide phosphide (InGaAsP) platform is the most well developed III-V integrated photonic material system. Starting with an InP substrate a stack of several material layers with varying concentrations of the four elements are selectively grown on the substrate in a molecular beam epitaxy (MBE) or metal organic vapor phase epitaxy (MOVPE) process. An InGaAsP layer with a band edge near 1250 nm is grown on the substrate to provide vertical index confinement and then etched to obtain lateral confinement, with waveguide losses typically ranging from 2–4 dB/cm depending on the exact waveguide shape [101]. Thin InGaAsP layers with band edges at a wavelength greater than 1250 nm can be grown as a series of quantum wells on select areas of the waveguides. The growth of a p-doped InP layer on top of the waveguide creates a PN junction across the quantum well with the n-doped InP substrate. Due to their direct bandgap these III-V devices can operate as highly efficient light emitters and detectors, with the

operating wavelength tuned by the composition of the quantum well layer. When operated in forward bias the PN junction device can act as an optical amplifier or laser which is electrically pumped via carrier injection with high efficiencies, such that 120 mA injection current is able to create 20 dB of modal gain in less than a 6 mm length [101]. When operated in reverse bias the PN junction device can act as a photodetector capable of approaching speeds of 80 Gb/s [102]. When the PN junction is fabricated in areas without the quantum well layers it can be used as an optical modulator via the plasma-dispersion effect, demonstrating up to 40 Gb/s modulation speeds [103,104]. The large two photon absorption coefficient in InGaAsP compounds, which can be almost an order of magnitude greater than those in silicon severely limit the non-linear applications of InGaAsP waveguides [105], however, AlGaAs is an alternative III-V combination which can have a band gap tuned from an approximately 900 to 600 nm photon absorption edge. While this limits applications of AlGaAs in modulation and detection at telecom wavelengths, it significantly reduces the two-photon absorption rate around 1550 nm wavelengths allowing for several demonstrations of non-linear processes in AlGaAs waveguide platforms [106-110].

While this section has provided an overview of many common materials it is not a comprehensive list and many other material systems of interest exist and have received significant attention in integrated photonics. For example, tantalum pentoxide (Ta_2O_5) [111,112] and phosphates [113] are other high index oxide glasses similar to Al_2O_3 and TeO_2 which have been studied for their nonlinear and rare earth doped properties. Additionally, non-oxide based glasses, such as chalcogenides [114,115] and fluorides [116,117], have many promising nonlinear and rare-earth spectroscopic properties, but suffer from poor thermal and chemical stabilities. Polymer and organic based materials, such as graphene layers, have potential for low-cost waveguide technologies with applications in rare-earth devices [118] as well as modulation [119] and detection [120], but have lifetime and degradation concerns which limit applications in some cases. Other crystalline material systems such as yttrium oxide (Y_2O_3) [121] and potassium yttrium double tungstate ($\text{KY}(\text{WO}_4)_2$) [122], offer high gain and efficient light emission in rare-earth doped devices, similar to LiNbO_3 , but do not have as well developed electrooptic functionality and are still under development for integrated optics.

1.3 Material and Waveguide Integration Schemes

The development of high index contrast integrated photonic platforms begins with the choice of material substrate, also known as the handle wafer, which is typically several hundred micrometers thick and provides both physical rigidity to the photonic chip and a platform for fabrication. Silicon is commonly used as the substrate material because silicon wafers are cheap and abundant, and because of the ability to easily oxidize the silicon wafer to form high-quality SiO_2 films on the substrate which acts as an effective lower cladding for waveguides. The primary waveguide core material is then introduced onto the oxidized wafer as a thin film. In general, crystalline materials including semiconductors require epitaxial growth on a lattice-matched substrate. For silicon [41] and lithium-niobate waveguides [91] the waveguiding layer

is implemented onto the substrate in a SmartCut process. Dielectric materials, such as silicon nitride [63] or oxide glasses [70,75], are highly versatile because they can be deposited on the wafer as a thin film in either a chemical or physical deposition process independent of the substrate. The thin film provides vertical confinement of the light within the core material. To achieve lateral confinement the thin film is then usually patterned via lithography and etched to form a waveguide. Waveguides can either be etched through to the lower cladding on either side of the core, as shown in Fig. 1.1(a), called a strip waveguide, or only partially etched as shown in Fig. 1.1(b), referred to as a ridge waveguide. While strip waveguides maximize confinement and can allow for tight bending radii and highly-compact devices, ridge waveguides reduce the optical mode overlap with the rough surface of the etched sidewall, which generally leads to reduced waveguide losses. After patterning, strip and ridge waveguides are typically top-cladded in a second low index material, such as a CVD-deposited SiO_2 layer. This is the typical process flow for the optical portion (electrical connections and doped regions for optoelectronic devices add additional layers and processing steps) of a single material system waveguide.

However, with a vast array of materials available for use in integrated photonics, more complex systems designs are moving towards combined-material-system platforms to take advantage of the different materials' specific strengths for different functions. Here, we consider two classes of combined material systems: multilayer and hybrid platforms. Multilayer systems occur when the different materials each have their own distinct waveguide core that confines an optical mode and light is transferred serially between the two different waveguide materials. Hybrid systems occur when the optical mode is confined in and travels through both material systems simultaneously in a single mode.

Multilayer platforms can either be implemented vertically, as shown in Fig. 1.1(c), or horizontally as shown in Fig. 1.1(d). Processing for vertical coupling integration schemes typically involves first fabricating the lower-level waveguide core similarly to the method just discussed for single layer systems. The top cladding layer is then planarized after its deposition in a chemical mechanical polishing (CMP) process to lie roughly a few hundred microns above the top of the lower-level waveguide. A secondary waveguide layer is then either bonded or deposited onto the planarized cladding, after which it also undergoes a similar waveguide patterning process. Much progress has been made on low-loss interlayer couplers [35,123] for vertically-coupled multilayer waveguide platforms. In particular, Si_3N_4 on Si, which combines the low-waveguide losses and high-performance passive devices available in Si_3N_4 with the optoelectronic functionality of Si, are quickly becoming one of the most advanced commercially available photonic platforms, such as the processes offered by AMF or AIM Photonics [35,36]. Recently multilayer coupling schemes have also been used to couple erbium-doped Al_2O_3 waveguide amplifiers to Si_3N_4 waveguides, demonstrating up to 18 dB of Si_3N_4 -to- Si_3N_4 gain at a 1532 nm wavelength [124], as well as LiNbO_3 modulators coupled to silicon waveguides for on-off keying modulation speeds of up to 100 Gb/s [94]. While vertical coupling can be an effective method to integrate multiple materials onto a single platform, and

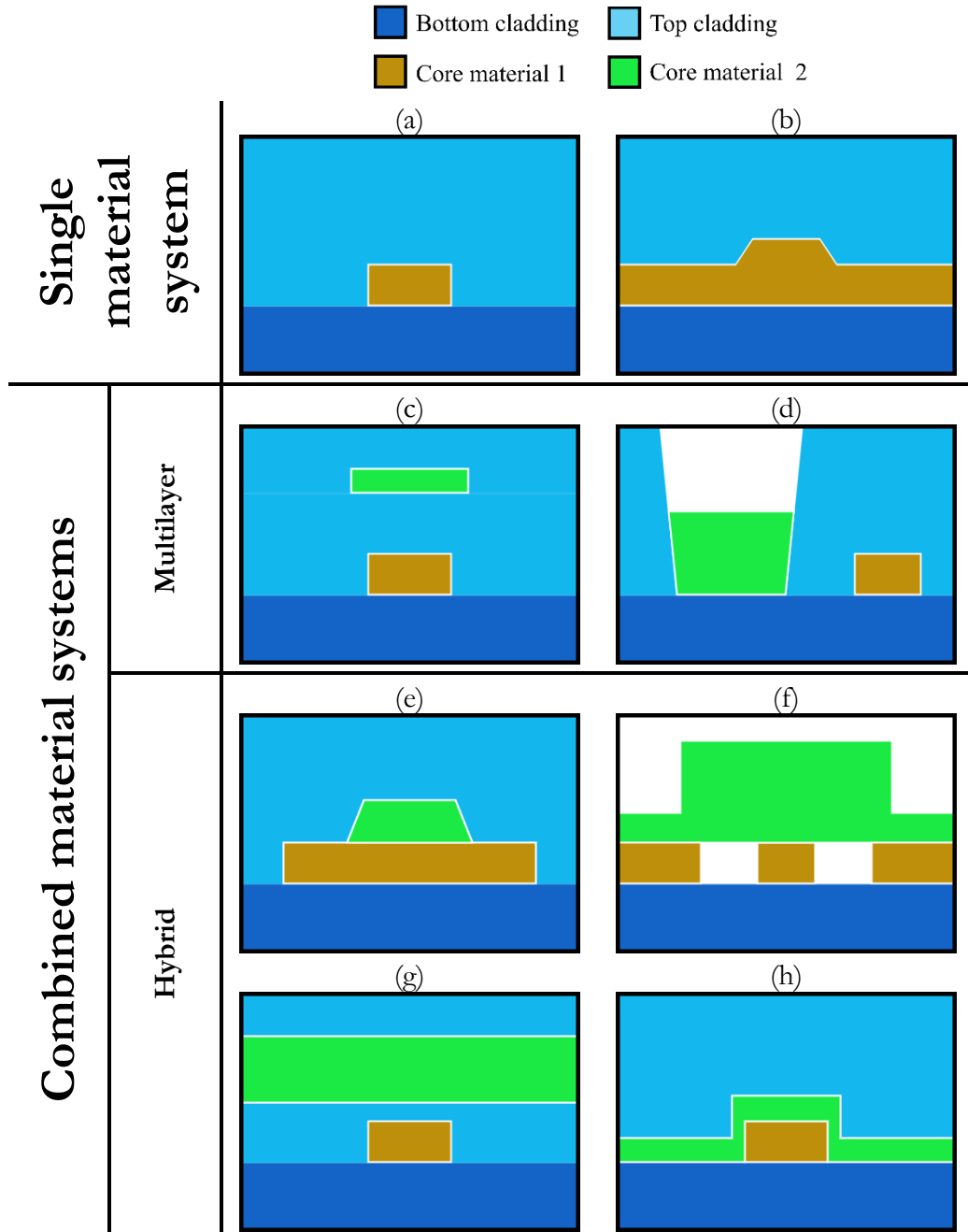


Fig. 1.1. Cross section of (a) strip and (b) ridge waveguides for single material system waveguide platforms. Combined materials systems can be categorized as (c) vertical or (d) lateral multilayer platforms with independent waveguide modes, or hybrid waveguides as demonstrated with (e) heteroepitaxy, (f) wafer/die bonding or straightforward (g) planar and (h) conformal coating techniques.

it allows for overlapping waveguides for denser integration, the need to pattern both layers requires precise alignment and high-resolution lithography and, in the cases of Al_2O_3 and LiNbO_3 , exotic and non-standard etching chemistries. An alternative method to integrate

novel materials onto waveguide platforms without the need for etching is the microtrench technique [125], where the top cladding is locally etched near the primary waveguide, rather than across the entire wafer or chip, and can then be coated in a secondary waveguide material. The secondary waveguide is then confined laterally by the shape of the etched microtrench, which is carried out in the foundry using a standard window etch step, and vertically by the thickness of the coating. This technique has been successfully used for Al_2O_3 coated microtrenches coupled to Si_3N_4 waveguides to fabricate high-quality factor microresonators [125], and erbium, ytterbium, and thulium doped lasers [126,127], including an $\text{Al}_2\text{O}_3:\text{Er}^{3+}$ -filled microtrench coupled to a Si_3N_4 Vernier filter for a tunable on-chip laser [128]. A similar microtrench technique has recently been used to couple chalcogenide films to Si waveguides [129]. While this technique avoids the need for additional etch steps during post-processing, which significantly reduces complexity, increases yield and avoids the requirement to develop non-standard etch recipes, there is minimal control over the shape of the secondary waveguide core and the lateral interlayer coupling is more challenging to design. It is also unsuitable for materials which cannot be coated onto samples, such as LiNbO_3 . Therefore, while vertical integration is preferential for combining well developed wafer-scale materials such as Si/ Si_3N_4 , lateral integration is of great interest for the post-processing integration of more novel material systems.

In hybrid waveguides, the optical mode supported by the waveguide structure is shared between two materials. For crystalline substrates, epitaxial layers of a different material system (heteroepitaxy) can be grown, provided any lattice mismatch between the two material systems can be minimized. The selective growth of epitaxial layers on the primary waveguide core can be used to fabricate heteroepitaxial hybrid waveguides, as diagrammed in Fig. 1.1(e). A prominent example of a heteroepitaxial hybrid waveguide is the growth of germanium on silicon waveguides, a process commonly used in active silicon photonic microsystems to fabricate photodetectors [54,55]. However, this type of hybrid integration is limited to a select few materials that can be lattice matched such as germanium and silicon. For materials that are not lattice matched, such as Si and III-Vs, hybrid integration must instead be achieved through flip chip bonding of dies and wafers. The hybrid integration of III-Vs on Si waveguides in this approach has been heavily explored with regard to on-chip amplifiers, lasers, modulators and photodetectors [130-133], with a cross sectional material profile similar to that shown in Fig. 1.1(f). In this design a small portion of the waveguide mode guided by the silicon extends into the III-V wafer stack, where interactions allow access to the various optoelectronic functions available in III-V waveguides. While these two hybrid material integration schemes have demonstrated excellent results, the methods used are highly specific to the material systems described, or expensive and difficult to fabricate as is the case in bonding. In contrast, the following two techniques, which involve a thin film coating that is grown or deposited onto the waveguide platforms without the need for secondary alignment or etching, can be applied more generally and at lower cost. The first method is the planar coating method, as displayed in Fig. 1.1(g), which appears very similar to the vertical multilayer

waveguide platform. However, in this approach the secondary waveguide material is not etched, instead sharing an optical mode with lateral confinement achieved due to the primary waveguide core. This design has been used effectively with planar Al_2O_3 coatings on Si_3N_4 waveguides, with distributed Bragg reflector (DBR) and distributed feedback (DFB) cavities patterned into the Si_3N_4 waveguide layer, to realize various rare-earth doped lasers [134-139], including a full-link data communication system on SOI [29]. A similar waveguide style implemented with PZT coatings was used in the demonstrations of PZT modulators on Si_3N_4 platforms [87,88]. While this remains a very attractive platform for secondary material integration, it requires careful chemical mechanical polishing of the SiO_2 top-cladding surface or high-quality etching processes with etch stop layers to maintain smooth interfaces and low waveguide losses [136], and typically results in low lateral confinement leading to large waveguide bends. Alternatively, a conformal coating technique can be used, in which the secondary waveguide material is deposited directly onto the primary waveguide core, as shown in Fig. 1.1(h). Although this method is expected to result in less optical overlap with the secondary waveguide material as compared to the planar coating method and there is potential for greater loss due to overlap of the mode with the secondary material's sidewall, the simpler fabrication process makes it an advantageous approach in terms of yield and cost, and the improved lateral confinement allows tighter waveguide bends for reduced size. A variation of this method has been used as a dispersion engineering technique for Si_3N_4 strip waveguides [140,141], and in the implementation of graphene for modulation and detection purposes [119,120]. Hybrid waveguide platforms are receiving increasing attention, and their importance will continue to grow with the demand for more functionalities in PICs.

1.4 Tellurite Glass

In this thesis we focus in particular on amorphous TeO_2 , or tellurite glass, as a material of significant interest for photonic integrated circuits. TeO_2 is optically transparent at wavelengths from the visible to the mid-infrared, making it suitable for applications ranging from sensors to telecommunications. TeO_2 has one of the largest linear refractive indices for oxide-based glasses of 2.08 at a 1550 nm wavelength [142], which is slightly larger than that of Si_3N_4 (1.99 at 1550 nm) [143], and lower than that of Si (3.47 at 1550 nm) [144]. This is an important property with regard to combined material systems, allowing TeO_2 waveguides to phase match to high-refractive-index-contrast material systems for efficient coupling, achieve high confinement in hybrid waveguide structures for high intensities and efficient all-optical processes, and have tight bends for compact devices. Tellurite has many excellent properties towards its potential use for nonlinear functionality, including its large nonlinear refractive index, measured to be $1.3 \times 10^{-18} \text{ m}^2/\text{W}$ at 1900 nm [145], low TPA and high Raman and Brillouin gain coefficients of $3 \times 10^{-12} \text{ m/W}$ [146] and $1.7 \times 10^{-10} \text{ m/W}$ [147], respectively. Additionally, it is an excellent material system for optical gain and lasing via introduction of rare-earth dopants, due its high rare-earth solubility, large emission cross-sections, wide emission bandwidths and low phonon energies which can reduce non-radiative decay and

enable emission at wavelengths which are not accessible in other oxide host materials [148-151]. A comparison of several of the materials properties of Si, Si₃N₄, and TeO₂ can be found in Table 1.2. It can be seen that TeO₂ offers relatively low waveguide losses, a large nonlinearity with negligible TPA, and the potential for rare earth doped devices that cannot be achieved by the other material platforms. Therefore, TeO₂ is a highly promising material for linear, nonlinear and active integrated optical devices.

Table 1.2. Comparison of selected properties of Si, Si₃N₄ and TeO₂

Material	Linear refractive index (1550 nm)	Waveguide loss (dB/cm)	Nonlinear refractive index (m ² /W)	TPA coefficient (m/W)	Rare earth dopant solubility	Opto-electronic functionality
Si [42-44,144,152-154]	3.47	2 – 3	9×10^{-18}	2×10^{-11}	Low	Yes
Si ₃ N ₄ [36,62,63,143,155]	2.00	0.001 – 0.1	2.4×10^{-19}	Negligible	Low	No
TeO ₂ [75,76,142,145, 148-151]	2.08	0.1 – 0.6	1.3×10^{-18}	Negligible	High	No

Tellurite glass has been widely studied in fiber-optic platforms [142, 145-151, 156], but it is less investigated as an integrated optical material. TeO₂ waveguides and devices have been defined in bulk glass by ion exchange and femtosecond laser irradiation [157-162]. However, these methods result in low-index-contrast waveguides which are useful for discrete components in fiber-optic or free-space optical systems but less suitable for compact integrated devices and PICs. With regard to high-index-contrast waveguides initial studies on TeO₂ thin films demonstrated the ability to achieve low planar film losses using reactive sputtering deposition [163]. Subsequent work on integrated TeO₂ waveguides demonstrated propagation losses of 5.7 dB/cm in a 0.7-cm-long ridge waveguide patterned with a shallow etch using an argon plasma [164]. In that study, the difficulties of patterning TeO₂ became evident, including the observation that TeO₂ is soluble in photoresist developers, thus requiring a secondary SiO₂ capping mask on the TeO₂ film in order to pattern waveguides. Shortly thereafter, TeO₂ ridge waveguides were dry etched in an H₂/CH₄/Ar gas chemistry and demonstrated significantly reduced waveguide losses of down to 0.1 dB/cm [75, 165] due to the improved etch process. Nonlinear spectral broadening was also demonstrated in [75]. Investigations of erbium-doped TeO₂ (TeO₂:Er³⁺) ridge waveguides on this platform demonstrated high quality waveguide amplifiers, achieving up to 14 dB of gain or 2.8 dB/cm gain per unit length in a 5-cm-long straight waveguide, as well as lasing when coupling to the chip with a reflective fiber [76,77]. However, further etching difficulties were observed, where rough columnar structures were produced on the TeO₂:Er³⁺ film surface during etching, such that the waveguide amplifiers required ridge structures formed by an etched undoped TeO₂ layer on top of the doped layer [76]. In addition, the structures were large due to patterning

via contact lithography, resulting in relatively large waveguides and mode areas, where smaller features are of interest for compact devices and advanced structures such as on-chip laser cavities. Furthermore, the demonstrations were limited to straight waveguides, and fundamental photonic building blocks such as couplers and resonators were not shown or extensively investigated. Despite the remaining challenges for developing TeO₂ as an integrated optical material, these waveguide results, which are summarized in Table 1.3, have demonstrated significant progress and the immense potential for TeO₂ devices in integrated photonic microsystems.

Table 1.3 Comparison of TeO₂ waveguide properties ($\lambda = 1.5 \mu\text{m}$, TE polarization)

Reference	[164]	[75]	[76,77]
Waveguide type	TeO ₂ ridge	TeO ₂ ridge	TeO ₂ :Er ³⁺ ridge
Single-/Multi- mode	Multi-mode	Multi-mode	Single-mode
TeO₂ etch chemistry	Ar	H ₂ /CH ₄ /Ar	H ₂ /CH ₄ /Ar
Waveguide width (μm)	4	4	2
TeO₂ layer thickness (μm)	1.1	1.8	1.88
TeO₂ confinement factor	96	99	98
Effective mode area (μm^2)	6.3	4.5	5.5
Effective refractive index	1.97	2.04	2.03
Waveguide loss (dB/cm)	5.7	0.1	0.6

As the integrated photonics industry transitions more and more towards fabless architectures in silicon and silicon nitride waveguide platforms the practicality and usage of stand-alone glass waveguide platforms is expected to diminish. However, the excellent material properties of glasses such as TeO₂ still have much functionality to offer integrated photonic microsystems, such as nonlinear optical processing and light emission and amplification in rare-earth doped devices. In this thesis we investigate the monolithic integration of TeO₂ devices into established photonic platforms in order to incorporate the promising optical functionality of TeO₂.

1.5 Thesis Objectives

The objective of this thesis is to investigate the design, fabrication, and characterization of TeO₂ films, waveguides and devices and their monolithic integration in silicon and silicon nitride photonic platforms. The achievement of this objective required the development of a high-quality tellurium oxide thin film fabrication process using reactive sputtering deposition, the design of silicon and silicon nitride photonic chips intended for post-processing integration of TeO₂ thin films, and the experimental measurement and analysis of various on-chip devices. This work aims to provide the design, fabrication and characterization frameworks as well as demonstrate significant experimental steps towards the realization of

high-quality passive, nonlinear, and rare-earth doped TeO₂ devices integrated on high performance silicon and silicon nitride photonic microsystems.

1.6 Statement of Thesis Work

This thesis consists of six chapters and discusses the design, fabrication, and characterization of TeO₂ thin films, waveguides and integrated optical devices.

Chapter 2 introduces the development of a high-quality TeO₂ reactive sputter deposition process and characterizes the material parameters of the TeO₂ thin films. This process was then extended to include the co-sputtering deposition of erbium dopants into TeO₂:Er³⁺ thin films, which were further characterized. Chapter 3 investigates hybrid TeO₂-coated Si₃N₄ strip waveguides. The waveguide designs were optimized using simulations to achieve large optical overlap in the TeO₂ thin films while maintaining tight bending radii. Fabrication and experimental characterization of waveguides was carried out to realize various on-chip devices, including the demonstration of low-loss waveguides as well as high quality factor microresonators. Chapter 4 investigates TeO₂:Er³⁺-coated Si₃N₄ strip waveguides for optical amplifiers on an Si₃N₄ platform. The spectroscopic material properties of the waveguides were investigated and internal net gain was demonstrated. To investigate and show the potential for enhanced device performance a rate equation model was developed and applied. Chapter 5 investigates coated microtrench resonators as a method of directly coupling TeO₂ devices to silicon photonic circuits. The simulated and experimentally measured optical properties of the TeO₂ microtrench cavities are discussed. The capabilities of the TeO₂ microtrench resonator as an environmental sensing device are also explored. Chapter 6 summarizes the major milestones achieved in this thesis and provides a guide on potential future research directions related to this work.

1.7 Publications

The following is a list of journal articles by the author that have contributed to the results presented in this thesis:

- **H. C. Frankis**, D. B. Bonneville, and J. D. B. Bradley, "Tellurite glass microcavity resonators integrated on a silicon photonics platform," *J. Opt. Microsys.* **1**(2), 024002 (2021).
- **H. C. Frankis**, H. M. Mbonde, D. B. Bonneville, C. Zhang, R. Mateman, A. Leinse, and J. D. B. Bradley, "Erbium-doped TeO₂-coated Si₃N₄ waveguide amplifiers with 5 dB net gain," *Photonics Res.* **8**(2), 127–134 (2020).
- **H. C. Frankis**, K. Mirabbas Kiani, D. B. Bonneville, C. Zhang, S. Norris, R. Mateman, A. Leinse, N. D. Bassim, A. P. Knights, and J. D. B. Bradley, "Low-loss TeO₂-coated Si₃N₄ waveguides for application in photonic integrated circuits," *Opt. Express* **27**(9), 12529–12540 (2019).

- **H. C. Frankis**, K. Mirabbas Kiani, D. Su, R. Mateman, A. Leinse, and J. D. B. Bradley, "High-Q tellurium-oxide-coated silicon nitride microring resonators," *Opt. Lett.* **44**(1), 118–121 (2019).
- **H. C. Frankis**, D. Su, D. B. Bonneville, and J. D. B. Bradley, "A tellurium oxide microcavity resonator sensor integrated on-chip with a silicon waveguide," *Sensors* **18**(11), 4061 (2018).

The author has also contributed to the following conference posters, presentations, and proceedings:

- **H. C. Frankis**, H. M. Mbonde, D. B. Bonneville, C. Zhang, R. Mateman, A. Leinse, and J. D. B. Bradley, "Erbium-doped tellurium-oxide-coated silicon nitride waveguide amplifiers," in Conference on Lasers and Electro-Optics, Virtual Conference, 2020, OSA Technical Digest (online) (Optical Society of America, 2020), paper SW3F.2.
- **H. C. Frankis**, D. Su, D. B. Bonneville, and J. D. B. Bradley, "Tellurium oxide resonator sensor integrated on a silicon chip," presented at Photonics North, Quebec City, Canada, 21–23 May 2019.
- **H. C. Frankis**, K. Mirabbas Kiani, D. B. Bonneville, C. Zhang, S. Norris, R. Mateman, A. Leinse, N. D. Bassim, A. P. Knights, and J. D. B. Bradley, "Low-loss TeO₂ waveguides integrated on a Si₃N₄ platform for active and nonlinear optical devices," in Conference on Lasers and Electro-Optics, San Jose, CA, 2019, OSA Technical Digest (online) (Optical Society of America, 2019), paper STh3N.6.
- J. D. B. Bradley, **H. C. Frankis**, K. Mirabbas Kiani, D. Su, R. Mateman, and A. Leinse, "High-Q tellurite glass microring resonators on a low-loss silicon-nitride-integrated optics platform," OPTO, Photonics West, San Francisco, California, 2019, Technical Abstract Summaries, Conference "Integrated Optics: Devices, Materials, and Technologies XXIII," Session 9, paper 10921-38.
- **H. C. Frankis**, D. B. Bonneville, D. Su, and J. D. B. Bradley, "Silicon waveguide integrated with a tellurium oxide whispering gallery resonator on chip," OPTO, Photonics West, San Francisco, California, 2019, Technical Abstract Summaries, Conference "Silicon Photonics XIV," Session 3, paper 10923-12.
- **H. C. Frankis**, C. Zhang, and J. D. B. Bradley, "CMOS compatible tellurium oxide waveguides for silicon photonic amplifiers," Photoluminescence in Rare Earths: Photonic Materials and Devices (PRE'17), Rome, Italy, November 2017.

- **H. C. Frankis** and J. D. B. Bradley, “Reactively sputtered tellurium oxide films for integrated photonics,” Photonics North, Ottawa, Canada, 2017, Proceedings of Photonics North, paper MATERIALS-54.

Additionally, the author has contributed to the following journal publications, which are not directly presented or discussed over the course of this thesis:

- Y. Xie, **H. C. Frankis**, J. D. B. Bradley, and A. P. Knights, “Post-fabrication resonance trimming of Si_3N_4 photonic circuits via localized thermal annealing of a sputter-deposited SiO_2 cladding,” *Opt. Mater. Express* **11**(8), 2401–2412 (2021).
- R. Wang, **H. C. Frankis**, H. M. Mbonde, D. B. Bonneville, and J. D. B. Bradley, “Erbium-ytterbium co-doped aluminum oxide thin films: co-sputtering deposition, photoluminescence, luminescent lifetime, energy transfer and quenching fraction,” *Opt. Mater.* **111**, 110692 (2020).
- K. Mirabbas Kiani, H. M. Mbonde, **H. C. Frankis**, R. Mateman, A. Leinse, A. P. Knights, and J. D. B. Bradley, “Four-wave mixing in high-Q tellurium-oxide-coated silicon nitride microring resonators,” *OSA Continuum* **3**(12), 3497–3507 (2020).
- N. Singh, H. M. Mbonde, **H. C. Frankis**, E. Ippen, J. D. B. Bradley, and F. X. Kärtner, “Nonlinear silicon photonics on CMOS compatible tellurium oxide,” *Photonics Res.* **8**(12), 1904–1909 (2020).
- D. B. Bonneville, **H. C. Frankis**, R. Wang, and J. D. B. Bradley, “Erbium-ytterbium co-doped aluminum oxide waveguide amplifiers fabricated by reactive co-sputtering and wet chemical etching,” *Opt. Express* **28**(20), 30130–30140 (2020).
- C. M. Naraine, J. W. Miller, **H. C. Frankis**, D. E. Hagan, P. Mascher, J. H. Schmid, P. Cheben, A. P. Knights, and J. D. B. Bradley, “Subwavelength grating metamaterial waveguides functionalized with tellurium oxide cladding,” *Opt. Express* **28**(12), 18538–18547 (2020).
- H. M. Mbonde, **H. C. Frankis**, and J. D. B. Bradley, “Enhanced nonlinearity and engineered anomalous dispersion in TeO_2 -coated Si_3N_4 waveguides,” *IEEE Photonics J.* **12**(2), 2200210 (2020).
- K. Mirabbas Kiani, **H. C. Frankis**, H. M. Mbonde, R. Mateman, A. Leinse, A. P. Knights, and J. D. B. Bradley, “Thulium-doped tellurium oxide waveguide amplifier with 7.6 dB net gain on a silicon nitride chip,” *Opt. Lett.* **44**(23), 5788–5791 (2019).
- D. B. Bonneville, M. A. Méndez-Rosales, **H. C. Frankis**, L. Monteiro Gonçalves, R. N. Kleiman, and J. D. B. Bradley, “Flexible and low-cost fabrication of optical

waveguides by UV laser resist-mask writing," *Opt. Mat. Express* **9**(4), 1728–1737 (2019).

- Z. Su, N. Li, **H. C. Frankis**, E. S. Magden, T. N. Adam, G. Leake, D. Coolbaugh, J. D. B. Bradley, and M. R. Watts, "High-Q-factor Al₂O₃ micro-trench cavities integrated with silicon nitride waveguides on silicon," *Opt. Express* **26**(9), 11161–11170 (2018).

References

- [1] S. E. Miller, "Integrated optics: An introduction," *Bell Syst. Tech. J.* **48**(7), 2059–2069 (1969).
- [2] H. E. Kogelnik, "An introduction to integrated optics," *IEEE Trans. Microw. Theory Techn.* **23**(1), 2–16 (1975).
- [3] R. Soref, "The past, present, and future of silicon photonics," *IEEE J. Sel. Top. Quantum Electron.* **12**(6), 1678–1687 (2006).
- [4] D. Thomson D, A. Zilkie, J. E. Bowers, T. Komljenovic, G. T. Reed, L. Vivien, D. Marris-Morini, E. Cassan, L. Viroth, J. M. Fédéli, J. M. Hartmann, J. H. Schmid, D. X. Xu, F. Boeuf, P. O'Brien, G. Z. Mashanovich, and M. Nedeljkovic, "Roadmap on silicon photonics," *J. Opt.* **18**(7), 073003 (2016).
- [5] Z. Zhou, R. Chen, X. Li, and T. Li, "Development trends in silicon photonics for data centers," *Opt. Fiber Technol.* **44**, 13–23 (2018).
- [6] Q. Cheng, Bahadori, M. Glick, S. Rumley, and K. Bergman, "Recent advances in optical technologies for data centers: a review," *Optica* **5**(11), 1354–1370 (2018).
- [7] Z. W. Xu, "Cloud-sea computing systems: Towards thousand-fold improvement in performance per watt for the coming zettabyte era," *J. Comput. Sci. Technol.* **29**(2), 177–181 (2014).
- [8] J. K. Doylend and S. Gupta, "An overview of silicon photonics for LIDAR," in *Silicon Photonics XV San Francisco, CA, 2020*, (International Society for Optics and Photonics), paper 112850J.
- [9] C. V. Poulton, M. J. Byrd, P. Russo, E. Timurdogan, M. Khandaker, D. Vermeulen, and M. R. Watts, "Long-range LiDAR and free-space data communication with high-performance optical phased arrays," *IEEE J. Sel. Top. Quantum Electron.* **25**(5), 1–8 (2019).
- [10] C. Martinez, V. Krotov, B. Meynard, and D. Fowler, "See-through holographic retinal projection display concept," *Optica* **5**(10), 1200–1209 (2018).
- [11] Y. H. Lee, T. Zhan, and S. T. Wu, "Prospects and challenges in augmented reality displays," *Virtual Real. Intell. Hardw.* **1**(1), 10–20 (2019).

- [12] J. Notaros, M. Raval, M. Notaros, and M. R. Watts, “Integrated-phased-array-based visible-light near-eye holographic projector,” in Conference on Lasers and Electro-Optics, San Jose, CA, 2019, OSA Technical Digest (online) (Optical Society of America, 2019), paper STu3O.4.
- [13] S. T. Fard, S. M. Grist, V. Donzella, S. A. Schmidt, J. Flueckiger, X. Wang, W. Shi, A. Millspaugh, M. Webb, D. M. Ratner, K. C. Cheung, and L. Chrostowski, “Label-free silicon photonic biosensors for use in clinical diagnostics,” in Silicon Photonics VIII San Francisco, CA, 2020, (International Society for Optics and Photonics), paper 862909.
- [14] A. Fernández Gavela, D. Grajales García, J. C. Ramirez, and L. M. Lechuga, “Last advances in silicon-based optical biosensors,” *Sensors* **16**(3), 285 (2016).
- [15] A. Politi, J. C. Matthews, M. G. Thompson, and J. L. O'Brien, “Integrated quantum photonics,” *IEEE J. Sel. Top. Quantum Electron.* **15**(6), 1673–1684 (2009).
- [16] J. C. Adcock, J. Bao, Y. Chi, X. Chen, D. Bacco, Q. Gong, L. K. Oxenløwe, J. Wang, and Y. Ding, “Advances in silicon quantum photonics,” *IEEE J. Sel. Top. Quantum Electron.* **27**(2), 1–24 (2020).
- [17] G. Serafino, C. Porzi, F. Falconi, S. Pinna, M. Puleri, A. D’Errico, A. Bogoni, and P. Ghelfi, “Photonics-assisted beamforming for 5G communications,” *IEEE Photon. Technol. Lett.* **30**(21), 1826–1829 (2018).
- [18] Sabella R, “Silicon photonics for 5G and future networks,” *IEEE J. Sel. Top. Quantum Electron.* **26**(2), 1–11 (2019).
- [19] J. S. Kilby, “Invention of the integrated circuit,” *IEEE Trans. Electron Devices* **23**(7), 648–654 (1976).
- [20] R. R. Schaller, “Moore's law: past, present and future,” *IEEE Spectr.* **34**(6), 52–59 (1997).
- [21] C. A. Mack, “Fifty years of Moore's law,” *IEEE Trans. Semicond. Manuf.* **24**(2), 202–207 (2011).
- [22] C. R. Doerr, “Silicon photonic integration in telecommunications,” *Front. Phys.* **3**, 37 (2015).
- [23] E. Timurdogan, Z. Su, R. J. Shiue, M. J. Byrd, C. V. Poulton, K. Jabon, C. DeRose, B. R. Moss, E. S. Hosseini, I. Duzevik, M. Whitson, R. P. Millman, D. A. Atlas, and M. R. Watts, “400G silicon photonics integrated circuit transceiver chipsets for CPO, OBO, and pluggable modules,” in Optical Fiber Communication Conference, San Diego, CA, 2020, OSA Technical Digest (online) (Optical Society of America, 2020), paper T3H.2.
- [24] E. Luan, H. Shoman, D. M. Ratner, K. C. Cheung, and L. Chrostowski, “Silicon photonic biosensors using label-free detection,” *Sensors* **18**(10), 3519 (2018).

- [25] J. S. Orcutt, B. Moss, C. Sun, J. Leu, M. Georgas, J. Shainline, E. Zraggen, H. Li, J. Sun, M. Weaver, and S. Urošević, “Open foundry platform for high-performance electronic-photonic integration,” *Opt. Express* **20**(11), 12222–12232 (2012).
- [26] M. Streshinsky, R. Ding, Y. Liu, A. Novack, C. Galland, A. J. Lim, P. G. Lo, T. Baehr-Jones, and M. Hochberg, “The road to affordable, large-scale silicon photonics,” *Opt. Photonics News* **24**(9), 32–39 (2013).
- [27] T. Horikawa, D. Shimura, H. Okayama, S. H. Jeong, H. Takahashi, J. Ushida, Y. Sobu, A. Shiina, M. Tokushima, K. Kinoshita, and T. Mogami, “A 300-mm silicon photonics platform for large-scale device integration,” *IEEE J. Sel. Top. Quantum Electron.* **24**(4), 1–5 (2018).
- [28] J. Wang and Y. Long, “On-chip silicon photonic signaling and processing: a review,” *Sci. Bull.* **63**(19), 1267–1310 (2018).
- [29] N. Li, M. Xin, Z. Su, E. S. Magden, N. Singh, J. Notaros, E. Timurdogan, P. Purnawirman, J. D. Bradley, and M. R. Watts, “A silicon photonic data link with a monolithic erbium-doped laser,” *Sci. Rep.* **10**(1), 1–9 (2020).
- [30] M. Hochberg and T. Baehr-Jones, “Towards fabless silicon photonics,” *Nat. Photonics* **4**(8), 492–494 (2010).
- [31] M. Hochberg, N. C. Harris, R. Ding, Y. Zhang, A. Novack, Z. Xuan, and T. Baehr-Jones, “Silicon photonics: the next fabless semiconductor industry,” *IEEE Solid-State Circuits Magazine.* **5**(1), 48–58 (2013).
- [32] K. Wörhoff, R. G. Heideman, A. Leinse, and M. Hoekman, “TriPleX: A versatile dielectric photonic platform,” *Adv. Opt. Technol.* **4**(2), 189–207 (2015).
- [33] C. G. H. Roeloffzen, M. Hoekman, E. J. Klein, L. S. Wevers, R. B. Timens, D. Marchenko, D. Geskus, R. Dekker, A. Alippi, R. Grootjans, A. van Rees, R. M. Oldenbeuving, J. P. Epping, R. G. Heideman, K. Wörhoff, A. Leinse, D. Geuzebroek, E. Schreuder, P. W. L. van Dijk, I. Visscher, C. Taddei, Y. Fan, C. Taballione, and Y. Liu, D. Marpaung, L. Zhuang, M. Benelajla and K. Boller, “Low Loss Si₃N₄ TriPleX optical waveguides: technology and applications overview,” *IEEE J. Sel. Top. Quantum Electron.* **24**(4), 1–21 (2018).
- [34] D. J. Blumenthal, R. Heideman, D. Geuzebroek, A. Leinse, and C. Roeloffzen, “Silicon nitride in silicon photonics,” *Proc. IEEE* **106**(12), 2209–2231 (2018).
- [35] W. D. Sacher, J. C. Mikkelsen, Y. Huang, J. C. Mak, Z. Yong, X. Luo, Y. Li, P. Dumais, J. Jiang, D. Goodwill, E. Bernier, P. G. Q. Lo, and J. K. S. Poon, “Monolithically integrated multilayer silicon nitride-on-silicon waveguide platforms for 3-D photonic circuits and devices,” *Proc. IEEE* **106**(12), 2232–2245 (2018).

- [36] E. Timurdogan, Z. Su, C. V. Poulton, M. J. Byrd, S. Xin, R. J. Shiue, B. R. Moss, E. S. Hosseini, and M. R. Watts, “AIM process design kit (AIMPDKv2. 0): Silicon photonics passive and active component libraries on a 300mm wafer,” *Optical Fiber Communications Conference and Exposition*, 1–3 (2018).
- [37] A. K. Hamze, M. Reynaud, J. Geler-Kremer, and A. A. Demkov, “Design rules for strong electro-optic materials,” *Npj Comput. Mater.* **6**(1), 1–9 (2020).
- [38] R. Soref and B. Bennett, “Electrooptical effects in silicon,” *IEEE J. Quantum Electron.* **23**(1), 123–129 (1987).
- [39] A. P. Jauho and K. Johnsen, “Dynamical franz-keldysh effect,” *Phys. Rev. Lett.* **76**(24), 4576 (1996).
- [40] R. W. Boyd, *Nonlinear optics* (Academic press, 2020).
- [41] M. Bruel, “Silicon on insulator material technology,” *Electron. Lett.* **31**(14), 1201–1202 (1995).
- [42] P. Dumon, W. Bogaerts, V. Wiaux, J. Wouters, S. Beckx, J. Van Campenhout, D. Taillaert, B. Luyssaert, P. Bienstman, D. Van Thourhout, and R. Baets, “Low-loss SOI photonic wires and ring resonators fabricated with deep UV lithography,” *IEEE Photon. Technol. Lett.* **16**(5), 1328–1330 (2004).
- [43] Y. A. Vlasov and S. J. McNab, “Losses in single-mode silicon-on-insulator strip waveguides and bends,” *Opt. Express* **12**(8), 1622–1631 (2004).
- [44] D. E. Hagan and A. P. Knights, “Mechanisms for optical loss in SOI waveguides for mid-infrared wavelengths around 2 μm ,” *J. Opt.* **19**(2), 025801 (2016).
- [45] M. R. Watts, J. Sun, C. DeRose, D. C. Trotter, R. W. Young, and G. N. Nielson, “Adiabatic thermo-optic Mach–Zehnder switch,” *Opt. Lett.* **38**(5), 733–735 (2013).
- [46] D. J. Thomson, F. Y. Gardes, J. M. Fedeli, S. Zlatanovic, Y. Hu, B. P. Kuo, E. Myslivets, N. Alic, S. Radic, G. Z. Mashanovich, and G. T. Reed, “50-Gb/s silicon optical modulator,” *IEEE Photon. Technol. Lett.* **24**(4), 234–236 (2011).
- [47] J. D. B. Bradley, P. E. Jessop, and A. P. Knights, “Silicon waveguide-integrated optical power monitor with enhanced sensitivity at 1550 nm,” *Appl. Phys. Lett.* **86**(24), 241103 (2005).
- [48] J. J. Ackert, D. J. Thomson, L. Shen, A. C. Peacock, P. E. Jessop, G. T. Reed, G. Z. Mashanovich, and A. P. Knights, “High-speed detection at two micrometres with monolithic silicon photodiodes,” *Nat. Photonics* **9**(6), 393–396 (2015).
- [49] H. Rong, R. Jones, A. Liu, O. Cohen, D. Hak, A. Fang, and M. Paniccia, “A continuous-wave Raman silicon laser,” *Nature* **433**(7027), 725–728 (2005).

- [50] A. G. Griffith, R. K. Lau, J. Cardenas, Y. Okawachi, A. Mohanty, R. Fain, Y. H. Lee, M. Yu, C. T. Phare, C. B. Poitras, A. L. Gaeta, and M. Lipson, “Silicon-chip mid-infrared frequency comb generation,” *Nat. Commun.* **6**(1), 1–5 (2015).
- [51] M. Cazzanelli, F. Bianco, E. Borga, G. Pucker, M. Ghulinyan, E. Degoli, E. Luppi, V. Véniard, S. Ossicini, D. Modotto, and S. Wabnitz, “Second-harmonic generation in silicon waveguides strained by silicon nitride,” *Nat. Mater.* **11**(2), 148–154 (2012).
- [52] N. Singh, M. Raval, A. Ruocco, and M. R. Watts, “Broadband 200-nm second-harmonic generation in silicon in the telecom band,” *Light Sci. Appl.* **9**(1), 1–7 (2020).
- [53] M. Nedeljkovic, J. S. Penades, V. Mittal, G. S. Murugan, A. Z. Khokhar, C. Littlejohns, L. G. Carpenter, C. B. Gawith, J. S. Wilkinson, and G. Z. Mashanovich, “Germanium-on-silicon waveguides operating at mid-infrared wavelengths up to 8.5 μm ,” *Opt. Express* **25**(22), 27431–27441 (2017).
- [54] L. Colace, G. Masini, F. Galluzzi, G. Assanto, G. Capellini, L. Di Gaspare, E. Palange, and F. Evangelisti, “Metal–semiconductor–metal near-infrared light detector based on epitaxial Ge/Si,” *Appl. Phys. Lett.* **72**(24), 3175–3177 (1998).
- [55] L. Vivien, A. Polzer, D. Marris-Morini, J. Osmond, J. M. Hartmann, P. Crozat, E. Cassan, C. Kopp, H. Zimmermann, and J. M. Fédéli, “Zero-bias 40 Gbit/s germanium waveguide photodetector on silicon,” *Opt. Express* **20**(2), 1096–1101 (2012).
- [56] R. E. Camacho-Aguilera, Y. Cai, N. Patel, J. T. Bessette, M. Romagnoli, L. C. Kimerling, and J. Michel, “An electrically pumped germanium laser,” *Opt. Express* **20**(10), 11316–11320 (2012).
- [57] S. A. Srinivasan, M. Pantouvaki, S. Gupta, H. T. Chen, P. Verheyen, G. Lepage, G. Roelkens, K. Saraswat, D. Van Thourhout, P. Absil, and J. Van Campenhout, “56 Gb/s germanium waveguide electro-absorption modulator,” *J. Light. Technol.* **34**(2), 419–424 (2015).
- [58] P. Xing, D. Ma, K. J. Ooi, J. W. Choi, A. M. Agarwal, and D. Tan, “CMOS-compatible PECVD silicon carbide platform for linear and nonlinear optics,” *ACS Photonics* **6**(5), 1162–1167 (2019).
- [59] J. Cardenas, M. Yu, Y. Okawachi, C. B. Poitras, R. K. Lau, A. Dutt, A. L. Gaeta, and M. Lipson, “Optical nonlinearities in high-confinement silicon carbide waveguides,” *Opt. Lett.* **40**(17), 4138–4141 (2015).
- [60] X. Wu, T. Fan, A. A. Eftekhari, and A. Adibi, “High-Q microresonators integrated with microheaters on a 3C-SiC-on-insulator platform,” *Opt. Lett.* **44**(20), 4941–4944 (2019).
- [61] T. Fan, X. Wu, A. A. Eftekhari, M. Bosi, H. Moradinejad, E. V. Woods, and A. Adibi, “High-quality integrated microdisk resonators in the visible-to-near-infrared wavelength range on a 3C-silicon carbide-on-insulator platform,” *Opt. Lett.* **45**(1), 153–156 (2020).

- [62] J. F. Bauters, M. J. Heck, D. D. John, J. S. Barton, C. M. Bruinink, A. Leinse, R. G. Heideman, D. J. Blumenthal, and J. E. Bowers, “Planar waveguides with less than 0.1 dB/m propagation loss fabricated with wafer bonding,” *Opt. Express* **19**(24), 24090–12401 (2011).
- [63] J. F. Bauters, M. J. R. Heck, D. John, D. Dai, M.-C. Tien, J. S. Barton, A. Leinse, R. G. Heideman, D. J. Blumenthal, and J. E. Bowers, “Ultra-low-loss high-aspect-ratio Si₃N₄ waveguides,” *Opt. Express* **19**(4), 3163–3174 (2011).
- [64] D. J. Moss, R. Morandotti, A. L. Gaeta, and M. Lipson, “New CMOS-compatible platforms based on silicon nitride and Hydex for nonlinear optics,” *Nat. Photonics* **7**(8), 597–607 (2013).
- [65] A. L. Gaeta, M. Lipson, and T. J. Kippenberg, “Photonic-chip-based frequency combs,” *Nat. Photonics* **13**(3), 158–169 (2019).
- [66] L. Zhuang, D. Marpaung, M. Burla, W. Becker, A. Leinse, and C. Roeloffzen, “Low-loss, high-index-contrast Si₃N₄/SiO₂ optical waveguides for optical delay lines in microwave photonics signal processing,” *Opt. Express* **19**(23), 23162–23170 (2011).
- [67] Y. P. Li and C. H. Henry, “Silica-based optical integrated circuits,” *IEE proc., Optoelectron.* **143**(5), 263–280 (1996).
- [68] M. Kawachi, “Silica waveguides on silicon and their application to integrated-optic components,” *Opt. Quantum Electron.* **22**(5), 391–416 (1990).
- [69] M. Kawachi, “Recent progress in silica-based planar lightwave circuits on silicon,” *IEE proc., Optoelectron.* **143**(5), 257–262 (1996).
- [70] K. Wörhoff, J. D. Bradley, F. Ay, D. Geskus, T. P. Blauwendraat, and M. Pollnau, “Reliable Low-Cost Fabrication of Low-Loss Al₂O₃:Er³⁺ Waveguides With 5.4-dB Optical Gain,” *IEEE J. Quantum Electron.* **45**(5), 454–461 (2009).
- [71] J. D. B. Bradley, L. Agazzi, D. Geskus, F. Ay, K. Wörhoff, and M. Pollnau, “Gain bandwidth of 80 nm and 2 dB/cm peak gain in Al₂O₃:Er³⁺ optical amplifiers on silicon,” *JOSA B* **27**(2), 187–196 (2010).
- [72] S. A. Vázquez-Córdova, M. Dijkstra, E. H. Bernhardt, F. Ay, K. Wörhoff, J. L. Herek, S. M. García-Blanco, and M. Pollnau, “Erbium-doped spiral amplifiers with 20 dB of net gain on silicon,” *Opt. Express* **22**(21), 25993–26004 (2014).
- [73] M. Pollnau and J. D. B. Bradley, “Optically pumped rare-earth-doped Al₂O₃ distributed-feedback lasers on silicon,” *Opt. Express* **26**(18), 24164–24189 (2018).
- [74] H. C. Frankis, Z. Su, N. Li, E. S. Magden, M. Ye, M. R. Watts, and J. D. B. Bradley, “Four-wave mixing in a high-Q aluminum oxide microcavity on silicon,” in *Conference on Lasers and Electro-Optics, San Jose, CA, 2018, OSA Technical Digest (online)* (Optical Society of America, 2018), paper STh3I.3.

- [75] S. J. Madden and K. T. Vu, “Very low loss reactively ion etched tellurium dioxide planar rib waveguides for linear and non-linear optics,” *Opt. Express* **17**(20), 17645–17651 (2009).
- [76] K. T. Vu and S. J. Madden, “Tellurium dioxide erbium doped planar rib waveguide amplifiers with net gain and 2.8dB/cm internal gain,” *Opt. Express* **18**(18), 19192–19200 (2010).
- [77] K. T. Vu, S. Farahani, and S. J. Madden, "980nm pumped erbium doped tellurium oxide planar rib waveguide laser and amplifier with gain in S, C and L band," *Opt. Express* **23**(2), 747–755 (2015).
- [78] K. Vu, K. Yan, Z. Jin, X. Gai, D. Y. Choi, S. Debbarma, B. Luther-Davies, and S. J. Madden, “Hybrid waveguide from As_2S_3 and Er-doped TeO_2 for lossless nonlinear optics,” *Opt. Lett.* **38**(11), 1766–1768 (2013).
- [79] J. D. B. Bradley and M. Pollnau, “Erbium-doped integrated waveguide amplifiers and lasers,” *Laser Photonics Rev.* **5**(3), 368–403 (2011).
- [80] C. Xiong, W. H. Pernice, and H. X. Tang, “Low-loss, silicon integrated, aluminum nitride photonic circuits and their use for electro-optic signal processing,” *Nano Lett.* **12**(7), 3562–3568 (2012).
- [81] C. Xiong, W. H. Pernice, X. Sun, C. Schuck, K. Y. Fong, and H. X. Tang, “Aluminum nitride as a new material for chip-scale optomechanics and nonlinear optics,” *New J. Phys.* **14**(9), 095014 (2012).
- [82] H. Jung, C. Xiong, K. Y. Fong, X. Zhang, and H. X. Tang, “Optical frequency comb generation from aluminum nitride microring resonator,” *Opt. Lett.* **38**(15), 2810–2813 (2013).
- [83] H. Jung and H. X. Tang, “Aluminum nitride as nonlinear optical material for on-chip frequency comb generation and frequency conversion,” *Nanophotonics* **5**(2), 263–271 (2016).
- [84] J. B. Surya, X. Guo, C. L. Zou, and H. X. Tang, “Efficient third-harmonic generation in composite aluminum nitride/silicon nitride microrings,” *Optica* **5**(2), 103–108 (2018).
- [85] J. P. George, P. F. Smet, J. Botterman, V. Bliznuk, W. Woestenborghs, D. Van Thourhout, K. Neyts, and J. Beeckman, “Lanthanide-assisted deposition of strongly electro-optic PZT thin films on silicon: toward integrated active nanophotonic devices,” *ACS Appl. Mater. Interfaces* **7**(24), 13350–13359 (2015).
- [86] Z. Qi, G. Hu, Q. Zhu, L. Zhang, M. Li, and Y. Cui, “Inductively coupled plasmas (ICP) etching of PZT thin films for fabricating optical waveguide with photoresist/aluminum bilayer masking,” *OPTO, Photonics West, San Francisco, California, 2015, Technical*

- Abstract Summaries, Conference “Integrated Optics: Devices, Materials, and Technologies XIX” SPIE Proceedings Volume 9365, paper 93650Z.
- [87] N. Hosseini, R. Dekker, M. Hoekman, M. Dekkers, J. Bos, A. Leinse, and R. Heideman, “Stress-optic modulator in TriPleX platform using a piezoelectric lead zirconate titanate (PZT) thin film,” *Opt. Express* **23**(11), 14018–14026 (2015).
- [88] K. Alexander, J. P. George, J. Verbist, K. Neyts, B. Kuyken, D. Van Thourhout, and J. Beeckman, “Nanophotonic Pockels modulators on a silicon nitride platform,” *Nat. Commun.* **9**(1), 1–6 (2018).
- [89] W. Sohler, H. Hu, R. Ricken, V. Quiring, C. Vannahme, H. Herrmann, D. Büchter, S. Reza, W. Grundkötter, S. Orlov, and H. Suche, “Integrated optical devices in lithium niobate,” *Opt. Photonics News* **19**(1), 24–31 (2008).
- [90] M. Bazzan and C. Sada, “Optical waveguides in lithium niobate: Recent developments and applications,” *Appl. Phys. Rev.* **2**(4), 040603 (2015).
- [91] D. Zhu, L. Shao, M. Yu, R. Cheng, B. Desiatov, C. J. Xin, Y. Hu, J. Holzgrafe, S. Ghosh, A. Shams-Ansari, and E. Puma, “Integrated photonics on thin-film lithium niobate,” *Adv. Opt. Photonics* **13**(2), 242–352 (2021).
- [92] I. Krasnokutskaya, J. L. Tambasco, X. Li, and A. Peruzzo, “Ultra-low loss photonic circuits in lithium niobate on insulator,” *Opt. Express* **26**(2), 897–904 (2018).
- [93] B. Desiatov, A. Shams-Ansari, M. Zhang, C. Wang, and M. Lončar, “Ultra-low-loss integrated visible photonics using thin-film lithium niobate,” *Optica* **6**(3), 380–384 (2019).
- [94] M. He, M. Xu, Y. Ren, J. Jian, Z. Ruan, Y. Xu, S. Gao, S. Sun, X. Wen, L. Zhou, and L. Liu, “High-performance hybrid silicon and lithium niobate Mach–Zehnder modulators for 100 Gbit s⁻¹ and beyond,” *Nat. Photonics* **13**(5), 359–364 (2019).
- [95] R. Brinkmann, I. Baumann, M. Dinand, W. Sohler, and H. Suche, “Erbium doped single- and double-pass Ti:LiNbO₃ waveguide amplifiers,” *IEEE J. Quantum Electron.* **30**(10), 2356–2360 (1994).
- [96] W. Sohler, B. K. Das, D. Dey, S. Reza, H. Suche, and R. Ricken, “Erbium-doped lithium niobate waveguide lasers,” *IEICE Trans. Electron.* **88**(5), 990–997 (2005).
- [97] Z. Chen, Q. Xu, K. Zhang, W. H. Wong, D. L. Zhang, E. Y. Pun, and C. Wang, “Efficient erbium-doped thin-film lithium niobate waveguide amplifiers,” *Opt. Lett.* **46**(5), 1161–1164 (2021).
- [98] Q. Luo, C. Yang, Z. Hao, R. Zhang, D. Zheng, F. Bo, Y. Kong, G. Zhang, and J. Xu, “On-chip erbium-doped lithium niobate waveguide amplifiers,” *Chin. Opt. Lett.* **19**(6), 060008 (2021).

- [99] C. Wang, M. Zhang, M. Yu, R. Zhu, H. Hu, and M. Loncar, “Monolithic lithium niobate photonic circuits for Kerr frequency comb generation and modulation,” *Nat. Commun.* **10**(1), 1–6 (2019).
- [100] M. Smit, K. Williams, and J. van der Tol, “Past, present, and future of InP-based photonic integration,” *APL Photonics* **4**(5), 050901 (2019).
- [101] M. Smit, X. Leijtens, H. Ambrosius, E. Bente, J. Van der Tol, B. Smalbrugge, T. De Vries, E. J. Geluk, J. Bolk, R. Van Veldhoven, L. Augustin, P. Thijs, D. D’Agostino, H. Rabbani, K. Lawniczuk, S. Stopinski, S. Tahvili, A. Corradi, E. Kleijn, D. Dzibrou, M. Felicetti, E. Bitincka, V. Moskalenko, J. Zhao, R. Santos, G. Gilardi, W. Yao, K. Williams, P. Stabile, P. Kuindersma, J. Pello, S. Bhat, Y. Jiao, D. Heiss, G. Roelkens, M. Wale, P. Firth, F. Soares, N. Grote, M. Schell, H. Debregas, M. Achouche, J. L. Gentner, A. Bakker, T. Korthorst, D. Gallagher, A. Dabbs, A. Melloni, F. Morichetti, D. Melati, A. Wonfor, R. Penty, R. Broeke, B. Musk, and D. Robbins, “An introduction to InP-based generic integration technology,” *Semicond. Sci. Technol.* **29**(8), 083001 (2014).
- [102] A. Beling and J. C. Campbell, “InP-Based high-speed photodetectors,” *J. Lightw. Technol.* **27**(3), 343–355 (2009).
- [103] L. M. Augustin, R. Santos, E. den Haan, S. Kleijn, P. J. Thijs, S. Latkowski, D. Zhao, W. Yao, J. Bolk, H. Ambrosius, S. Mingaleev, A. Richter, A. Bakker, and T. Korthorst, “InP-based generic foundry platform for photonic integrated circuits,” *IEEE J. Sel. Top. Quantum Electron.* **24**(1), 6100210 (2017).
- [104] W. Yao, M. K. Smit, and M. J. Wale, “Monolithic 300 Gb/s parallel transmitter in InP-based generic photonic integration technology,” *IEEE J. Sel. Top. Quantum Electron.* **24**(1), 6100711 (2017).
- [105] S. Saeidi, P. Rasekh, K. M. Awan, A. Tüngen, M. J. Huttunen, and K. Dolgaleva, “Demonstration of optical nonlinearity in InGaAsP/InP passive waveguides,” *Opt. Mater.* **84**, 524–530 (2018).
- [106] C. Lacava, V. Pusino, P. Minzioni, M. Sorel, and I. Cristiani, “Nonlinear properties of AlGaAs waveguides in continuous wave operation regime,” *Opt. Express* **22**(5), 5291–5298 (2014).
- [107] P. Apiratikul, J. J. Wathen, G. A. Porkolab, B. Wang, L. He, T. E. Murphy, and C. J. Richardson, “Enhanced continuous-wave four-wave mixing efficiency in nonlinear AlGaAs waveguides,” *Opt. Express* **22**(22), 26814–26824 (2014).
- [108] M. Pu, L. Ottaviano, E. Semenova, and K. Yvind, “Efficient frequency comb generation in AlGaAs-on-insulator,” *Optica* **3**(8), 823–826 (2016).
- [109] S. May, M. Kues, M. Clerici, and M. Sorel, “Second-harmonic generation in AlGaAs-on-insulator waveguides,” *Opt. Lett.* **44**(6), 1339–1342 (2019).

- [110] L. Chang, W. Xie, H. Shu, Q. F. Yang, B. Shen, A. Boes, J. D. Peters, W. Jin, C. Xiang, S. Liu, G. Moille, S. Yu, X. Wang, K. Srinivasan, S. B. Papp, K. Vahala, and J. E. Bowers, “Ultra-efficient frequency comb generation in AlGaAs-on-insulator microresonators,” *Nat. Commun.* **11**(1), 1–8 (2020).
- [111] A. Z. Subramanian, C. J. Oton, D. P. Shepherd, and J. S. Wilkinson, “Erbium-doped waveguide laser in tantalum pentoxide,” *IEEE Photon. Technol. Lett.* **22**(21), 1571–1573 (2010).
- [112] C. Y. Tai, J. S. Wilkinson, N. M. Perney, M. C. Netti, F. Cattaneo, C. E. Finlayson, and J. J. Baumberg, “Determination of nonlinear refractive index in a Ta₂O₅ rib waveguide using self-phase modulation,” *Opt. Express.* **12**(21), 5110–5116 (2004).
- [113] Y. C. Yan, A. D. Faber, H. De Waal, P. G. Kik, and A. Polman, “Erbium-doped phosphate glass waveguide on silicon with 4.1 dB/cm gain at 1.535 μm ,” *Appl. Phys. Lett.* **71**(20), 2922–2924 (1997).
- [114] X. Gai, T. Han, A. Prasad, S. Madden, D. Y. Choi, R. Wang, D. Bulla, and B. Luther-Davies, “Progress in optical waveguides fabricated from chalcogenide glasses,” *Opt. Express* **18**(25), 26635–26646 (2010).
- [115] B. J. Eggleton, B. Luther-Davies, and K. Richardson, “Chalcogenide photonics,” *Nat. Photonics* **5**(3), 141 (2011).
- [116] I. Vasilief, S. Guy, B. Jacquier, B. Boulard, Y. P. Gao, C. Duverger, H. Haquin, V. Nazabal, J. L. Adam, M. Couchaud, and L. Fulbert, “Propagation losses and gain measurements in erbium-doped fluoride glass channel waveguides by use of a double-pass technique,” *Appl. Opt.* **44**(22), 4678–4683 (2005).
- [117] H. Haquin, G. Fonteneau, and J. L. Adam, “Recent developments in ion-exchanged fluoride glass planar waveguides,” *J. Non-Cryst. Solids* **326**, 460–463 (2003).
- [118] A. Q. Le Quang, R. Hierle, J. Zyss, I. Ledoux, G. Cusmai, R. Costa, A. Barberis, and S. M. Pietralunga, “Demonstration of net gain at 1550 nm in an erbium-doped polymer single mode rib waveguide,” *Appl. Phys. Lett.* **89**(14), 141124 (2006).
- [119] M. Liu, X. Yin, and X. Zhang, “Double-layer graphene optical modulator,” *Nano Lett.* **12**(3), 1482–1485 (2012).
- [120] Y. Gao, L. Tao, H. K. Tsang, and C. Shu, “Graphene-on-silicon nitride waveguide photodetector with interdigital contacts,” *Appl. Phys. Lett.* **112**(21), 211107 (2018).
- [121] T. H. Hoekstra, P. V. Lambeck, H. Albers, and T. J. Popma, “Sputter-deposited erbium-doped Y₂O₃ active optical waveguides,” *Electron. Lett.* **29**(7), 581–583 (1993).
- [122] C. I. Van Emmerik, R. Frentrop, M. Dijkstra, F. Segerink, R. Kooijman, M. Muneeb, G. Roelkens, E. Ghibaudo, J. E. Broquin, and S. M. Garcia-Blanco, “Heterogeneous

- integration of KY(WO₄)₂-on-glass: a bonding study,” *OSA Continuum* **2**(6), 2065–2076 (2019).
- [123] J. Mu, M. Dijkstra, and S. M. García-Blanco, "Resonant Coupling for Active–passive monolithic integration of Al₂O₃ and Si₃N₄," *IEEE Photon. Tech. Lett.* **31**(10), 771–774 (2019).
- [124] J. Mu, M. Dijkstra, J. Korterik, H. Offerhaus, and S. M. García-Blanco, “High-gain waveguide amplifiers in Si₃N₄ technology via double-layer monolithic integration,” *Photonics Res.* **8**(10), 1634–1641 (2020).
- [125] Z. Su, N. Li, H. C. Frankis, E. S. Magden, T. N. Adam, G. Leake, D. Coolbaugh, . D. B. Bradley, and M. R. Watts, “High-Q-factor Al₂O₃ micro-trench cavities integrated with silicon nitride waveguides on silicon,” *Opt. Express* **26**(9), 11161–11170 (2018).
- [126] J. D. B. Bradley, E. Shah Hosseini, Purnawirman, Z. Su, T. N. Adam, G. Leake, D. Coolbaugh, and M. R. Watts, “Monolithic erbium- and ytterbium-doped microring lasers on silicon chips,” *Opt. Express* **22**(10), 12226–12237 (2014).
- [127] Z. Su, N. Li, E. S. Magden, M. Byrd, Purnawirman, T. N. Adam, G. Leake, D. Coolbaugh, J. D. B. Bradley, and M. R. Watts, “Ultra-compact and low-threshold thulium microcavity laser monolithically integrated on silicon,” *Opt. Lett.* **41**(24), 5708–5711 (2016).
- [128] N. Li, D. Vermeulen, Z. Su, E. S. Magden, M. Xin, N. Singh, A. Ruocco, J. Notaros, C. V. Poulton, E. Timurdogan, C. Baiocco, and M. R. Watts, “Monolithically integrated erbium-doped tunable laser on a CMOS-compatible silicon photonics platform,” *Opt. Express* **26**(13), 16200–16211 (2018).
- [129] P. Jean, A. Douaud, V. Michaud-Belleau, S. H. Messaddeq, J. Genest, S. LaRochelle, Y. Messaddeq, and W. Shi, “Etchless chalcogenide microresonators monolithically coupled to silicon photonic waveguides,” *Opt. Lett.* **45**(10), 2830–2833 (2020).
- [130] A. W. Fang, H. Park, O. Cohen, R. Jones, M. J. Paniccia, and J. E. Bowers, "Electrically pumped hybrid AlGaInAs-silicon evanescent laser," *Opt. Express* **14**(20), 9203–9210 (2006).
- [131] D. Liang and J. E. Bowers, “Recent progress in lasers on silicon,” *Nat. Photonics* **4**(8), 511–517 (2010).
- [132] G. Roelkens, L. Liu, D. Liang, R. Jones, A. Fang, B. Koch, and J. E. Bowers, “III-V/silicon photonics for on-chip and intra-chip optical interconnects,” *Laser Photonics Rev.* **4**(6), 751–779 (2010).
- [133] M. J. Heck, J. F. Bauters, M. L. Davenport, J. K. Doylend, S. Jain, G. Kurczveil, S. Srinivasan, Y. Tang, and J. E. Bowers, “Hybrid silicon photonic integrated circuit technology,” *IEEE J. Sel. Top. Quantum Electron.* **19**(4), 6100117 (2012).

- [134] M. Belt, T. Huffman, M. L. Davenport, W. Li, J. S. Barton, and D. J. Blumenthal, "Arrayed narrow linewidth erbium-doped waveguide-distributed feedback lasers on an ultra-low-loss silicon-nitride platform," *Opt. Lett.* **38**(22), 4825–4828 (2013).
- [135] M. Belt and D. J. Blumenthal, "Erbium-doped waveguide DBR and DFB laser arrays integrated within an ultra-low-loss Si₃N₄ platform," *Opt. Express* **22**(9), 10655–10660 (2014).
- [136] E. S. Hosseini, Purnawirman, J. D. B. Bradley, J. Sun, G. Leake, T. N. Adam, D. D. Coolbaugh, and M. R. Watts, "CMOS-compatible 75 mW erbium-doped distributed feedback laser," *Opt. Lett.* **39**(11), 3106–3109 (2014).
- [137] Purnawirman, N. Li, E. S. Magden, G. Singh, N. Singh, A. Baldycheva, E. S. Hosseini, J. Sun, M. Moresco, T. N. Adam, G. Leake, D. Coolbaugh, J. D. B. Bradley, and M. R. Watts, "Ultra-narrow-linewidth Al₂O₃:Er³⁺ lasers with a wavelength-insensitive waveguide design on a wafer-scale silicon nitride platform," *Opt. Express* **25**(12), 13705–13713 (2017).
- [138] E. S. Magden, N. Li, Purnawirman, J. D. B. Bradley, N. Singh, A. Ruocco, G. S. Petrich, G. Leake, D. D. Coolbaugh, E. P. Ippen, M. R. Watts, and L. A. Kolodziejski, "Monolithically-integrated distributed feedback laser compatible with CMOS processing," *Opt. Express* **25**(15), 18058–18065 (2017).
- [139] N. Li, E. S. Magden, Z. Su, N. Singh, A. Ruocco, M. Xin, M. Byrd, P. T. Callahan, J. D. B. Bradley, C. Baiocco, D. Vermeulen, and M. R. Watts, "Broadband 2-μm emission on silicon chips: monolithically integrated Holmium lasers," *Opt. Express* **26**(3), 2220–2230 (2018).
- [140] X. Liu, W. M. Green, X. Chen, I. W. Hsieh, J. I. Dadap, Y. A. Vlasov, and R. M. Osgood Jr, "Conformal dielectric overlayers for engineering dispersion and effective nonlinearity of silicon nanophotonic wires," *Opt. Lett.* **33**(24), 2889–2891 (2008).
- [141] J. Riemensberger, K. Hartinger, T. Herr, V. Brasch, R. Holzwarth, and T. J. Kippenberg, "Dispersion engineering of thick high-Q silicon nitride ring-resonators via atomic layer deposition," *Opt. Express* **20**(25), 27661–27669 (2012).
- [142] A. Jha, B. D. O Richards, G. Jose, T. T. Fernandez, C. J. Hill, J. Lousteau, and P. Joshi, "Review on structural, thermal, optical and spectroscopic properties of tellurium oxide based glasses for fibre optic and waveguide applications," *Int. Mater. Rev.* **57**(6), 357–382 (2012).
- [143] K. Luke, Y. Okawachi, M. R. E. Lamont, A. L. Gaeta, and M. Lipson, "Broadband mid-infrared frequency comb generation in a Si₃N₄ microresonator," *Opt. Lett.* **40**(21) 4823–4826 (2015)
- [144] H. H. Li, "Refractive index of silicon and germanium and its wavelength and temperature derivatives," *J. Phys. Chem. Ref. Data* **9**(3), 561–658 (1993).

- [145] S. H. Kim, T. Yoko, and S. Sakka, “Linear and nonlinear optical properties of TeO₂ glass,” *J. Am. Ceram. Soc.* **76**(10), 2486–2490 (1993).
- [146] R. Stegeman, L. Jankovic, H. Kim, C. Rivero, G. Stegeman, K. Richardson, P. Delfyett, Y. Guo, A. Schulte, and T. Cardinal, “Tellurite glasses with peak absolute Raman gain coefficients up to 30 times that of fused silica,” *Opt. Lett.* **28**(13), 1126–1128 (2003).
- [147] G. Qin, A. Mori, and Y. Ohishi, “Brillouin lasing in a single-mode tellurite fiber,” *Opt. Lett.* **32**(15), 2179–2181 (2007).
- [148] A. Mori, Y. Ohishi, and S. Sudo, “Erbium-doped tellurite glass fibre laser and amplifier,” *Electron. Lett.* **33**(10), 863–864 (1997).
- [149] Y. Ohishi, A. Mori, M. Yamada, H. Ono, Y. Nishida, and K. Oikawa, “Gain characteristics of tellurite-based erbium-doped fiber amplifiers for 1.5- μ m broadband amplification,” *Opt. Lett.* **23**(4), 274–276 (1998).
- [150] A. Mori, K. Kobayashi, M. Yamada, T. Kanamori, K. Oikawa, Y. Nishida, and Y. Ohishi, “Low noise broadband tellurite-based Er³⁺-doped fibre amplifiers,” *Electron. Lett.* **34**(9):887–888 (1998).
- [151] A. Jha, B. Richards, G. Jose, T. Teddy-Fernandez, P. Joshi, X. Jiang, and J. Lousteau, “Rare-earth ion doped TeO₂ and GeO₂ glasses as laser materials,” *Prog. Mater. Sci.* **57**(8), 1426–1491 (2012).
- [152] H. Fukuda, K. Yamada, T. Shoji, M. Takahashi, T. Tsuchizawa, T. Watanabe, J. I. Takahashi, and S. I. Itabashi, “Four-wave mixing in silicon wire waveguides,” *Opt. Express* **13**(12), 4629–4637 (2005).
- [153] A. J. Kenyon, “Erbium in silicon,” *Semicond. Sci. Technol.* **20**(12), R65 (2005).
- [154] A. D. Bristow, N. Rotenberg, and H. M. Van Driel, “Two-photon absorption and Kerr coefficients of silicon for 850–2200 nm,” *Appl. Phys. Lett.* **90**(19), 191104 (2007).
- [155] M. A. G. Porcel, F. Schepers, J. P. Epping, T. Hellwig, M. Hoekman, R. G. Heideman, P. J. M. van der Slot, C. J. Lee, R. Schmidt, R. Bratschitsch, C. Fallnich, and K.-J. Boller, “Two-octave spanning supercontinuum generation in stoichiometric silicon nitride waveguides pumped at telecom wavelengths,” *Opt. Express* **25**(2), 1542–1554 (2017).
- [156] J. S. Wang, E. M. Vogel, and E. Snitzer, “Tellurite glass: a new candidate for fiber devices,” *Opt. Mater.* **3**(3), 187–203 (1994).
- [157] Y. Ding, S. Jiang, T. Luo, Y. Hu, and N. Peyghambarian, “Optical waveguides prepared in Er³⁺-doped tellurite glass by Ag⁺-Na⁺ ion-exchange,” *Proc. SPIE* **4282**, 23–30 (2001).
- [158] E. Chierici, M. C. Didavide, A. Moro, O. Rossotto, and L. Tallone, “Direct writing of channel waveguide on a tellurite glass using a focused ultraviolet laser beam,” in *Proceedings of 2002 IEEE/LEOS Workshop on Fibre and Optical Passive Components (IEEE, 2002)*, 24–28.

- [159] Y. Tokuda, M. Saito, M. Takahashi, K. Yamada, W. Watanabe, K. Itoh, and T. Yoko, “Waveguide formation in niobium tellurite glasses by pico- and femtosecond laser pulses,” *J. Non-Cryst. Solids* **326-327**, 472–475 (2003).
- [160] G. Nunzi Conti, S. Berneschi, M. Bettinelli, M. Brenci, B. Chen, S. Pelli, A. Speghini, and G. C. Righini, “Rare-earth doped tungsten tellurite glasses and waveguides: Fabrication and characterization,” *J. Non-Cryst. Solids* **345-346**, 343–348 (2004).
- [161] P. Nandi, G. Jose, C. Jayakrishnan, S. Debbarma, K. Chalapathi, K. Alti, A. K. Dharmadhikari, J. A. Dharmadhikari, and D. Mathur, “Femtosecond laser written channel waveguides in tellurite glass,” *Opt. Express* **14**(25), 12145–12150 (2006).
- [162] T. T. Fernandez, G. Della Valle, R. Osellame, G. Jose, N. Chiodo, A. Jha, and P. Laporta, “Active waveguides written by femtosecond laser irradiation in an erbium-doped phospho-tellurite glass,” *Opt. Express* **16**(19), 15198–15205 (2008).
- [163] R. Nayak, V. Gupta, A. L. Dawar, and K. Sreenivas, “Optical waveguiding in amorphous tellurium oxide thin films,” *Thin Solid Films* **445**(1), 118–126 (2003).
- [164] S. M. Pietralunga, M. Lanata, M. Ferè, D. Piccinin, G. Cusmai, M. Torregiani, and M. Martinelli, “High-contrast waveguides in sputtered pure TeO₂ glass thin films,” *Opt. Express* **16**(26), 21662–21670 (2008).
- [165] K. T. Vu and S. J. Madden, “Reactive ion etching of tellurite and chalcogenide waveguides using hydrogen, methane, and argon,” *J. Vac. Sci. Technol. A* **29**(1), 011023 (2011).

CHAPTER 2

Low-Loss Tellurium Oxide Thin Film Deposition by RF Reactive Sputtering

This chapter presents the development of a deposition process for high quality tellurium oxide (TeO_2) thin films by radio frequency (RF) reactive sputtering from a metallic tellurium target. The properties of the fabricated films were optimized by varying the deposition parameters including the RF-forward power applied to the tellurium target and the flow rate of oxygen into the chamber. The tellurite thin films were analyzed by ellipsometry, prism coupling, and Rutherford backscattering spectrometry (RBS) to characterize their thicknesses, refractive indices, planar optical propagation losses and O-Te compositional ratios. It was demonstrated that to achieve low-loss samples with high refractive indices it is important to deposit TeO_2 thin films near the stoichiometric O-Te ratio of 2. A repeatable, room-temperature process for the fabrication of low-loss TeO_2 films with a refractive index of 2.07 at 1550 nm wavelength and at an average deposition rate of 25-nm/min was developed using 125 W of RF forward power and between 9 and 11 sccm of O_2 flow. Prism coupling measurements on high-quality TeO_2 films demonstrate optical propagation losses as low as 0.4 and 0.1 dB/cm at 638 and 1550 nm wavelength, respectively. To function as an optical gain material, the TeO_2 films require the incorporation of rare-earth dopants, particularly erbium for communications applications around 1550 nm. Accordingly, erbium-doped TeO_2 ($\text{TeO}_2:\text{Er}^{3+}$) films were prepared by simultaneously co-sputtering from a metallic erbium target during the developed low-loss TeO_2 deposition process. A first set of $\text{TeO}_2:\text{Er}^{3+}$ films was deposited with 30 to 60 W of applied RF erbium sputtering power with a tellurium target at a 160-V DC-bias offset and 10.5 sccm of O_2 flow. Erbium concentrations ranging from 0.6 to 2.0×10^{20} ions/cm³ were determined using optical propagation loss measurements and the Er absorption cross sections around 1550 nm. For a second set of $\text{TeO}_2:\text{Er}^{3+}$ films deposited with a tellurium target at a 130-V DC bias offset and a 9.5 sccm O_2 flow rate the erbium concentration ranged from 1.0 to 2.7×10^{20} ions/cm³ for 38 to 53 W of RF-forward-power applied to the erbium target. The refractive index of the tellurite films was observed to decrease with increasing erbium concentration, down to 1.99 at 1550 nm for an erbium concentration of 2.7×10^{20} ions/cm³. While a small increase in background loss was observed in the doped films, <1 dB/cm of background loss at 1550 nm was observed in all of the $\text{TeO}_2:\text{Er}^{3+}$ films. With these results we demonstrate a cost-effective and versatile deposition process for the integration of low-loss undoped and doped tellurite films on photonic chips.

2.1. Introduction

Tellurium oxide (TeO_2) [1] has attracted interest in integrated optics due to its many promising material properties, including as a low-loss waveguide material, an efficient medium for nonlinear optical processes and a rare-earth host for optical amplifiers and lasers. TeO_2 is optically transparent from visible to mid-infrared wavelengths and has been used to demonstrate low-loss fibers, [2] thin films and ridge waveguides [3], with losses of less than 1 dB/m in fiber and 0.1 dB/cm in films and waveguides. Because of its large linear refractive index (2.08 at 1550 nm) [4] tellurite glass enables high confinement waveguides with small mode areas and tight bends for efficient and compact integrated devices. Tellurite also has many excellent non-linear figures of merit, including a nonlinear refractive index of $1.3 \times 10^{-18} \text{ m}^2/\text{W}$ at a 1900 nm wavelength [5], which is approximately $50\times$ that of silicon dioxide (SiO_2) and one of the highest nonlinearities for an oxide glass material. TeO_2 also demonstrates a large peak Raman gain coefficient ($3 \times 10^{-12} \text{ m/W}$) [6], and Brillouin gain coefficient ($1.7 \times 10^{-10} \text{ m/W}$) [7]. Tellurite glass therefore has wide reaching applications as a material for harmonic generation [8], four-wave mixing [9], and Raman [10,11] and Brillouin [12] amplifiers and lasers. In addition, TeO_2 is an excellent host for rare-earth dopants due to the unique site variability in the TeO_2 glass matrix enabling a high rare-earth solubility and large rare-earth emission bandwidths [13-16]. Tellurite fibers and ridge waveguides have been used to demonstrate high-performance erbium-doped amplifiers and lasers [13-18], with up to 14 dB gain at a 1530-nm wavelength shown in an erbium-doped ridge waveguide amplifier [17,18]. Additionally, TeO_2 has a low maximum phonon energy ($\sim 700\text{--}800 \text{ cm}^{-1}$), which reduces the rate of non-radiative transitions in erbium, allowing access to additional emission bands that are typically only accessible in fluoride hosts [16].

Based on these properties TeO_2 glass can be considered an ideal material for use in integrated photonic systems. However, although TeO_2 ridge waveguides with low waveguide losses [19] and high optical gain [17,18] had been previously demonstrated, issues remain with regard to patterning devices due to the solubility of TeO_2 in developer, [19,20] and a suitable etch recipe for rare-earth doped TeO_2 has proven challenging [17]. TeO_2 thin films can be grown by reactive sputtering deposition [17-21], which provides fast, uniform and low propagation loss films that can be fabricated on a wafer scale. Additionally the reactive sputtering process can be easily modified to include rare-earth dopants via co-sputtering, while introducing minimal OH^- incorporation into the film, which can cause detrimental effects in the operation of rare-earth amplifiers. The ability to deposit high-quality TeO_2 films at low temperatures [17-21] on a variety of substrates, is particularly attractive for the back-end integration of TeO_2 on active integrated optics platforms, such as silicon-on-insulator, without the risk of damaging metals. By incorporating TeO_2 thin films into existing photonic platforms [23,24], we can leverage their mature, high resolution patterning methods and fabricate TeO_2 devices without the need to etch the TeO_2 layer, and co-integrate TeO_2 devices with other established passive and optoelectronic photonic building blocks (thermo-optic switches, electro-optic modulators, photodetectors, etc.) for advanced photonic integrated circuits. In

order to achieve successful co-integration of TeO₂ devices on these platforms, it is first critical to optimize the fabrication process and optical properties of the TeO₂ layer. This chapter focuses on the development of a deposition process for low-loss passive and erbium doped TeO₂ thin films by reactive sputtering. In following chapters this deposition process is applied to monolithically integrate TeO₂ devices into standard silicon-nitride and silicon photonic fabrication platforms.

2.2. Tellurite Film Deposition System and Procedures

Tellurium oxide (TeO_x) thin films were grown using a Kurt J. Lesker PVD Pro 200 deposition system, in the cleanroom of McMaster University's Centre for Emerging Device Technologies (CEDT). The system features a deposition chamber, a load-lock with transfer arm, and an instrument control tower. The deposition chamber is fit with a cryogenic-pump that typically maintains a temperature of 15 K and keeps the deposition chamber at a pressure of 10⁻⁸ Torr, while the load-lock is fit with a turbo-pump which is backed by a mechanical pump and can reach pressures of 10⁻⁷ Torr. A picture of the deposition system can be seen in Fig. 2.1.



Fig. 2.1. Picture of Kurt J. Lesker PVD Pro 200 thin film deposition system in the CEDT cleanroom, with control tower on the left and vacuum chamber on the right.

Samples are loaded into the chamber through the load-lock in an upside-down orientation, such that the sample surface faces down towards the ground. The 150-mm diameter sample stage in the chamber is driven by a motor and can rotate at up to 10 revolutions per minute (RPM). The sample stage is backed by a resistive heating coil, which has a maximum temperature setting of 600 °C, and an RF substrate bias plasma source to provide kinetic energy into the samples. Between the sample stage and the sputter guns there is a ‘butterfly’ shield that is used to block samples from being deposited on during pre-sputtering and can be opened when the deposition process begins. Around the chamber sample stage there is ‘shower ring’ gas inlet connected to an oxygen supply line. Between the inlet and the oxygen

supply bottle there is a gas valve and a mass flow controller (MFC) to control the rate of oxygen flow into the chamber of up to 20 sccm. The chamber has three upwards facing, 3” diameter magnetron sputter guns, two of which are connected to radio-frequency (RF) power supplies with a 600 W maximum output, while the other is connected to both a direct-current (DC) and RF power supply with a 300 W maximum output. The centers of the guns are located at a vertical and lateral distance relative to the edge of the substrate of 150 and 50 mm, respectively and are tilted at an angle of 20 degrees. All depositions discussed in this thesis use RF powers. Each sputter gun also has a ‘clamshell’ cover that can be used to protect targets from being deposited on when not in use. On the bottom of the chamber near the targets there is a gas inlet on each side of the chamber connected to an argon supply line. Each argon inlet has its own gas valve while they are both connected to the same MFC, controlling the total flow rate of argon into the chamber up to a 120 sccm maximum. For consistency both inlets are always left open when running a deposition recipe. The control tower contains the RF power supply controllers and phase matching units as well as the instrument control computer that is responsible for monitoring and adjusting valves and motors, MFCs and power supply setpoints and tuning ratios using a LabVIEW based software (eKlipse). The software contains several recipes for basic functions such as venting and pumping the vacuum chambers, transferring samples between the load lock and process chamber, and editable deposition recipes. A diagram of the internal features of the deposition chamber can be seen in Fig. 2.2.

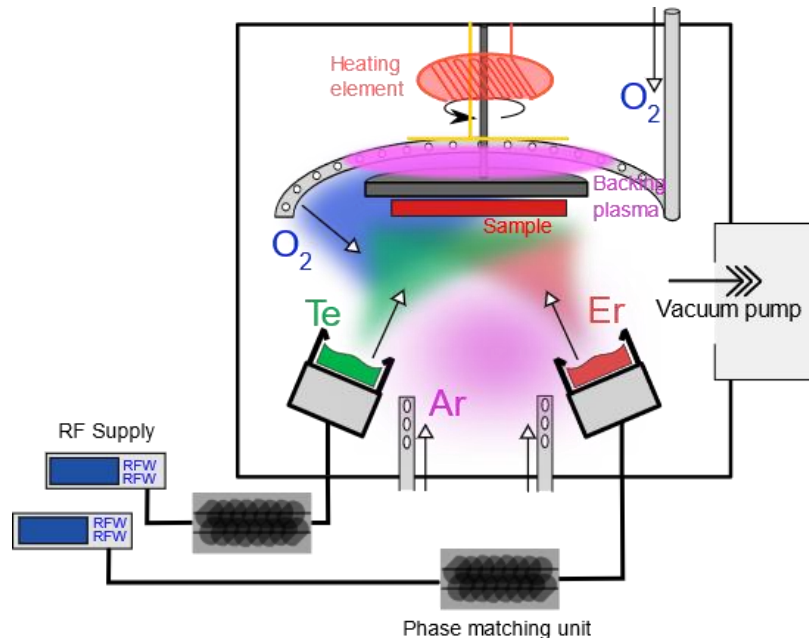


Fig. 2.2. Diagram of the interior of sputter deposition system, featuring an inverted 6-inch sample holder on a rotating platform backed by a heater and a substrate plasma, with confocal magnetron sputtering guns with metallic tellurium and erbium targets at the bottom of the chamber connected to an RF power supply. Argon gas is inlet through two valves at the bottom of the chamber, while oxygen is inlet through a ring coiled around the substrate holder.

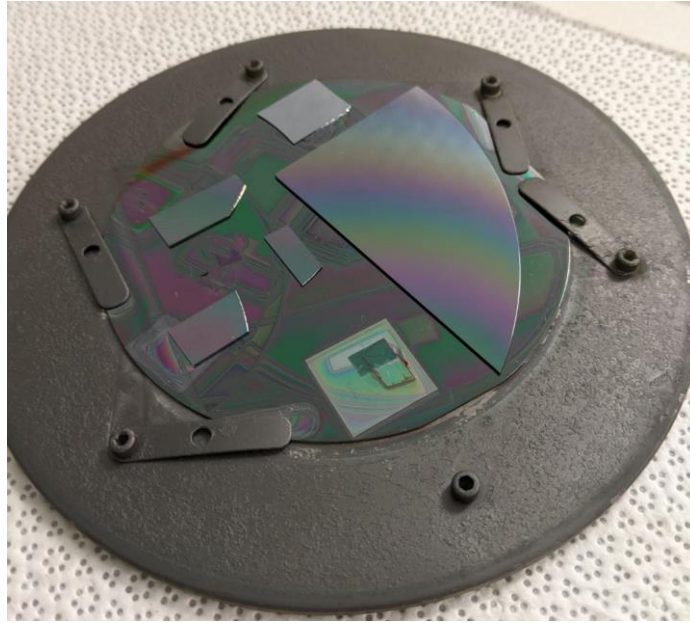


Fig. 2.3. A bare silicon, thermally oxidized silicon, and glass slide test piece as well as several chips mounted onto the substrate holder.

The samples are mounted onto a 150-mm diameter substrate holder which fits onto the transfer arm and sample rotation stage in the deposition chamber. A 100-mm bare silicon wafer is attached to the substrate holder by clamps to block the screw holes of the substrate holder, preventing deposition material from sputtering onto the heater that is located behind the sample stage. Samples under test are then mounted onto the clamped bare silicon wafer by double sided carbon tape (Nisshin EM Co., Ltd.). To ensure adhesion without potentially damaging the chip surface the samples are typically gently placed on the carbon tape on the mount and then pressed on tightly by blowing down on the samples with a nitrogen gun. The samples loaded for each deposition include a bare silicon test piece, an unpatterned thermally oxidized silicon wafer piece and a blank glass side. An example of a set of samples as mounted on the substrate holder can be seen in Fig. 2.3. Once the samples are mounted, the sample holder is placed upside down into the vented load lock. The load lock is then pumped down to a pressure of 10^{-6} Torr before the samples are transferred into the main chamber. Once inside, the instrument control computer is used to run a preprogrammed deposition recipe. The general order of the recipe is to initially flow argon gas into the chamber in order to achieve a pressure of 10 mTorr. Once pressurized the power supplies for the sputter targets are turned on at 50 W forward power for the tellurium target and 30 W forward power for the erbium target if being used, igniting the plasmas. Once the plasmas have been ignited the argon gas flow is reduced to the processing conditions, which is set to be 12 sccm, and the oxygen supply valve is opened and inlet at a flow rate of typically 9 to 11 sccm. The forward powers supplied to the sputter targets are then ramped from their initial condition to the processing setpoint, which is typically 125 W for the tellurium target and between 20 to 70 W for the erbium target, at a rate of 1 W/minute. Once at the processing setpoint the targets are pre-

sputtered for 5-minutes with the sample blocked by the butterfly shield. After 5-minutes the sample stage begins rotation at 8 RPM and the shield is opened to deposit onto the samples. In this work, depositions for the purpose of thin film characterization were run for 10 minutes, while depositions on integrated photonic chips are run for a set time based on the deposition rate in order to achieve a targeted film thickness. Once the deposition time is reached the butterfly shield is closed, the sample stage rotation is stopped and the RF forward power applied to the sputtering targets is ramped down to the initial value, after which the power is turned off. Once the power supplies are turned off the argon and oxygen gas flow rates are set to 0 and the gas inlet valves are closed. After the deposition chamber has returned to a vacuum of less than 10^{-6} mTorr, the samples can be transferred to the load-lock and unloaded.

2.3. Tellurite Film Characterization Methods

To develop a thin film deposition process to achieve high-quality films with high-deposition rates, high-refractive index, low optical attenuation and desired O-Te compositional ratios, the fabricated films must be carefully characterized. Three main characterization techniques were employed for the optimization of TeO_x thin film deposition recipes, including: ellipsometry for measurement of the films' refractive index and thickness, prism coupling into the planar waveguide modes for optical attenuation measurements and Rutherford backscattering spectrometry (RBS) for compositional ratio characterization.

2.3.1 Ellipsometry

Ellipsometry measurements were performed using a J.A Woollam variable angle spectroscopic ellipsometer (VASE), as part of McMaster's CEDT material characterization lab. The measurements were carried out on tellurium oxide thin films deposited on unpatterned bare silicon test pieces. Ellipsometry characterization operates based on measuring the differences between complex refraction of transverse electric (TE) and transverse magnetic (TM)-polarized light from a surface. From the Fresnel reflection coefficients [25], the complex reflection from a surface for each polarization state can be described by the magnitude of the reflected electric-field (r) and phase shift upon reflection (Φ) as follows,

$$\begin{aligned} r_{\text{TE}} &= |r_{\text{TE}}|e^{i\Phi_{\text{TE}}} \\ r_{\text{TM}} &= |r_{\text{TM}}|e^{i\Phi_{\text{TM}}}, \end{aligned} \quad (2.1)$$

where the reflection coefficients for each polarization are dependent on the refractive index of the test sample (n) and incident angle of the light. The ratio between the reflected electric fields for the two different polarization states can be described as follows,

$$\frac{r_{\text{TE}}}{r_{\text{TM}}} = \frac{|r_{\text{TE}}|}{|r_{\text{TM}}|} e^{i(\Phi_{\text{TE}} - \Phi_{\text{TM}})} = \tan(\Psi)e^{i\Delta}. \quad (2.2)$$

The ellipsometer then measures the relative magnitude ratio($\tan(\Psi)$) and phase difference (Δ) in the reflected light from the sample in the two different polarization orientations. The experimental ellipsometry setup operates by launching a polarized beam of light onto a sample at a specified angle, and detecting the reflected light through a second, rotatable polarizer (analyzer). Assuming that the sample under test is completely uniform, and only light reflected from the sample surface is detected the refractive index of the material can be calculated directly from the measured data. A bare silicon substrate with a roughened back surface is a close approximation of the ideal sample, as the majority of light that does not reflect off the surface of the film, will travel through the bulk of the film and either be absorbed or scattered off the back surface. However, a thin film on a silicon test piece does not fall under this ideal case, as a significant portion of the light that transmits through the thin film will reflect off the film/Si substrate interface and re-exit the film from the front surface. This creates a thin film interference pattern that will affect the measured magnitude and phase difference constants. Therefore, to extract the parameters of the thin film a more complex model involving the reflection/transmission of light from multiple surfaces and the resulting interference pattern through different optical paths must be established. For a homogenous TeO_x thin film on an idealized silicon substrate the resulting interference pattern will be determined by the thickness and refractive index of the thin film, considering a silicon substrate with a known refractive index. However, because different combinations of film thickness and refractive index can create the same optical interference pattern at a single wavelength the properties of the film still cannot be measured directly. Therefore, to analyze the results, measurements are taken over a range of wavelengths and a common material refractive index dispersion relationship is assumed. For a transparent thin film such as TeO_2 the Sellmeier dispersion relation [26] provides a reliable model of refractive index dispersion from the visible to the near infrared. The Sellmeier dispersion relation, to the first order, can be described as follows,

$$n(\lambda) = \left(D_{\text{Sellmeier}} + \frac{E_{\text{Sellmeier}} \lambda^2}{\lambda^2 - F_{\text{Sellmeier}}^2} \right)^{\frac{1}{2}}, \quad (2.3)$$

where λ is the wavelength of the incident light, $D_{\text{Sellmeier}}$ is a constant refractive index offset for the material, and $E_{\text{Sellmeier}}$ and $F_{\text{Sellmeier}}$ are the amplitude and resonance wavelength from the dipole oscillator model of a material. A model of the $D_{\text{Sellmeier}}$, $E_{\text{Sellmeier}}$, and $F_{\text{Sellmeier}}$ parameters of Equation 2.3, as well as the film thickness is then used to calculate the expected spectroscopic psi and delta values based on the model, with the parameters then varied to best fit the experimental psi and delta values obtained from the measurement.

2.3.2 Prism Coupling

A thin film characterization method which is particularly relevant to waveguides is the prism coupling/m-line measurement technique [27,28]. In this method, the planar waveguide modes of the thin film of interest are excited by evanescently coupling a beam of light into the film,

from an internal reflection off the face of a prism pressed onto the film. A model describing the refractive index and thickness of the thin film can then be developed by identifying the optical propagation constants of the waveguide modes supported by the thin film. Although it is highly accurate (± 0.005) and straightforward to extract the film parameters using this method, the alignment process for this technique can be time consuming and measurements can only be carried out at a single wavelength at a time. Therefore, while ellipsometry is generally preferred for analyzing a sample's refractive index and thickness properties in this study, prism coupling results can be used to confirm the ellipsometry modelling. However, an additional feature of prism coupling is the ability to characterize the planar waveguide loss of the film. By exciting an optical mode to travel along the film the attenuation of light versus distance travelled can be measured and fit as the loss of the film. In contrast, the propagation length in ellipsometry is short, which makes it difficult to measure attenuation in low loss materials. Accurate characterization of optical loss via a technique such as prism coupling is particularly important for the optimization of thin film waveguide materials. A derivation of the theory of operation for the prism coupling method can be found in these references [27,28] and is also provided here.

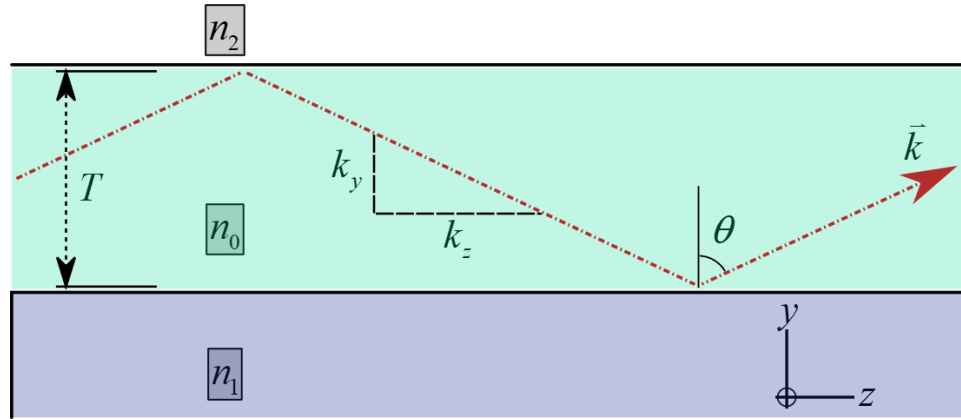


Fig. 2.4. Diagram of light ray travelling through planar thin film of thickness T , with a refractive index of n_0 and cladding refractive indices of n_1 and n_2 .

Consider a thin film of refractive index n_0 , with a thickness T , deposited on a substrate of refractive index n_1 , and with air upper cladding with a refractive index of n_2 . A light ray travelling through the film at an angle of θ relative to the normal of the film-cladding interface, as diagrammed in Fig 2.4, can be described by its wave vector \vec{k} , which includes a y and z component as follows,

$$\vec{k} = (k_0 n_0 \cos \theta) \hat{y} + (k_0 n_0 \sin \theta) \hat{z}, \quad (2.4)$$

where the wave vector magnitude k_0 is related to the free space wavelength λ of light as shown in Equation 2.5,

$$k_0 = \frac{2\pi}{\lambda}. \quad (2.5)$$

Assuming that the thin film is surrounded by media of lower refractive index, such as a thermal SiO₂ cladding under a TeO_x thin film exposed to air, it can support total internal reflection (TIR) at light propagation angles, θ , above the critical angle (θ_c) [29]. A beam of light travelling through the film can then be confined totally within the film. However destructive interference from out of phase light will quickly attenuate the propagating light, unless a constructive interference condition is met. Therefore, to achieve lossless propagation of light through the film it must also satisfy the condition such that rays of light travelling through the film on the same phase front have a round trip phase shift that is equal to a unit multiple of 2π . The optical path length can be described by the distance travelled from one interface of the thin film to the other, and back again, with each interface contributing a phase shift of ϕ upon reflection. The interference condition can be described by:

$$2k_0n_0T \cos \theta + \phi_1 + \phi_2 = 2m\pi, \quad (2.6)$$

where ϕ_1 and ϕ_2 are the phase shift upon reflection from the lower and upper boundary respectively, and the interference term, m , must be an integer to satisfy the constructive interference condition. The angular dependance of the relationship can then be redescribed in terms of the propagation constant, which is the value of the wavevector along the z-axis (k_z), of the planar waveguide as follows,

$$\sin \theta = \frac{k_z}{k_0n_0}, \quad (2.7)$$

which is used to redescribe the cosine of the angle from the Pythagorean identity as follows.

$$\begin{aligned} \cos \theta &= \sqrt{1 - \sin^2 \theta} \\ &= \sqrt{1 - \left(\frac{k_z}{k_0n_0}\right)^2} \\ &= \frac{1}{k_0n_0} \sqrt{k_0^2n_0^2 - k_z^2}. \end{aligned} \quad (2.8)$$

The phase change upon reflection can be calculated from the Fresnel equations, and will vary depending on whether the light is TE or TM-polarized. For example, for the TE-polarized case, the phase change upon reflection can be calculated as,

$$\phi_j = -2 \tan^{-1} \left(\frac{\sqrt{\sin^2 \theta - (n_j/n_0)}}{\cos \theta} \right), \quad (2.9)$$

where n_0 is the refractive index of the thin film and n_j is either the refractive index of the substrate or air depending on the boundary. The phase shift can then be written in terms of the propagation constant using the relationships of Equation 2.7 and 2.8 as shown below:

$$\begin{aligned} \phi_j &= -2 \tan^{-1} \left(\frac{\sqrt{\left(\frac{k_z}{k_0 n_0}\right)^2 - \left(\frac{n_j}{n_0}\right)^2}}{\frac{1}{k_0 n_0} \sqrt{k_0^2 n_0^2 - k_z^2}} \right) \\ &= -2 \tan^{-1} \left(\frac{\frac{1}{k_0 n_0} \sqrt{k_z^2 - k_0^2 n_j^2}}{\frac{1}{k_0 n_0} \sqrt{k_0^2 n_0^2 - k_z^2}} \right) \\ &= -2 \tan^{-1} \left(\frac{\sqrt{k_z^2 - k_0^2 n_j^2}}{\sqrt{k_0^2 n_0^2 - k_z^2}} \right). \end{aligned} \quad (2.10)$$

With these equations the interference condition can now be described totally in terms of the material refractive indices, thickness of the waveguiding film and propagation constant of the light. Fig. 2.5 shows the calculated interference term (m) from Equation 2.6 versus the propagation constant of light for a TeO₂ thin film on a thermal oxide layer at TeO₂ film thicknesses of 200, 400 and 600 nm at a wavelength of 638 nm. It was assumed in these calculations that the TeO₂ film has a refractive index of 2.15 [21] and the thermal oxide has a refractive index of 1.44 [30]. The range of accessible propagation constants in the film is limited on the lower end by the need to maintain the critical angle condition ($\theta \geq \theta_c$) and on the upper end by a 90 degree propagation angle ($\theta \leq 90$). For the supposed TeO₂ film properties the accessible propagation constants are then limited to between 16.2 and 21.0 μm^{-1} . The points where the calculated interference terms cross one of the dotted lines identifies propagation constants where the constructive interference condition is satisfied and a propagating planar film mode is supported by the system. The 200-nm-thick TeO₂ film is shown to support a single propagating film mode ($m = 0$) while the 400- and 600-nm-thick TeO₂ films support two ($m = 0, 1$) and three ($m = 0, 1, 2$) unique waveguide modes, respectively.

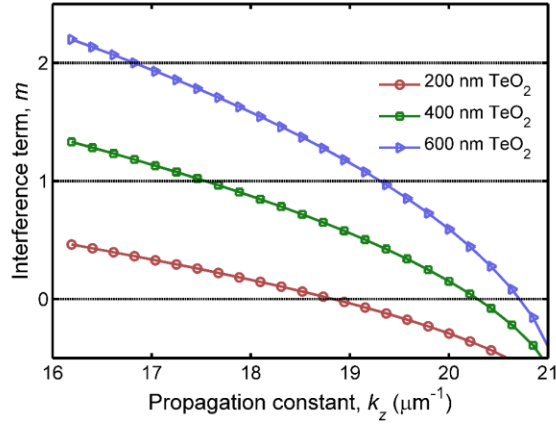


Fig. 2.5. Solutions of the interference term versus propagation constant for a TeO₂ thin film on thermal oxide at a wavelength of 638 nm and TE polarization, for TeO₂ film thicknesses of 200, 400, and 600 nm.

If an incident ray of light experiences an internal reflection at an interface (e.g., a prism-air boundary) near the surface of the thin film the evanescent tail [25,27-29] of this reflection can overlap into the thin film. Moreover, if the propagation vector of the light ray overlapping into the thin film matches one of the propagating optical modes of the planar waveguide the optical power can be transferred into the film. An internal reflection can be achieved near the planar thin film by reflecting light off the face of glass prism that is clamped into close contact (\sim quarter of a wavelength [27]) with the thin film, such that the evanescent tail of the light ray reflecting off the prism/air interface overlaps into the film. Fig. 2.6. shows a diagram of a light ray incident on a prism which experiences TIR from the base of the prism. For a prism with a sidewall angle of ϵ , an incident light ray at an angle of α to the sidewall normal will refract into the prism at an angle of ν , found from Snell's law. This results in an internal reflection occurring at the prism base at an angle of σ .

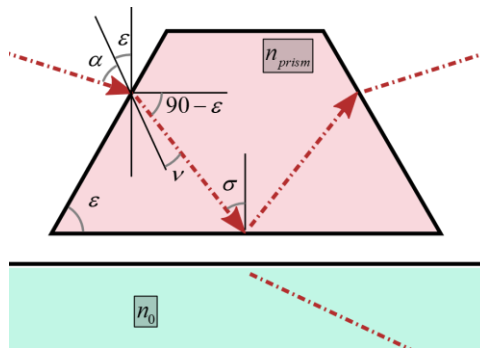


Fig. 2.6. A light ray incident on a prism face at an angle of α to the sidewall normal will refract into the prism and experience an internal reflection from the base of the prism at an angle of σ .

Similar to the thin film waveguide, the propagation constant of light in the prism (k_{prism}) can be related to the angle of reflection from the prism base (σ) and index of the prism (n_{prism}) as follows,

$$\sin \sigma = \frac{k_{\text{prism}}}{k_0 n_{\text{prism}}}, \quad (2.11)$$

where the reflection angle σ can be determined from the angle of the prism input face and incident angle relative the prism face normal α from Snell's law [29] as follows:

$$\sigma = \epsilon + \sin^{-1} \left(\frac{n_2}{n_{\text{prism}}} \sin(\alpha) \right). \quad (2.12)$$

Therefore, by rotating the angle of the incident light beam onto the prism sidewall the propagation constant of light within the prism can be changed. Because changes in the incident angle correspond to a proportionally smaller change in the prism's internal reflection angle very precise control of the propagation constant can be achieved. When the propagation constant in the prism is matched to that of the thin film the light can couple into and propagate through the film. By identifying the propagation constants of the prism at which light couples into the thin film a system of equations can be derived that are used to calculate the refractive index and thickness of a thin film as described in the following references [27,28]. If there are two or more modes confined by the thin film, the system of equations can be solved by only a unique pair of refractive index and thickness values, removing any uncertainty from modelling in the evaluation of film properties.

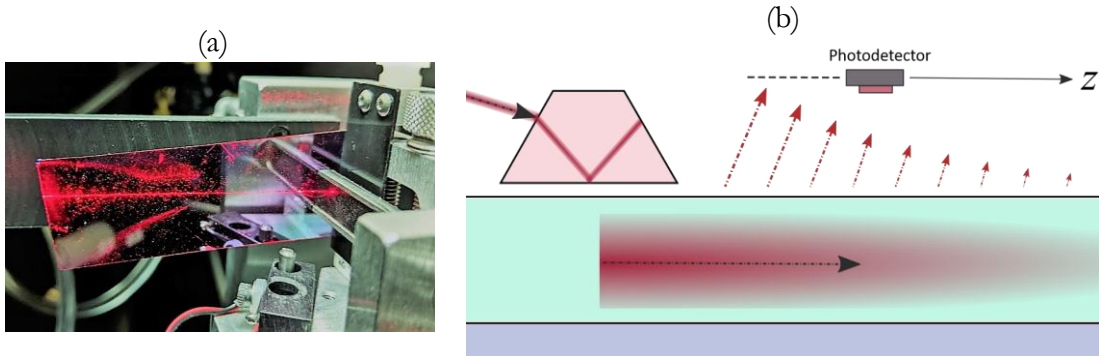


Fig. 2.7. (a) Red light streak propagating through tellurium oxide thin film in prism coupler. (b) Diagram of how prism coupler collects scattered light for loss measurements.

Once the optical mode is excited, light propagates across the film, as seen for the red-light example in Fig 2.7(a). The visibility of the light streak from the top of the film is a result of light scattering from the film surface, which is a source of loss in the film along with absorption within the film itself. By tracking the decay in the optical intensity of the scattered light as it propagates along the film the loss characteristics of the film can be evaluated. Loss measurements are performed by using a scanning photodetector to collect the scattered light, as seen in the diagram of Fig. 2.7(b). Assuming a consistent surface roughness which scatters a uniform fraction of the light intensity travelling through the thin film at all points, the decay of optical intensity can be determined by monitoring the intensity of the scattered light versus distance from the coupling point. From the Beer-Lambert law [31], the decay of optical

intensity (I) in the waveguide should follow an exponential trend versus propagation length (z) through the medium. Assuming a uniform loss throughout the planar waveguide, the relative optical attenuation (a) can be described as follows,

$$a = \frac{I_z}{I_0} = e^{-\mu z}, \quad (2.13)$$

where I_0 is the initial optical intensity, I_z is the optical intensity after propagating a distance of z and the rate of attenuation is determined by the attenuation coefficient (μ). Taking the log of Equation 2.13, the loss per unit length (A) in the waveguide in the dB scale is found by Equation 2.14.

$$A = 10 \log_{10}(e)\mu. \quad (2.14)$$

An example of the scattered intensity at 638 nm measured in a TeO_2 film, fit with an attenuation coefficient of 0.7 cm^{-1} based on Equation 2.13, is shown in Fig. 2.8. This attenuation corresponds to a 3.0 dB/cm waveguide propagation loss from Equation 2.14. As seen in Fig. 2.8 there are occasionally small spikes in the scattered intensity away from the fitted curve, typically as a result of a scratch or dust particle on the film surface increasing the scattered intensity at that particular point. The data is typically fit to the low points of scattered light intensity, because this is considered to represent the baseline scattering occurring off the surface roughness that is uniform across the film. For lower loss films ($<1 \text{ dB/cm}$) the variance created by non-uniformities in surface roughness becomes more prevalent, creating large spikes in measured data. For these samples it becomes much more difficult to estimate loss, so the data is typically fit with a best- and worst-case scenario, such that the calculated loss is the average of the two values with an uncertainty based on the difference.

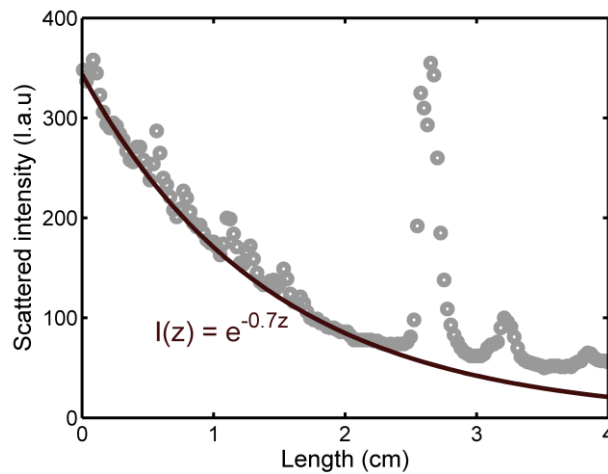


Fig. 2.8. Sample measured intensity of scattered light through the top of a TeO_2 film, versus distance away from coupling point. The data is fit with an exponential equation to estimate a 3.7 dB/cm optical propagation loss.

2.3.3 Rutherford Backscattering Spectrometry

The compositional ratio of thin films fabricated by reactive sputtering can have significant variations based on the deposition process parameters. For example, sputtering a tellurium target with no oxygen in the chamber would result in a purely tellurium thin film being grown. Increasing the oxygen flow rate will result in increasing ratios of oxygen in the TeO_x film, where x is the O-Te ratio, which will affect the refractive index, absorption, deposition rate, chemical stability and several other material parameters of the TeO_x film relevant to waveguide applications. Stoichiometric tellurium oxide thin films where $x = 2$ have been shown to result in the lowest optical propagation losses, with large refractive indices [19]. Therefore, it is important to quantify the composition of the deposited tellurite films, which can be effectively carried out using the Rutherford backscattering spectrometry (RBS) technique.

RBS measurements were made at the Tandatron Accelerator Laboratory at the University of Western Ontario on tellurium oxide thin films deposited on bare silicon test pieces. The accelerator is used to launch helium ions (${}^4\text{He}^+$) at a 1.8 MeV energy (E_0) into the sample under test. Particles of this mass and energy can penetrate through the majority of the film under test with minimal changes to their energy or travel direction caused by the electron clouds in the material's lattice. However, if incident upon the nucleus of an atom the incident particle will experience an elastic scattering event based on the Coulomb interaction between the two nuclei that causes the incident particle to change direction. It is intuitive that the larger the size and charge of the particles the more likely an interaction between the two is. Additionally, a collision between an incident particle near the edge of the scattering center particle can be expected to cause a minor change in the angle of the incident particle, while a more direct collision will cause a greater change in direction. A diagram showing three particles incident at different positions on a scattering center and the differences expected in their scattered trajectory are shown in Fig. 2.9.

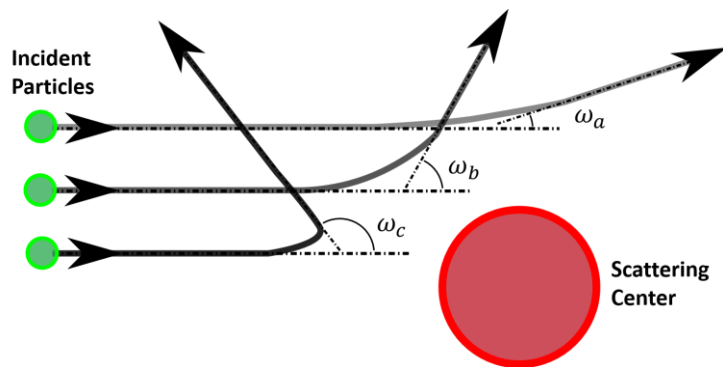


Fig. 2.9. Three particles incident on a scattering center at different relative positions are scattered off the sample at different angles.

By calculating the Coulombic repulsion between the two nuclei, the probability of an incident particle scattering off the nucleus of a scattering center atom at a specific angle (ω), referred to as the scattering cross section (σ_{scatter}), can be determined. For an incident particle

with an atomic number of Z_1 launched at an energy of E_0 and a scattering center particle of atomic number Z_2 the scattering cross section is found to be,

$$\sigma_{\text{scatter}}(\omega) = \left(\frac{Z_1 Z_2 e^{-2}}{4E_0 \sin^2 \left(\frac{\omega}{2} \right)} \right)^2 \quad (2.15)$$

where e^- is the elementary charge of an electron [32]. Assuming that the scattering center particle is initially stationary the incident particle will impart some energy and momentum to it. The total energy must be conserved by altering the energy and momentum of the scattered particle. The ratio of the incident particle's energy after scattering (E_1), compared to its initial energy is referred to as the kinematical factor (k), and can be calculated by solving the energy and momentum conservation equations at a scattering angle of ω with respect to the mass of the incident (m_1) and scattering particle (m_2),

$$\frac{E_1}{E_0} = k = \left(\frac{m_1 \cos \omega \pm \sqrt{m_2^2 - m_1^2 (\sin^2 \omega)}}{m_1 + m_2} \right)^2 \quad (2.16)$$

where the square root term in the numerator is positive when the launched particle is lighter than the scattering site particle, which for the case of helium ions is always true, except in the case of detecting hydrogen. The RBS instrument then collects an energy spectrum based on the number of backscattered particles that occur at various energies, for a specific backscattering angle. An example energy spectrum measured for a TeO_2 film on a silicon substrate can be found in Fig. 2.10.

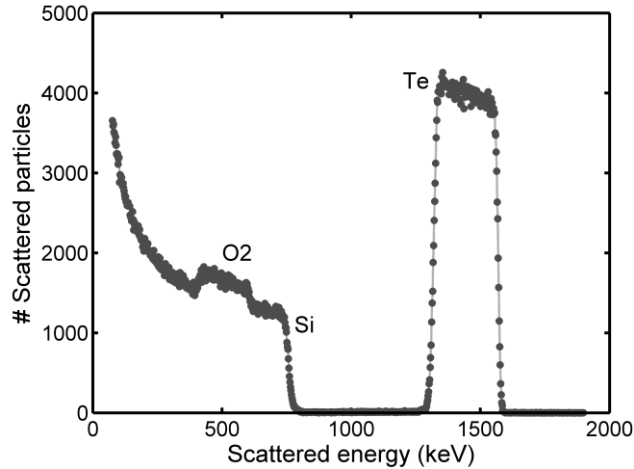


Fig. 2.10. Example of a measured RBS spectrum showing the number of scattered particles with different energies for a TeO_2 film on a silicon substrate, with scatterings from Te atoms seen near 1500 keV, a broad spectrum of Si scatterings below 800 keV, and small signature of O scatterings around 600 keV.

Because the expected energy and frequency of backscattered particles can be predicted from Equations 2.14 and 2.15, the measured data can be fit to determine the elements making up the sample and their densities. Although a higher ratio of incident particles are scattered at small angles, the variation in energy between different ion masses is difficult to distinguish, particularly for heavier particles. To optimize mass resolution and the ratio of detectable particles detection is carried out at an angle of 170 degrees. In a real sample many higher order effects, such as multiple collisions and energy straggling cause the measured energy spectra of scattered ions to broaden [33,34]. The energy spectra were then fit with an advanced modelling software (SIMNRA) that accounts for these effects to extract the composition of the thin film.

2.4. Optimization of TeO₂ Deposition Recipe

Reactive RF sputtering is an effective method to fabricate high-quality, low propagation loss metal-oxide thin films on a variety of substrates with high-deposition rates, and wafer-scale uniformity [22]. The work of Nayak demonstrated initial results of TeO_x films fabricated via reactive sputtering with losses of down to 0.26 dB/cm at 633 nm [21]. Vu and Madden confirmed the fabrication of stoichiometric TeO₂ thin films fabricated by reactive RF sputtering with losses of 0.1 dB/cm at a 1550 nm wavelength [19]. Through this work they determined that the tellurite film optical losses are primarily determined by the O-Te compositional ratio of the TeO_x film, where stoichiometric films ($x = 2$) were observed to have refractive indices of 2.08 ± 0.03 at a 1550 nm wavelength, and low propagation losses of < 0.1 dB/cm. Oxygen rich films ($x > 2$) were seen to have a moderate increase in loss and lower refractive index, while tellurium rich films ($x < 2$) exhibited a significant increase in loss due to the absorption from the excess metal atoms as well as an increase in refractive index. Therefore, to maximize the refractive index of the film for compact optical devices and achieve low waveguide losses a TeO₂ deposition recipe that achieves near stoichiometric films is required. Two deposition parameters were generally varied to achieve stoichiometric low-loss films using our deposition system because of their strong influence on the composition of the films: the flow rate of oxygen into the chamber and the RF forward power applied to the metallic tellurium target. Increasing or decreasing the oxygen flow rate is expected to have the corresponding effect on the oxygen content of the film, while increasing/decreasing the RF power applied to the tellurium target is expected to have the corresponding effect on the ratio of tellurium in the film. However due to the constantly changing oxidation state and topography of the target through its operational lifetime, the RF sputtering power was found to be a poor indicator of the rate of tellurium atom sputtering. Instead, the DC bias offset of the RF signal applied to the target was used to monitor the relative sputter yield with much more consistent results. Other potential parameters which could be adjusted but were generally left constant include the argon flow rate, the chamber pressure, and the sample temperature. The vacuum pump on the system does not have a variable throttle, thus the vacuum system must be run in either a constant flow or constant pressure mode where both the chamber pressure and flow rate cannot be adjusted simultaneously. A constant flow

operation mode with 12 sccm of argon, which typically results in a chamber pressure of 2.8-mTorr, was used to maintain a relatively consistent argon to oxygen ratio in the chamber. As low-loss TeO_2 films can be achieved at room-temperature [19,21], the depositions were all run without the use of the sample heater. The ability to run depositions at low temperatures is highly promising for integrating TeO_2 films onto optoelectronic chips with metals and other temperature sensitive layers. However, as will be discussed further in Chapter 4, moderate increases to temperature might be of interest in future for investigating further improvement to film losses and reducing rare-earth ion quenching in erbium doped films.

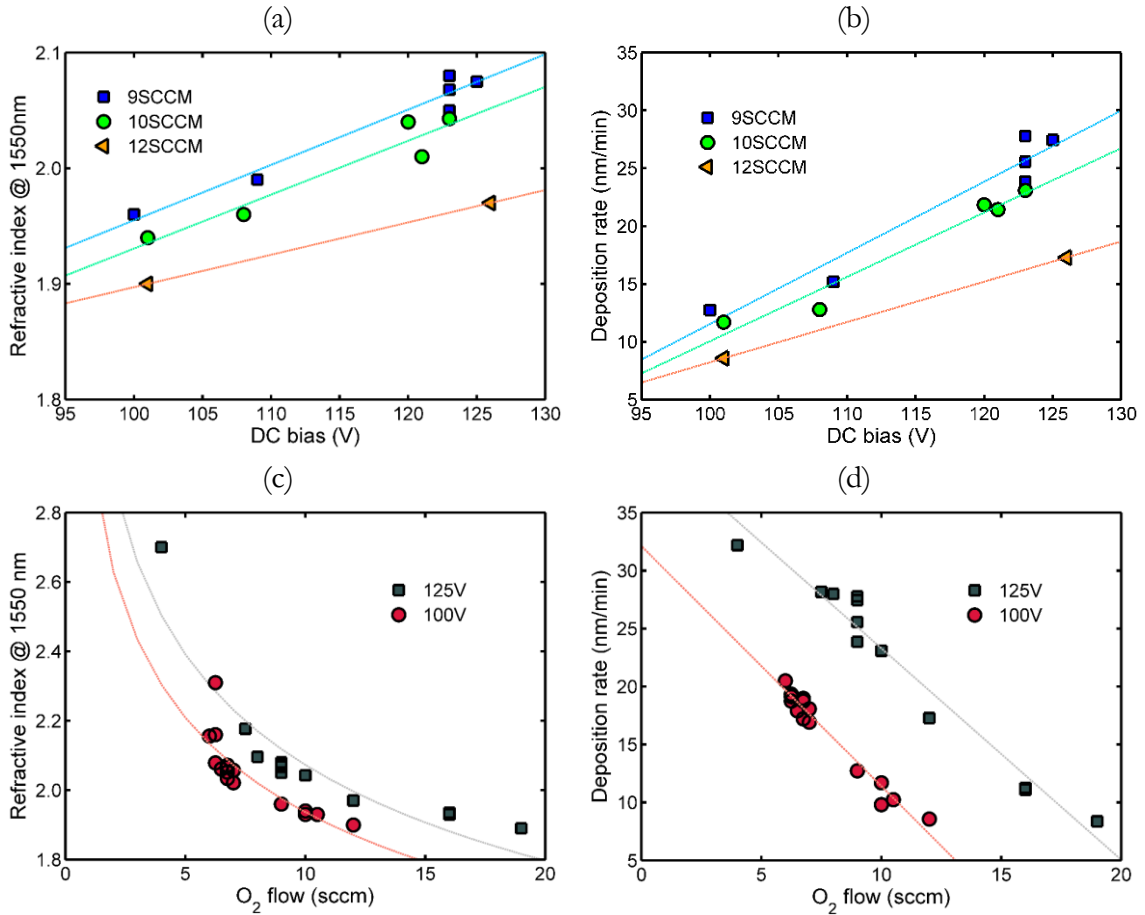


Fig. 2.11. Measured refractive index at 1550 nm and deposition rate versus (a and b) DC bias applied to the Te sputtering target and (c and d) O₂ flow rate of several fabricated tellurite thin films.

To optimize the TeO_2 deposition recipe a series of depositions with a 99.999% pure 3” diameter \times 0.125” thick metallic Te target mounted to a copper backing plate with the same dimensions and varying oxygen flow and DC offset parameters was performed, and the refractive index and deposition rate of the films were measured. Figures 2.11(a) and (b) show the measured refractive index and deposition rate of films for oxygen flow rates of 9, 10 and 12 sccm versus the DC bias applied to the tellurium target. Plots of refractive index and deposition rate versus O₂ flow rate for constant DC biases applied to the tellurium target are

shown in Fig. 2.11(c) and (d). Increasing the DC bias for a constant oxygen flow rate is seen to result in an approximately linear increase to the refractive index of the film. Lower oxygen flow rates result in a higher refractive index for a set DC bias. Increasing the DC bias also results in higher sputter deposition rates, as the tellurium sputter yield increases, while increasing the O₂ flow is seen to result in a decreased deposition rate, as although there is more oxygen in the chamber the tellurium target is expected to begin oxidizing and the rate of tellurium sputtering is reduced. From the data, the expected stoichiometric TeO₂ film conditions based on achieving a refractive index at a 1550-nm wavelength of approximately 2.08 [21] occur for a 125 V DC bias with ~9 sccm of oxygen flow or at a 100 V DC bias with ~7 sccm of oxygen flow. At these settings the films were measured to have deposition rates of approximately 25 and 20 nm/min, respectively.

With the general relationships between bias and oxygen flow rate and basic film properties established, a set of five tellurite films were fabricated at different oxygen flow rates to determine the propagation losses versus the refractive index and composition of the film. The five films under test were measured to have refractive indices of 1.99, 2.10, 2.13, 2.16 and 2.24 at 633 nm wavelength, and 1.93, 2.04, 2.07, 2.10, and 2.18 at a 1310 nm wavelength. The losses of the films at these two wavelengths were characterized by the prism coupling method. A picture of each thin film as deposited on a glass microscope slide, with their respective refractive index, optical propagation loss, and O-Te ratio, measured at 633 nm can be seen in Fig. 2.12(a). The two films with larger refractive indices were not observed to have measurable light streaks as a result of large optical propagation losses, suggesting that they were below the stoichiometric ratio ($x < 2$). To confirm this the samples underwent RBS characterization to determine the O-Te ratio. As expected, the three samples with the lowest refractive indices and measurable light streaks had O-Te ratios of $x > 2$, with measured values of 2.84, 2.46, and 2.36. Although the sample with the refractive index of 2.16 at a 633 nm wavelength was measured to have an O-Te ratio of 2.08, which indicates that the film is expected to be slightly oxygen rich, the lack of a light streak suggests that the film is metal rich and/or there are incompletely oxidized Te atoms in the glass matrix. A roughly ± 0.1 uncertainty in the O-Te ratio from RBS allows that the sample might actually be slightly in the metal rich regime. The fifth sample is clearly in the metal rich regime, with a measured O-Te ratio of 1.85, which can be seen by observing the darkness of the film on the glass slide in Fig. 2.12(a). The measured loss of the films versus refractive index and film stoichiometry are plotted in Figs. 2.12(b) and (c). The figures identify a clear trend of improving loss as the refractive index increases and the sample becomes more stoichiometric, with the sample at an O-Te ratio of 2.36 measured to have 4.2 and 0.6 dB/cm of optical propagation loss at 633 and 1310 nm wavelengths, respectively. This trend abruptly ends once the sample becomes metal-rich which is estimated to occur near the vertical lines on the figures.

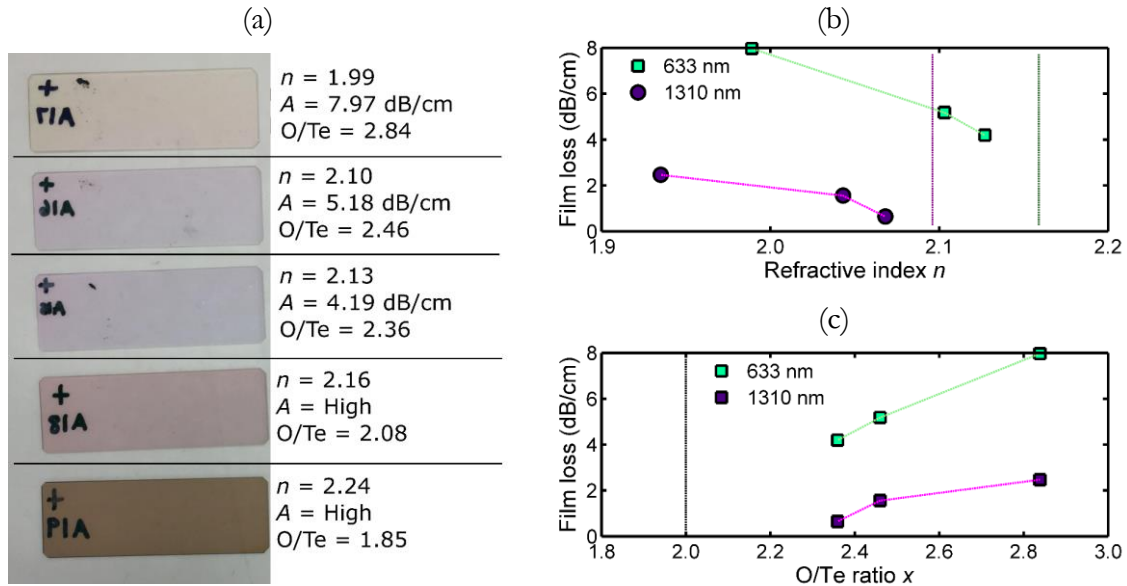


Fig. 2.12. (a) A set of tellurite films deposited on glass slides at different O_2 flow rates, with measured refractive index and optical propagation loss at 633 nm indicated. Measured film loss of samples at 633 and 1310 nm versus (b) refractive index and (c) O/Te ratio of samples. Vertical lines represent the $x < 2$ stoichiometric limit of TeO_x , beyond which film losses were seen to increase beyond the measurable limit (~ 25 dB/cm).

Based on these results a general deposition process was established to reliably achieve high-quality TeO_2 films. For subsequent work, including when first testing a deposition recipe from a new tellurium target or carrying out a series of depositions on photonic chips, the following procedure was followed. An RF sputtering power of 125 W was used, intended to achieve film deposition rates of between 20 and 25 nm/min, and the oxygen flow rate was initially set at 10 sccm. The oxygen flow rate was then altered during the course of the deposition to stabilize the DC offset of the tellurium target. If the DC bias was seen to be rising in time the oxygen flow rate was increased, while if the DC bias was dropping the oxygen flow rate was decreased. This process was iterated until a relatively stable DC bias offset was maintained over several minutes, which for the initial run on a new tellurium target will typically occur around a 160-180 V DC bias and an O_2 flow of between 9 and 11 sccm. Once a stable oxygen flow rate was established a second deposition run was performed at that flow rate to verify that the refractive index of the film was near the expected stoichiometric TeO_2 refractive index value of 2.08 at 1550 nm. Assuming that it was, minor adjustments to the oxygen flow rate were then made over several subsequent depositions to finely tune the refractive index and loss of films. A general rule of thumb is that a 0.3 increase/decrease to O_2 flow will correspond to a roughly 0.02 increase/decrease in the refractive index of the film. Once a near-stoichiometric low-loss film recipe was found the same recipe was typically run over a 30-minute-long deposition to further stabilize the recipe. An example of the deposition parameters and measured thin film properties for the first several runs of a newly installed tellurium target can be seen in Table 2.1. As can be seen in the table, within only a few

depositions of using this optimization method the process yields films with low losses and refractive indices around the expected values for stoichiometric TeO₂.

Table 2.1. Deposition parameters and thin film properties over the first several deposition processes for a newly installed Te target at a 125 W forward sputtering power.

#	O ₂ flow (sccm)	DC bias (v)	Deposition time (min)	Deposition rate (nm/min)	Refractive index		Loss (dB/cm)	
					@ 638	@ 1550	@ 638	@ 1550
1	10	178	15	21.3	2.100	2.043	4.2±0.3	1.4±0.3
2	9.7	174	15	22.9	2.126	2.071	0.9±0.4	0.5±0.3
3	9.7	171	15	22.2	2.116	2.060	1.0±0.3	0.4±0.3
4	9.7	171	15	23.1	2.130	2.076	1.1±0.4	0.1±0.1
5	9.8	170	35	22.2	2.128	2.068	1.3±0.4	0.1±0.1
6	9.8	168	15	23.0	2.133	2.078	0.8±0.3	0.1±0.1

Once stabilized the deposition process can be reliably used to fabricate high-quality TeO₂ thin films. As the target is worn the DC bias of the target will drop approximately 1-2 V for every 30 minutes of deposition time, until a DC bias of ~120 V is reached, at which point the target is near fully consumed. This process has led to the deposition of TeO₂ samples with very low optical propagation losses, from the visible through to infrared wavelengths. For example, Fig. 2.13(a) shows TE-polarized film losses of 0.4, 0.3, 0.1 and 0.1 dB/cm at 638, 847, 1310 and 1550 nm wavelengths, respectively. These values are near or at the minimum resolvable loss of the prism coupling system of 0.1 dB/cm. An example of the measured scattered light intensity and fitted loss at 638 nm can be seen in Fig. 2.13(b). The plot shows a relative drop in scattered intensity of only 10% on the linear scale over a 3 cm distance, which gives an indication of how measurements approach the detection limit.

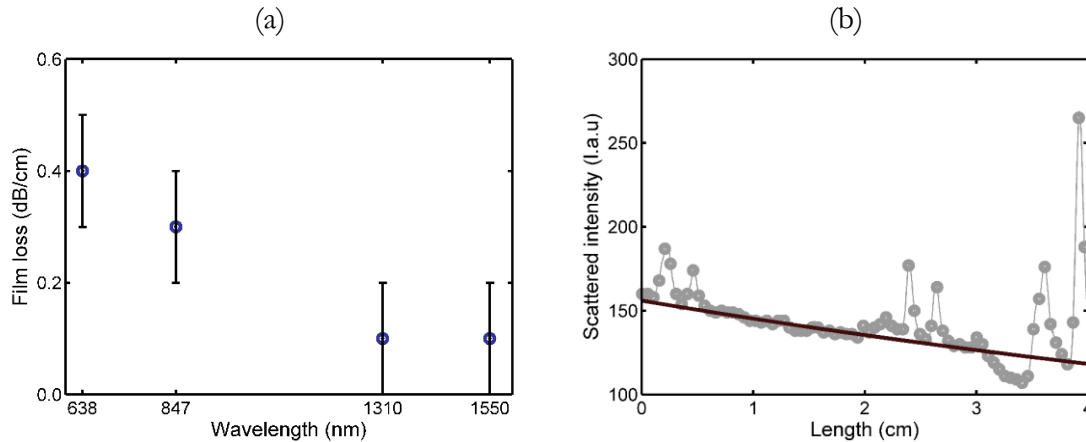


Fig. 2.13. (a) Loss at 638, 847, 1310, and 1550 nm-wavelengths of 0.4, 0.3, 0.1 and 0.1 dB/cm respectively measured in a high quality 436-nm-thick TeO₂ film by prism coupling. (b) Scattered intensity versus propagation length for the 638-nm-wavelength light streak.

These results were measured on a 436-nm-thick film grown at a deposition rate of 24.2 nm/min with an RF forward power of 125 W applied to the tellurium target, resulting in a DC

bias offset of 146 V, with an oxygen flow rate of 10.4 sccm and the standard argon flow rate of 12 sccm, resulting in a chamber pressure of 2.8 mTorr. The general parameters to fabricate low-loss and stoichiometric TeO₂ thin films by RF reactive sputtering in the deposition system described here are summarized in Table 2.2.

Table 2.2. Optimized deposition parameters for RF reactive sputtered TeO₂ thin films.

Deposition parameter	Value
Temperature (°C)	20
RF forward power (W)	125
DC bias offset (V)	120 – 180
Ar flow (sccm)	12
O ₂ flow (sccm)	9 – 11
Chamber pressure (mTorr)	2.8 – 3.0

The dispersion profiles of a set of 14 TeO₂ films near the optimized stoichiometric ratio with low optical propagation losses were measured using ellipsometry. The films were fit to have Sellmeier $D_{\text{Sellmeier}}$, $E_{\text{Sellmeier}}$ and $F_{\text{Sellmeier}}$ parameters of 2.52 ± 0.21 , 1.72 ± 0.25 and 0.24 ± 0.01 μm , respectively, based on the average and standard deviation measured across the samples. The samples with larger $D_{\text{Sellmeier}}$ parameters were found to have smaller $B_{\text{Sellmeier}}$ and $C_{\text{Sellmeier}}$ parameters. The resulting dispersion relationship with uncertainty is plotted in Fig. 2.14(a), giving a refractive index of 2.07 ± 0.01 for low loss samples at a 1550 nm wavelength. To confirm the accuracy of the Sellmeier model the refractive indices of a set of three TeO₂ samples were also characterized at single wavelengths using the prism coupling method and compared to their specific Sellmeier model, as shown in Fig. 2.14(b). The Sellmeier fits generally follow the results from prism coupling, with the Sellmeier slightly overpredicting values at longer wavelengths.

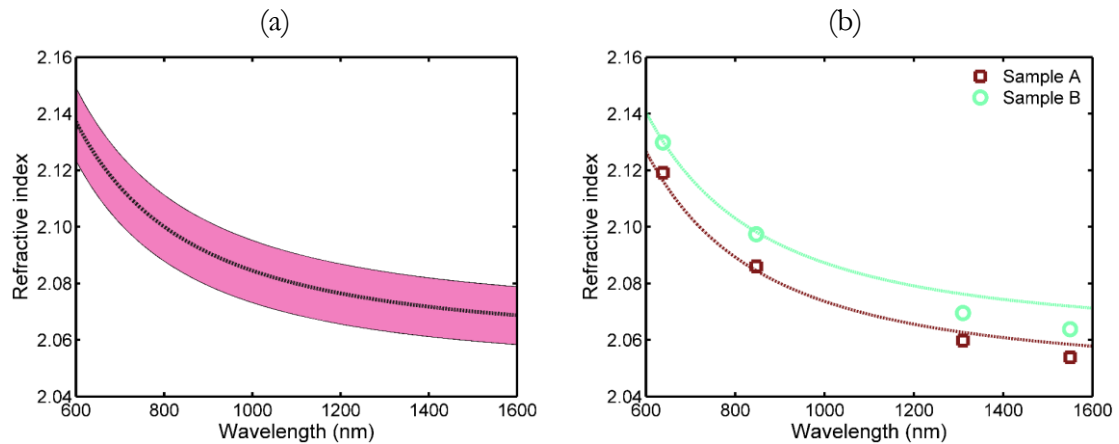


Fig. 2.14. (a) Sellmeier fits from several low loss samples used to obtain an average refractive index dispersion profile (black line), and standard deviation of variation (red zone). (b) Comparison of measured refractive index dispersion profiles from ellipsometry to refractive indices measured at different wavelengths by prism coupling.

For wafer-scale fabrication the properties of the deposited thin film must remain relatively consistent across a large surface area. Accordingly, a wafer map of the thickness and refractive index uniformity of a TeO_2 thin film prepared using the optimized deposition process was characterized by measuring a 3-inch silicon wafer placed on the center of the deposition stage at various points across its surface using ellipsometry. The resulting map of the thin film’s refractive index and thickness variations can be seen in Figs. 2.15(a) and (b), respectively. The average refractive index at 1550 nm was 2.048, with a slightly smaller refractive index typically measured on one side of the wafer versus the other but very small variations of less than 0.2 % overall. A more prominent variation was seen in the thickness, which on average was measured to be 309.4 nm, and varied from 306.1 nm near the center to 313.5 nm near the edge of the wafer. This is likely a result of the direction of maximum sputter yield in the confocal arrangement being purposefully offset from the center of the deposition stage to provide better uniformity over 6-inch-diameter samples and it is predicted that the thickness will begin to decrease outside of this range.

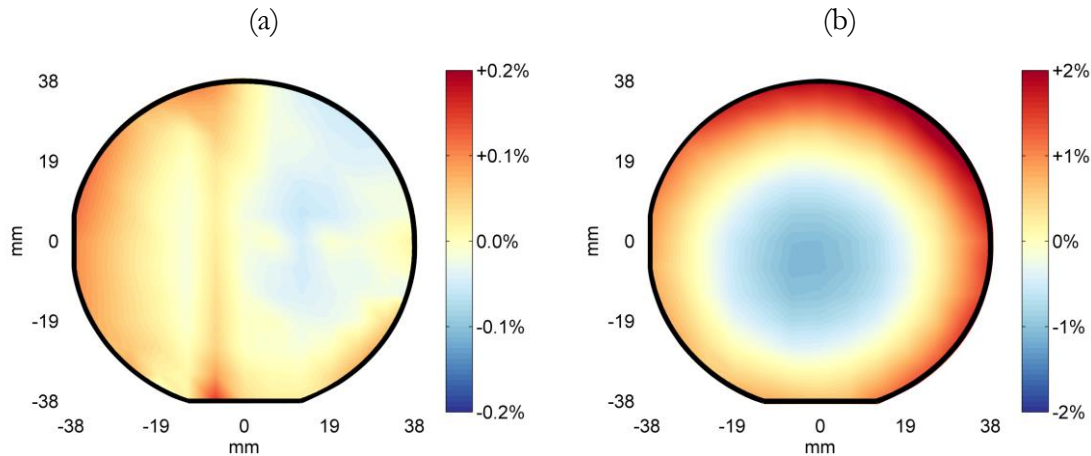


Fig. 2.15. Map of variation in tellurite film (a) refractive index at 1550 nm and (b) thickness, compared to average value measured over a 3-inch silicon wafer by ellipsometry. The average refractive index and film thickness are 2.048 and 309.4 nm, respectively.

2.5. Co-sputtering of Erbium Dopants into Tellurite Films

Tellurium oxide thin films are partially of interest in integrated photonic microsystems because of their excellent properties as a rare earth host for light emission. While many methods exist to incorporate rare earth dopants into thin films, including ion implantation [35] and the sol-gel method [36], in-situ co-sputtering of rare-earth dopants into thin films allows for uniform rare earth incorporation, precise control of dopant concentrations, high quality films with minimal defects and impurities and straightforward, low-cost fabrication due to no additional processing steps [22]. Of particular interest for optical systems are erbium-doped materials, which emit light around 1450 to 1600 nm in the telecom S-, C- and L-bands, the most commonly used wavelengths of optical communication systems. Co-sputtering of erbium-

doped TeO₂ thin films (TeO₂:Er³⁺) can be performed by running an optimized low-loss TeO₂ deposition recipe, while simultaneously sputtering from an erbium target during the deposition. The erbium-ion concentration in the films can then be tuned based on the RF-forward power applied to the erbium sputtering target. Here, sets of erbium-doped TeO₂ films were deposited using the optimized recipe and by varying the sputtering power applied to a 3” diameter x 0.125” thick metallic erbium target mounted to a copper backing plate and of 99.9% purity from a second sputtering gun in the deposition system.

Optical propagation loss measurements by the prism coupling method were used to measure the erbium dopant concentration of thin films fabricated under different sputtering conditions. The prism coupling method was used to characterize the optical propagation losses of thin films at different wavelengths across the erbium absorption band. The probability of an erbium-ion absorbing an incident photon can be described by its absorption cross section (σ_{Abs}). The optical attenuation coefficient (μ from Equation 2.13) is then related to the absorption cross section multiplied by the number of erbium ions per unit volume (N_{Er}) as shown in Equation 2.17,

$$\mu = \sigma_{\text{Abs}} \cdot N_{\text{Er}} . \quad (2.17)$$

The specific energy level splitting of erbium ions in a host material results in a characteristically varying probability of absorption at different wavelengths, which is discussed in further detail in Section 4.2.3. The absorption cross section versus wavelength of TeO₂:Er³⁺ thin films around 1500–1600 nm was previously characterized by Vu and Madden [18], which was used here to determine the expected erbium related loss of the film (A_{Er}), in dB/cm, at different wavelengths as follows:

$$A_{\text{Er}}(\lambda) = 10 \log(e) \cdot \sigma_{\text{Abs}}(\lambda) \cdot N_{\text{Er}} \cdot \Gamma . \quad (2.18)$$

As not all the intensity of the mode confined by the planar waveguide travels through the TeO₂:Er³⁺ film the absorption must be scaled by the intensity overlap (Γ) of light in the film that will interact with the erbium dopants. Although the confinement factor has a small difference across wavelengths, to simplify the calculation it is assumed to be constant and the value at 1550 nm is taken. The films studied here were generally around 300 nm thick, with approximately 60 % optical confinement in the TeO₂ layer for the fundamental TE mode. Including the background optical propagation loss of the sample (A_{back}), which results from scattering loss and non-erbium related absorption, the total film optical propagation loss per unit length (A) of the sample (in dB) can be described by Equation 2.19:

$$\begin{aligned} A(\lambda) &= A_{\text{back}} + A_{\text{Er}}(\lambda) \\ &= A_{\text{back}} + \sigma_{\text{Er}}(\lambda) \cdot \Gamma \cdot N_{\text{Er}} \cdot 10 \log(e) . \end{aligned} \quad (2.19)$$

By measuring the optical propagation loss of thin films at several different wavelengths across the absorption band of erbium the loss versus wavelength can be found. Figure 2.16(a) shows the measurement results for two different $\text{TeO}_2:\text{Er}^{3+}$ films. The two measurement sets generally follow the expected erbium absorption profile, with the exception of the more strongly doped sample near the absorption peak around 1530 nm, where there is a small reduction in measured loss compared to what is expected, likely as a result of pump absorption saturation [37]. To estimate the concentration the loss data was related to the known absorption cross section at each wavelength [18] and replotted as shown in Fig. 2.16(b). The slope of the line can then be used to estimate the erbium ion concentration, from Equation 2.19, which was fit for the two samples to be $1.4 \pm 0.1 \times 10^{20}$ and $2.7 \pm 0.2 \times 10^{20}$ ions/cm³. The y-intercept of the fit also gives the background loss, determined to be 0.6 ± 0.2 and 0.8 ± 0.3 dB/cm, respectively. In general, we observe a small increase to the estimated background waveguide loss in $\text{TeO}_2:\text{Er}^{3+}$ films, but they generally remain <1 dB/cm. Additionally, the uncertainty in the background loss typically experiences a small increase as a result of the uncertainty in the fit versus absorption cross section.

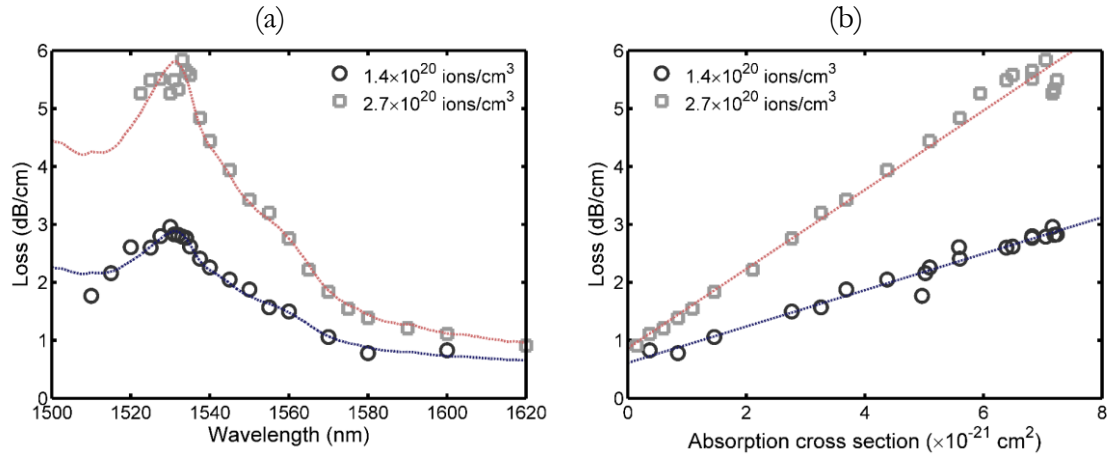


Fig. 2.16. Film loss, as measured by prism coupling versus (a) wavelength and (b) Er^{3+} absorption cross section at each wavelength, used to fit erbium concentrations of 1.4×10^{20} and 2.7×10^{20} ions/cm³ for two sample $\text{TeO}_2:\text{Er}^{3+}$ films.

A set of several different films with varying RF forward powers applied to the erbium sputter target were fabricated and tested, with the calculated erbium-ion concentration versus erbium target power is shown in Fig. 2.17. This process was performed in two trials, using the same erbium sputtering target but different tellurium sputtering targets under different processing conditions. In the first trial the tellurium target was sputtered at a DC bias of 165-V with 10.5 sccm of oxygen flow at a passive TeO_2 deposition rate of 25.0 nm/min (Trial A), while in the second trial a different tellurium target was sputtered at a 130-V bias with 9.5 sccm of oxygen flow for a passive film deposition rate of 23.9 nm/min (Trial B). The trend for each trial follows the expected exponential increase in erbium ion concentration versus RF forward power applied to the erbium target [22,38], however, a more rapid increase is seen in the

samples of Trial B. The variation can be partly attributed to the lower TeO_2 deposition rate, which increases the rate of erbium incorporation into the film, but this does not seem significant enough to cause such a large difference in concentration. The difference is likely more a result of minor changes in the plasma conditions and variations in the oxidation state of the erbium target at the different oxygen flow rates affecting the sputter rate of the erbium target. Based on these results, it becomes apparent that the doping concentration is highly dependent on the tellurium target condition and it's the associated optimized deposition parameters in addition to the RF forward power applied to the erbium target.

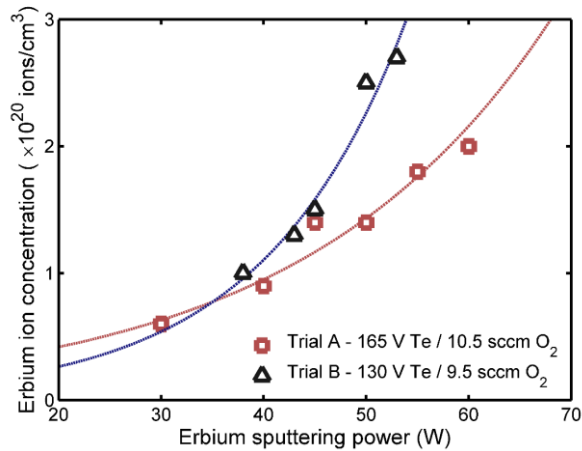


Fig. 2.17. Measured erbium ion concentration of thin films versus RF sputtering power applied to the erbium target for two different tellurium targets that are sputtered at different conditions. Trial A sputtered a tellurium target near a 165 V bias with 10.5 sccm of O_2 flow, while Trial B sputtered a different tellurium target near a 130 V bias with 9.5 sccm of O_2 flow.

As well as affecting the optical absorption, the introduction of erbium dopants was also observed to lower the refractive index of the TeO_2 films, due to the interstitial incorporation of erbium into the glass matrix [39], as has been seen in other erbium-doped TeO_2 studies [17]. Ellipsometry measurements of the films' refractive index at wavelengths of 633 and 1550 nm versus erbium dopant concentration are shown in Figs. 2.18(a) and (b), respectively. The reduction in refractive index is seen to be more significant at lower wavelengths, where a sample with an Er concentration of 2.0×10^{20} ions/cm³ was seen to experience a drop in refractive index of approximately 0.06 at a 633 nm, while it experienced a drop of approximately 0.04 at a 1550 nm. When comparing the results from the films sputtered from the different targets and under different conditions it can be seen that they both follow the same general curve, with the exception of one spurious data point from the results in Trial B. Refractive index tracking could therefore provide a useful mechanism for determining the erbium concentrations of films in the future.

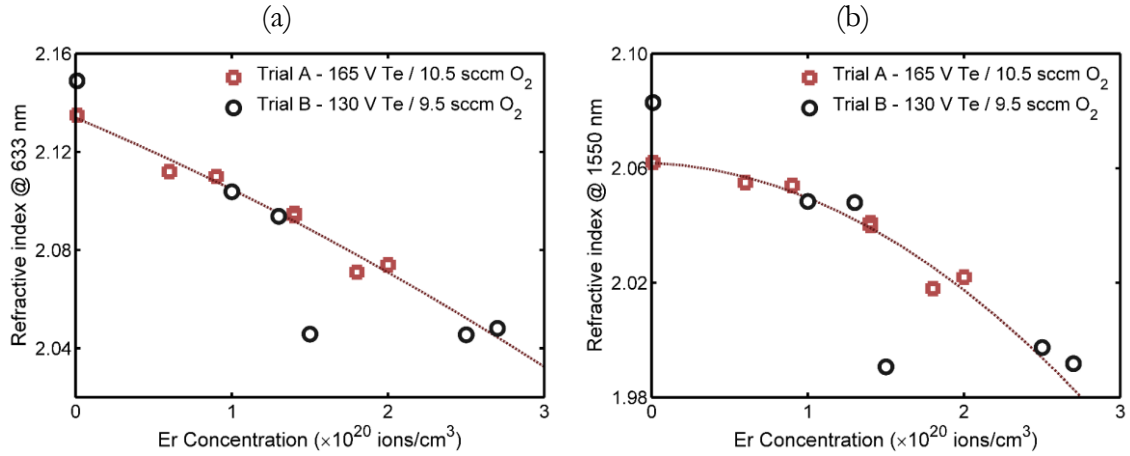


Fig. 2.18. Refractive index of films at (a) 633 and (b) 1550 nm wavelength versus erbium ion concentration, showing a decrease in the measured refractive index with increasing erbium dopant concentration.

2.6. Conclusion

In summary, we have developed a high-quality, low-loss, reactively sputtered TeO₂ thin film deposition process. The tellurite films are deposited with a forward power of 125 W applied to a 3" diameter Te sputter target and an oxygen flow rate between a 9–11 sccm, leading to deposition rates of ~ 25 nm/min. Planar film losses of 0.1 ± 0.1 dB/cm and < 0.5 dB/cm were consistently measured at 1550 and 638 nm, respectively. Low-loss films had an average refractive index of 2.07 ± 0.01 at a 1550 nm based on a Sellmeier fit to ellipsometry measurements, with confirmation of the model by prism coupling agreeing with the Sellmeier fits. A high refractive index uniformity of less than ± 0.2 % variation was measured across a 78-mm-diameter silicon wafer at the center of the substrate holder. A thickness uniformity of ± 2 % variability was measured across the same wafer. Erbium-doped TeO₂ (TeO₂:Er³⁺) thin films were fabricated by in-situ co-sputtering from an erbium target during depositions. The erbium ion concentrations in thin films were characterized by loss measurements using prism coupling at different wavelengths. For TeO₂:Er³⁺ films sputtered using a 160 V DC-bias offset applied to the tellurium target and 10.5 sccm of oxygen flow, the Er concentration increased from a 0.6×10^{20} ions/cm³ concentration 2.0×10^{20} ions/cm³ with 30 and 60 W RF power applied to the Er target, respectively. A trial with a second tellurium target which was sputtered at a 130 V DC-bias in 9.5 sccm of oxygen flow demonstrated a sharper increase rate of erbium-ion concentration versus sputtering power was measured, with concentrations of 1.0×10^{20} ions/cm³ and 2.7×10^{20} ions/cm³ at RF powers of 38 and 53 W, respectively. These results provide a guide for variations in Er concentration with deposition recipe and selecting the Er concentration for device fabrication. The demonstration of high-quality undoped and erbium-doped TeO₂ thin films provides a promising pathway for the integration of TeO₂ thin films onto silicon-based photonic platforms, as is investigated throughout the remainder of this thesis.

References

- [1] J. E. Stanworth, “Tellurite glasses,” *Nature* **169**(4301), 581–582 (1952).
- [2] J. S. Wang, E. M. Vogel, and E. Snitzer, “Tellurite glass: a new candidate for fiber devices,” *Opt. Mater.* **3**(3), 187–203 (1994).
- [3] K. T. Vu and S. J. Madden, “Tellurium dioxide erbium doped planar rib waveguide amplifiers with net gain and 2.8dB/cm internal gain,” *Opt. Express* **18**(18), 19192–19200 (2010).
- [4] A. Jha, B. D. O Richards, G. Jose, T. T. Fernandez, C. J. Hill, J. Lousteau, and P. Joshi, “Review on structural, thermal, optical and spectroscopic properties of tellurium oxide based glasses for fibre optic and waveguide applications,” *Int. Mater. Rev.* **57**(6), 357–382 (2012).
- [5] S. H. Kim, T. Yoko, and S. Sakka, “Linear and nonlinear optical properties of TeO₂ glass,” *J. Am. Ceram. Soc.* **76**(10), 2486–2490 (1993).
- [6] R. Stegeman, L. Jankovic, H. Kim, C. Rivero, G. Stegeman, K. Richardson, P. Delfyett, Y. Guo, A. Schulte, and T. Cardinal, “Tellurite glasses with peak absolute Raman gain coefficients up to 30 times that of fused silica,” *Opt. Lett.* **28**(13), 1126–1128 (2003).
- [7] T. Yano, A. Fukumoto, and A. Watanabe, “Tellurite glass: A new acousto-optical material,” *J. Appl. Phys.* **42**(13), 1126–1128 (2003).
- [8] T. Cheng, L. Zhang, X. Xue, D. Deng, T. Suzuki, and Y. Ohishi, “Broadband cascaded four-wave mixing and supercontinuum generation in a tellurite microstructured optical fiber pumped at 2 μm ,” *Opt. Express* **23**(4), 4125–4134 (2015).
- [9] T. Cheng, D. Deng, X. Xue, T. Suzuki, and Y. Ohishi, “Continuous-wave four-wave mixing in a single-mode tellurite fiber,” *Appl. Phys. Lett.* **104**(25), 251903 (2014).
- [10] A. Mori, H. Masuda, K. Shikano, K. Oikawa, K. Kato, and M. Shimizu, “Ultra-wideband tellurite-based Raman fibre amplifier,” *Electron. Lett.* **37**(24), 1442–1443 (2001).
- [11] G. Qin, M. Liao, T. Suzuki, A. Mori, and Y. Ohishi, “Widely tunable ring-cavity tellurite fiber Raman laser,” *Opt. Lett.* **33**(17), 2014–2016 (2008).
- [12] G. Qin, A. Mori, and Y. Ohishi, “Brillouin lasing in a single-mode tellurite fiber,” *Opt. Lett.* **32**(15), 2179–2181 (2007).
- [13] A. Mori, Y. Ohishi, and S. Sudo, “Erbium-doped tellurite glass fibre laser and amplifier,” *Electron. Lett.* **33**(10), 863–864 (1997).
- [14] Y. Ohishi, A. Mori, M. Yamada, H. Ono, Y. Nishida, and K. Oikawa, “Gain characteristics of tellurite-based erbium-doped fiber amplifiers for 1.5- μm broadband amplification,” *Opt. Lett.* **23**(4), 274–276 (1998).

- [15] A. Mori, K. Kobayashi, M. Yamada, T. Kanamori, K. Oikawa, Y. Nishida, and Y. Ohishi, “Low noise broadband tellurite-based Er^{3+} -doped fibre amplifiers,” *Electron. Lett.* **34**(9), 887–888 (1998).
- [16] A. Jha, B. Richards, G. Jose, T. Teddy-Fernandez, P. Joshi, X. Jiang, and J. Lousteau, “Rare-earth ion doped TeO_2 and GeO_2 glasses as laser materials,” *Prog. Mater. Sci.* **57**(8), 1426–1491 (2012).
- [17] K. T. Vu and S. J. Madden, “Tellurium dioxide erbium doped planar rib waveguide amplifiers with net gain and 2.8dB/cm internal gain,” *Opt. Express* **18**(18), 19192–19200 (2010).
- [18] K. T. Vu, S. Farahani, and S. J. Madden, “980nm pumped erbium doped tellurium oxide planar rib waveguide laser and amplifier with gain in S, C and L band,” *Opt. Express* **23**(2), 747–755 (2015).
- [19] S. J. Madden and K. T. Vu, “Very low loss reactively ion etched tellurium dioxide planar rib waveguides for linear and non-linear optics,” *Opt. Express* **17**(20), 17645–17651 (2009).
- [20] S. M. Pietralunga, M. Lanata, M. Ferè, D. Piccinin, G. Cusmai, M. Torregiani, and M. Martinelli, “High-contrast waveguides in sputtered pure TeO_2 glass thin films,” *Opt. Express* **16**(26), 21662–21670 (2008).
- [21] R. Nayak, V. Gupta, A. L. Dawar, and K. Sreenivas, “Optical waveguiding in amorphous tellurium oxide thin films,” *Thin Solid Films* **445**(1), 118–126 (2003).
- [22] K. Worhoff, J. D. Bradley, F. Ay, D. Geskus, T. P. Blauwendraat, and M. Pollnau, “Reliable Low-Cost Fabrication of Low-Loss $\text{Al}_2\text{O}_3:\text{Er}^{3+}$ Waveguides With 5.4-dB Optical Gain,” *IEEE J. Quantum Electron.* **45**(5), 454–461 (2009).
- [23] T. Horikawa, D. Shimura, H. Okayama, S. H. Jeong, H. Takahashi, J. Ushida, Y. Sobu, A. Shiina, M. Tokushima, K. Kinoshita, and T. Mogami, “A 300-mm silicon photonics platform for large-scale device integration,” *IEEE J. Sel. Top. Quantum Electron.* **24**(4), 1–5 (2018).
- [24] K. Wörhoff, R. G. Heideman, A. Leinse, and M. Hoekman, “TriPleX: A versatile dielectric photonic platform,” *Adv. Opt. Technol.* **4**(2), 189–207 (2015).
- [25] M. Born and E. Wolf, *Principles of optics* (Oxford, 1970).
- [26] G. Ghosh, “Sellmeier coefficients and dispersion of thermo-optic coefficients for some optical glasses,” *Appl. Opt.* **36**(7), 1540–1546 (1997).
- [27] F. Ay, *Silicon base dielectrics: growth, characterization, and applications in integrated optics* (Doctoral dissertation, Bilkent University).
- [28] P. K. Tien and R. Ulrich, “Theory of prism–film coupler and thin-film light guides,” *JOSA* **60**(10), 1325–1337 (1970).

- [29] F. L. Pedrotti, L. M. Pedrotti, and L. S. Pedrotti, Introduction to optics (Cambridge, 2006).
- [30] I. H. Malitson, “Interspecimen comparison of the refractive index of fused silica,” JOSA **55**(10), 1205–1209 (1965).
- [31] D. F. Swinehart, “The beer-lambert law,” J. Chem Educ. **39**(7), 333 (1962).
- [32] International Bureau of Weights and Measures, SI brochure: the international system of units (SI) (ISBN 978-92-822-2272-0).
- [33] M. Mayer, “Rutherford Backscattering Spectrometry (RBS),” Workshop on Nuclear Data for Science and Technology: Materials Analysis, May 2003.
- [34] M. Mayer, SIMNRA user’s guide. Max-Planck-Institut für Plasmaphysik Garching, 1997.
- [35] A. Polman, “Erbium implanted thin film photonic materials,” J. Appl. Phys. **82**(1), 1–39 (1997).
- [36] X. Orignac, D. Barbier, X. M. Du, and R. M. Almeida, “Fabrication and characterization of sol-gel planar waveguides doped with rare-earth ions,” Appl. Phys. Lett. **69**(7), 895–897 (1996).
- [37] L. Agazzi, E. H. Bernhardt, K. Wörhoff, and M. Pollnau, “Impact of luminescence quenching on relaxation-oscillation frequency in solid-state lasers,” Appl. Phys. Lett. **100**(1), 011109 (2012).
- [38] J. D. B. Bradley, $\text{Al}_2\text{O}_3:\text{Er}^{3+}$ as a gain platform for integrated optics (Doctoral dissertation, University of Twente).
- [39] P. Loiko, N. Ismail, J. D. B. Bradley, M. Götelid, and M. Pollnau, “Refractive-index variation with rare-earth incorporation in amorphous Al_2O_3 thin films,” J. of Non-Cryst. Solids **476**, 95–99 (2017).

CHAPTER 3

Passive Tellurium Oxide Coated Silicon Nitride Waveguides and Devices

This chapter describes a novel passive tellurium oxide (TeO_2) coated silicon nitride (Si_3N_4) waveguide platform, its simulated optical properties and the experimental characterization of waveguides, fiber-chip couplers, directional couplers and microring resonators. The platform is motivated by combining the material advantages of TeO_2 with the low losses and well-established integrated photonics fabrication methods of Si_3N_4 . We show that a conformal TeO_2 layer deposited onto patterned Si_3N_4 waveguides creates a combined waveguide core with light guided by both material systems. Finite element eigenmode simulations of the waveguide cross sections for various TeO_2 coating thicknesses, Si_3N_4 waveguide widths and Si_3N_4 layer thickness are used to optimize the dimensions for devices. The simulations show that a 0.2- μm -thick Si_3N_4 layer with strip widths of around 1 μm , coated in TeO_2 films with thicknesses between 200 and 500 nm provide the optimum dimensions to realize devices with low losses, small bend radii, small effective mode areas and moderate optical confinement within the TeO_2 coating. Transmission measurements in 1.2- μm -wide silicon nitride strips coated in a 380-nm-thick tellurium oxide layer were used to characterize the optical propagation loss at wavelengths from 638 to 2000 nm by the cutback method. The losses were measured to be 8.4 ± 1.1 , 3.1 ± 0.3 , 0.8 ± 0.3 , 0.8 ± 0.3 and 0.6 ± 0.2 dB/cm at 638, 980, 1310, 1550 and 2000 nm, respectively. Mode overlap simulations for edge couplers show that the theoretical fiber-chip coupling losses can approach approximately 3 dB/facet for the TeO_2 -coated waveguide design with 2.5 μm spot size tapered fibers. Although the roughness of optical facets prepared by dicing and deep-etching methods are seen to increase the coupling loss to over 10 dB/facet, it is found that polishing facets by focused-ion-beam milling can reduce losses to 5.4 dB/facet. Directional couplers with 1- μm -wide Si_3N_4 strips separated by a 0.8- μm inner wall gap and coated in a 150-nm-thick TeO_2 layer were characterized and demonstrate 100 % cross-over ratio at 1550 nm for a coupler length of 80 μm . The measured cross-over ratios of the coupler are found to be in good agreement with the supermode coupling model if a coupling gap of 0.96 μm is used in simulations. A series of 300- μm -radius microring resonators with a 330-nm-thick TeO_2 -coating demonstrate internal Q factors of 7.3×10^5 around 1550 nm, corresponding to a waveguide loss of 0.5 dB/cm. Minimal change in loss is seen for microring radii $> 300 \mu\text{m}$, while a small decrease in Q factor for 200 μm radii rings, and a significant decrease in Q factor for 100 μm rings suggest that devices operating around 1550 nm can reasonably be bent down to $\sim 250 \mu\text{m}$ radius with negligible bend loss.

These results demonstrate, for the first time to our knowledge, low-loss compact integrated tellurite glass waveguides and devices.

The results presented in this chapter have contributed towards the following two journal publications:

- H. C. Frankis, K. Mirabbas Kiani, D. Su, R. Mateman, A. Leinse, and J. D. B. Bradley, "High-Q tellurium-oxide-coated silicon nitride microring resonators," *Optics Letters* **44**(1), 118–121 (2019).
- H. C. Frankis, K. Mirabbas Kiani, D. B. Bonneville, C. Zhang, S. Norris, R. Mateman, A. Leinse, N. D. Bassim, A. P. Knights, and J. D. B. Bradley, "Low-loss TeO₂-coated Si₃N₄ waveguides for application in photonic integrated circuits," *Optics Express* **27**(9), 12529–12540 (2019).

3.1 Introduction

Tellurium oxide (TeO₂) is a promising material for optical applications due to its high linear refractive index, transparency, rare-earth solubility and nonlinearity, among other reasons [1-4]. Previous works on integrated TeO₂ waveguides in bulk glass [5-10] and thin films [11-14] have demonstrated low film and waveguide losses, as well as high-performance erbium-doped amplifiers and lasers [15,16] and nonlinear optical devices [17]. For integrated optical applications, waveguide structures based on TeO₂ thin films are preferable to bulk glass because they enable high refractive index contrast and small bending radius, compact size, design versatility and integration with other photonic devices on one substrate. However, etching ridge waveguides in TeO₂ thin films requires non-standard recipes and gases [13,14] and those same recipes result in high sidewall roughness and columnar structures when etching rare-earth doped TeO₂ films [15]. Furthermore, previous studies were limited to relatively large waveguide cross-sections due to the etching and lithography methods applied, and important building blocks for photonic devices and integrated circuits, such as microring resonators, were not demonstrated. In the preceding chapter a deposition process for high-quality tellurium-oxide (TeO₂) thin film coatings was described. In this chapter the integration of TeO₂ films onto silicon nitride (Si₃N₄) photonic chips to realize a hybrid TeO₂-Si₃N₄ waveguide platform is investigated. Coating Si₃N₄ chips in TeO₂ films via post processing allows the development of TeO₂ based photonic devices using a versatile and well-established integrated photonic platform. This technique takes advantage of high quality, cost-effective and standardized device fabrication procedures used in commercial foundry processes, while avoiding the need to etch the TeO₂ film directly. Here we used Si₃N₄ photonic chips fabricated through the Lionix foundry in the Netherlands, as part of their TriPleX platform [18-20]. The combined platform can then utilize the material advantages of tellurium oxide, such as enhanced nonlinearity and optical amplification via rare-earth-doping, with the wafer-scale and high-resolution fabrication and low-loss waveguides available in Si₃N₄ technology [21,22]. An integrated photonics platform that combines the nonlinear and rare-earth functionality of

TeO₂ with well-established Si₃N₄ passive devices, and potentially optoelectronic functionality of emerging Si₃N₄-Si platforms [23-26] has numerous prospective applications, including in environmental and biological sensors [27], LiDAR transmitters [28,29] and telecommunication systems [30,31]. This chapter discusses the design and optical properties of TeO₂-Si₃N₄ waveguides, as well as the experimental characterization of low-loss waveguides, fiber-chip edge couplers, directional coupler, and high Q factor microring resonators in this platform.

3.2 Waveguide Fabrication and Structure

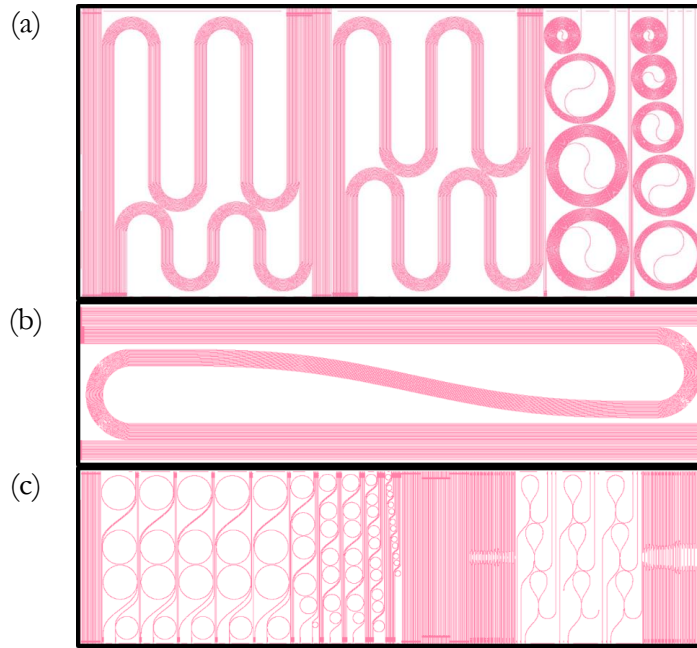


Fig. 3.1. Mask layouts of (a) Chiplet A containing paperclips of various length, (b) Chiplet B containing longer paperclips and (c) Chiplet C containing several passive devices, including directional couplers and ring resonators.

The hybrid TeO₂-Si₃N₄ platform was developed using a wafer-scale Si₃N₄ waveguide process at the LioniX foundry. Although many different Si₃N₄ waveguide geometries are currently available through this process, including box [32,33] and double stripe [34] structures, the most commonly used waveguide geometry is the simple strip waveguide because of their ultra-low waveguide losses. In this work, Si₃N₄ strip waveguide structures were patterned into a 0.2- μ m-thick low-pressure chemical vapor deposition (LPCVD) Si₃N₄ film on 10-cm-diameter silicon wafer with an 8- μ m-thick wet thermal oxide lower cladding layer. The Si₃N₄ layer thickness was selected as a compromise, to be thick enough to achieve sufficient lateral waveguide effective index contrast and compact bending radius, while being thin enough to avoid Si₃N₄ film cracking due to stress [18,19] and maintain minimal scattering loss due to interaction of the optical mode with sidewall roughness from etching. Further justification for the 0.2- μ m Si₃N₄ layer thickness is provided by the optical simulation results in section 3.3. After waveguide patterning by reactive ion etching, the wafers were annealed in a nitrogen

atmosphere at high temperature to drive hydrogen out of the Si_3N_4 layer, because hydrogen is well known to cause excess absorption around 1500-nm wavelengths [20]. Typically, the waveguide would then be top-cladded in a plasma-enhanced chemical vapor deposition (PECVD) SiO_2 layer or a wafer bonded thermal oxide [22] in the LioniX process for ultra-low loss waveguides. However, for this custom fabrication run, the chips were left uncladded to allow for the TeO_2 coating to be deposited onto the Si_3N_4 strip waveguides. Nine replications of a 2.2 cm \times 2.2 cm chip design were patterned on each wafer using stepper lithography. Each chip was further divided into 3 smaller chiplet designs. A summary of the devices patterned into each chiplet which are relevant to the simulation or experimental results of this thesis is provided below, and a diagram of the mask layout is shown in Fig. 3.1. A full list of devices on the design is provided in Appendix A

- **Chiplet A:** Chiplet A is 1.0-cm-across by 2.2-cm-wide and contains paperclip waveguides with nominal Si_3N_4 strip widths of 0.6, 0.8, 1.0, 1.2 μm . The paperclips include a series of four 180° bends and the length of the straight section between consecutive 180° bends is adjusted to achieve four different paperclip lengths of 2.45, 2.93, 3.45 and 3.93 cm. The paperclips are grouped into sets of the same length, with each set having 4 repeated waveguides of each width. To save physical space on the layout and keep propagation lengths consistent, independent paperclips are interlocked into a set by varying the bending radius at each 180° bend, with bending radii between 600 and 1020 μm . A minimum bending radius of 600 μm was selected to ensure negligible bending radiation loss.
- **Chiplet B:** Chiplet B is 2.2-cm-across by 0.6-cm-wide and contains 6.7-cm long paperclip waveguide structures with nominal Si_3N_4 strip widths of 0.6, 0.8, 1.0, 1.2 and 1.4 μm , with each width repeated 4 times. Here, the minimum and maximum bend radius of the interlocked paperclips are 1000 and 1570 μm , respectively. Between the two bends there is also a full period sine bend with an amplitude of 1800 μm and a length of 17000 μm , which is used to reduce the physical size the structure takes up on the mask layout.
- **Chiplet C:** Chiplet C is 0.6-cm-across by 2.2-cm-wide and contains several passive optical devices, including, directional couplers and ring resonators. The directional couplers consist of two 1- μm -wide waveguides (arms) separated by 30- μm near the chip edges which transition into close proximity of each other through a sine bend with an amplitude of 15 μm and a length of 300 μm on each arm, resulting in a gap of 0.8 μm between the inner walls of the two waveguides. Directional coupler lengths of 1 – 110 μm are included. The chiplet also contains a series of ring resonators with waveguide widths of 0.8, 1.0 and 1.2 μm with a radius of 600 μm . The rings are point-coupled to bus waveguides of the same width, with minimum gaps of 1.0 to 3.0 μm between the inner walls of the Si_3N_4 strips defining the ring and bus. For 1.0- μm -wide waveguides there are also sets

of rings with radii of 400, 300, 200 and 100 μm , and nominal coupling gaps between 0.5 and 2.5 μm .

Each chiplet also contains at least one set of straight waveguides, with Si_3N_4 strip widths of 0.5 to 2 μm .

Before transfer from the foundry, each wafer was diced into individual chiplets. For some wafers the dicing process was also used to define the optical facets of waveguides, while other wafers included a 100- μm -wide deep trench etch along the borders of each chiplet to define the optical facets, before dicing. The diced wafers were then shipped from the foundry to be coated in TeO_2 layers using the film deposition process described in Chapter 2 and investigate the TeO_2 coated Si_3N_4 waveguide platform. Although the coating process can be performed over entire wafers to scale up production, for the purpose of studying device properties the depositions in this work were typically performed on a small number of chiplets. The individual chiplets were carefully removed from the larger wafer, which was shipped on the dicing tape, by using tweezers. They were then cleaned in an acetone bath for 5 minutes to remove the photoresist coating applied to protect devices during dicing and shipment, after which the acetone was removed by multiple rinses in isopropanol and drying using a nitrogen gun. The chiplets were then mounted onto the deposition stage by adhering the samples with carbon tape. Bare silicon and an unpatterned thermally oxidized silicon test pieces, which were used to characterize the optical properties of the TeO_2 thin films, were also mounted on the deposition stage as described in Chapter 2. After the TeO_2 layer was deposited, the chiplets were removed from the sample stage by tweezers and placed into gel-boxes which were stored in a desiccator to prevent moisture absorption in the film. In some cases, the TeO_2 coated Si_3N_4 waveguide chips were additionally coated in a fluoropolymer (Cytop) top cladding layer using a spin-on and bake process to protect the waveguides. A spin speed of 1750 RPM for 60 seconds followed by three consecutive baking steps of 50, 80, and 180 $^\circ\text{C}$ for 10, 30, and 30 minutes, respectively, was used to achieve a hardened, 1- μm -thick polymer cladding with low-loss. The full hybrid TeO_2 - Si_3N_4 waveguide fabrication process is summarized in Fig. 3.2.

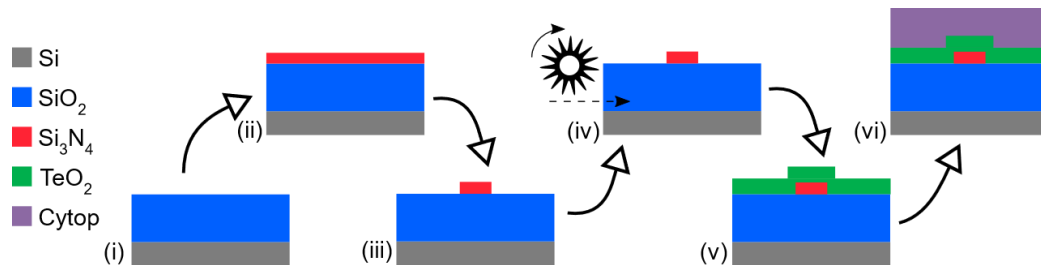


Fig. 3.2. Diagram of fabrication process used to form TeO_2 coated Si_3N_4 waveguides, starting with growth of an 8- μm -thick wet thermal oxide on a 4-inch silicon wafer (i), followed by the deposition of a 0.2- μm -thick Si_3N_4 film in an LPCVD process (ii), which is then patterned using stepper lithography and reactive ion etching to form Si_3N_4 strips (iii), after which the wafer is diced into chiplets and transferred from the foundry to the Centre for Emerging Device Technologies (CEDT) at McMaster University (iv), where it is coated in a reactively sputtered TeO_2 film (v) and, in some cases, top-cladded in a spin-on fluoropolymer layer (vi).

In order to consider the design of TeO₂ coated Si₃N₄ waveguides it is important to characterize the profile of the TeO₂ film surrounding the Si₃N₄ waveguide. As shown in the scanning electron microscope (SEM) image in Fig. 3.3 (a), the confocal arrangement of the sputtering gun results in the tellurium oxide coating conforming as a ridge around the silicon nitride strip. Based on the SEM images, we developed an approximate model for the TeO₂ hybrid waveguide structure. The Si₃N₄ strip width and height are $W_{\text{Si}_3\text{N}_4}$ and $h_{\text{Si}_3\text{N}_4}$, respectively. We take the TeO₂ thickness measured on the bare silicon test samples (h_{TeO_2}) as the thickness of the TeO₂ slab on the chiplet everywhere away from the Si₃N₄ strip. Near the Si₃N₄ strip the TeO₂ forms a ridge around it, such that the top of the TeO₂ layer is also $h_{\text{TeO}_2} + h_{\text{Si}_3\text{N}_4}$ above the box along the width of the Si₃N₄ strip plus half of the TeO₂ coating thickness on each side. A diagram of the TeO₂-Si₃N₄ hybrid waveguide structure is shown in Fig. 3.3 (b).

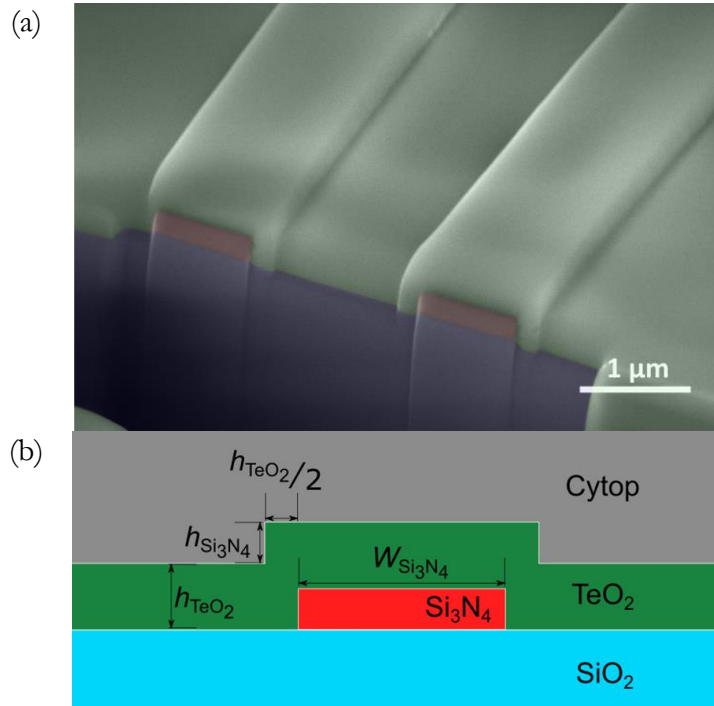


Fig. 3.3. (a) SEM cross section of two nearby TeO₂ coated Si₃N₄ waveguides after a focused ion beam (FIB) cut, showing the SiO₂ lower cladding, the Si₃N₄ strips and the conformal TeO₂ coating. (b) Cross-sectional diagram of the TeO₂-Si₃N₄ hybrid waveguide structure.

Figure 3.4 shows the refractive index of the materials defining the waveguide structure, including TeO₂, LPCVD Si₃N₄, thermal SiO₂, and Cytop fluoropolymer at wavelengths from 0.6 to 2.0 μm. The refractive index of Si₃N₄ is taken from [35] and has a value of 1.998 at 1550 nm, while the refractive index of thermal SiO₂ is taken from [36], with a value of 1.444 at a 1550 nm. The refractive indices of tellurium oxide and Cytop were obtained from ellipsometry measurements (see section 2.2.1), with values of 2.078 and 1.330 at 1550 nm, respectively. In cases where devices are not top-cladded in Cytop the waveguide interacts directly with air, which is assumed to have a refractive index of 1.000 at all wavelengths.

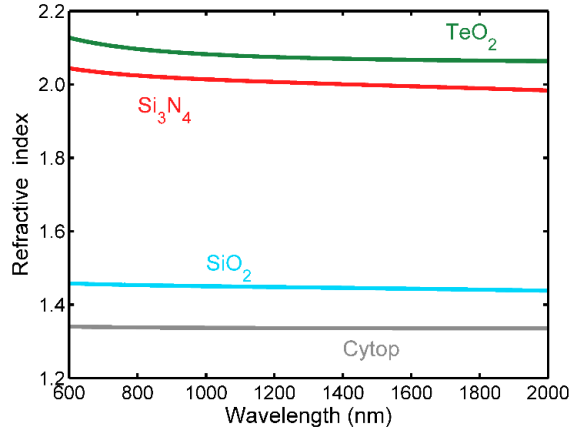


Fig. 3.4. Dispersion of materials used in the waveguide structure including TeO₂, LPCVD Si₃N₄, thermal SiO₂, and Cytop. The SiO₂ and Si₃N₄ refractive indices are from reference data [35,36] and the TeO₂ and Cytop refractive indices are from ellipsometry measurements.

3.3 Simulated Waveguide Properties

The TeO₂-Si₃N₄ waveguide properties were investigated using 2D finite element eigenmode simulations, on commercial electromagnetic software, Synopsys RSoft. The simulations use waveguide dimensions from the cross-sectional model described in Fig. 3.3(b), and the refractive index dispersion profiles shown in Fig. 3.4, assuming the devices are cladded in infinitely thick SiO₂ layer below and an infinitely thick Cytop or air layer above.

In a conventional strip waveguide structure, the silicon nitride strip lies on a lower index bottom cladding, such as thermal SiO₂, and is coated in a top cladding of similar refractive index to the lower cladding, such as a CVD-deposited or wafer-bonded thermal SiO₂. However, in our case the TeO₂ coating has a larger refractive index than the Si₃N₄ strip and does not act as a traditional cladding because total internal reflection cannot be achieved at the Si₃N₄-TeO₂ interface. Instead, the TeO₂-coated Si₃N₄ strip structure acts as a combined (hybrid) ridge waveguide core, in which light is confined below by the Si₃N₄-SiO₂ interface and above by either the TeO₂-air or TeO₂-Cytop interface. Lateral optical confinement is obtained at the sides of the ridge waveguide due to the effective index contrast between the TeO₂-air or TeO₂-Cytop interface at the conformal ridge. An example of simulated optical mode profiles for 1.0- μ m-wide by 0.2- μ m-thick Si₃N₄ strips coated in 200, 400, and 600-nm of TeO₂ at a 1550 nm wavelength can be seen in Fig. 3.5.

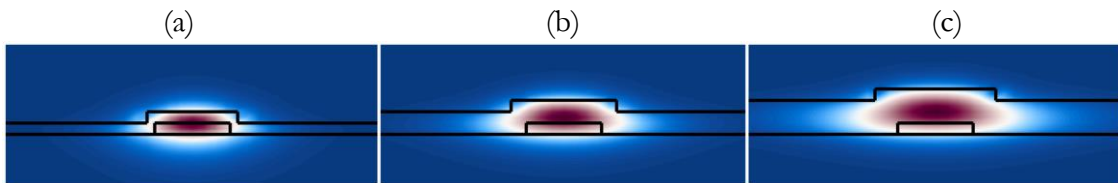


Fig. 3.5. Simulated electric-field mode profiles of 1.0 μ m \times 0.2 μ m Si₃N₄ strips coated in (a) 200, (b) 400 and (c) 600-nm-thick TeO₂-coatings at 1550 nm wavelengths.

Based on the hybrid waveguide structure, the parameters that can be varied during the fabrication process are the thickness of the Si_3N_4 layer, the thickness of the TeO_2 -coating and the designed width of the Si_3N_4 waveguide. In practice, due to the stress difference between the silicon substrate leading to film cracking for thick LPCVD Si_3N_4 films, we assumed the thickness of the Si_3N_4 layer is limited to $h_{\text{Si}_3\text{N}_4} < 0.4 \mu\text{m}$ [18,19]. Therefore, we limit ourselves to the consideration of 0.1, 0.2 and 0.3 μm thick Si_3N_4 layers in designs. Although TeO_2 films could theoretically be deposited to any thickness, the time and cost of depositing films to large thickness must be considered, along with maintaining reasonable vertical and lateral confinement of the optical mode. Therefore, we generally considered TeO_2 film thicknesses in the range of 200 to 600 nm in these designs. Within these limits, the most important consideration in regard to the design of Si_3N_4 waveguide width is to maintain single mode propagation.

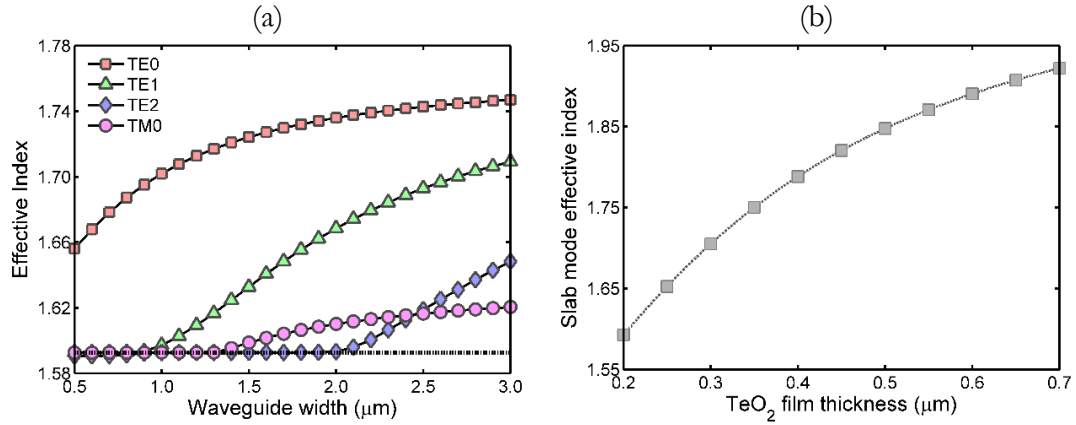


Fig. 3.6. (a) Simulated effective index of the first four waveguide modes for waveguide widths from 0.5 to 3.0 μm for a 0.2- μm -thick silicon nitride strip coated in a 200-nm-thick TeO_2 film at 1550 nm wavelength. The waveguide is seen to reach the single mode condition at Si_3N_4 strip widths below 1 μm as the TE1 mode begins to radiate into the slab. (b) Simulated effective index of the fundamental TE polarized SiO_2 - TeO_2 -Cytop slab mode for different thicknesses of TeO_2 .

Waveguide widths that support only a single transverse-electric (TE) and/or transverse-magnetic (TM) polarized mode each are typically used to prevent modal dispersion and interference. We initially determined the single mode conditions of the waveguide structure by calculating the effective index of the first four optical modes for waveguide widths from 0.5 to 3.0 μm , with $\sim 0.5 \mu\text{m}$ being the minimum attainable resolution of the stepper lithography system used by the foundry. Sample simulated effective index data for the first four modes of a 0.2- μm -thick Si_3N_4 layer with a 200-nm-thick TeO_2 -coating at 1550 nm is shown in Fig. 3.6.(a). The effective index for modes is seen to decrease as $W_{\text{Si}_3\text{N}_4}$ decreases, because the evanescent field of the mode expands further into the cladding layers and TeO_2 slab surrounding the waveguide. Eventually when the Si_3N_4 strip width becomes small enough the modes radiate into the slab and are no longer guided by the Si_3N_4 - TeO_2 waveguide core. For example, as can be seen in Fig. 3.6.(a), the effective index of the TE1 mode reaches that of the slab and the mode is cut off at around $W_{\text{Si}_3\text{N}_4} = 1 \mu\text{m}$. For small waveguide cross

sections such as this structure, the radiation modes of both the TE and TM-polarized waveguide modes are determined by the slab mode with the largest effective index independent of its respective polarization [37]. The fundamental TE slab mode effective index of an SiO₂-TeO₂-Cyttop planar waveguide, which is the primary radiation mode in this structure, is calculated at 1550 nm for different TeO₂ film thicknesses, is shown in Fig. 3.6.(b).

The single mode condition is determined as the waveguide width at which all higher order modes above the fundamental TE and TM polarized mode have radiated into the slab. Similar simulations were performed for TeO₂ layer thicknesses of 200, 400 and 600 nm on 0.1, 0.2 and 0.3- μ m-thick silicon nitride strip waveguides for wavelengths from 600–2000 nm to determine the single mode condition for each set of parameters. Fig 3.7.(a) shows the calculated single mode cutoff width versus wavelength for $h_{\text{TeO}_2} = 200, 400$ and 600 nm and $h_{\text{Si}_3\text{N}_4} = 0.2$ μ m, and Fig. 3.7.(b) shows the single mode cutoff width for $h_{\text{TeO}_2} = 400$ nm and $h_{\text{Si}_3\text{N}_4} = 0.1, 0.2$ and 0.3 μ m. The simulations show that thicker TeO₂ coatings and thinner Si₃N₄ strips have a wider Si₃N₄ strip width single mode condition. Of particular interest is transmission in the common telecommunications band, centered around a 1550 nm wavelength, which has single mode cutoffs for Si₃N₄ waveguide widths in the range of 1.0 to 1.5 μ m. Therefore, in simulations we generally consider waveguide widths in this range.

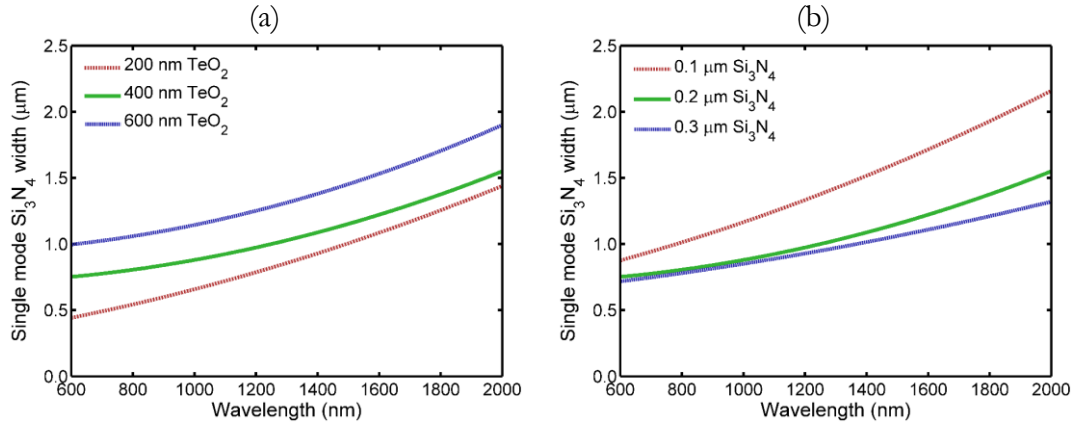


Fig. 3.7. Single mode conditions at wavelengths from 600 to 2000 nm for (a) 200, 400 and 600-nm- thick tellurium oxide coatings on a 0.2 μ m tall silicon-nitride waveguide and (b) a 400-nm-thick tellurium oxide coating on 0.1, 0.2 and 0.3- μ m-thick silicon nitride strip waveguides.

In Fig. 3.6.(a) it can be seen that for $1.0 \mu\text{m} < W_{\text{Si}_3\text{N}_4} < 1.3 \mu\text{m}$ the lowest order TM-polarized mode radiates into the TeO₂ slab while two propagating TE-polarized modes are still supported by the hybrid waveguide. Therefore, in this waveguide design to reach the single mode condition the fundamental TM mode must be completely cutoff, such that the waveguide supports only a single TE-polarized mode and no TM-polarized mode. This phenomenon results from the large difference in the refractive index profile of the waveguide between the lateral and vertical dimensions. Designs with less refractive index profile differences between the lateral and horizontal dimensions of the waveguide, such that the core appears more square shaped, allows waveguides that can support both TE and TM-polarized

light in the single mode condition. Figure 3.8. (a) and (b) show maps of waveguide dimensions which support a TE-polarized mode only or both TE- and TM-polarized modes for varying h_{TeO_2} and $h_{\text{Si}_3\text{N}_4}$, respectively. From both figures, it can be seen that shorter wavelengths, thinner TeO_2 coatings, and thicker Si_3N_4 strip heights, which all tend to increase the effect of the hybrid TeO_2 - Si_3N_4 ridge in confining the mode, more readily guide both a TE and TM-polarized mode in the single mode condition. Because not all TeO_2 - Si_3N_4 structures can support both TE and TM modes, the waveguide simulations and experimental characterization of devices here are primarily focused on the fundamental TE mode. The simulated TE and TM polarized modes for a 1.0- μm -wide and 0.3- μm -thick Si_3N_4 strip coated in a 400-nm-thick TeO_2 layer are shown in Fig. 3.8(c) and (d) respectively. Both modes can be seen to have generally similar shapes, with similar optical confinement factors in the TeO_2 layer.

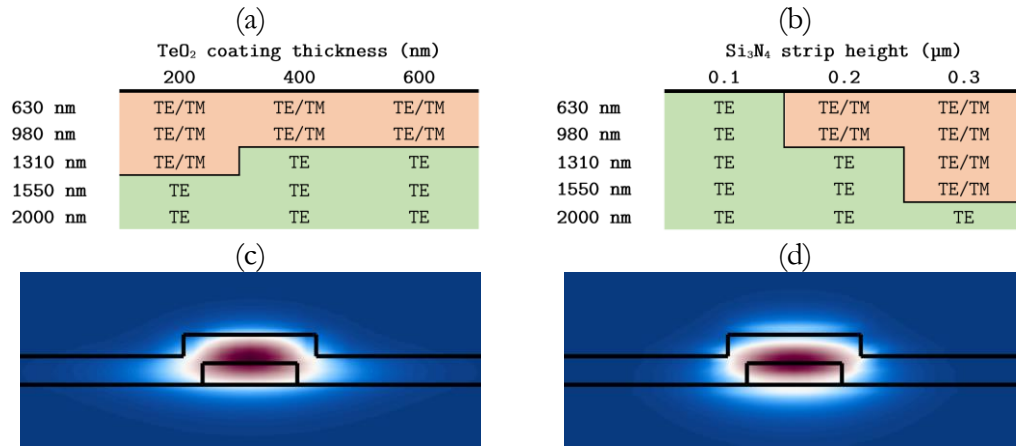


Fig. 3.8. Maps indicating whether the TeO_2 - Si_3N_4 waveguide supports only a TE polarized mode (green) or both a TE and TM polarized mode (red) under the single mode condition for (a) a 0.2 μm Si_3N_4 strip height with 200, 400, and 600-nm-thick TeO_2 -coatings and (b) a 400-nm-thick TeO_2 -coating and 0.1, 0.2 and 0.3 μm Si_3N_4 strip height at 630, 980, 1310, 1550 and 2000 nm wavelengths. Simulated electric-field mode profile of the fundamental (c) TE and (d) TM polarized modes of a 1.0 $\mu\text{m} \times 0.3 \mu\text{m}$ Si_3N_4 strip coated in a 400-nm-thick TeO_2 layer.

After defining a general range of appropriate dimensions for the Si_3N_4 strip layer thickness and width and TeO_2 coating thickness, a more rigorous study of the optical properties of the TeO_2 - Si_3N_4 waveguides was performed. Several key parameters were identified for this optimization study. An important parameter of consideration for the design of TeO_2 - Si_3N_4 waveguides is to achieve large optical confinement within the TeO_2 layer, in order to take advantage of the unique material properties of TeO_2 , such as enhanced nonlinearity and light emission in rare-earth-doped films. For many applications it is also important to maintain a compact mode size, so that the light confined within the TeO_2 has a large optical intensity, which is directly related to the efficiency of nonlinear processes [38,39] and optical pumping of rare-earth ions [40]. On an integrated platform it is also essential to reduce the footprint of devices as much as possible, so that a large number of devices can be fabricated on a single

chip/wafer. This is primarily achieved by reducing the bend radius of waveguides to package devices into compact resonant structures and spirals, which can allow greater interaction of light with the TeO₂ film over long waveguide lengths. Therefore, optical confinement, mode area and minimum bend radius are considered the primary device parameters of interest for designing TeO₂-Si₃N₄ waveguides in this work. A series of simulations was carried out to determine the influence of TeO₂-coating thickness and the silicon-nitride strip dimensions on the optical properties of devices, to determine the optimal waveguide dimensions.

Firstly, the effect of the TeO₂-coating thickness on the waveguide properties was investigated. The calculated optical properties for the fundamental TE polarized mode of the TeO₂-Si₃N₄ waveguides at wavelengths from 600 to 2000 nm, with silicon-nitride strip dimensions of 1.2- μ m-wide \times 0.2- μ m-thick and 200, 400 and 600-nm-thick TeO₂ layers, are displayed in Fig. 3.9.

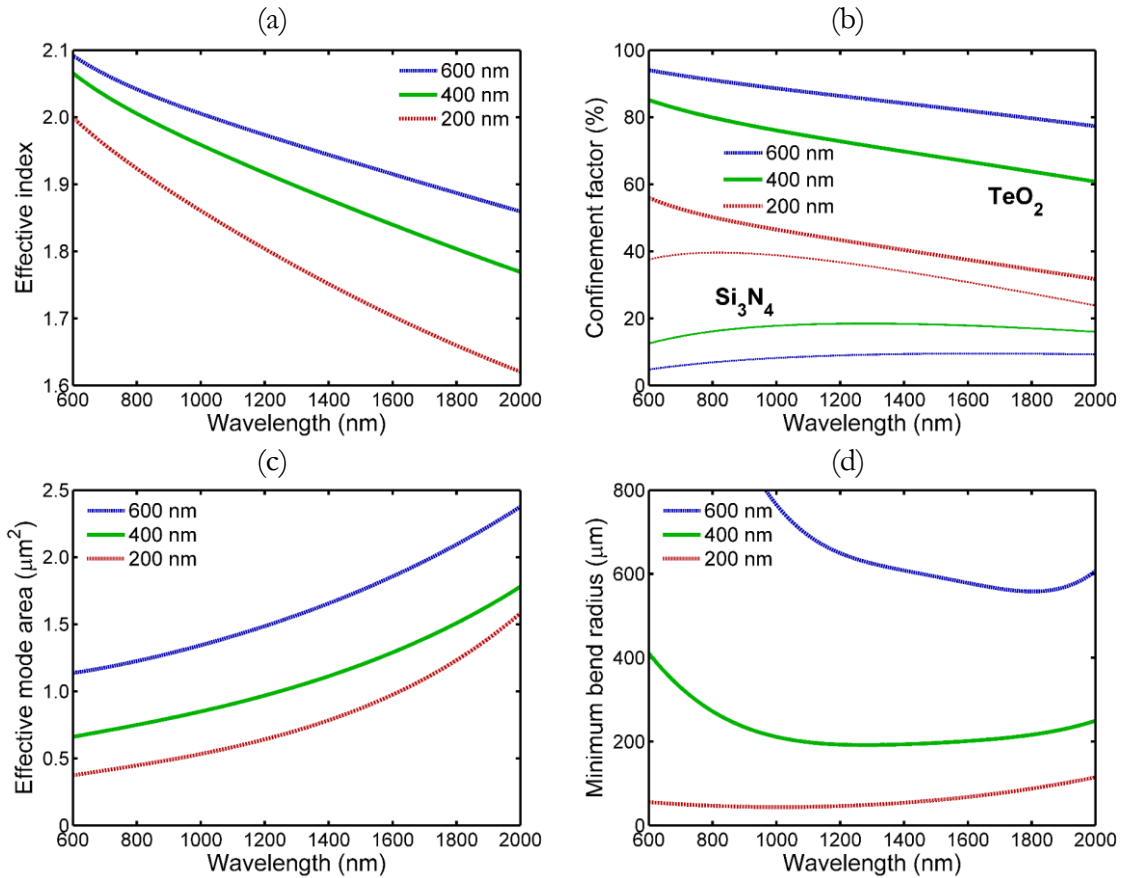


Fig. 3.9. Simulated TeO₂-Si₃N₄ waveguide properties for varying TeO₂ film thickness, including (a) effective index, (b) optical confinement factor within the silicon nitride strip and tellurite glass coating, (c) effective mode area and (d) minimum bend radius at which the waveguide is able to maintain radiation losses less than 0.01 dB/cm for the fundamental TE mode for a 1.2 μ m \times 0.2 μ m silicon nitride strip waveguide with 200, 400 and 600-nm-thick TeO₂-coatings at visible to near-infrared wavelengths.

Figure 3.9(a) shows the simulated effective refractive index versus wavelength, while Fig. 3.9(b) shows the optical intensity confinement percentage in both the Si_3N_4 waveguide and TeO_2 -coating. Figure 3.9(a) shows that the effective index decreases at longer wavelengths. This is partly a result of the material's dispersion relationships reducing material refractive indices, as seen in Fig. 3.4, but more prominently a result of the evanescent tail of the mode expanding further into the SiO_2 and Cytop claddings, which have lower refractive indices. This can be seen in the optical confinement plots which show a general trend in decreased confinement of light within both the Si_3N_4 and TeO_2 layers at longer wavelengths. It can also be seen that thicker TeO_2 films lead to larger effective indices at all wavelengths as the mode increasingly shifts to being more confined in the TeO_2 . The results show that for $h_{\text{TeO}_2} = 200, 400$ and 600 -nm-thick at a wavelength of 1550 nm approximately 39, 68 and 83% of the optical power is confined in the TeO_2 , respectively. For TeO_2 layer thicknesses of greater than 600 nm there is minimal increase in confinement in the TeO_2 . However, increasing the tellurium oxide coating thickness is seen to have drawbacks regarding the other two parameters of importance for the waveguide design; that is, it results in larger mode areas and increased radiation loss in the waveguide bends. Figure 3.9(c) shows the simulated effective mode area versus TeO_2 film thickness, defined as the area over which optical intensity remains above $1/e^2$ the peak intensity value of the mode [41]. As an example, waveguides with $h_{\text{TeO}_2} = 200, 400$ and 600 nm have mode areas of $0.90, 1.20$ and $1.75 \mu\text{m}^2$ at 1550 nm, respectively, which shows that the mode area doubles by increasing the TeO_2 coating thickness from 200 to 600 nm. When comparing to the mode area of a standard $9/125$ single mode fiber ($\sim 80 \mu\text{m}^2$), the mode areas of the TeO_2 - Si_3N_4 waveguides are approximately 1-2% of the size. Figure 3.9(d) shows the minimum bending radius for the different waveguide designs, selected as the bending radius below which radiation loss exceeds 0.01 dB/cm, which was calculated using RSoft's eigenmode bend solver tool. The minimum bending radius is strongly wavelength and TeO_2 film height dependent. The data shows that waveguides with $h_{\text{TeO}_2} = 200, 400$ and 600 nm can be bent down to radii of $70, 200,$ and $590 \mu\text{m}$, respectively, at a wavelength of 1550 nm. Thicker TeO_2 coatings are seen to have a larger minimum bend radius at all wavelengths. At longer wavelengths, the minimum bend radius increases due to coupling to radiation modes from the evanescent tail as the mode expands and has reduced confinement in the waveguide core, as is common in most waveguide structures. However, as the wavelength is reduced below $\sim 1 \mu\text{m}$ the minimum bend radius begins to increase again, as the mode more readily radiates into the TeO_2 slab around the waveguide due to a closer match to the slab mode effective index. These two effects, slab radiation at short wavelengths and evanescent radiation at long wavelengths, which are diagrammed in Fig. 3.10 (a), combine to result in the total radiation loss of the hybrid waveguide structure, as illustrated in the minimum bend radius versus wavelength example in Fig. 3.10 (b). The relative influence of the two effects differs significantly for different TeO_2 - Si_3N_4 waveguide parameter spaces. For thinner TeO_2 films, evanescent radiation is more dominant, while for thicker TeO_2 films slab radiation is more dominant. Based on these results, it becomes clear that the optimization between achieving

high optical intensities in the TeO_2 layer while also maintaining tight bending radii for compact devices occurs for TeO_2 coating thicknesses between approximately 200 to 500 nm.

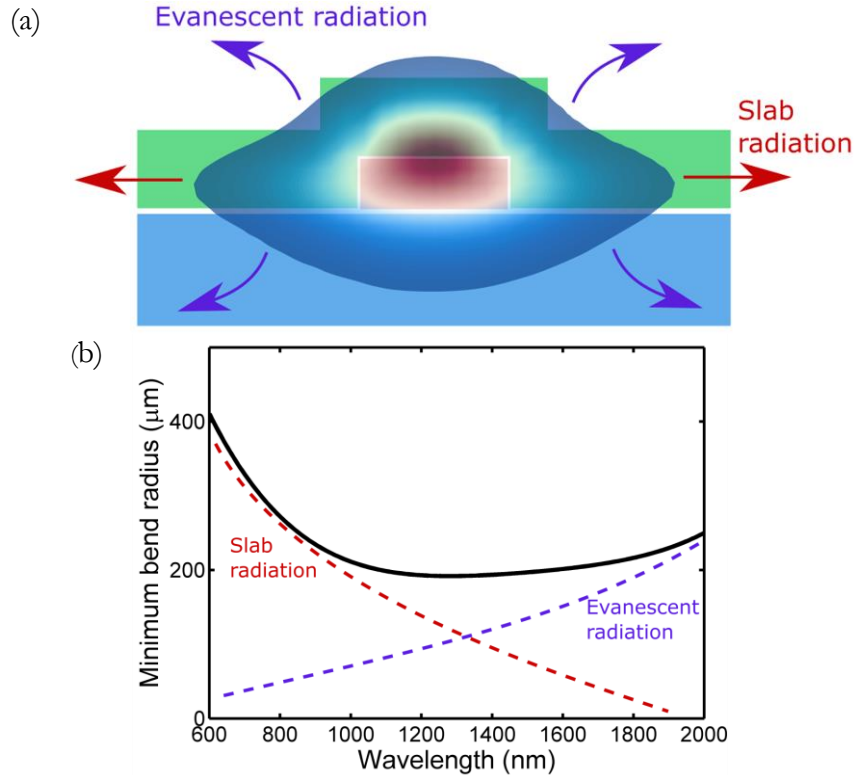


Fig. 3.10. Illustration showing (a) difference between evanescent and slab radiation in waveguide structure and (b) how the minimum waveguide bend radius of the hybrid waveguide structure is predominantly affected by radiation from the evanescent field at longer wavelengths (blue line), and radiation into the tellurite slab surrounding the waveguide at shorter wavelengths (red line).

The effect of silicon-nitride strip width on devices was investigated next, with the simulation results for a 400-nm-thick TeO_2 coating on a 0.2- μm -thick Si_3N_4 strip with widths of 1.0, 1.2 and 1.4 μm summarized in the plots of Fig. 3.11. From the plots of Fig. 3.11, which show nearly overlapping lines, it is clear that changes to waveguide widths over this range will have minimal effect on the overall performance of devices. Using wider waveguides is shown to result in a very minor reduction in the optical confinement within the TeO_2 coating, from 69 to 67% for 1.0 to 1.4 μm wide waveguides at a 1550 nm wavelength. While mode size is also relatively unaffected, there is a slight reduction in the minimum bend radius for wider waveguides because the mode is more strongly confined in the hybrid TeO_2 - Si_3N_4 core. Increasing $W_{\text{Si}_3\text{N}_4}$ from 1.0 to 1.4 μm decreases the minimum bend radius from 225 to 180 μm . In general, using wider Si_3N_4 strip widths, typically up to the single mode cutoff width, should lead to lower waveguide losses due to reduced sidewall interaction, with minimal impact on the optical properties of devices, except for a small reduction in the minimum bend radius.

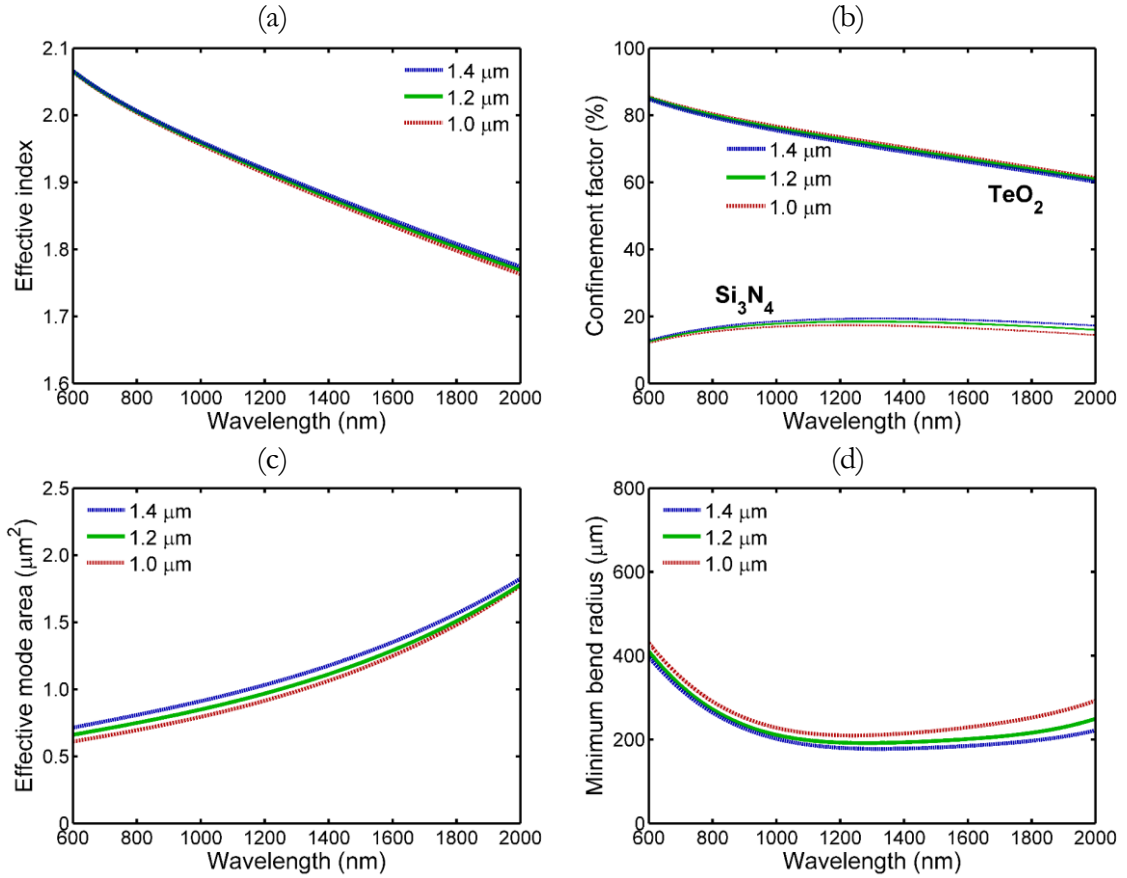


Fig. 3.11. Simulated TeO₂-Si₃N₄ waveguide properties for varying Si₃N₄ strip width, including (a) effective index (b) optical confinement factor within the silicon nitride strip and tellurium oxide coating, (c) effective mode area and (d) minimum bend radius at which the waveguide is able to maintain radiation losses less than 0.01 dB/cm for the fundamental TE mode for 1.0, 1.2 and 1.4 μm × 0.2 μm silicon nitride strip waveguides with a 400-nm-thick TeO₂-coating at visible to near-infrared wavelengths.

Lastly, it is also important to investigate the influence of Si₃N₄ layer height on waveguide properties for the hybrid TeO₂-Si₃N₄ platform. Simulations of the optical properties of waveguides with a 1.2-μm-wide Si₃N₄ strip coated in a 400-nm-thick TeO₂ film and Si₃N₄ layer heights of 0.1, 0.2 and 0.3 μm were carried out and the results are summarized in Fig. 3.12. As expected, thicker Si₃N₄ waveguides confine the optical mode more strongly within the Si₃N₄ layer, reducing the optical mode overlap with the TeO₂. Increasing $h_{\text{Si}_3\text{N}_4}$ from 0.1 to 0.3 μm leads to a decrease in TeO₂ overlap from 73 to 62 % at 1550 nm. For shorter wavelengths the optical mode size is relatively unaffected by changes in the Si₃N₄ layer thickness because the mode is predominantly confined within the TeO₂ coating. However, for longer wavelengths the mode size begins to expand significantly for thinner Si₃N₄ strip heights because the evanescent field is larger. With regard to minimum bend radius, it can be seen that larger Si₃N₄ strip heights allow for tighter bending radii due to larger mode confinement in the waveguide core and increased lateral effective index contrast with the slab.

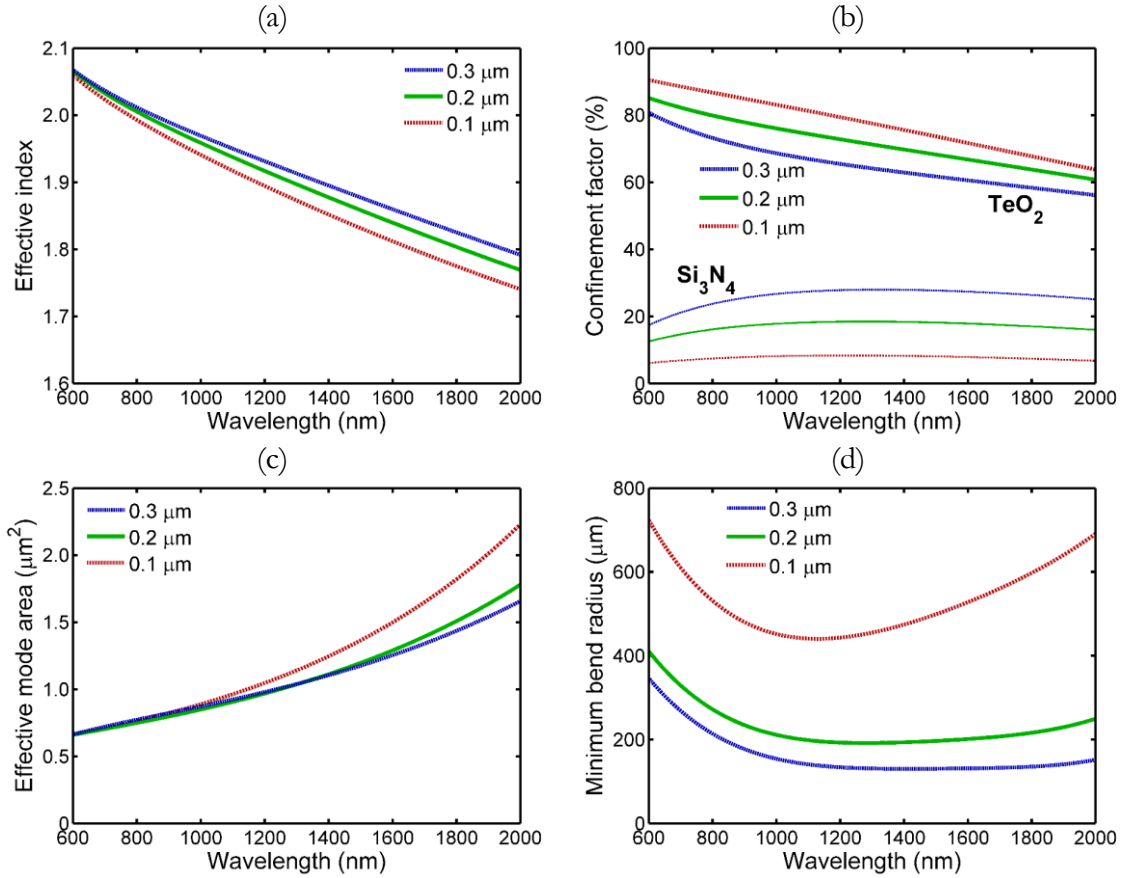


Fig. 3.12. Simulated TeO₂-Si₃N₄ waveguide properties for varying Si₃N₄ strip height, including (a) effective index (b) optical confinement factor within the silicon nitride strip and tellurium oxide coating, (c) effective mode area and (d) minimum bend radius at which the waveguide is able to maintain radiation losses less than 0.01 dB/cm for the fundamental TE mode for 1.2 μm × 0.1, 0.2 and 0.3 μm silicon nitride strip waveguides with a 400-nm-thick TeO₂-coating at visible to near-infrared wavelengths.

Based on these simulations a Si₃N₄ layer thickness of 0.2 μm was selected for the experimentally fabricated chips because it allows for the best compromise between devices with compact bending radius and sufficient optical confinement within the TeO₂-coating. However, thinner Si₃N₄ layers might be of interest for ultra-low loss waveguides due to the reduced sidewall roughness [21,22], and thicker Si₃N₄ platforms are of interest for dispersion engineering and nonlinear optical applications [38,42]. For a 0.2-μm-thick Si₃N₄ layer, strip widths of approximately 0.8 to 1.4 μm maintain the single mode condition, with some variation depending on the operating wavelength and TeO₂-coating thickness. In general, using the largest possible single-mode waveguide width results in the lowest optical propagation losses and smallest bending radius, with minimal changes in optical confinement. TeO₂-coating thicknesses of between 200 and 500 nm offer a good compromise between high TeO₂ optical overlap and tight bending radius devices. Therefore, these are the TeO₂-Si₃N₄ waveguide dimensions which are investigated experimentally in the following sections.

3.4 Passive Photonic Devices

In this section the theory and measured properties of passive optical devices fabricated on the $\text{TeO}_2\text{-Si}_3\text{N}_4$ hybrid waveguide platform are investigated. This includes the characterization of optical transmission losses from visible to infrared wavelengths in paperclip waveguides, fiber-chip edge coupling losses, directional couplers, and high Q microring resonators.

The passive devices were characterized using a fiber-chip-fiber edge coupling setup, shown in the diagram in Fig. 3.13. The input side of the setup includes an input signal laser, which couples to a set of polarization rotation paddles to control the input polarization of light relative to the chip under test. Light sources at 638, 980, 1310, 1550 and 2000 nm wavelengths are used in characterization. The output power of the lasers can be controlled, and in the case of the 1550 nm laser, can be tuned precisely to wavelengths from 1460 to 1640 nm. The polarization of light incident on the chip is controlled by adjusting the polarization paddles. The input signal is then coupled onto the chip by aligning a tapered fiber, with a $2.5\ \mu\text{m}$ spot size, to the waveguide facet using an xyz alignment stage. Another tapered fiber is then aligned to the opposite edge facet of the waveguide to collect the light that has been transmitted across the chip. The collected light is then routed through a fiber to a photodetector which reads the optical power.

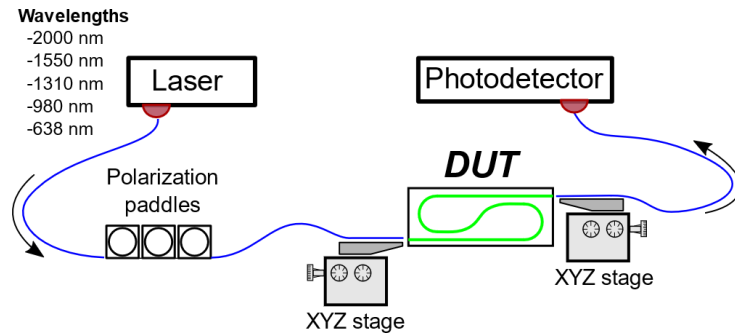


Fig. 3.13. Diagram of fiber-chip coupling setup used in passive device characterization. Signal light is polarized with a set of polarization paddles and launched into then off the chip by aligning fibers to optical facets of waveguide with xyz stage. Intensity of light coupled off chip is measured by a photodetector.

During measurements the position of the optical fiber stages and the orientation of the polarization paddles were aligned to maximize the optical transmission through the waveguide. It was assumed that the polarization paddle orientation that gives the highest optical transmission corresponds to coupling into the TE-polarized mode of the device, because in most cases the $\text{TeO}_2\text{-Si}_3\text{N}_4$ waveguide did not support a TM-polarized mode. This could be clearly observed when measuring devices, where switching the polarization paddles to a TM-polarization caused the measured transmitted power to drop significantly.

The total loss through the setup (L_{Total}), measured as the difference in power measured at the photodetector (P_{Detect}) compared to the power output from the laser (P_{Laser}), results from the combined contributions of:

- System loss (L_{Fiber}) due to attenuation by the optical fibers and misalignments between the fiber connectors and signal laser and photodetector.
- Coupling loss (L_{Coupling}) from mode mismatch, reflections and scattering when transitioning between the optical fibers and the on-chip waveguides.
- Transmission loss ($L_{\text{Transmission}}$) through the waveguides on the device under test, as a result of waveguide propagation loss (L_{WG}) and any device loss, such as interference losses in microring resonators.

The total loss measured across the setup is then a linear combination of all three independent loss sources (in dB scale), as shown in Equation 3.1:

$$L_{\text{Total}} = L_{\text{Fiber}} + L_{\text{Coupling}} + L_{\text{Transmission}} \quad (3.1)$$

In most cases only the coupling losses and transmission losses through the chip under test are of interest for characterizing devices. The system loss can be characterized by removing the chip from the setup, such that there are no coupling or transmission losses, and aligning the two fibers between each other to maximize the detected power. Subtracting the measured system losses from the total loss during measurements on a chip leaves only the coupling and transmission losses, referred to as the insertion loss ($L_{\text{Insertion}}$), calculated as shown in Equation 3.2:

$$\begin{aligned} L_{\text{Insertion}} &= L_{\text{Total}} - L_{\text{Fiber}} \\ &= L_{\text{Coupling}} + L_{\text{Transmission}} \end{aligned} \quad (3.2)$$

3.4.1. Visible to Infrared Waveguide Loss Characterization

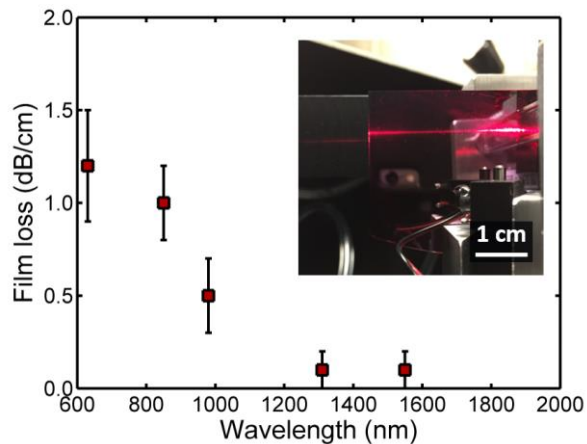


Fig. 3.14. Loss of a TeO_2 thin film on an unpatterned thermally oxidized silicon wafer measured by the prism coupling method at 638, 847, 980, 1310 and 1550 nm wavelengths. Inset: image showing red light propagation in the TeO_2 film.

The waveguide optical propagation loss was characterized by the cutback method, using the paperclip waveguides of different lengths and Si₃N₄ strip widths of 1.2 μm patterned on chiplet design A. The chip was coated in a 380-nm-thick TeO₂ film with losses of 0.1±0.1 dB/cm at 1310 and 1550 nm and 1.2±0.3 dB/cm at 638 nm measured using prism coupling. The TeO₂ film loss data is shown in Fig. 3.14.

Similar to the propagation loss discussed for the thin films in Chapter 2, the optical intensity travelling through a waveguide also experiences an exponential decay according to the Beer-Lambert law. Accordingly, the insertion loss is given by:

$$L_{\text{Insertion}} = L_{\text{Coupling}} + A \cdot l, \quad (3.3)$$

where A is the per unit length propagation loss of the waveguide and l is the length of the waveguide. The total optical propagation loss is then described by the variable L_{WG} . The insertion loss then increases linearly as the waveguide length increases, with a constant offset resulting from fiber-chip coupling losses. The cutback method involves measuring the insertion loss versus length for a set of waveguides with varying lengths and extracting the loss coefficient by fitting the slope. To accurately measure samples via the cutback method, especially for lower loss samples, the fiber-chip coupling loss must be relatively consistent between the different waveguide samples. Here, the optical facets of the waveguides under test were polished using a focused-ion-beam (FIB) cut, to smooth any surface roughness near the facet, which, as discussed in the next section, produces the least variation in optical coupling loss. After the FIB cut the sample was cladded in a spin-on polymer (Cytop) top-cladding.

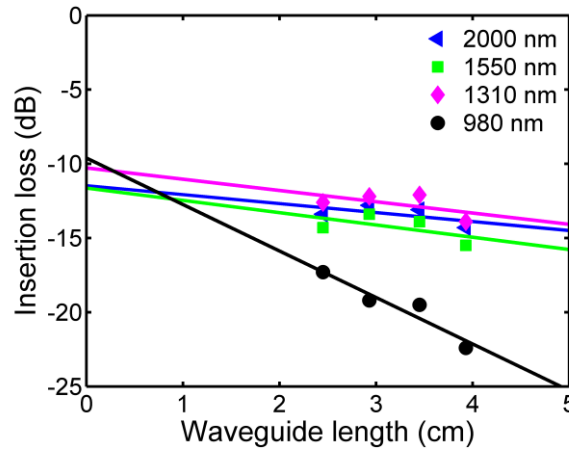


Fig. 3.15. Insertion loss measured versus waveguide length at 980, 1310, 1550 and 2000 nm, fit to have optical propagation losses of 3.1 ± 0.3 , 0.8 ± 0.3 , 0.8 ± 0.3 , and 0.6 ± 0.2 dB/cm, respectively.

The optical insertion loss was then measured in 2.45, 2.93, 3.45 and 3.93-cm-long TeO₂-Si₃N₄ paperclip waveguides with the 980, 1310, 1550 and 2000 nm wavelength light sources. The loss at each wavelength was fit using linear regression, with results shown in Fig. 3.15.

The y-intercept, corresponding to a waveguide length of 0 cm, can be interpreted as the total fiber chip coupling loss, and ranges from 9.6 dB at 980 nm to 11.6 dB at 1550 nm, which corresponds to a fiber-chip coupling loss of 5-6 dB at each facet. The fitted propagation loss is 0.8 ± 0.3 , 0.8 ± 0.3 and 0.6 ± 0.2 dB/cm at 1310, 1550 and 2000 nm wavelengths respectively. At 980 nm the loss is seen to increase to 3.1 ± 0.3 dB/cm, largely because of the increased TeO_2 films losses as seen in Fig. 3.14, as well as the increased scattering loss from the waveguide sidewalls at shorter wavelengths expected from Rayleigh scattering [43].

To measure propagation losses in the visible regime, using the 638 nm laser, cleaved 630-nm fibers were used to couple the light onto the chip, rather than the tapered fibers used at other test wavelengths. These fibers were used because single mode 638-nm tapered fibers were not available, which resulted in a significant increase to the fiber-chip coupling losses because of the greater mode mismatch. The higher coupling loss combined with the larger optical propagation losses through the waveguide meant that the insertion loss could not be measured above the noise level, making the cutback method inaccurate. Instead, the waveguide propagation loss was measured using top-down image analysis of light coupled into the 3.45 cm long waveguide sample, as seen in Fig. 3.16(a). The relative intensity of red light as it propagates along the waveguide was determined by image processing software, and fit against the propagation distance along the waveguide, as shown in Fig. 3.16(b). This fit gives a propagation loss of 8.4 ± 1.1 dB/cm at 638 nm.

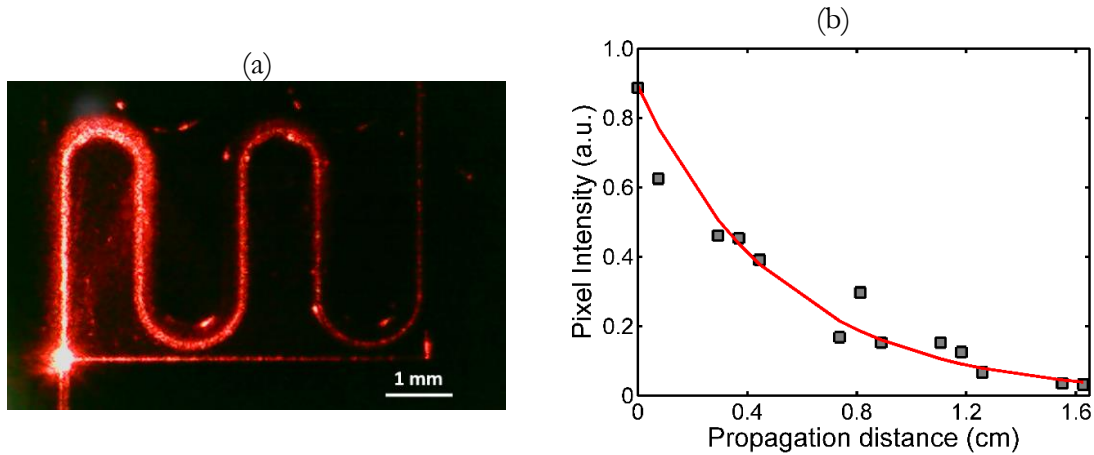


Fig. 3.16. (a) Top-down image of red light propagating through a 3.45-cm-long $\text{TeO}_2\text{-Si}_3\text{N}_4$ waveguide. (b) Pixel intensity of image versus propagation length along the waveguide, fit to have an optical propagation loss of 8.4 ± 1.1 dB/cm.

These results demonstrate low to moderate optical propagation losses for visible to near-infrared wavelengths which is promising towards the realization of linear, nonlinear and rare-earth doped TeO_2 devices in compact and high confinement $\text{TeO}_2\text{-Si}_3\text{N}_4$ waveguides.

3.4.2. Fiber-Chip Edge Couplers

Because of the mode mismatch and discontinuities between large fibers and compact integrated waveguides, the optical losses associated with coupling from an optical fiber to a photonic integrated circuit can significantly outweigh the on-chip optical propagation losses. In the practical implementation of devices, it is important to minimize the fiber-chip coupling losses as much as possible. This is especially relevant in nonlinear and rare-earth doped devices, which typically require large on-chip optical pump intensities. The sources of fiber-chip coupling loss are composed of reflection losses at fiber and chip interfaces due to refractive index contrast, mode mismatch losses between the mode of the fiber and the mode of the waveguide and scattering losses from roughness along the chip's optical facet. While the Fresnel and mode mismatch losses can be minimized by appropriate design of the waveguide, the scattering associated losses are predominantly determined by the fabrication process and resulting quality of the optical facet. Reflection losses (R_{Fresnel}) occur at the interface between materials of different refractive indices, and are described by the Fresnel equations. Assuming normally incident light, the ratio of optical power that is transmitted across the interface relative to the incident power (T_{Fresnel}) is given by Equation 3.4:

$$T_{\text{Fresnel}} = 1 - R_{\text{Fresnel}} = 1 - \left| \frac{n_1 - n_2}{n_1 + n_2} \right|^2, \quad (3.4)$$

where (n_1) and (n_2) are the refractive indices of the two media. In the case of tapered fibers, they must be placed at a working distance of several microns away from the edge facet of the chip in order to focus to the 2.5 μm beam diameter. Therefore, an incident signal must pass through both the fiber-air and air-waveguide planes of interface. The reflection at the fiber-air interface is independent of waveguide design, and is calculated to have a 96.6% transmission ratio ($T_{\text{Fresnel(Fiber-Air)}}$), assuming a refractive index of 1.444 and 1 for the fiber and air, respectively. The air-waveguide interface loss will vary based on the effective index of the waveguide under test, which in our case changes depending on the size of the Si_3N_4 strip and TeO_2 -coating. The calculated transmission ratio into the waveguide from the air ($T_{\text{Fresnel(Air-Waveguide)}}$) based on Fresnel losses in the range of effective indices typical for a TeO_2 - Si_3N_4 waveguide is found to be between 90 and 95 %, with thinner TeO_2 -coatings experiencing greater transmission as the lower waveguide effective index provides less contrast to the air interface. In contrast to tapered fibers, cleaved fibers placed directly against the chip can eliminate the air interface and reduce the reflection-based losses during coupling but typically incur significantly more mode mismatch losses due to their much lower optical overlap with the optical mode of the waveguide. As discussed earlier the optical modes of the waveguide are generally less than 5% the optical mode size of a standard 9/125 single mode (SM) fiber. The optical overlap losses for SM fiber are calculated to exceed 15 dB, which is far too large for practical devices. Therefore, tapered fibers are generally used when measuring devices, to achieve better optical overlap with the waveguide mode. The mode mismatch is determined based on the calculated mode profile of the TeO_2 -coated Si_3N_4 waveguide and

optical fiber which is assumed to have a gaussian intensity profile with a $1/e^2$ diameter of $2.5 \mu\text{m}$. The calculation was performed using an RSoft simulation with the horizontal center of the fiber mode positioned at the center of the Si_3N_4 strip, and its vertical position varied from the base of the Si_3N_4 layer to the top of the TeO_2 -coating to find the position that gives the highest coupling ratio. The theoretical ratio of optical power which is transmitted into the waveguide (T_{Overlap}) is calculated using the mode overlap integral in Equation 3.5:

$$T_{\text{Overlap}} = \frac{\iint_{x,y} (E_{\text{Waveguide}}^2 E_{\text{Fiber}}^2) dA}{\iint_{x,y} (E_{\text{Waveguide}}^2) dA \cdot \iint_{x,y} (E_{\text{Fiber}}^2) dA}, \quad (3.5)$$

where $E_{\text{Waveguide}}$ and E_{Fiber} are the electric field distributions describing the optical mode profiles of the waveguide and optical fiber, respectively. The combined contributions of reflection losses at interfaces and mode mismatch losses between the fiber and waveguide modes were considered to determine the theoretical minimum coupling loss (L_{Coupling}) that can be achieved in the waveguide, which can be converted to coupling loss in dB by the following equation:

$$L_{\text{Coupling}} = 10 \log_{10} (T_{\text{Overlap}} \cdot T_{\text{Fresnel}(\text{Fiber-Air})} \cdot T_{\text{Fresnel}(\text{Air-Waveguide})}). \quad (3.6)$$

The coupling loss was calculated for Si_3N_4 strip widths of $0.5, 1.0$ and $2.0 \mu\text{m}$ and TeO_2 film thicknesses of 100 to 500 nm at 1550 nm , with the results shown in Fig. 3.17.

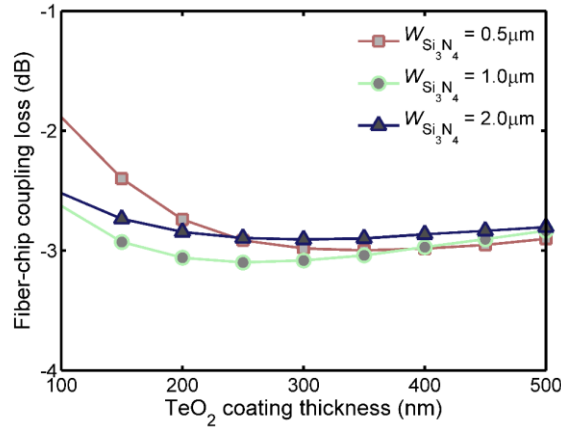


Fig. 3.17. Simulated fiber-chip coupling loss at 1550 nm , accounting for Fresnel reflection losses and mode mismatch of a $2.5 \mu\text{m}$ spot size fiber with TeO_2 - Si_3N_4 waveguides with varying width and TeO_2 layer thickness.

In the parameter range investigated here there is minimal difference in coupling loss at different waveguide widths, which matches the minimal change in properties seen in simulations. At the TeO_2 -coating thicknesses of main interest between 200 and 500 nm there is also minimal difference in coupling efficiency, remaining around 3 dB of loss. A small improvement of loss up to $\sim 2 \text{ dB}$ is seen for thinner TeO_2 -coatings of less than 150 nm as

the evanescent field of the waveguide mode begins to expand. However, despite the improved coupling losses, coatings of that thickness are typically too thin to provide adequate overlap with the TeO_2 for effective light-matter interactions in the waveguide.

The waveguide designs of interest can therefore be expected to have a maximum theoretical coupling efficiency of approximately 3 dB per facet. However, the effects of scattering loss at the waveguide interface will reduce the actual efficiency below this value. Three different facet preparation methods for devices were investigated, including optical facets defined by dicing, a deep dry etch followed by dicing, and FIB polishing after depositing the TeO_2 coating. Figure 3.18 shows an example of the optical facets of a waveguide prepared by each method before a TeO_2 coating was deposited.

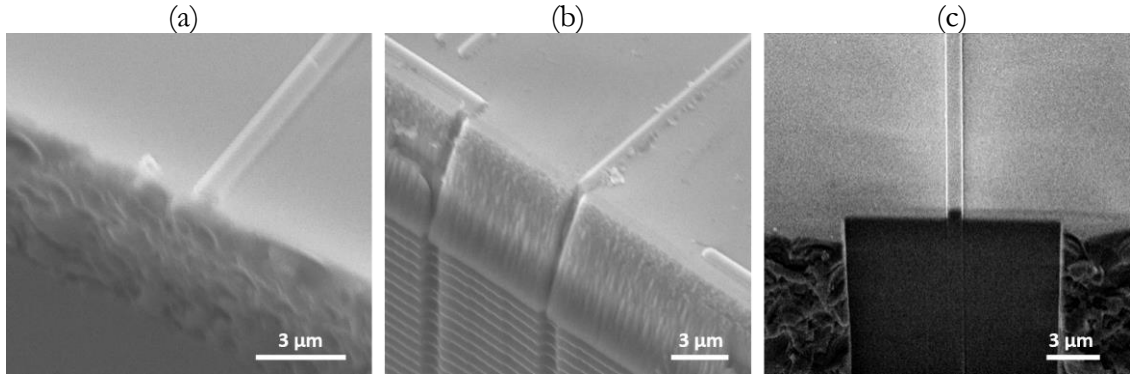


Fig. 3.18. Optical facets of uncoated Si_3N_4 waveguides prepared by (a) dicing, (b) etching and (c) focused-ion-beam polishing.

The diced sample, seen in Fig. 3.18(a), shows significant roughness along the facet. The etched sample, seen in Fig. 3.18(b), demonstrate relatively smooth SiO_2 sidewalls, except for near the waveguide, where the Si_3N_4 protruding into the etch region has created a ridge during the SiO_2 deep-etch due to the different etch rate of Si_3N_4 . FIB polished facets, seen in Fig. 3.18(c), exhibit smooth surfaces, but still lead to a small ridge around the waveguide due to the different mill rates between SiO_2 and Si_3N_4 . Several chips prepared with each facet type were coated in TeO_2 layers around 300-nm-thick and were characterized for insertion loss across short 0.6-cm-long straight waveguides in order to minimize variations in optical propagation losses between samples. The coupling loss per facet was taken as the average measured insertion loss measured in 20 different waveguides minus the estimated 0.5 dB of optical propagation loss in the waveguide and divided by 2. The median and standard deviation for coupling loss for each facet type is shown below in Table 3.1.

Table 3.1. Average and standard deviation of coupling loss per facet measured on diced, etched, and FIB polished TeO_2 - Si_3N_4 waveguides using tapered fibers.

	Dice	Etch	FIB
Average coupling loss	11.0	12.8	5.4
Standard deviation	4.0	1.7	0.8

The results show that the diced and etched facets typically exhibit over 10 dB of optical coupling loss per facet. This is significantly larger than the expected theoretical loss, arising as a result of the large interface roughness that can be seen in the SEM images in Fig. 3.18. The diced facets show lower average loss but more variability compared to the etched facets. For FIB milling, the coupling loss is around 5 dB per facet which approaches the theoretical limit. Although this shows a significant improvement compared to the other methods there still remains some additional scattering loss due to the FIB milled structure. Due to the serial nature of the FIB milling process, it is time consuming and expensive and difficult to scale up to wafer or even chip level processing. Meanwhile, although they are higher loss, the benefit of the diced and etched facets is they do not require extra expense and processing steps. Considering these tradeoffs, a combination of diced, etched and FIB-milled facets were used in the TeO₂-Si₃N₄ hybrid devices investigated in this thesis.

3.4.3. Directional Couplers

Directional couplers are essential components in integrated photonic systems, for the purpose of splitting or combining light between multiple pathways of a photonic circuit. Wavelength multiplexors [44] and interferometric cavities, such as Mach-Zehnder interferometers [45], microring resonators [46], and Sagnac mirrors [47], are all typically implemented in integrated photonic systems using one or a combination of multiple directional couplers. These devices are directly relevant to nonlinear and rare-earth doped photonic devices, as pump and signal wavelength multiplexors and resonant feedback cavities for laser oscillators. Therefore, it is important to precisely model and design the splitting ratio of waveguide-waveguide directional couplers for the realization of more advanced photonic circuit designs in the TeO₂-coated Si₃N₄ photonic platform.

When two waveguides are in close proximity the evanescent field of the independent modes confined by each waveguide experience significant optical overlap. This overlap allows the optical power confined within the first independent waveguide mode to be transferred into the optical mode confined by the second waveguide. The ratio of initially launched light that is transferred into the second waveguide is described by the cross-over ratio (κ) as follows:

$$\kappa = \frac{P_{\text{Drop}}}{P_0}, \quad (3.7)$$

where P_0 is the initially incident power to the directional coupler in the first waveguide and P_{Drop} is the power transferred into the second waveguide, referred to as the drop waveguide. Assuming that the two waveguides are identical, such that light propagates with the same phase constant, the cross over ratio after propagating along a variable length (z) of the coupler is given by Equation 3.8 [48]:

$$\kappa = \sin^2(C \cdot z), \quad (3.8)$$

where C is the coupling rate parameter. Assuming that no significant waveguide loss occurs over the length of the coupler, any power that has not transferred into drop waveguide will remain in the original waveguide, referred to as the thru waveguide, to maintain the conservation of energy. The transmission ratio (β) which describes the ratio of initially launched light that remains in the thru waveguide can be described as follows:

$$\begin{aligned}\beta &= \frac{P_{\text{Thru}}}{P_0} \\ &= \cos^2(C \cdot z).\end{aligned}\tag{3.9}$$

The solution to Equations 3.8 and 3.9 demonstrates a relationship where the optical power oscillates from the thru waveguide to the drop waveguide and back again, with a periodicity determined by the coupling rate parameter. A larger coupling rate will increase the frequency at which the light transfers back and forth between the two waveguides. A model for determining the coupling rate for a directional coupler can be developed using the eigenmode expansion simulation method [49,50], which simulates the eigenmodes supported by the combined waveguide system. The confined modes of the coupled system can be considered as a summation of the independent modes confined by each waveguide, and can be solved for either the symmetric case, where both modes are in phase, or the antisymmetric case, where both modes are out of phase. The simulated eigenmodes of a coupled TeO₂-coated Si₃N₄ waveguide structure are shown for the symmetric and antisymmetric mode cases in Fig. 3.19(a) and (b) respectively.

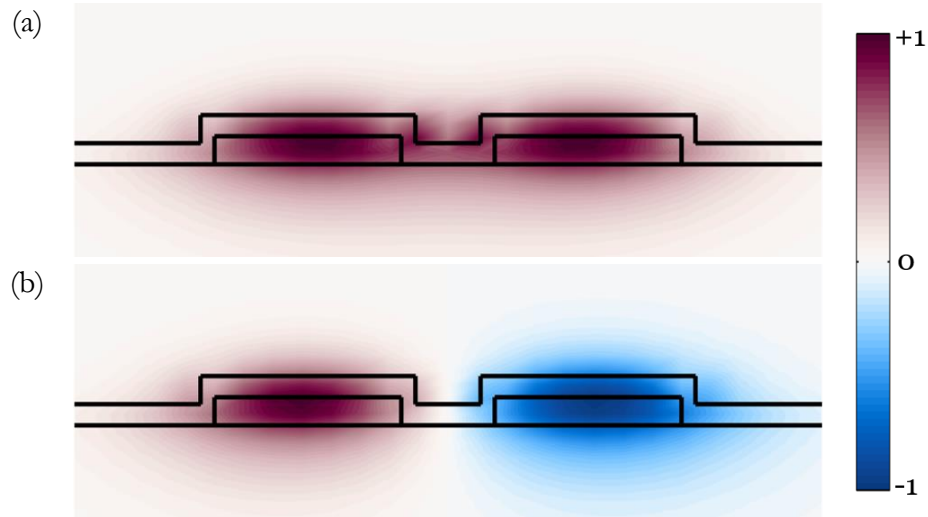


Fig. 3.19. Simulated electric field profiles at 1550 nm of the (a) symmetric and (b) antisymmetric modes of 1-μm-wide Si₃N₄ waveguides with a 0.5 μm coupling gap between the interior walls of the two waveguides, coated in a 150-nm-thick TeO₂ film.

In the antisymmetric case there exists a region where the electric field magnitude of the coupled modes crosses 0, which does not occur in the symmetric case. This results in the

antisymmetric mode to experience a slightly lower effective refractive index than the symmetric case, analogous to the energy splitting seen when the electron wavefunctions of two nearby atoms overlap in solid state physics. The difference in the effective indices of the symmetric (n_S) and antisymmetric (n_A) modes at a wavelength of λ can be used to calculate the coupling coefficient of the device using equation 3.10:

$$C = \frac{\pi(n_S - n_A)}{\lambda}. \quad (3.10)$$

The coupling rate therefore depends on the geometry of the waveguides, the gap between them and the wavelength of light. It is intuitive that as the gap between the two waveguides is decreased the optical overlap of the thru and drop waveguide modes will increase, resulting in greater mode splitting and a larger coupling rate parameter. The effective indices of the symmetric and antisymmetric supermodes of a coupled waveguide system with 1- μm -wide Si_3N_4 strips coated in a 150-nm-thick TeO_2 thin film at a wavelength of 1550 nm and separated by nominal coupling gaps between the interior walls of the Si_3N_4 strips of 0.5 to 4 μm are shown in Fig. 3.20. From the figure it can be seen that at gaps of 2 μm and above, the effective index of the two supermodes are relatively similar, while they begin to split rapidly as the coupling gap becomes smaller. This results in an exponential increase in coupling rate parameter with decreasing coupling gap, as is also plotted in Fig. 3.20.

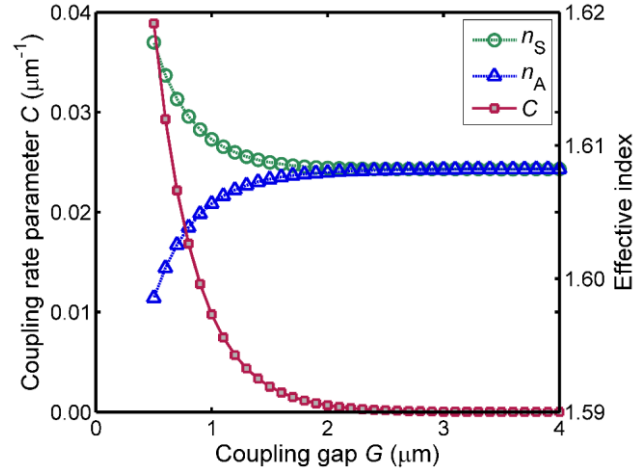


Fig. 3.20. Calculated coupling rate parameter (C) between the two waveguides shown in Fig. 3.18 versus coupling gap. The coupling coefficient is proportional to the difference in the effective index of the symmetric mode (n_S) and antisymmetric mode (n_A).

The cross-over and transmission ratio of the directional coupler for a known waveguide geometry can therefore be designed based on the nominal coupling gap (G_0), and the designed length of the coupler (l_{coupler}). While small coupling gaps can achieve a large cross-over in short coupling lengths, they become more sensitive to fabrication errors and can be limited by the resolution of the lithographic process. However, coupling gaps that are too large will require excessively long coupler lengths. Furthermore, in the practical implementation of a

directional coupler, regions away from the designed coupler should be a sufficient distance away from each other so as to prevent additional, unwanted, coupling or cross-talk between the waveguides. In general in our designs, a $30\ \mu\text{m}$ distance between independent waveguides was used in the fabricated devices to prevent any non-intended coupling. Therefore, there must exist a transition region from the independent waveguides, which are spaced far apart, to the coupled system. To maintain adiabatic transitions and eliminate any straight to curved waveguide mode mismatch loss, a sine bend transition was used to bring together and separate waveguides before and after the coupler. The layout of the directional coupler, including the transition region, is shown in Fig. 3.21.

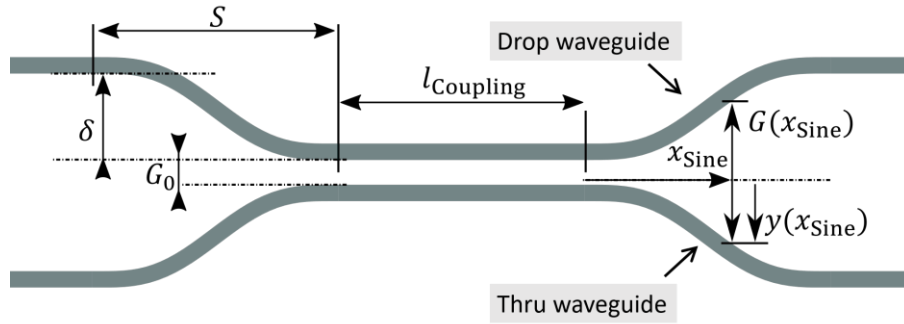


Fig. 3.21. Layout of a directional coupler system, with a defined coupler length of l_{Coupling} separated by a minimum coupling gap of G_0 with sine bend transitions with an amplitude of δ for a full period length of S on each side.

The vertical offset (y) of the sine bend transition versus the position along the length of the sine bend (x_{Sine}) is defined by Equation 3.11:

$$y(x_{\text{Sine}}) = \frac{\delta}{S} x_{\text{Sine}} - \frac{\delta}{2\pi} \sin\left(\frac{2\pi}{S} x_{\text{Sine}}\right), \quad (3.11)$$

where δ is the amplitude of the sine wave, defining the total vertical displacement that the transition will undergo after travelling one period S of the sine bend. Here, a $15\ \mu\text{m}$ sine bend amplitude was used to achieve the $30\ \mu\text{m}$ separation between the independent regions of the waveguides in the system. The period of the sine bend must then be chosen at an appropriate length in order to maintain the bend radius of the sine bend above the minimum waveguide bend radius to avoid the introduction of radiation losses. The radius of curvature (R_{Curv}) along the length of the sine bend can be found from Equation 3.12:

$$R_{\text{Curv}}(x_{\text{Sine}}) = \left| \frac{(1 + y')^{\frac{3}{2}}}{y''} \right|, \quad (3.12)$$

where y' and y'' are the first and second derivatives of Equation 3.11, respectively. A sine bend period of $300\ \mu\text{m}$, which corresponds to a minimum bend radius of $960\ \mu\text{m}$ based on Equation 3.12, is well above the bend loss threshold for $\text{TeO}_2\text{-Si}_3\text{N}_4$ waveguides and was used

in the fabricated couplers. As both the thru and drop waveguides contain a sine bend the total gap between the two waveguides in this region is found from the designed coupling gap of the coupler region (G_0), and the vertical offset created by the sine bend on both the thru and drop waveguides. The total coupling gap in the sine region ($G(x_{\text{Sine}})$) can then be described as follows:

$$G(x_{\text{Sine}}) = G_0 + 2(y(x_{\text{Sine}})). \quad (3.13)$$

Although for the majority of the sine bend region the two waveguides are sufficiently far away that they do not interact with each other, they will eventually allow a noticeable exchange of power between waveguides as they are brought closer together before entering and when first leaving the designed optical coupler. Therefore, the contribution of the sine bend to the total coupled power must also be accounted for in the design. By considering the sine bend as a series of small straight waveguide sections, with the gap between the thru and drop waveguide at any point defined by equation 3.13, a corresponding coupling rate parameter ($C(x_{\text{Sine}})$) between the two waveguides for the small section can be found from the eigenmode expansion method. The sum of each small straight waveguide section then contributes to the total coupling rate term, which can be expressed mathematically as the integration of the coupling rate along the length of the sine bend. The cross-over ratio of the coupler is then found from the contribution over the length of the straight directional coupler region and the sine bend transition on each side to the coupling term, as expressed in Equation 3.14:

$$\kappa = \sin^2 \left(C_0 l_{\text{Coupler}} + 2 \int_{x_{\text{Sine}}=0}^{x_{\text{Sine}}=S} C(x_{\text{Sine}}) \cdot dx_{\text{Sine}} \right). \quad (3.14)$$

Experimentally, a series of directional couplers were included in chip design C, featuring 1- μm -wide Si_3N_4 strips separated by a mask-designed interior wall coupling gap of 0.8 μm and coupler lengths (l_{Coupler}) ranging from 1 to 80 μm . The layout of each coupler follows the diagram shown in Fig 3.21, with all four ports of the device routed to an etched-facet fiber-chip edge coupler. A chip coated in 150-nm of TeO_2 was prepared and measured to extract the cross-over ratio versus coupler length and verify the coupler simulation model. The cross-over ratio is defined in equation 3.5 as the ratio of power that enters the drop waveguide compared to the power incident on the coupler. However, the experimental measurement of this ratio must account for additional losses from coupling onto/off the chip (L_{Coupling}), and waveguide propagation losses (L_{WG}) when routing from edge couplers to the directional coupler from each port of the device. The variables T_{C} and T_{WG} are used to describe the ratio of light that transmits across the fiber-chip edge couplers and down each arm of the directional coupler, respectively, defined as follows:

$$T_{\text{C}} = 10^{-\frac{L_{\text{Coupling}}}{10}}, \quad (3.15)$$

$$T_{WG} = 10^{-\frac{L_{WG}}{10}}. \quad (3.16)$$

Considering the coupler as a lumped device with a cross-over ratio of κ , the path of light and its associated losses from an input fiber to an output fiber on either the thru or drop port of the waveguide is shown in Fig. 3.22.

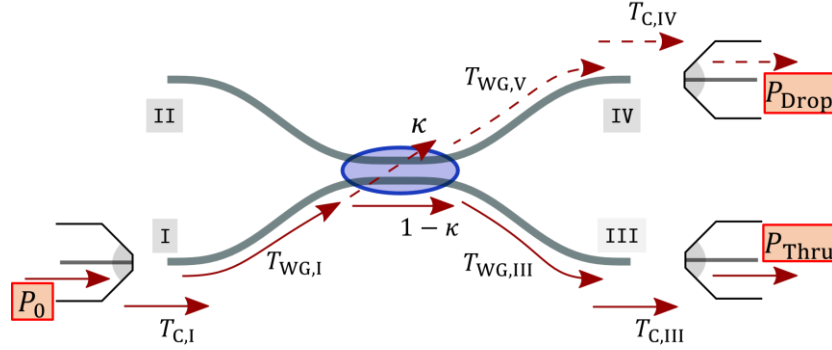


Fig. 3.22. Diagram showing contributions to loss when measuring directional coupler circuits. Light coupled through Port I will transmit a ratio of $T_{C,I}$ of the incident light as it is coupled onto the chip, after which it experiences a waveguide propagation loss of $T_{WG,I}$ while travelling down the arm of Port I. A certain percentage of light is coupled between waveguides in the coupling region, and an output signal can then be measured on either the thru or drop port of the coupler, ports III and IV respectively, each with their own associated coupling and propagation losses.

The transmitted power measured at the thru (P_{Thru}) and drop (P_{Drop}) ports of the coupler by the photodetector for a laser power of P_0 incident on Port I of the device can be found by the following set of equations:

$$P_{Drop,I} = (\kappa)(T_{C,IV}T_{WG,IV})(T_{C,I}T_{WG,I})P_0, \quad (3.17)$$

$$P_{Thru,I} = (1 - \kappa)(T_{C,III}T_{WG,III})(T_{C,I}T_{WG,I})P_0. \quad (3.18)$$

Therefore, to calculate the cross-over ratio based on the measured transmission values the coupling losses, waveguide propagation losses, and incident signal power must all be well known, which can be difficult to achieve. Therefore, to calculate the cross-over ratio of a device the measured power at the drop waveguide is compared to the total power measured at both the output thru and drop waveguides as done in the following equation:

$$\begin{aligned} & \frac{P_{Drop,I}}{P_{Thru,I} + P_{Drop,I}} \\ &= \frac{(\kappa)(T_{C,IV}T_{WG,IV})(T_{C,I}T_{WG,I})P_0}{(1 - \kappa)(T_{C,III}T_{WG,III})(T_{C,I}T_{WG,I})P_0 + (\kappa)(T_{C,IV}T_{WG,IV})(T_{C,I}T_{WG,I})P_0}. \end{aligned} \quad (3.19)$$

It can be immediately seen that the incident signal power can be eliminated from the equation. To simplify the equation further, it was assumed that because the arms of each port of the

device are the same length the optical propagation losses along each arm are all approximately equal and can be treated as a constant value. This assumption allows the optical propagation losses and coupling losses at Port I to be eliminated from Equation 3.19 as shown in the following:

$$\frac{P_{\text{Drop,I}}}{P_{\text{Thru,I}} + P_{\text{Drop,I}}} = \frac{T_{\text{C,IV}}}{T_{\text{C,III}} + (T_{\text{C,IV}} - T_{\text{C,III}})(\kappa)} (\kappa). \quad (3.20)$$

Furthermore, by assuming that the difference in coupling losses between the two output ports of the device are relatively small, which is a reasonable approximation for etched facets as seen in the previous subsection, the second term of the denominator can also be eliminated to simplify the relationship further to:

$$\frac{P_{\text{Drop,I}}}{P_{\text{Thru,I}} + P_{\text{Drop,I}}} \cong \frac{T_{\text{C,IV}}}{T_{\text{C,III}}} (\kappa). \quad (3.21)$$

Although the same logic could be applied to also eliminate the fiber-chip coupling loss ratio term from the right hand side of Equation 3.21, it is left in to account for small variations in coupling loss between different waveguides. These differences can be averaged out and the cross-over ratio can then be found experimentally by taking the mean value of Equation 3.21 measured for an initial light source incident on each of the four different ports of the device as shown in the following:

$$\kappa = \frac{1}{4} \left(\frac{\frac{P_{\text{Drop,I}}}{P_{\text{Thru,I}} + P_{\text{Drop,I}}} + \frac{P_{\text{Drop,II}}}{P_{\text{Thru,II}} + P_{\text{Drop,II}}} + \dots}{\frac{P_{\text{Drop,III}}}{P_{\text{Thru,III}} + P_{\text{Drop,III}}} + \frac{P_{\text{Drop,IV}}}{P_{\text{Thru,IV}} + P_{\text{Drop,IV}}}} \right). \quad (3.22)$$

Therefore, for each directional coupler four sets of thru and drop port transmission measurements were taken to determine the cross-over ratio. This method was applied to measure the cross-over ratio versus coupler length at 1550 nm for the series of couplers on the chip, and the results are plotted in Fig. 3.23(a). It can be seen from the data that even at a coupler length of only 1 μm , approximately 50% of power is coupled into the drop-port waveguide. This is primarily due to the coupling that occurs over the length of the sine bend rather than the coupler itself, and shows that the contributions of the sine bend to the cross-over ratio of the device can be significant. The cross-over ratio is then seen to continually rise as the length of the coupler increases until it reaches an approximately 100 % cross-over ratio at a coupling length of 80 μm , beyond which it would be expected to decrease again following the sinusoid coupling relationship. When comparing the measured data to the expected cross-over ratio simulated for this waveguide geometry a mismatch is observed. The simulation predicts an approximately 80% cross-over ratio at a coupling length of 0 μm and total cross-over for a 30- μm -long coupler. By increasing the waveguide-waveguide gap of the coupler

model a good fit to the experimental data can be found by using a gap of $0.96\ \mu\text{m}$ as seen in Fig. 3.23(a). The same devices were also measured at 1510, 1570 and 1630 nm wavelengths, and the data was fit against the coupling model also using a $0.96\ \mu\text{m}$ coupling gap, as displayed in Fig 3.23(b). Good agreement is observed between measured and simulated data for all wavelengths. From the data it is seen that longer wavelengths reach a 100 % cross-over ratio at shorter coupling lengths compared to shorter wavelengths, which is due to the larger evanescent field at longer wavelengths increasing the coupling coefficient. This effect can lead to relatively large variation in the cross-over ratio of the device at different wavelengths for the same coupler.

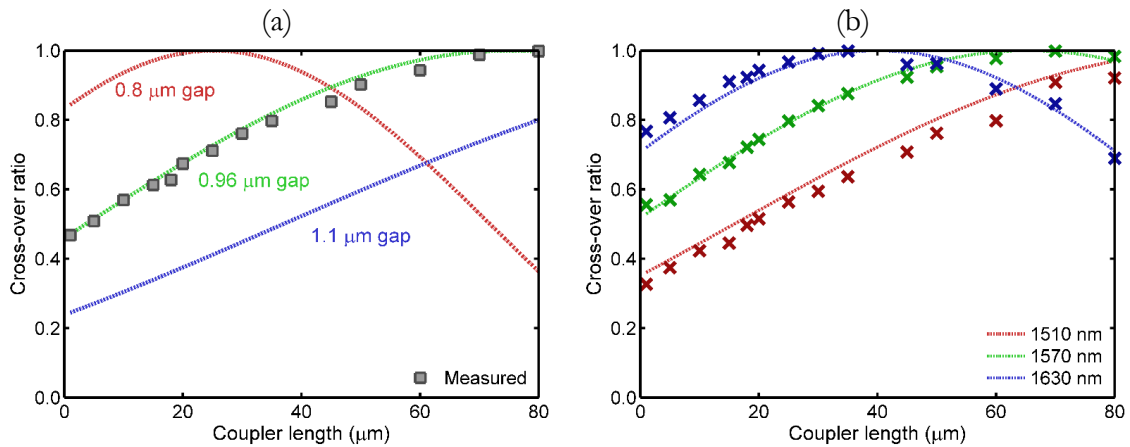


Fig. 3.23. Measured directional coupler cross-over ratio for 1- μm -wide Si_3N_4 strips with a $0.8\ \mu\text{m}$ nominal coupling gap and coupling lengths from 0 to $80\ \mu\text{m}$ coated in a 150-nm -thick TeO_2 -coating at a $1550\ \text{nm}$ wavelength. Also shown are the simulated cross-over ratios for the same structure with 0.8 , 0.96 and $1.1\ \mu\text{m}$ nominal coupling gaps, demonstrating better agreement with the simulated results for $0.96\ \mu\text{m}$ gap. (b) Measured and simulated cross-over ratios at 1510 , 1570 and $1630\ \text{nm}$ wavelengths, compared to the simulated $0.96\ \mu\text{m}$ coupling gap.

To investigate the cause of the discrepancy between the designed coupling gap and the estimated coupling gap based on simulation two other chips; one coated in a 300-nm -thick TeO_2 layer and another cladded in Cytop with no underlying TeO_2 layer were investigated. The measured cross-over ratios and simulated best fit for the three samples at a wavelength of $1570\ \text{nm}$ can then be seen in Fig. 3.24. The chips with 150- and 300-nm -thick TeO_2 -coatings, shown in Fig. 3.24(a) and (b), respectively, demonstrate very similar cross-over ratios versus length despite their different coating thicknesses. This is because although the thinner coating has a larger evanescent tail which is expected to increase the coupling rate the thicker coating reduces the effective distance between waveguides, which also serves to increase the coupling rate, with the two effects relatively cancelling out. Simulations of both the 150- and 300-nm -thick coated $\text{TeO}_2\text{-Si}_3\text{N}_4$ directional couplers are best fit to simulated coupling gaps of 0.96 and $0.95\ \mu\text{m}$, respectively. To investigate whether this offset could be a result of the lithographic and etching process with regard to the Si_3N_4 increasing the fabricated gap from the mask design, a Si_3N_4 waveguide sample was cladded in Cytop. The measured cross-over

ratio for this sample can be seen in Fig. 3.24 (c), as well as its simulated cross-over ratio which is best fit to a $0.78\ \mu\text{m}$ coupling gap, in good agreement with the designed $0.80\ \mu\text{m}$ coupling gap. This result suggests that the effective increase in simulated coupling gap for the TeO_2 - Si_3N_4 waveguides is likely a result of the TeO_2 processing, such as the TeO_2 slab thickness being slightly reduced between the waveguides due to a shadowing effect during sputtering.

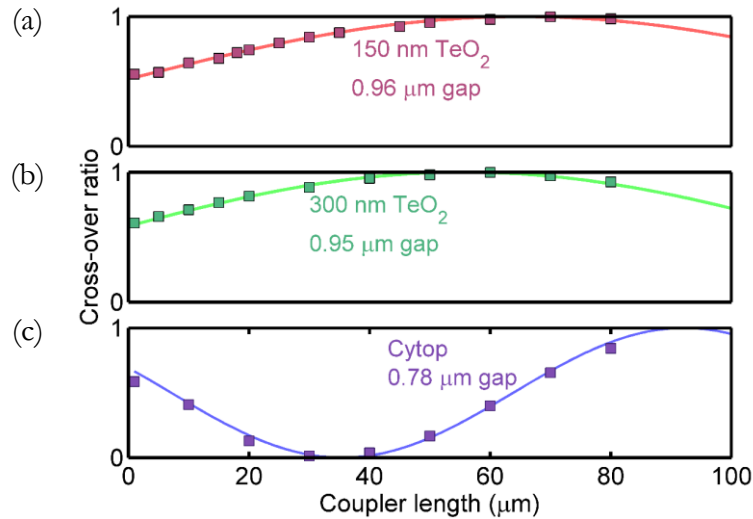


Fig. 3.24. Measured directional coupler cross-over ratio for $1\text{-}\mu\text{m}$ -wide Si_3N_4 strips with a $0.8\ \mu\text{m}$ nominal coupling gap at a $1570\ \text{nm}$ wavelength with (a) a 150-nm -thick TeO_2 -coating, (b) a 300-nm -thick TeO_2 -coating and (c) a Cytop cladding with no TeO_2 -coating, which are best fit to simulated coupling gaps of 0.96 , 0.95 , and $0.78\ \mu\text{m}$, respectively.

An understanding of the coupling characteristics of TeO_2 - Si_3N_4 waveguides is an important step to be able to appropriately design directional couplers for use in power splitters and wavelength multiplexing devices. Precise control of the cross-over ratios can also be used to design several interferometric devices of interest, such as the high- Q -factor microring resonators demonstrated in the following section.

3.4.4. High Q Microring Resonators

An important integrated photonic device that can be designed using the directional couplers developed in the previous section is the microring resonator. Microring resonators are used in applications ranging from light switching and filtering to resonant feedback cavities for laser oscillators as well as being a tool for characterizing fundamental waveguide properties such as loss. Prior to this work, tellurite glass microring resonators had not been investigated. Developing microring resonators on the tellurite glass platform is an important step to realizing passive, active and nonlinear optical devices of interest such as nonlinear Kerr comb generation and rare earth doped laser oscillators. In this section we investigate the theory, design, fabrication and characterization of TeO_2 microring resonators on a low-loss silicon nitride platform.

In the previous section the directional coupler was analyzed in the power domain because the optical power was the measured property of the device. However, to properly describe an interferometric device such as a microring resonator, the phase relationship between waves becomes important and the device must be modelled in the electric field domain. In general, the power of a wave is proportional to the square amplitude of its field. By applying this relationship to the cross-over ratio (κ) described earlier in equation 3.7, it can be redefined as follows:

$$\kappa = \frac{P_{\text{Drop}}}{P_0} = \frac{|E_k|^2}{|E_0|^2}, \quad (3.23)$$

where $|E_0|$ is the initially launched magnitude of the electric field and $|E_k|$ is the magnitude of the electric field that has crossed-over into the drop waveguide. The relationship between the two electric fields can then be described by the cross-over coefficient, k , as follows:

$$k = \frac{|E_k|}{|E_0|} = \sqrt{\kappa}, \quad (3.24)$$

while a similar equation relating the initially launched electric field to the magnitude of the electric field that remains in the initial waveguide ($|E_t|$) to the transmission ratio (β) can be developed. This relationship is described by the transmission coefficient (t) as follows:

$$t = \frac{|E_t|}{|E_0|} = \sqrt{\beta} = \sqrt{1 - \kappa}. \quad (3.25)$$

It is important to note that the transmission and cross-over coefficients refer only to the ratio of the magnitudes of the transmitted and coupled electric fields to that of the incident electric field. As shown in Fig. 3.19, the antisymmetric mode of the combined eigenmode system has a negative electric field in the drop waveguide. Through the linear combination of the symmetric and antisymmetric supermodes this results in an effective half π phase difference between the light propagating in the drop waveguide compared to the thru waveguide. Mathematically the dropped and passed electric field through a directional coupler can then be expressed as a function of the incident electric field by:

$$E_k = ik \cdot E_0, \quad (3.26)$$

$$E_t = t \cdot E_0. \quad (3.27)$$

Having developed the electric-field equations for the directional coupler, this can now be used as the starting point for the microring resonator design. Similar to the directional coupler shown in Fig. 3.21, Ports I and III, define the thru port of the microring resonator and remain routed away from the device towards fiber-chip edge couplers. However, the drop waveguide now routes Port IV of the coupler back to be connected to Port II, such that the dropped

electric field is fed back into the directional coupler, as shown in the diagram of Fig. 3.25. This light can either recirculate around the ring, or couple out of and transmit past the resonator. The waveguide defining Ports I and III of the system is now referred to as the bus waveguide, while the waveguide defining Ports II and IV is now referred to as the microring resonator.

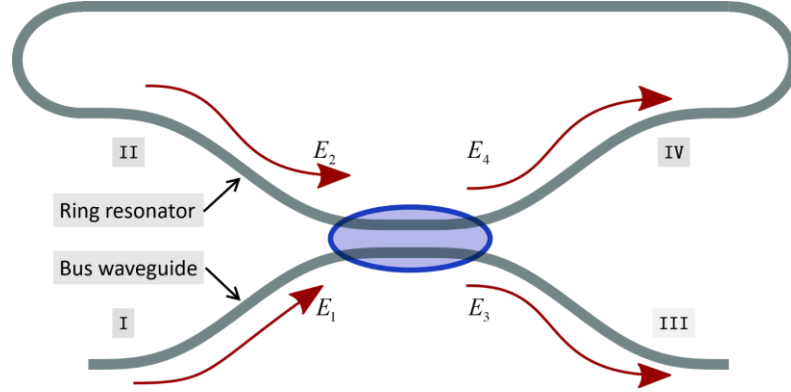


Fig. 3.25. Diagram of a microring resonator. Incident light from Port I of the bus waveguide that is coupled into the ring resonator through Port IV returns via Port II, creating an interference pattern in the transmitted signal power in Port III.

The electric-field that transmits past the ring and out of the system (E_3), as well as the electric-field at the beginning of the ring (E_4), can be determined at steady state by the initially incident electric-field from the bus waveguide (E_1) and the electric-field that has circled around the ring and returned to the coupler (E_2), using the transmission and cross-over coefficients describing the coupler as follows:

$$E_3 = (t \cdot E_1) + (ik \cdot E_2) , \quad (3.28)$$

$$E_4 = (ik \cdot E_1) + (t \cdot E_2) . \quad (3.29)$$

The electric-field that circles the ring and returns to the coupler results from the electric-field at the beginning of the ring, after travelling along the path from Port IV to II. Along this path the electric-field will experience a phase shift (ϕ) based on the length of the ring and group index of light. The electric-field will also experience some attenuation as a result of the waveguides intrinsic loss. For a waveguide propagation loss of A (in dB/cm) the amplitude attenuation coefficient (η), relating the ratio of the recirculated electric field to the initial electric field can be described as follows:

$$\eta^2 = e^{-\frac{A}{10 \log_{10}(e)} \cdot l_{\text{Ring}}} . \quad (3.30)$$

where l_{Ring} is the round trip length of the resonator. The electric field returning to the coupler from Port II can then be described based on the initial field at the beginning of the ring by:

$$E_2 = \eta E_4 e^{i\phi} . \quad (3.31)$$

Using this relationship, the system of equations given by Equations 3.28 and 3.29 can be simplified. The electric-field transmitting past the ring and the electric-field at the beginning of the ring can then be found relative to the initially incident electric field, respectively, as:

$$\frac{E_3}{E_1} = \frac{t - \eta e^{i\phi}}{1 - t\eta e^{i\phi}}, \quad (3.32)$$

$$\frac{E_4}{E_1} = \frac{ik}{1 - t\eta e^{i\phi}}. \quad (3.33)$$

By taking the squared amplitudes of Equations 3.32 and 3.33, the ratios of power that transmits across the ring (T_{Ring}), and power that is built up in the ring (B_{Ring}) relative to the initially incident power can be found as follows:

$$T_{\text{Ring}} = \frac{P_3}{P_1} = \frac{|E_3|^2}{|E_1|^2}, \quad (3.34)$$

$$B_{\text{Ring}} = \frac{P_4}{P_1} = \frac{|E_4|^2}{|E_1|^2}. \quad (3.35)$$

The transmitted and built-up power ratios are then a function of the coupler transmission coefficient, the propagation loss of the waveguide, and the phase shift experienced around the ring. Over a small wavelength range the transmission coefficient and propagation loss can be considered relatively constant. The transmitted and built-up power ratios are then primarily a function of the phase shift experienced around the ring, which can vary rapidly over a short wavelength range, especially for cavities with a long optical path length. As an example, the ring build and ring transmission ratios versus phase shift are calculated based on Equations 3.34 and 3.35 for a given amplitude attenuation coefficient and three different coupler transmission coefficients, with results shown in Fig. 3.26.

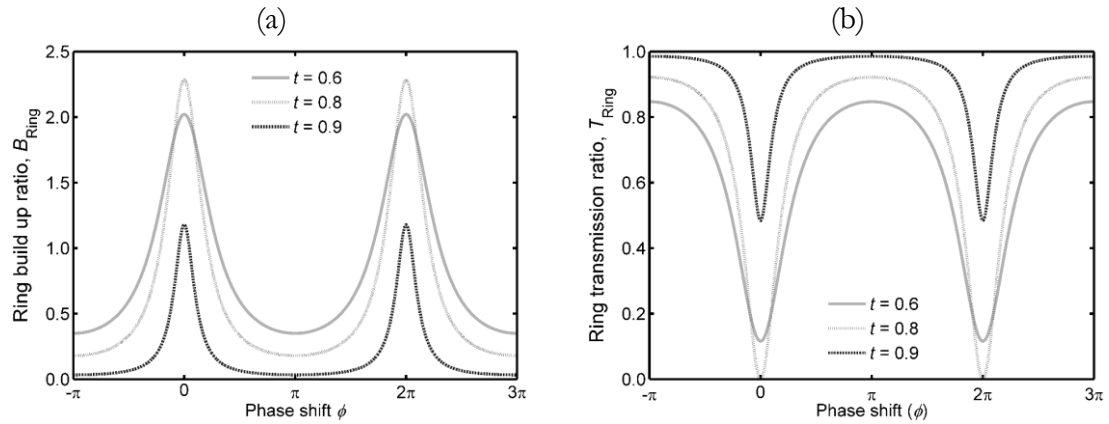


Fig. 3.26. Simulated (a) ring build up (B_{Ring}) and (b) ring transmission (T_{Ring}) ratios for a ring resonator versus the phase shift around the ring, for an amplitude attenuation coefficient of $\eta = 0.75$, and coupler transmission coefficients of $t = 0.6, 0.8$ and 0.9 .

The results show that as the phase shift approaches an integer multiple of 2π , the optical intensity within the ring builds up (Fig. 3.26(a)) due to the constructive interference between the light returning around the ring and the light entering from the bus waveguide. As the intensity of the light builds up within the ring, the light returning around the ring that couples out will destructively interfere with the light transmitting across the bus waveguide, resulting in extinguishing the transmitted power (Fig. 3.26(b)). The relationship between the amplitude attenuation coefficient and the coupler transmission coefficient will then affect the level of constructive/destructive interference which determines the magnitude of the peak/dip of the ring build-up and transmission ratios. This can be seen in Fig. 3.26 by the different curves for the various coupler transmission coefficients simulated. For resonant systems it is often convenient to quantify the response of a device in terms of the quality factor (Q factor), which describes the rate of energy build up and dissipation near the resonance frequency/wavelength. From the general equation for the temporal response of a resonator [46,51], a description of the ring transmission ratio versus wavelength (λ) in terms of the Q factors can be developed, as shown below in Equation 3.36:

$$T_{\text{Ring}} = \frac{\left| 2i \frac{\lambda_0 - \lambda}{\lambda} + \frac{1}{Q_i} - \frac{1}{Q_c} \right|^2}{\left| 2i \frac{\lambda_0 - \lambda}{\lambda} + \frac{1}{Q_i} + \frac{1}{Q_c} \right|^2}, \quad (3.36)$$

where λ_0 is the resonance wavelength of the ring that results in a 2π phase shift. Two Q factor terms are used, the intrinsic Q factor (Q_i) which describes energy dissipation as a result of propagation loss in the ring resonator and the external Q factor (Q_c) which describes the energy dissipation due to coupling from the ring into the bus waveguide. The Q factors can be related to the previously discussed terms describing the steady state response of the microring system by the following two equations:

$$Q_i = \frac{2\pi n_g \cdot 10 \log_{10}(e)}{\lambda_0 A} \quad (3.37)$$

$$Q_c = \frac{2\pi c}{\lambda_0 k} \quad (3.38)$$

where n_g is the group index of light, and c is the speed of light. The combined effect of the two Q factors on the transmission relationship can be described by the loaded Q factor (Q_L) as follows:

$$\frac{1}{Q_L} = \frac{1}{Q_i} + \frac{1}{Q_c}. \quad (3.39)$$

Experimentally, microring resonators were fabricated based on chip design C. We used a straightforward point-coupled microring resonator design. In such a design, the ring is

patterned into a circle, while a straight bus waveguide approaches the ring to a point where it is separated from the ring by a minimum coupling gap (G) between the interior walls of the Si_3N_4 strips and continues straight on afterwards. A diagram of the ring layout can be seen in Fig. 3.27(a). Although there is no straight coupling length, the transfer of light that occurs as the ring and bus waveguides narrow to the minimum coupler gap is enough to allow sufficient transfer of power, as seen in the previous subsection. The strength of the bus to ring transmission coefficient can then be varied by adjusting the minimum coupling gap. A top-view SEM image of a fabricated device can be seen in Fig. 3.27(b), and a close up of the bus and ring waveguide near the coupling point is shown in Fig. 3.27(c).

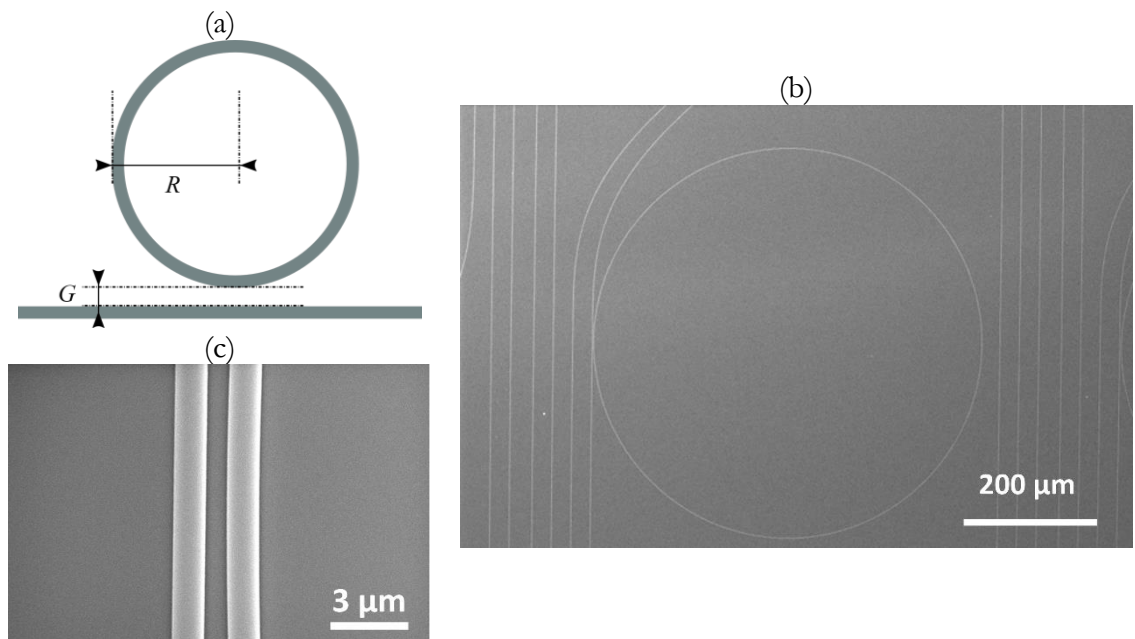


Fig. 3.27. (a) Diagram of a microring resonator showing the radius R and coupling gap G , and top view SEM images of (b) a $\text{TeO}_2\text{-Si}_3\text{N}_4$ ring resonator and (c) the bus waveguide to ring coupling section.

Initial microring resonator measurements were undertaken on a chip coated in a 330-nm-thick TeO_2 film. The rings were characterized by testing the relative transmission of light at wavelengths from 1510 to 1640 nm. An example spectrum for a 1- μm -wide Si_3N_4 ring with a radius of 300 μm and nominal coupling gap of 1.5 μm is shown in Fig. 3.28(a), with a close up from 1620 – 1622 nm shown in Fig. 3.28(b). The data shows narrow resonances with a regular spacing corresponding to a single resonant mode.

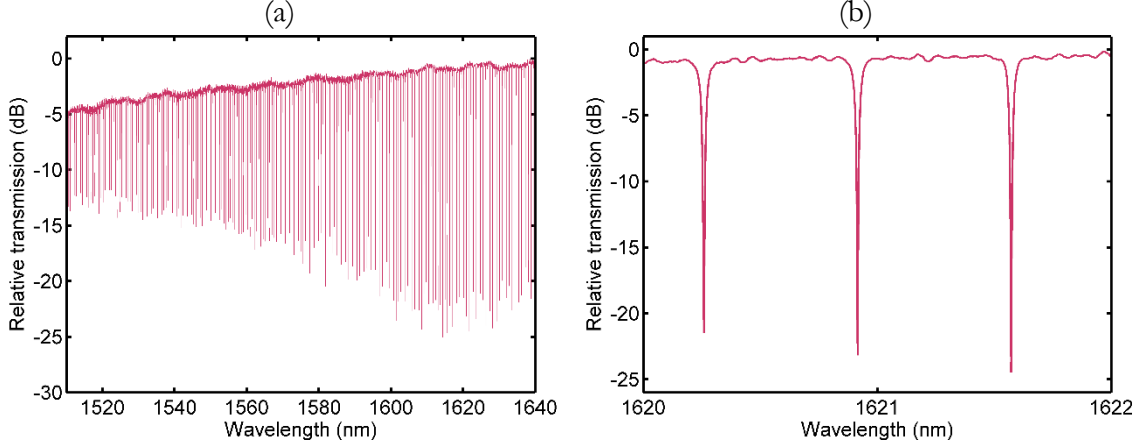


Fig. 3.28. Measured resonance spectrum of a $\text{TeO}_2\text{-Si}_3\text{N}_4$ ring resonator (a) from 1510–1640 nm and (b) over a shorter wavelength range from 1620–1622 nm.

The resonance dips occur at wavelengths that experience a 2π phase shift around the device. The phase shift is related to wavelength and the optical path length around the ring by Equation 3.40 below:

$$\phi = \frac{2\pi \cdot n_g \cdot l_{\text{Ring}}}{\lambda}, \quad (3.40)$$

where l_{Ring} is the path length, equal to $2\pi R$ for a ring of radius R . Experimentally it is more convenient to discuss the wavelength spacing between resonances, known as the free spectral range (FSR), rather than phase shifts. From Equation 3.40 the FSR ($\Delta\lambda$) between adjacent resonances can be found by:

$$\Delta\lambda = \frac{\lambda_1 \lambda_2}{2\pi R \cdot n_g} \cong \frac{\lambda_0^2}{2\pi R \cdot n_g}, \quad (3.41)$$

where λ_1 and λ_2 are the two resonance wavelengths of interest. For most cases, where the difference in wavelengths is small this can be simplified to the average between the two wavelengths (λ_0). The chip coated in a 330-nm-thick TeO_2 film was found to have an FSR of 0.57 nm at a wavelength of 1510 nm, continually increasing to an FSR of 0.67 nm at 1640. With the FSR found by the spectral measurement, and the radius of the ring known by the mask design, the FSR can be used to experimentally determine the group index of the waveguide, which is important for determining the temporal broadening of non-purely monochromatic signals in a waveguide. The group index (n_g) of light in a waveguide is related to the effective index (n_{Eff}) and its wavelength dispersion by Equation 3.42:

$$n_g = n_{\text{Eff}} + \lambda \left(\frac{dn_{\text{Eff}}}{d\lambda} \right), \quad (3.42)$$

The effective index of the waveguide and its dispersion relationship can be calculated using an eigenmode simulation at different wavelengths. Here, the effective index of the resonator waveguide with a 330-nm-thick TeO₂-coating was found versus wavelength using RSoft eigenmode simulations, which were used to calculate the group index by Equation 3.40 with the results shown in Fig. 3.29(a). The simulated group index shows agreement to the experimentally measured group index based on the FSR, within a $\pm 2\%$ difference in the simulated TeO₂ material refractive index, as shown in Fig. 3.29(b).

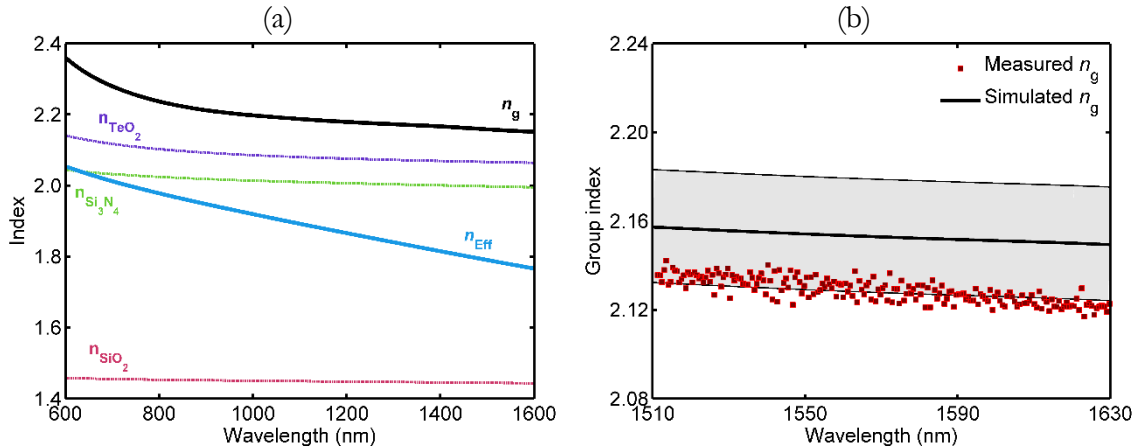


Fig. 3.29. (a) TeO₂, Si₃N₄ and SiO₂ material dispersion relations from 600 to 1600 nm used to simulate the effective index, n_{Eff} , of a TeO₂-Si₃N₄ waveguide with Si₃N₄ strip dimensions of 1.0 $\mu\text{m} \times 0.2 \mu\text{m}$ and TeO₂-coating thickness of 330 nm, which is then used to calculate the group index, n_g . (b) Comparison of the group index calculated based on simulation, with error bars based on a ± 0.03 difference in TeO₂ refractive index, to the measured group index based on the microring resonator FSR.

From Fig. 3.28(a) it can be seen that resonances near 1620 nm reach a peak extinction ratio of approximately 25 dB, with smaller extinction ratios at longer and shorter wavelengths. Based on the results seen when characterizing directional couplers in the previous section, weaker coupling coefficients can be expected at shorter wavelengths, while stronger coupling occurs at longer wavelengths. This results in shorter wavelengths having greater coupling Q factors (i.e., lower coupling loss in the microring resonator), while longer wavelengths have larger coupling Q factors (i.e., higher coupling loss). As shown in Equations 3.36 the relationship between the coupling and internal Q factors determines the shape of the resonance spectrum. In general, the resonance condition can be considered in one of three regimes:

- **Overcoupled ($Q_c < Q_i$)**, where the coupling Q factor is less than the intrinsic Q factor, such that the predominant loss mechanism in the ring is through coupling into the bus waveguide. The more strongly overcoupled the ring is, the lower the loaded Q factor will become and the smaller the extinction ratio of the resonance.

- **Critically coupled ($Q_c \approx Q_i$)**, where the coupling Q factor is approximately equal to the intrinsic Q factor. Critically coupled rings will experience large extinction ratios, and a loaded Q of half the intrinsic value based on Equation 3.24.
- **Undercoupled ($Q_c > Q_i$)**, where the coupling Q factor is greater than the intrinsic Q factor, such that the predominant loss mechanism is through optical propagation loss in the ring. The more strongly undercoupled the ring is the greater the loaded Q factor will become and the smaller the extinction ratio of the resonance.

From Fig. 3.28(a) the resonances near 1620 nm are considered critically coupled, while the resonances at shorter wavelengths are undercoupled and longer wavelengths are overcoupled. Besides adjusting the wavelength, the coupling regime can be controlled by varying the coupling gap between the ring and bus waveguide. The resonance spectra around 1550 nm were measured for the 300 μm rings at different coupling gaps, where for each ring the tunable laser was swept from 1550 to 1560 nm in steps of 0.1 μm . A peak finding algorithm was used to locate the resonances of each device and determine their extinction ratio. The transmission equation described in Equation 3.36 was then fit to the resonance, using the MATLAB code provided in Appendix B to determine the internal and external Q factor that best fits the measured data. However, by only considering the fit, the values determined for the internal and external Q factors are interchangeable. Therefore, it is important to understand the coupling regime the device is in to properly assign the fitted Q factor values to their appropriate source. The coupling regime can be determined by measuring the loaded Q factors of devices at different gaps and wavelengths. We expect stronger coupling coefficients at smaller coupling gaps and at longer wavelengths, as was demonstrated in the directional coupler results of the previous section. This means the external Q factor should be expected to increase with gap. The internal Q factor is determined by the propagation loss of the waveguide, which in the absence of major defects between devices should be approximately equal between all rings at different gaps.

In Fig. 3.30 we see the measured resonance data and loaded Q factors found by fitting three rings at different coupling gaps. At a gap of 0.9 μm the resonance is seen to have an extinction ratio of 6.2 dB and is fit with a loaded Q factor of 1.6×10^5 . At a gap of 1.3 μm the resonance linewidth narrows slightly, is seen to have a large increase in extinction ratio up to almost 25 dB and is fit with a loaded Q factor of 2.8×10^5 . This extinction ratio corresponds to only 0.3% of incident light transmitted past the resonator, placing this gap very near the critical coupling regime. Increasing the coupling gap further to 2.0 μm is seen to produce a resonance with both a narrower linewidth, and smaller extinction ratio of only approximately 2 dB. From the inset of Fig. 3.30, which shows a zoomed-in view of this resonance, it can be seen that the resonance actually has two nearby peaks. This is a phenomenon known as resonance splitting, whereby the backwards propagating mode of the resonator, excited by some back-scattered light travelling through the ring builds up enough power to affect the

resonance spectrum of the transmitted light. This resonance mode was fit with a slightly altered version of Equation 3.36, with code also provided in Appendix B, that accounts for resonance splitting, to have a loaded Q factor of 6.3×10^5 . With the gap now increased beyond what was found to be the critical coupling point, the fit gives an internal Q factor of the device of 7.3×10^5 . This corresponds to a waveguide propagation loss of ~ 0.5 dB/cm in the ring by applying Equation 3.37, which is comparable to but slightly lower than the propagation loss measured in waveguides with a thicker TeO_2 film by the cutback method in section 3.4.1.

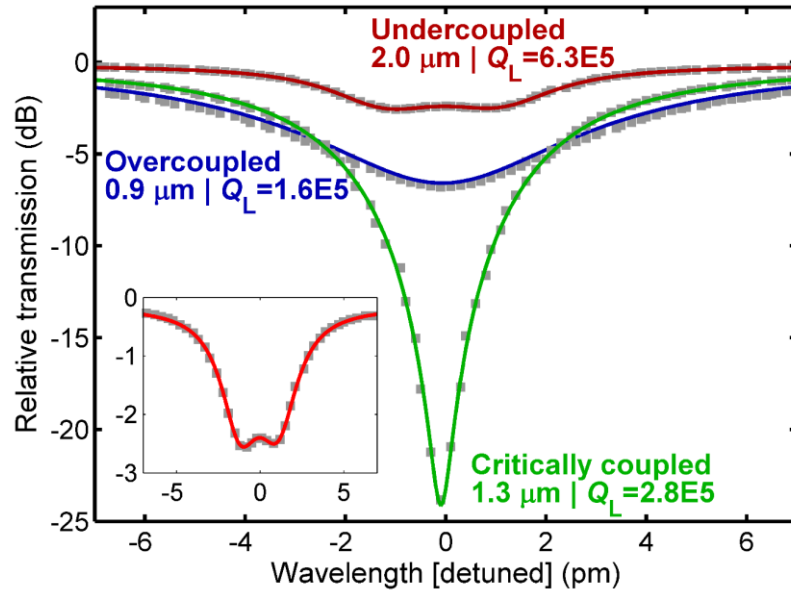


Fig. 3.30. Transmission of 300 μm radius ring resonators with gaps of 0.9, 1.3 and 2.0 μm near 1550 nm wavelengths. The measured data points are fit using the coupled mode theory transmission equation to find loaded Q factors of 1.6×10^5 , 2.8×10^5 and 6.3×10^5 in the overcoupled, critically coupled and undercoupled regimes, respectively. The inset shows a close up view of the transmission of the undercoupled resonator.

The loaded Q factor was similarly determined for all the coupling gaps of between 0.7 to 2.0 μm on the chip, and the results are plotted in Fig. 3.31(a). Assuming that the internal Q factor of 7.3×10^5 was constant across all the rings the loaded Q factor was used to determine the external Q factor versus coupling gap. The results show that at small gaps the low external Q factor dominates the loaded Q factor of devices. As the gap increases so too does the external Q factor, which results in an increase in the loaded Q factor until it reaches critical coupling at a coupling gap of approximately 1.4 μm . The loaded Q factor then begins to approach and become limited by the internal Q factor as the gap is increased further. The measured extinction ratio versus coupling gap is plotted similarly in Fig. 3.31(b), and compared to the extinction ratio calculated from Equation 3.36, assuming a constant internal Q factor of 7.3×10^5 and varying the external Q factor based on its relationship with gap which was determined in Fig. 3.31(a). The equation predicts a peak in extinction ratio near the critical coupling point around a gap of 1.4 μm , with sharply decreasing extinction ratios on either side.

The measured extinction ratio follows this general trend with some experimental variation, which likely comes from small intrinsic Q factor variations between the different rings and slight changes in the resonant wavelength measurements are taken at.

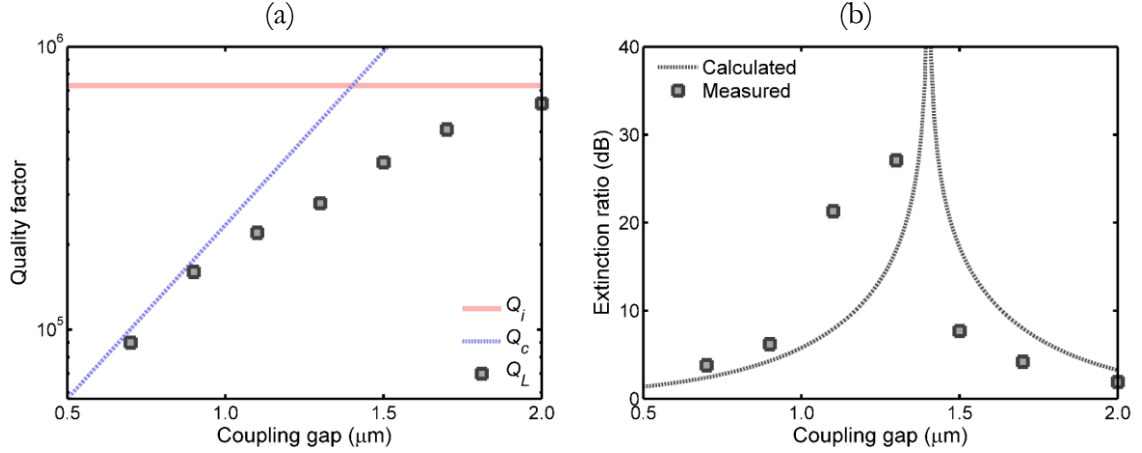


Fig. 3.31. (a) Loaded Q factor measured in rings with different coupling gaps, compared with the fitted maximum internal Q factor (Q_i) of 7.3×10^5 , which is used to calculate the external Q factor (Q_c) at each gap. (b) Measured and calculated extinction ratio of rings at different coupling gaps.

While comparing ring resonator devices with a constant radius of $300 \mu\text{m}$, it has generally been assumed that optical propagation loss is the same between all devices. However, changes to radius can be expected to change the propagation loss of the waveguide through bending radiation losses, especially for devices with small radii. The radiation loss expected for the TeO_2 -coated Si_3N_4 waveguide structure at different bending radii was calculated and then converted to an equivalent radiation-limited internal Q factor versus ring radius (Q_R), assuming that bending radiation is the only source of waveguide loss, using the following equation:

$$Q_R = \frac{n_r}{4\pi \cdot n_i}, \quad (3.43)$$

where n_r and n_i are the real and imaginary parts of the effective waveguide index calculated in the bend mode solver, respectively. The simulated radiation-limited Q factor is shown in Fig. 3.32. The simulation predicts a radiation-limited Q factor of 10^4 at a radius of $80 \mu\text{m}$, that sharply rises to 10^8 at a radius of $160 \mu\text{m}$. When bending loss becomes negligible, the internal Q factor of the resonator becomes limited by the waveguide propagation losses of the device. The simulated radiation losses were then compared to the measured internal Q factor of ring resonators with radii of 100 , 200 , 300 , and $400 \mu\text{m}$, also displayed in Fig. 3.32. The internal Q factors of the 300 and $400 \mu\text{m}$ radius rings were measured to be 7.3×10^5 , indicating that they experience negligible bending loss and are limited by the waveguide propagation loss of 0.5 dB/cm . At a radius of $200 \mu\text{m}$, some additional loss is observed, possibly attributed to the mode shifting radially outward and causing greater scattering at the waveguide sidewall, resulting in a slight decrease in the internal Q factor down to 4.5×10^5 . At a radius of $100 \mu\text{m}$,

the radiation loss becomes the dominant source of loss, and the internal Q factor is seen to drop significantly to 4×10^4 , which is close to the simulated radiation-limited Q factor. These results show that such waveguides can be bent well below a 500 μm radius before introducing significant radiation losses, allowing for the fabrication of compact integrated TeO_2 devices.

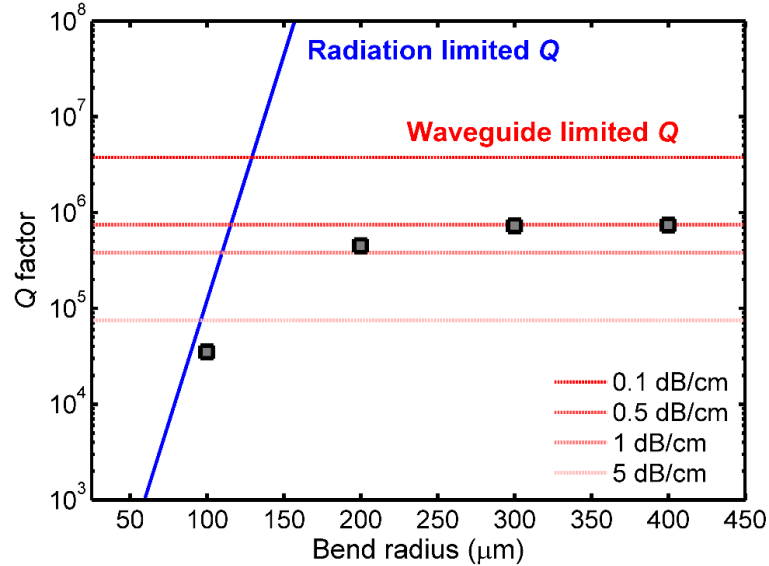


Fig. 3.32. Measured Q factor of 100, 200, 300 and 400 μm radius ring resonators. Radii of 300 μm and above demonstrate little difference in Q factor and are limited by the waveguide loss of 0.5 dB/cm. The 200 μm radius ring experiences a small drop in Q factor, while the 100 μm radius ring is dominated by radiation and experiences a significant drop in Q factor.

Lastly, the effect of waveguide width and TeO_2 -coating thickness on the intrinsic Q factor of rings was studied. Microring resonators were measured with Si_3N_4 strip widths of 0.8, 1.0 and 1.2 μm and a radius of 600 μm , which should eliminate any sources of bending radiation loss for TeO_2 -coatings up to a thickness of ~ 500 nm. The measured Q factors can then be directly related to the waveguide optical propagation loss. Seven different chips were coated in TeO_2 films with thicknesses of between 100 and 500 nm and characterized, and the measured waveguide losses versus waveguide width and TeO_2 -coating thickness are plotted in Fig. 3.33.

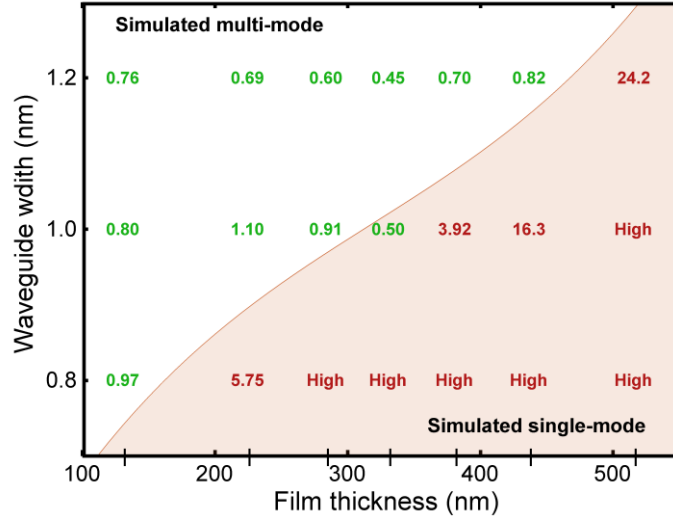


Fig. 3.33. Measured loss in 600 μm radii rings with 0.8, 1.0 and 1.2- μm -wide Si_3N_4 strips coated in tellurium-oxide layers of 130, 224, 283, 330, 380, 436 and 515 nm thickness. The data shows that waveguides with TeO_2 -coatings that are close to or thinner than the simulated single-mode TeO_2 thickness for a given Si_3N_4 strip width can maintain low waveguide losses, while thicker TeO_2 -coatings begin to experience a significant increase in waveguide loss.

The data shows that for a given Si_3N_4 width, once the TeO_2 film thickness exceeds a certain point, the hybrid TeO_2 - Si_3N_4 waveguide propagation loss sharply increases, to the point that transmission across the chip drops and the resonances disappear and cannot be measured. At TeO_2 -coating thicknesses below the cut-off point the waveguide losses remain generally low, near or below 1 dB/cm of waveguide propagation loss for all Si_3N_4 strip widths, with some variation due to differences in TeO_2 film quality from run to run. In general, wider waveguides exhibit slightly lower optical propagation losses, which is consistent with lower scattering loss due to reduced sidewall interaction. It can also be seen that wider waveguides can support thicker TeO_2 -coatings before the waveguide propagation loss rapidly increases. By comparing the data to the simulated single mode Si_3N_4 strip width condition versus TeO_2 film thickness it appears that the high-loss cut-off point occurs once the waveguide transitions from the simulated multi-mode to single-mode condition. Although waveguides on the left side of the line on Fig. 3.33 should be able to support higher order modes based on simulations, no other modes or multimode interference patterns are observed in the resonance spectra. The higher losses observed past the cut-off point can be attributed to radiation of the optical mode into the TeO_2 slab surrounding the waveguide. The greater confinement of the mode provided by the wider Si_3N_4 strip increases the TeO_2 thicknesses required for radiation into the slab. The simulated single-mode cut-off line of Fig. 3.33 also corresponds to the region in which the TeO_2 - Si_3N_4 waveguide fundamental modes have an effective index difference of > 0.04 compared to the simulated TeO_2 slab mode for each respective TeO_2 -coating thickness. This supports the concept that the high losses result from radiation into the slab and the absence of higher order modes in the hybrid waveguide structure. The optimal waveguide

width/coating thickness design for low-loss single-mode devices is such that the fundamental waveguide mode, but no other modes, maintain a high enough effective index to propagate without experiencing radiation into the TeO₂ slab. This provides an important design guideline for future hybrid TeO₂-Si₃N₄ photonic devices.

3.5 Conclusion

In summary this chapter has demonstrated the design, fabrication and experimental characterization of a low-loss TeO₂-coated Si₃N₄ waveguide platform. A series of simulations determined optimal waveguide dimensions, including a 0.2- μm -thick Si₃N₄ layer patterned into approximately 1- μm -wide Si₃N₄ strips and 0.2 to 0.5- μm -thick TeO₂ films, for optical confinement in the TeO₂ layer of > 50 % and minimum bend radii of < 0.5 mm. Experimental characterization of devices demonstrates waveguide losses of down to 0.6 ± 0.2 dB/cm at 2000 nm via the cutback method, and 0.5 dB/cm at a 1550 nm wavelength by ring resonator characterization. Waveguide losses of <1 dB/cm were generally observed at infrared wavelengths >1300 nm, but losses were seen to increase at shorter wavelengths due to increased film loss, sidewall scattering and TeO₂ slab radiation. Although fiber-chip coupling losses are found to theoretically be as low 3 dB per facet using tapered fibers, the losses on chips as received from the foundry were on average measured to be greater than 10 dB per facet because of high edge facet roughness. Using FIB polishing, the coupling losses were reduced to 5.4 ± 0.8 dB per facet, which is significantly closer to the theoretical loss. The potential for more advanced integrated photonic circuitry on this platform was demonstrated through the characterization of directional couplers and microring resonators. A series of couplers with were characterized with 100 % cross-over measured at coupler lengths of 80 μm . Close alignment to the cross-over ratio predicted by the eigenmode expansion method was found when a larger effective coupling gap was used in simulations, which provides a guideline for the design of couplers in future. High Q factor tellurite microring resonators, with intrinsic Q factors of up to 7.3×10^5 were realized for ring radii down to 300 μm . These results demonstrate a low-loss hybrid TeO₂-Si₃N₄ waveguide platform which is highly promising for passive, active and nonlinear photonic devices and integrated circuits.

References

- [1] R. A. H. El-Mallawany, *Tellurite Glasses Handbook: Physical Properties and Data*, Second Edition (CRC Press, 2012).
- [2] V. A. G. Rivera and D. Manzani, *Technological Advances in Tellurite Glasses: Properties, Processing, and Applications* (Springer, 2017).
- [3] A. Jha, B. D. O Richards, G. Jose, T. T. Fernandez, C. J. Hill, J. Lousteau, and P. Joshi, "Review on structural, thermal, optical and spectroscopic properties of tellurium oxide based glasses for fibre optic and waveguide applications," *Int. Mater. Rev.* **57**(6), 357–382 (2012).

- [4] J. S. Wang, E. M. Vogel, and E. Snitzer, “Tellurite glass: a new candidate for fiber devices,” *Opt. Mater.* **3**, 187–203 (1994).
- [5] Y. Ding, S. Jiang, T. Luo, Y. Hu, and N. Peyghambarian, “Optical waveguides prepared in Er^{3+} -doped tellurite glass by Ag^+ - Na^+ ion-exchange,” *Proc. SPIE* **4282**, 23–30 (2001).
- [6] E. Chierici, M. C. Didavide, A. Moro, O. Rossotto, L. Tallone, and E. Monchiero, “Direct writing of channel waveguide on a tellurite glass using a focused ultraviolet laser beam”, in *Proceedings of 2002 IEEE/LEOS Workshop on Fibre and Optical Passive Components (IEEE, 2002)*, 24–28.
- [7] Y. Tokuda, M. Saito, M. Takahashi, K. Yamada, W. Watanabe, K. Itoh, and T. Yoko, “Waveguide formation in niobium tellurite glasses by pico- and femtosecond laser pulses,” *J. Non-Cryst. Solids* **326&327**, 472–475 (2003).
- [8] G. Nunzi Conti, S. Berneschi, M. Bettinelli, M. Brenci, B. Chen, S. Pelli, A. Speghini, and G. C. Righini, “Rare-earth doped tungsten tellurite glasses and waveguides: Fabrication and characterization,” *J. Non-Cryst. Solids* **345&346**, 343–348 (2004).
- [9] P. Nandi, G. Jose, C. Jayakrishnan, S. Debbarma, K. Chalapathi, K. Alti, A. K. Dharmadhikari, J. A. Dharmadhikari, and D. Mathur, “Femtosecond laser written channel waveguides in tellurite glass,” *Opt. Express* **14**(25), 12145–12150 (2006).
- [10] T. T. Fernandez, G. D. Valle, R. Osellame, G. Jose, N. Chiodo, A. Jha, and P. Laporta, “Active waveguides written by femtosecond laser irradiation in an erbium-doped phospho-tellurite glass,” *Opt. Express* **16**(19), 15198–15205 (2008).
- [11] R. Nayak, V. Gupta, A. L. Dawar, and K. Sreenivas, “Optical waveguiding in amorphous tellurium oxide thin films,” *Thin Solid Films* **445**(1), 118–126 (2003).
- [12] S. M. Pietralunga, M. Lanata, M. Ferè, D. Piccinin, G. Cusmai, M. Torregiani, and M. Martinelli, “High-contrast waveguides in sputtered pure TeO_2 glass thin films,” *Opt. Express* **16**(26), 21662–21670 (2008).
- [13] S. J. Madden and K. T. Vu, “Very low loss reactively ion etched tellurium dioxide planar rib waveguides for linear and nonlinear optics,” *Opt. Express* **17**(20), 17645–17651 (2009).
- [14] K. T. Vu and S. J. Madden, “Reactive ion etching of tellurite and chalcogenide waveguides using hydrogen, methane, and argon,” *J. Vac. Sci. Technol. A* **29**(1), 011023 (2011).
- [15] K. T. Vu and S. J. Madden, “Tellurium dioxide erbium doped planar rib waveguide amplifiers with net gain and 2.8dB/cm internal gain,” *Opt. Express* **18**(18), 19192–19200 (2010).

- [16] K. T. Vu, S. Farahani, and S. J. Madden, "980nm pumped erbium doped tellurium oxide planar rib waveguide laser and amplifier with gain in S, C and L band," *Opt. Express* **23**(2), 747–755 (2015).
- [17] K. Vu, K. Yan, Z. Jin, X. Gai, D.Y. Choi, S. Debbarma, B. Luther-Davies and S. J. Madden, "Hybrid waveguide from As_2S_3 and Er-doped TeO_2 for lossless nonlinear optics," *Optics letters* **38**(11), 1766–1768 (2013).
- [18] K. Wörhoff, R. G. Heideman, A. Leinse, and M. Hoekman, "TriPleX: A versatile dielectric photonic platform," *Adv. Opt. Technol.* **4**(2), 189–207 (2015).
- [19] C. G. H. Roeloffzen, M. Hoekman, E. J. Klein, L. S. Wevers, R. B. Timens, D. Marchenko, D. Geskus, R. Dekker, A. Alippi, R. Grootjans, A. van Rees, R. M. Oldenbeuving, J. P. Epping, R. G. Heideman, K. Wörhoff, A. Leinse, D. Geuzebroek, E. Schreuder, P. W. L. van Dijk, I. Visscher, C. Taddei, Y. Fan, C. Taballione, and Y. Liu, D. Marpaung, L. Zhuang, M. Benelajla and K. Boller, "Low Loss Si_3N_4 TriPleX optical waveguides: technology and applications overview," *IEEE J. Sel. Top. Quantum Electron.* **24**(4), 1–21 (2018).
- [20] D. J. Blumenthal, R. Heideman, D. Geuzebroek, A. Leinse, and C. Roeloffzen, "Silicon nitride in silicon photonics," *Proc. IEEE* **106**(12), 2209–2231 (2018).
- [21] J. F. Bauters, M. J. R. Heck, D. John, D. Dai, M.-C. Tien, J. S. Barton, A. Leinse, R. G. Heideman, D. J. Blumenthal, and J. E. Bowers, "Ultra-low-loss high-aspect-ratio Si_3N_4 waveguides," *Opt. Express* **19**(4), 3163–3174 (2011).
- [22] J. F. Bauters, M. J. R. Heck, D. D. John, J. S. Barton, C. M. Bruinink, A. Leinse, R. G. Heideman, D. J. Blumenthal, and J. E. Bowers, "Planar waveguides with less than 0.1 dB/m propagation loss fabricated with wafer bonding," *Opt. Express* **19**(24), 24090–24101 (2011).
- [23] W. D. Sacher, J. C. Mikkelsen, Y. Huang, J. C. Mak, Z. Yong, X. Luo, Y. Li, P. Dumais, J. Jiang, D. Goodwill, E. Bernier, P. G. Q. Lo, and J. K. S. Poon, "Monolithically integrated multilayer silicon nitride-on-silicon waveguide platforms for 3-D photonic circuits and devices," *Proc. IEEE*, **106**(12), 2232–2245 (2018).
- [24] E. Timurdogan, Z. Su, C. V. Poulton, M. J. Byrd, S. Xin, R. J. Shiue, B. R. Moss, E. S. Hosseini, and M. R. Watts, "AIM process design kit (AIMPDKv2. 0): Silicon photonics passive and active component libraries on a 300mm wafer," *Optical Fiber Communications Conference and Exposition*, 1–3 (2018).
- [25] J. Notaros, N. Li, C. V. Poulton, Z. Su, M. J. Byrd, E. S. Magden, E. Timurdogan, C. Baiocco, N. M. Fahrenkopf, and M. R. Watts, "CMOS-compatible optical phased array powered by a monolithically-integrated erbium laser," *J. Light. Technol.* **37**(24), 5982–5987 (2019).

- [26] N. Li, M. Xin, Z. Su, E. S. Magden, N. Singh, J. Notaros, E. Timurdogan, P. Purnawirman, J. D. B. Bradley, and M. R. Watts, “A silicon photonic data link with a monolithic erbium-doped laser,” *Sci. Rep.* **10**(1), 1–9 (2020).
- [27] A. Fernández Gavela, D. Grajales García, J. Ramirez, and L. Lechuga, “Last advances in silicon-based optical biosensors,” *Sensors* **16**(3), 285 (2016).
- [28] C. V. Poulton, M. J. Byrd, P. Russo, E. Timurdogan, M. Khandaker, D. Vermeulen, and M. R. Watts, “Long-range LiDAR and free-space data communication with high-performance optical phased arrays,” *IEEE J. Sel. Top. Quantum Electron.* **25**(5), 1–8 (2019).
- [29] T. Kim, P. Bhargava, C. V. Poulton, J. Notaros, A. Yaacobi, E. Timurdogan, C. Baiocco, N. Fahrenkopf, S. Kruger, T. Ngai, Y. Timalcina, M. R. Watts, and V. Stojanović, “A single-chip optical phased array in a wafer-scale silicon photonics/CMOS 3D-integration platform,” *IEEE J. Solid-State Circuits* **54**(11), 3061–3074 (2019).
- [30] R. M. De Ridder, K. Warhoff, A. Driessen, P. V. Lambeck, and H. Albers, “Silicon oxynitride planar waveguiding structures for application in optical communication,” *IEEE J. Sel. Top. Quantum Electron.* **4**(6), 930–937 (1998).
- [31] C. G. Roeloffzen, L. Zhuang, C. Taddei, A. Leinse, R. G. Heideman, P. W. van Dijk, R. M. Oldenbeuving, D. A. Marpaung, M. Burla, and K. J. Boller, “Silicon nitride microwave photonic circuits,” *Opt. Express* **21**(19), 22937–22961 (2013).
- [32] F. Morichetti, A. Melloni, M. Martinelli, R. G. Heideman, A. Leinse, D. H. Geuzebroek, and A. Borreman, “Box-shaped dielectric waveguides: A new concept in integrated optics?,” *J. Light Technol.* **25**(9) 2579–2589 (2007).
- [33] D. Marpaung, C. Roeloffzen, A. Leinse, and M. Hoekman, “Photonic chip based frequency discriminator for a high performance microwave photonic link,” *Opt. Express* **18**(26) 27359–27370 (2010).
- [34] L. Zhuang, D. Marpaung, M. Burla, W. Beeker, A. Leinse, and C. Roeloffzen, “Low-loss, high-index-contrast $\text{Si}_3\text{N}_4/\text{SiO}_2$ optical waveguides for optical delay lines in microwave photonics signal processing,” *Opt. Express* **19**(23), 23162–23170 (2011).
- [35] K. Luke, Y. Okawachi, M. R. E. Lamont, A. L. Gaeta, and M. Lipson, “Broadband mid-infrared frequency comb generation in a Si_3N_4 microresonator,” *Opt. Lett.* **40**(21) 4823–4826 (2015).
- [36] I. H. Malitson, “Interspecimen comparison of the refractive index of fused silica,” *JOSA* **55**(10), 1205–1209 (1965).
- [37] X. Xu, S. Chen, J. Yu, and X. Tu, “An investigation of the mode characteristics of SOI submicron rib waveguides using the film mode matching method,” *J. Opt. A-Pure Appl. Opt.* **11**(1), 015508 (2008).

- [38] H. M. Mbonde, H. C. Frankis, and J. D. B. Bradley, “Enhanced Nonlinearity and Engineered Anomalous Dispersion in TeO₂-coated Si₃N₄ Waveguides,” *IEEE Photonics J.* **12**(2), 1–10 (2020).
- [39] Q. Lin, O. J. Painter, and G. P. Agrawal, “Nonlinear optical phenomena in silicon waveguides: modeling and applications,” *Opt. Express.* **15**(25), 16604–16644 (2007).
- [40] L. Agazzi, K. Worhoff, and M. Pollnau, “Energy-transfer-upconversion models, their applicability and breakdown in the presence of spectroscopically distinct ion classes: A case study in amorphous Al₂O₃: Er³⁺,” *J. Phys. Chem. C* **117**(13), 6759–6776 (2013).
- [41] I. D. Rukhlenko, M. Premaratne, and G. P. Agrawal, “Effective mode area and its optimization in silicon-nanocrystal waveguides,” *Opt. Lett.* **37**(12), 2295–2297 (2012).
- [42] J. P. Epping, M. Hoekman, R. Mateman, A. Leinse, R. G. Heideman, A. van Rees, P. J. M. van der Slot, C. J. Lee, and K. J. Boller, “High confinement, high yield Si₃N₄ waveguides for nonlinear optical applications,” *Opt. Express* **23**(2), 642–648 (2015).
- [43] P. K. Tien, “Light waves in thin films and integrated optics,” *Appl. Opt.* **10**(11), 2395–2413 (1971).
- [44] Z. Lu, H. Yun, Y. Wang, Z. Chen, F. Zhang, N. A. Jaeger, and L. Chrostowski, “Broadband silicon photonic directional coupler using asymmetric-waveguide based phase control,” *Opt. Express* **23**(3), 3795–3808 (2015).
- [45] K. Jingui, “Mach-zehnder interferometer type optical waveguide coupler with wavelength-flattened coupling ratio,” *Electron. Lett.* **26**(17), 1326–1327 (1990).
- [46] B. E. Little, S. T. Chu, H. A. Haus, J. A. Foresi, and J. P. Laine, “Microring resonator channel dropping filters,” *J. Light. Technol.* **15**(6), 998–1005 (1997).
- [47] Y. Zhang, S. Yang, H. Guan, A. E. Lim, G. Q. Lo, P. Magill, T. Baehr-Jones, and M. Hochberg, “Sagnac loop mirror and micro-ring based laser cavity for silicon-on-insulator,” *Opt. Express* **22**(15), 17872–17879 (2014).
- [48] A. Yariv, “Coupled-mode theory for guided-wave optics,” *IEEE J. Quantum Electron.* **9**(9), 919–933 (1973).
- [49] L. Chrostowski and M. Hochberg, *Silicon photonics design: from devices to systems* (Cambridge University, 2015).
- [50] A. Yariv and P. Yeh, *Optical electronics in modern communications* (Oxford University, 2006).
- [51] M. Soltani, *Novel integrated silicon nanophotonic structures using ultra-high Q resonators* (Doctoral dissertation, Georgia Institute of Technology).

CHAPTER 4

Erbium-Doped Tellurium Oxide Coated Silicon Nitride Waveguide Amplifiers

This chapter investigates the theory, design, fabrication and characterization of erbium-doped tellurium oxide ($\text{TeO}_2:\text{Er}^{3+}$) coated silicon nitride (Si_3N_4) waveguide amplifiers. The absorption and emission cross sections, propagation loss, excited state luminescent lifetime and ion quenching fraction were characterized on a set of samples with measured erbium dopant concentrations of between 0.6 and 2.8×10^{20} ions/ cm^3 . Similar wideband emission spectra and Er^{3+} ${}^4\text{I}_{15/2} \leftrightarrow {}^4\text{I}_{13/2}$ absorption and emission cross sections were observed compared to previous measurements in tellurite glass. Low background waveguide losses comparable to passive $\text{TeO}_2\text{-Si}_3\text{N}_4$ waveguides were observed in $\text{TeO}_2:\text{Er}^{3+}$ waveguides. The average luminescent lifetime of the ${}^4\text{I}_{13/2}$ state was found to be 0.20 ± 0.08 ms, with a minimum value of 0.09 ms and maximum value of 0.31 ms at Er^{3+} concentrations of 2.8 and 0.9×10^{20} ions/ cm^3 , respectively, and a correlation of shorter lifetimes with respect to increased concentrations was observed. The measured luminescent lifetimes were found to be significantly shorter than the expected 4.5 -ms radiative lifetime from Fuchtbauer-Ladenburg theory, suggesting that OH^- impurities are the predominant decay mechanism as has been observed in other $\text{TeO}_2:\text{Er}^{3+}$ platforms. The concentration of fast-quenched erbium ions in the samples was characterized using absorption saturation measurements at 1530 nm wavelength, and the quenching ratios were seen to vary from 14% to as high as 54% for erbium dopant concentrations of 0.9×10^{20} and 2.8×10^{20} ions/ cm^3 , respectively. To attempt to reduce OH^- impurities a $\text{TeO}_2:\text{Er}^{3+}$ sample was deposited at a moderately higher temperature of 140 °C. It was found to have a concentration of 2.2×10^{20} ions/ cm^3 , and a ${}^4\text{I}_{13/2}$ luminescent lifetime of 0.48 ms and quenching ratio of only 22% , which are significantly greater and less than the lifetimes and quenching ratios, respectively, measured in the lower-temperature samples. Due to this higher-temperature sample's promising spectroscopic properties, as well as its ultra-low background optical propagation losses of 0.25 dB/cm, as measured by a ring resonator with a Q factor of 1.3×10^6 at a 1637 nm, it was selected for detailed gain measurements. In a 2.2 -cm-long waveguide, peak internal net gain per unit length of 1.7 and 1.4 dB/cm at a signal wavelength of 1533 nm was observed for 970 and 1470 nm pump wavelengths, respectively. In a 6.7 -cm-long paperclip waveguide, total peak internal net gain of 1.1 and 5.0 dB was measured at a signal wavelength of 1558 nm for 970 and 1470 nm pump wavelengths, respectively, with the total gain limited by unoptimized fiber-chip coupling efficiency and the maximum pump power of ~ 40 mW launched onto the chip. To investigate the prospective performance of $\text{TeO}_2:\text{Er}^{3+}\text{-Si}_3\text{N}_4$ hybrid waveguide amplifiers,

a three-level rate equation model was developed. The model accurately fits the experimental gain results, and predicts that the total gain can reach 8.6 dB, at 1558 nm with improved coupling and 150 mW of 1470 nm pump power launched into the 6.7-cm-long waveguide. Furthermore, simply by increasing the waveguide length to 10 cm, while keeping all other waveguide properties identical, it is predicted that gain of 21 dB at 1533 nm and more than 10 dB across the entire C-band (1530–1565 nm) can be achieved with 150 mW of launched 1470-nm pump power. These results show that TeO₂:Er³⁺-coated Si₃N₄ waveguides are highly promising for compact and high gain optical amplifiers on silicon photonic platforms.

The results presented in this chapter have contributed to the following journal publication:

- H. C. Frankis, H. M. Mbonde, D. B. Bonneville, C. Zhang, R. Mateman, A. Leinse, and J. D. B. Bradley, "Erbium-doped TeO₂-coated Si₃N₄ waveguide amplifiers with 5 dB net gain," *Photonics Research* **8**(2), 127–134 (2020).

4.1. Introduction

Silicon-nitride (Si₃N₄) photonic integrated circuits (PICs) are widely used in applications including sensing [1], nonlinear optics [2] and telecommunications [3,4] due to their high transparency and mature and cost-effective fabrication methods. Silicon nitride is an ideal material system for passive photonic components, such as filters and multiplexors, because of its high refractive index contrast which allows for compact devices and capability for ultra-low waveguide losses [5,6]. Because silicon nitride can be processed at a wafer-scale using silicon-compatible processing steps [7], advanced photonic circuits combining passive silicon nitride circuitry with active optoelectronic silicon (Si) devices have also been recently developed [8-10]. Although these platforms provide access to a large library of photonic components a continuing challenge for both Si₃N₄ and Si material systems is the monolithic integration of gain materials for optical amplifiers and lasers [11].

Several methods for the integration of amplifiers and lasers in both silicon nitride and silicon photonic microsystems have been developed. III-V semiconductor optical amplifiers (SOAs) butt coupled to silicon nitride resonant cavities [12-14] and flip chip bonding of III-V dies and wafers onto silicon waveguides have been used to demonstrate on-chip lasing [15-18]. Although the ability to achieve high optical gain through electrically pumped III-V SOAs can provide a promising approach for the realization of amplifiers and lasers in photonic microsystems, the integration of such devices in large scale production is costly and challenging. An alternative approach to incorporating optical gain into integrated photonic systems is through rare-earth dopants, a commonly used gain mechanism in optical fibers [19]. However, the low rare-earth solubilities of silicon [20,21] and LPCVD silicon nitride [22] make them unsuitable material systems for rare-earth doped devices.

Rare-earth-doped oxide thin films, such as tellurium oxide (TeO_2), aluminum oxide (Al_2O_3), and tantalum pentoxide (Ta_2O_5) exhibit high rare earth solubilities and gain under optical pumping, moderately high refractive indices for compact devices, and can be fabricated monolithically on silicon using standard, low-cost wafer-scale methods, while potentially enabling reduced nonlinearities and noise compared to III-V optical gain solutions [23-24]. Erbium, in particular, is an attractive rare-earth dopant because of its emission around 1550 nm for communications applications. Pioneering work on erbium-doped waveguides in host materials including phosphosilicates [25-27], lithium niobate [28-30], phosphate glass [31-34], and aluminosilicate glass [35] showed the promise of on-chip amplifiers and lasers. More recent work on thin film waveguide amplifiers includes the demonstration of on-chip optical gain of up to 14 dB corresponding to 2.8 dB/cm in erbium-doped tellurium oxide ($\text{TeO}_2:\text{Er}^{3+}$) [36,37], 20 dB corresponding to 1.6 dB/cm in erbium-doped aluminum oxide ($\text{Al}_2\text{O}_3:\text{Er}^{3+}$) [38], and 4.8 dB corresponding to 2.1 dB/cm in erbium-doped tantalum pentoxide ($\text{Ta}_2\text{O}_5:\text{Er}^{3+}$) [39]. However, these amplifiers were fabricated as single material systems platforms, and cannot take advantage of the wafer-scale, high resolution processing and passive and optoelectronic capabilities provided by silicon nitride and silicon photonic circuits. Ideally, rare-earth-doped oxide gain materials monolithically integrated onto Si_3N_4 and Si platforms would provide a platform for fully integrated optical systems. Rare-earth-doped Al_2O_3 coatings have been deposited onto planarized oxide layers over silicon nitride waveguides to form a hybrid mode between the two materials. Using this approach distributed Bragg reflector (DBR) and distributed feedback laser (DFB) cavities have been patterned in the Si_3N_4 layer to demonstrate lasing [40-46], and Al_2O_3 coated trenches coupled to Si_3N_4 photonic circuits have been developed for microcavity and tunable lasers [47-49]. Recently an $\text{Al}_2\text{O}_3:\text{Er}^{3+}$ ridge waveguide amplifier has been fabricated on a Si_3N_4 photonic chip to couple light between the passive silicon nitride layer and the aluminum oxide amplifier, demonstrating total gain and gain per unit length of 18.1 dB and 1.8 dB/cm, respectively [50]. However, this method requires the additional fabrication steps of etching ridge waveguides in the $\text{Al}_2\text{O}_3:\text{Er}^{3+}$ layer, which must be accurately aligned to the underlying silicon nitride waveguide to maintain low inter-layer coupling losses [51,52]. A simpler fabrication approach is to coat exposed Si_3N_4 waveguides in a rare-earth-doped thin film that requires no post-processing on the gain layer. An Si_3N_4 slot waveguide coated in an $\text{Al}_2\text{O}_3:\text{Er}^{3+}$ film by atomic layer deposition (ALD) has been reported with optical gain of up to 20.1 dB/cm due to the high erbium concentrations that can be achieved in ALD films [53,54]. However, gain has only been demonstrated in waveguides with lengths of less than 0.2 cm, and a high-resolution lithography slot structure is required to increase the optical confinement that can be achieved in the $\text{Al}_2\text{O}_3:\text{Er}^{3+}$ film.

Tellurium oxide is a promising candidate for monolithic gain layers in Si_3N_4 photonic circuits due to its large refractive index (2.08) which enables large confinement factors within the TeO_2 film and small waveguide bend radii, potential for low waveguide losses [55], high rare-earth solubility and broad rare-earth emission spectra [56,57]. Developing $\text{TeO}_2:\text{Er}^{3+}$ amplifiers on the Si_3N_4 platform can also leverage Si_3N_4 's low losses and mature, high-

resolution patterning methods, allowing for versatile designs and high-performance devices. This chapter investigates the spectroscopic properties of $\text{TeO}_2:\text{Er}^{3+}$ -coated Si_3N_4 waveguides and the demonstration of internal net gain, as well as a rate equation model to analyze the potential future performance of optical amplifiers on this platform.

4.2. Spectroscopic Properties of Erbium-Doped Tellurium Oxide

This section presents the theory and characterization of the optical and spectroscopic properties relevant to the operation of $\text{TeO}_2:\text{Er}^{3+}$ -coated Si_3N_4 waveguide amplifiers, primarily from the viewpoint of experimentally characterizing a set several waveguide samples with varying erbium-dopant concentrations. Firstly, the general theory of optical processes and transition of electrons between energy states, the conditions for optical gain or amplification, and the electronic energy diagram of erbium-dopants are discussed. The absorption and emission cross sections and background waveguide losses are then investigated in the context of waveguide transmission measurements. The ${}^4\text{I}_{13/2}$ luminescent lifetime of the samples was then characterized by measuring the decay rate of spontaneous emission and the fast-quenching of erbium dopants was investigated using the absorption saturation method. The section ends with a summary and comparison of the parameters and trends measured between the different samples.

4.2.1. Optical Processes and Gain

Figure 4.1 depicts the three optical processes that can occur in a system with an excited and ground energy state, of spontaneous emission, optical absorption, and stimulated emission. Although the energy states can be of many different forms, we limit our discussion here to the consideration of an electron of an atom transitioning between the two distinct electron configuration energy levels.

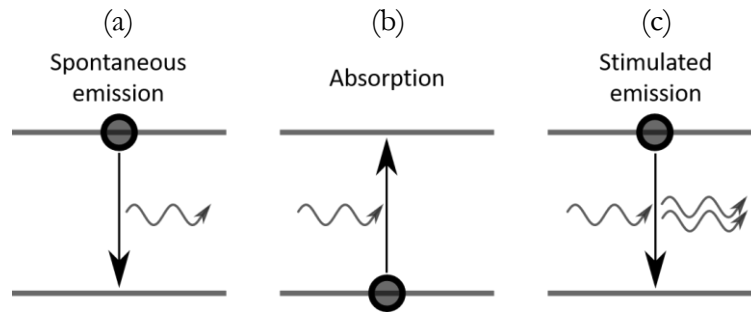


Fig. 4.1. Optical processes in a two-level energy system, including (a) spontaneous emission, (b) optical absorption, and (c) stimulated emission.

The Einstein coefficients [58,59] describe the mathematical relationship between all three processes for an idealized, non-degenerate two-level energy system. Spontaneous emission results from an electron in the excited energy state decaying to the ground state, in which a

photon with the energy of the difference between the two levels is radiated, as shown in Fig. 4.1(a). A spontaneous emission event can occur for an electron in the excited state at any time, with no external influence applied on the system. Although the amount of time for an individual electron to experience a spontaneous emission event will vary, for a large collection of electrons and neglecting non-radiative decay mechanisms the average time in which they experience decay after being excited, referred to as the excited state lifetime (τ), can be used. The probability of an electron experiencing a spontaneous emission at any given moment, can then be characterized as the inverse of the excited state lifetime, referred to as the spontaneous emission rate (γ_{Rad}). The rate of spontaneous photon emission is then proportional to the spontaneous emission rate and the population density of electrons in the excited state (N_2) (ions/cm³). As each spontaneous emission event results in an electron leaving the excited state, this can also be used to describe the population transition rate of the excited state (dN_2/dt) as shown in Equation 4.1:

$$\frac{dN_2}{dt} = -\gamma_{\text{Rad}}N_2 = -\frac{N_2}{\tau}, \quad 4.1$$

where the electrons decaying from the excited state populate the ground state level, whose population transition rate is then the opposite to that of the excited state as shown in Equation 4.2:

$$\frac{dN_1}{dt} = -\frac{dN_2}{dt} = \frac{N_2}{\tau}. \quad 4.2$$

As well as emission there is also a probability that a photon travelling through the medium with an energy equal to the difference between its two energy states is absorbed, resulting in a ground state electron being excited to the higher energy state. The probability of a photon experiencing an absorption event via a ground state electron is described by the absorption cross section (σ_{abs}) (cm²) of the material. The transition rates of the two energy levels are proportional to the number of electrons in the ground state (N_1) and the photon flux travelling through the material (ϕ) (photons/cm³/s) by the absorption cross section, as shown in Equation 4.3:

$$\frac{dN_1}{dt} = -\frac{dN_2}{dt} = -\sigma_{\text{abs}}N_1\phi. \quad 4.3$$

While optical absorption results in the promotion of an electron, this process also requires the loss of the photon which created the event, reducing the photon flux travelling through the medium. The amount of photon flux loss per unit length of the medium can then be similarly found from the transition rate as shown in Equation 4.4:

$$\frac{d\phi}{dz} = -\sigma_{\text{abs}}N_1\phi. \quad 4.4$$

However, because the optical absorption depends on the photon flux, and spontaneous emission does not, Einstein determined that thermal equilibrium could not be maintained with only these two processes. Therefore, Einstein theorized that a third optical process, the decay of an excited electron to the ground state induced by an incident photon that results in the release of a second photon, referred to as stimulated emission, must exist. The probability of a photon inducing a stimulated emission event is characterized by the emission cross section (σ_{em}) (cm^2), where, similar to absorption, the transition rate is proportional to the photon flux and population of the excited state as shown in Equation 4.5:

$$\frac{dN_2}{dt} = -\frac{dN_1}{dt} = -\sigma_{em}N_2\phi, \quad 4.5$$

and each stimulated emission event will contribute an additional photon to the photon flux, as shown in Equation 4.6:

$$\frac{d\phi}{dz} = \sigma_{em}N_2\phi. \quad 4.6$$

With all of the fundamental optical processes described, the total net population transition rate for the ground and excited state, as well as the net photon flux as the result of all the optical processes can be described as shown in Equations 4.7–4.9 respectively:

$$\frac{dN_1}{dt} = (\sigma_{em}N_2 - \sigma_{abs}N_1)\phi + \frac{N_2}{\tau}, \quad 4.7$$

$$\frac{dN_2}{dt} = -(\sigma_{em}N_2 - \sigma_{abs}N_1)\phi - \frac{N_2}{\tau}, \quad 4.8$$

$$\frac{d\phi}{dz} = (\sigma_{em}N_2 - \sigma_{abs}N_1)\phi. \quad 4.9$$

At thermal equilibrium, the population transition rates of each energy level in Equations 4.7 and 4.8 should be equal to zero. Using this it can be proved that the absorption and emission cross-sections must be equal [58,59]. Therefore, if an equilibrium state can be achieved in which the steady state population of the excited state is larger than that of the ground state, which requires a three- or four-level system, the potential for light propagating through the medium to experience an increased photon flux, or optical gain, can be realized.

4.2.2. Erbium Energy Diagram

The idealized two-level energy diagram discussed in the previous subsection is similar to the energy diagram seen in a gas atom, such as hydrogen, where relatively isolated atoms are able to maintain distinct electron energy states corresponding to different orbital energy levels. For solids however, the close spacing between atoms typically results in the accessible energy levels of the electrons splitting into approximately continuous energy bands as opposed to distinct levels. Notable exceptions to this phenomenon are the rare-earth ions, such as erbium, where

the valence 4f electron shell is shielded by the larger, filled 5s and 5p electron shells. This allows small concentrations of erbium ions to be doped into a material while maintaining distinct, atomic like energy levels, which are largely independent of the host material [60-63]. For trivalent erbium ions (Er^{3+}) doped in a material a wide range of excited electron energy states are accessible due to the large number of electrons in the valence shell (11). However, we limit our discussion here to the energy states most relevant to erbium amplifiers operating in the telecom C-band (1530–1565 nm). The excited energy states of the Er^{3+} ions are typically described using the Russell-Saunders notation [64], with the general form $^{2S+1}L_J$, where S represents the spin angular momentum based on the spin-spin coupling of electrons, L represents the orbital angular momentum from orbit-orbit coupling, and J represents the total angular momentum of spin-orbit coupling. The ground state of the erbium atom has 3 unpaired electrons, each with a spin angular momentum of 1/2, and a net orbital angular momentum of 6 (referred to as I in the Russel-Saunders notation), for a maximum total angular momentum of 15/2, which is represented as the $^4I_{15/2}$ state.

The transition of electrons between energy states in erbium ions can generally be broken down into optical, electrical, and thermally-based processes. A diagram summarizing the relevant energy states of the erbium ion and their associated transition processes can be found in Fig. 4.2. The diagram shows the eight lowest lying energy states of erbium ions, with the four lowest levels corresponding to the different spin-orbit coupling orientations. Transitions between the first excited state ($^4I_{13/2}$) and the ground state have an energy difference of approximately 0.8 eV, corresponding to a photon wavelength of around 1530 nm, and are the primary energy states of interest for amplification applications in the C-band.

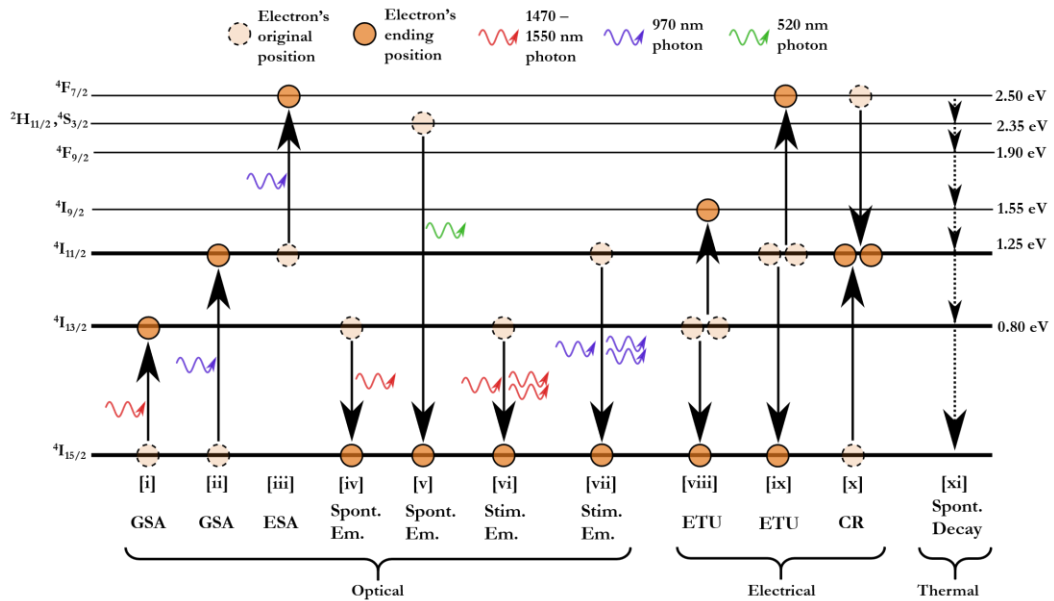


Fig. 4.2. Energy level diagram of Er^{3+} ions in tellurium oxide and the relevant electron transition processes for an amplifier operating in the C-band, including optical, electrical, and thermal transitions.

Optical transitions include the optical absorption and spontaneous and stimulated emission processes discussed in the previous subsection, and result in either the emission or absorption of a photon. While absorption events can occur between any two states if a photon has the correct energy, for amplifier applications we are primarily interested in photons around 1550 nm which create transition events into the ${}^4I_{13/2}$ state ([i]) and 970 nm which induce transitions into the ${}^4I_{11/2}$ state ([ii]) via ground state absorption (GSA). Additionally, if an ion is already excited into the ${}^4I_{11/2}$ state and absorbs a 970 nm photon it can experience an excited state absorption (ESA) event, which promotes the electron further to the ${}^4F_{7/2}$ state ([iii]). Again, while a spontaneous emission event can occur from any energy level, with regards to amplifiers we are particularly interested in spontaneous emission from the ${}^4I_{13/2}$ state, which emits a 1550 nm photon ([iv]), and from either of the closely spaced ${}^2H_{11/2}$ or ${}^4S_{3/2}$ state, which emit an ~ 520 nm photon ([v]), which although not particularly relevant to amplifier operation results in a visible green glow to erbium-doped waveguides when pumped. Lastly stimulated emission events between the ${}^4I_{13/2}$ level and ground state ([vi]) and ${}^4I_{11/2}$ level and ground state ([vii]) are important for amplification of 1550 nm signals and relevant for 970 nm optical pumping, respectively.

Electrical energy-transfer processes result from the interactions between two erbium ions [65,66]. These processes can either result in one of two initially excited ions interacting such that one ion decays to the ground state while the other ion is promoted to a higher excited state, referred to as energy transfer upconversion (ETU), or for a highly excited ion to decay to a lower excited state while causing a ground state electron to be excited to a higher energy state, referred to as cross relaxation (CR). The potential transitions of electrical processes are more limited because two ions are involved and the energy loss/gain between the states must be conserved. This allows ETU processes of interest to occur for a pair of electrons initially both in the ${}^4I_{13/2}$ ([viii]) or ${}^4I_{11/2}$ ([ix]) state, resulting in the excitation of one electron into the ${}^4I_{9/2}$ or ${}^4F_{7/2}$ state, respectively, and de-excitation of one electron into the ground state in both cases, as well as cross relaxation between a ground state and ${}^4F_{7/2}$ electron pair converting both into the ${}^4I_{11/2}$ state ([x]).

Lastly the effects of thermal processes through interaction with the lattice must be considered. While thermal excitation events can result in the natural promotion of some electrons into the excited states, the large energy difference between states means that the thermal populations of the higher energy levels are small at room temperatures. Additionally, an excited erbium ion may interact and impart its energy to the host through a lattice vibration (phonon) in a non-radiative decay event ([xi]) [67]. Non-radiative decay is an important process in three level pumping schemes, allowing electrons pumped to the ${}^4I_{9/2}$ state to transition into the ${}^4I_{11/2}$ state. The decay rate as a result of spontaneous emission and thermal decay can be combined in the luminescent lifetime, describing the average lifetime of an electron in a given state before either a spontaneous or thermal decay event occurs.

4.2.3. Absorption and Emission Cross Sections

To this point we have considered the erbium ion energy states as pure discrete states. However, the fundamental time-energy uncertainty relation prevents the concept of discrete states, resulting in energy states broadening into bands which ions will have an energy somewhere within [68]. Furthermore, although ion-lattice interactions are mostly shielded by the outer electron shells, the local electric field of the host material induces Stark splitting [61-63,69], separating the broadened singular energy states into a multiplet of several closely spaced energy states. For amorphous glass hosts the lack of long range order results in the Stark states of each individual ion shifting into slightly different energy levels based on the local crystal field environment of the host [62,63].

For a collection of many erbium ions in a host the individually split and broadened energy states of the ions become difficult to resolve and begin to appear as energy bands. Band-to-band transitions can therefore occur between any of the various sub-levels of the bands, as shown in Fig. 4.3(a), creating a range of photon wavelengths that can be absorbed/emitted in optical processes between the Er^{3+} levels, rather than singular wavelengths. Because determining the exact spectral lineshapes of transitions between individual Stark levels is difficult [70-72], it becomes more convenient to discuss energy splitting with regards to how it affects the overall band-band optical transition probabilities, using wavelength-dependent absorption and emission cross sections. Based on thermodynamic principles the ions in each energy state will distribute their energies throughout the band according to Boltzmann statistics, such that a majority of ions are near the bottom of each band. In general, the transition process with the greatest probability is between the lowest lying levels of each band, which are separated by the central energy E_0 [73,74]. As can be seen from Fig. 4.3(a), absorption events require photons with an energy equal to or greater than the central energy to be promoted from near the bottom of the ground state band to between the bottom and top of the excited state band, while ions predominantly excited to the lower portion of the upper manifold require less energy to transition to the upper portion of the lower manifold. Therefore, the absorption events occur with highest probability for photons with a wavelength corresponding to the center energy, with a gradual decrease for higher energy photons which transition from the bottom of the ground state into the upper manifolds of the excited state, and an exponential decrease for lower energy photons which require thermally excited ions in the ground state. The opposite trend is seen for emission events, where a low-lying ion in the excited state band is likely to undergo transitions into the ground state with energy differences equal to the central energy or less, resulting in a higher probability of emission of longer wavelength photons. The small thermal occupancy of the upper portion of the excited manifold results in a sharp decrease in the probability of emitting shorter wavelength photons [75]. The typical absorption and emission cross sections for a commercially available erbium doped fiber can be seen in Fig. 4.3(b) [76]. Both the absorption and emission processes peak near a 1530 nm wavelength, corresponding to the center energy, with absorption dropping off quickly at longer wavelengths, and emission at shorter wavelengths. The absorption and

emission cross sections of most erbium-doped amorphous glasses have a generally similar shape to the one shown here with minor variations based on the exact splitting and broadening mechanisms of the glass host and corresponding distinct transition probabilities between each sub level.

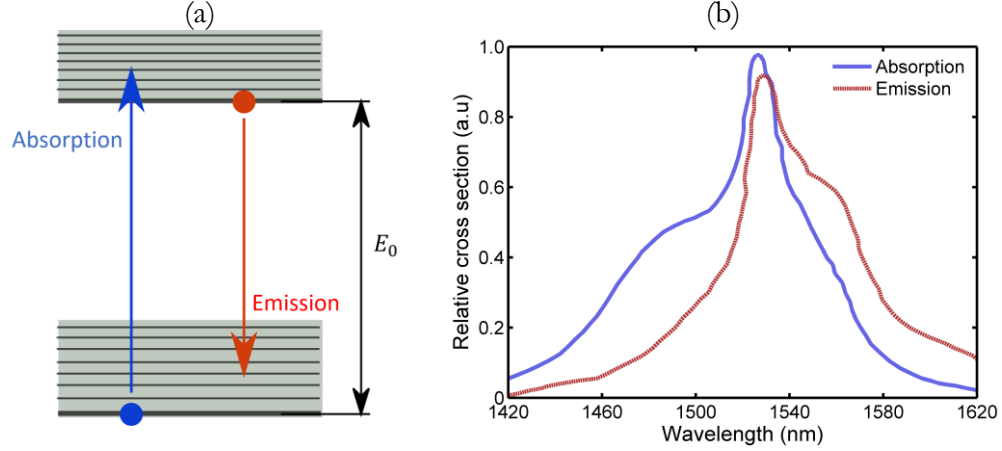


Fig. 4.3. (a) Diagram of sub-level absorption and emission process between broadened ground and excited state energy bands. (b) Normalized, absorption and emission cross sections between the ${}^4I_{15/2}$ and ${}^4I_{13/2}$ energy bands of an erbium doped silica fiber [76].

Optical transmission measurements in $\text{TeO}_2:\text{Er}^{3+}\text{-Si}_3\text{N}_4$ waveguides were used to extract information about the absorptions cross sections and concentration of erbium-dopants in our $\text{TeO}_2:\text{Er}^{3+}$ films. Due to the large energy gap between the ${}^4I_{15/2}$ ground state and the excited states almost all erbium ions are in the ground state at thermal equilibrium. In this case the erbium ions primarily act as absorbers, with the concentration of erbium dopants and the wavelength-dependent value of the absorption cross section affecting the magnitude of absorption. The transmission measurements, which were carried out in erbium-doped waveguides around 1550 nm using a fiber-chip coupling setup (see Fig. 3.13), include losses in the fibers and fiber connectors ($L_{\text{Fiber}}(\lambda)$), losses due to coupling light onto and off the chip ($L_{\text{Coupling}}(\lambda)$), the background waveguide losses caused by scattering, radiation, and non-erbium related absorption ($L_{\text{WG}}(\lambda)$), as well as losses as a result of ground state absorption of ${}^4I_{15/2}$ electrons into the ${}^4I_{13/2}$ state through the waveguide ($L_{\text{Er}}(\lambda)$). The total transmission loss of the system ($D(\lambda)$) can then be described by Equation 4.10 as follows:

$$L_{\text{Total}}(\lambda) = L_{\text{Fiber}}(\lambda) + L_{\text{Coupling}}(\lambda) + L_{\text{WG}}(\lambda) + L_{\text{Er}}(\lambda) . \quad 4.10$$

To characterize the absorption cross section each contribution to the total loss must be carefully identified. Fiber losses can be determined simply by a fiber-to-fiber transmission measurement without the chip. However, separating the contribution of other loss terms can be more difficult, so several assumptions are typically made. Firstly, it can be assumed that the minimum transmission loss measured at a wavelength greater than 1600 nm is outside the absorption band of the erbium dopants, seen in the small relative absorption cross sections of

Fig. 4.3(b), and has negligible erbium absorption loss ($L_{\text{Er}} = 0$), such that the measured transmission loss at this wavelength is solely the result of the now characterized fiber losses, coupling loss, and background waveguide loss. Secondly, although there is some wavelength dependence of coupling loss and background optical propagation loss, it can typically be assumed that they are constant over the measured signal wavelength range. Although the cutback method can be used to estimate both the coupling loss and background optical propagation loss together, this requires measurements to be made over several different waveguide lengths with highly repeatable coupling loss between waveguides, which has been shown to be challenging due to variability in waveguide facet quality (see Section 3.4.2). Alternatively, another method can be used to estimate the background optical propagation loss using appropriate structures on the same chip, and then the remaining loss in the waveguide transmission measurement can be attributed to the coupling loss. This approach assumes that losses are similar in waveguides with the same dimensions across the chip. The exception is when there is a noticeable macroscopic defect due to fabrication, which can typically be seen by scattered green light in pumped Er-doped samples or visible light coupled into undoped samples. A simple and accurate way to estimate the optical propagation loss of a waveguide independent of its coupling loss is through the characterization of a ring resonator's internal Q factor (see Section 3.4.4). By measuring the transmission spectrum of a ring resonator with the same waveguide dimensions and coated in the same film as the amplifier device at wavelengths around 1630 nm, where it is assumed that there is negligible erbium absorption loss, the background optical propagation loss per unit length of the waveguide can be found. The total background propagation loss can then be found by multiplying the waveguide loss per unit length times the length of the amplifier. Any remaining unaccounted-for loss after subtracting the fiber and waveguide losses is then considered to be the result of fiber-chip coupling loss.

Figure 4.4 shows a sample transmission measurement from 1510 to 1630 nm in a 1.2- μm -wide Si_3N_4 strip patterned into a 2.93-cm-long paperclip waveguide and coated in a 330-nm-thick $\text{TeO}_2:\text{Er}^{3+}$ film. The loss is broken down into the calculated contribution from each source discussed above. The total fiber losses in the setup measured by a fiber-to-fiber transmission measurement are found to be 2.9 dB at 1510 nm, increasing to 3.6 dB at 1630 nm. The minimum transmission loss measured is 16.7 dB at 1622 nm, which is assumed to include no erbium absorption loss. This leaves 13.2 dB of loss that is assumed to be the result of background optical propagation loss and fiber-chip coupling losses. A 600- μm -radius ring resonator with a gap of 2.0 μm on a chip coated in the same film was measured to have an internal Q factor of 4.3×10^5 at a wavelength of 1630 nm. This converts into an estimated 0.8 dB/cm of background waveguide propagation loss, which corresponds to 2.3 dB of total background signal loss in the amplifier. Subtracting this value from the remaining loss yields 5.4 dB/facet of optical coupling loss. Because the optical facets on this chip were polished with a FIB cut, this value agrees well with the expected coupling losses found from the cutback method (see Sections 3.4.1 and 3.4.2).

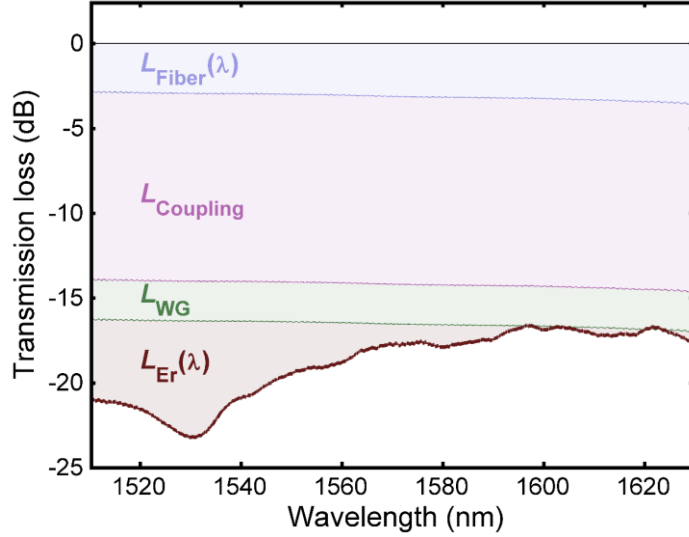


Fig. 4.4. Measured transmission loss in a 2.93-cm-long $\text{TeO}_2:\text{Er}^{3+}\text{-Si}_3\text{N}_4$ waveguide from 1510 to 1630 nm, broken down into contributions from fiber losses ($L_{\text{Fiber}}(\lambda)$), fiber-chip coupling losses (L_{Coupling}), background waveguide optical propagation loss (L_{WG}), and erbium absorption loss ($L_{\text{Er}}(\lambda)$).

Differences in the measured transmission loss compared to those expected from the now characterized fiber, coupling, and background waveguide losses can then be assumed to be the result of erbium related absorption. The magnitude of erbium related absorption will depend on the waveguide length (l), optical overlap into the $\text{TeO}_2:\text{Er}^{3+}$ film (Γ), the absorption cross section (σ_{abs}) and the erbium dopant concentration (N_{Er}). The waveguide length can be easily found from the Si_3N_4 waveguide mask design and the $\text{TeO}_2:\text{Er}^{3+}$ film overlap from an eigenmode simulation of the waveguide cross-section in RSoft. Once the absorption cross section of a material is known the erbium dopant concentration can be found from the optical transmission results. However, to initially characterize the absorption cross section an alternative method for determining the erbium ion concentration in the $\text{TeO}_2:\text{Er}^{3+}$ films, such as Rutherford Backscattering Spectrometry (RBS), must be used. To calculate the cross-section of our films a 350-nm thick $\text{TeO}_2:\text{Er}^{3+}$ film was deposited onto a bare silicon sample and a Si_3N_4 waveguide sample. RBS measurements (see Section 2.2.3) on the bare silicon sample determined an erbium concentration of 0.6 atomic %. Taking the known density of TeO_2 as 5.46 g/cm^3 [77], the concentration of erbium ions in the sample (N_{Er}) was estimated to be $2.6 \times 10^{20} \text{ ions/cm}^3$ [78]. Transmission measurements were then carried out in the waveguide sample and the erbium-related losses (L_{Er}) estimated assuming minimal erbium absorption loss at a 1640 nm wavelength as described earlier. This was used to calculate the absorption cross section as shown in Equation 4.11:

$$\sigma_{\text{abs}}(\lambda) = \frac{L_{\text{Er}}(\lambda)}{10 \log_{10}(e) \cdot N_{\text{Er}} \cdot l \cdot \Gamma}, \quad 4.11$$

where $10 \log_{10}(e)$ is a constant used to scale the Er absorption loss from the dB scale. Equation 4.11 assumes the signal intensity is small, such that most Er^{3+} ions are in the ground state. The resulting calculated absorption cross section of our $\text{TeO}_2:\text{Er}^{3+}$ films, with a range accounting for a $\pm 5\%$ error in the simulated optical overlap can be seen in Fig. 4.5(a). The peak cross section was determined to be $7.1 \pm 0.6 \times 10^{-21} \text{ cm}^2$ at 1531 nm, in good agreement with the previously characterized absorption cross sections of $\text{TeO}_2:\text{Er}^{3+}$ thin films [37].

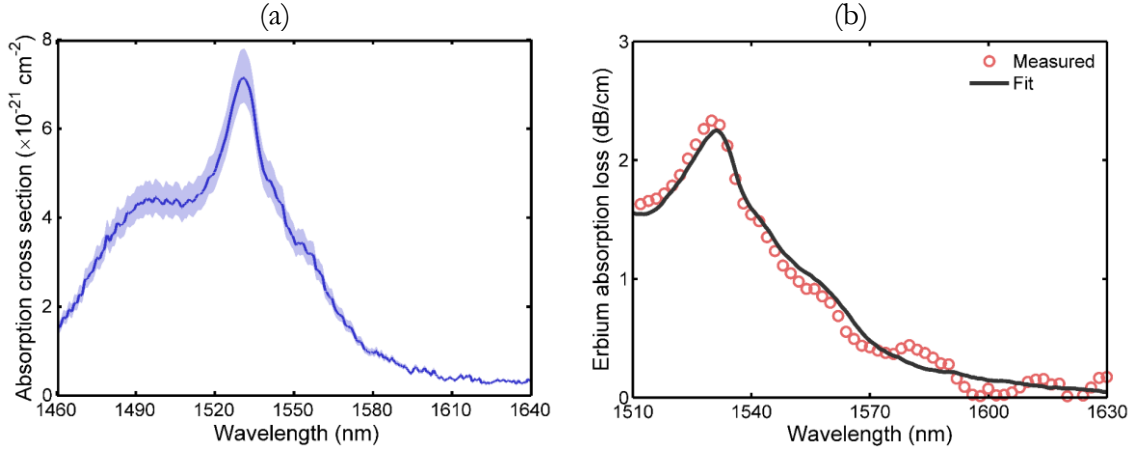


Fig. 4.5. (a) Erbium absorption cross section as estimated from RBS, with a peak cross section of $7.1 \pm 0.6 \times 10^{-21} \text{ cm}^2$ at 1531 nm measured in a $\text{TeO}_2:\text{Er}^{3+}$ waveguide with a concentration of $2.6 \times 10^{20} \text{ ions/cm}^3$. (b) Measured and calculated erbium absorption loss for a $\text{TeO}_2:\text{Er}^{3+}$ waveguide with an Er^{3+} concentration of $1.5 \times 10^{20} \text{ ions/cm}^3$ and 58 % optical confinement in the $\text{TeO}_2:\text{Er}^{3+}$ coating.

With the absorption cross section of our $\text{TeO}_2:\text{Er}^{3+}$ films now characterized, it can be used to calculate the dopant concentration of samples based on transmission measurements. Returning to the sample described in Fig. 4.4, the measured erbium loss is divided by the waveguide length (A_{Er}) and replotted in Fig. 4.5(b). This absorption data was fit to Equation 4.11, which was rearranged to solve for the erbium ion concentration, using the now known absorption cross section versus wavelength and the mode overlap, which was simulated to be 58 % for this sample. This sample was then fit to have an erbium concentration of $1.5 \pm 0.1 \times 10^{20} \text{ ions/cm}^3$, with good agreement to the measured absorption loss. This agrees within error of the $1.4 \pm 0.1 \times 10^{20} \text{ ions/cm}^3$ concentration measured from planar film optical propagation loss measurements for the same film (see Fig. 2.16). Characterizing the erbium absorption via waveguide transmission measurements can be advantageous compared to thin film loss measurements using prism coupling in that all measurements are taken at once enabling characterization to be performed more quickly, and the fitting uncertainty differences between individual wavelengths that exists in prism coupling is removed.

The mechanisms which lead to energy state broadening similarly affect the cross sections of the other optical transitions processes. The ground state absorption cross section for the $^4\text{I}_{15/2}$ to $^4\text{I}_{11/2}$ transition was characterized, in a similar manner to the absorption around 1550 nm, by waveguide transmission measurements using a tunable 970 nm laser. The

measurements were carried out in a 6.7-cm-long waveguide sample, coated in a 340-nm-thick $\text{TeO}_2:\text{Er}^{3+}$ film with an estimated erbium ion concentration of 2.2×10^{20} ions/ cm^3 , found from 1550 nm absorption measurements. By assuming constant background propagation and coupling losses, as well as negligible erbium absorption losses at a 930 nm, the erbium related loss around this wavelength was characterized. The measured loss was then used in Equation 4.11 to characterize the ${}^4\text{I}_{11/2}$ absorption cross section in our $\text{TeO}_2:\text{Er}^{3+}$ films, with the results shown in Fig. 4.6, where a peak absorption cross section of 2.8×10^{-21} cm^2 was measured at 968 nm.

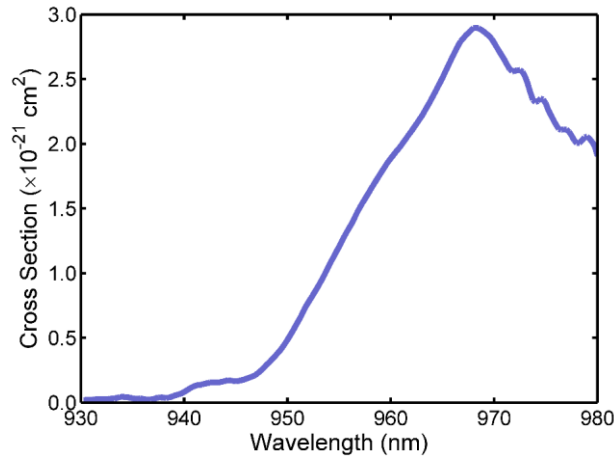


Fig. 4.6. Estimated erbium absorption cross section around 970 nm, based on 970-nm transmission measurements and the ion concentration of the device found from 1550-nm spectroscopy, with a peak cross section of 2.8×10^{-21} cm^2 at 968 nm.

In contrast to absorption measurements where a low-power signal is used, to measure the $\text{TeO}_2:\text{Er}^{3+}$ emission cross sections the samples must be optically pumped using a higher power source. As discussed earlier at thermal equilibrium very few ions are in the excited energy states, resulting in few emission events. To create a measurable signal of emission events an external excitation source, such as a high-power diode laser, is used to excite erbium dopants into the excited states. Assuming the erbium ions are excited and reach a thermal equilibrium within the upper manifold, emission events will occur at the different wavelengths in ratios corresponding to the emission cross sections of the material. The emission cross section for erbium-doped TeO_2 was therefore characterized experimentally by optically exciting a $\text{TeO}_2:\text{Er}^{3+}\text{-Si}_3\text{N}_4$ waveguide with a 970 nm pump diode, such that ions were pumped in the ${}^4\text{I}_{11/2}$ state and then decay into the ${}^4\text{I}_{13/2}$ where they were available to undergo spontaneous radiative transitions back to the ground state. The emission around 1550 nm was back-collected from the waveguide by the fiber coupling the optical pump signal and routed to an optical spectrum analyzer (OSA) via a wavelength division multiplexor (WDM), as shown in Fig. 4.7(a). The emission spectrum measured by the OSA was then used to calculate the relative emission cross section. However, because the intensity of radiated emission is affected by the ratio of radiative and non-radiative decay events and the various coupling and fiber losses

reduce the measured signal, it is difficult to characterize the magnitude of the emission cross section from this measurement. Assuming that the absorption and emission cross section peaks correspond to transitions between similar manifolds of the two energy bands, they can taken to be approximately equal, based on the relationship of the Einstein coefficients discussed earlier [79]. Therefore, the measured peak of the emission spectrum was normalized to the absorption cross-section peak measured earlier in Fig. 4.5(a) to determine the emission cross-section of the $\text{TeO}_2:\text{Er}^{3+}$ films, as shown in Fig. 4.7 (b). In general, the shape of the emission spectrum agrees well with the results measured previously in $\text{TeO}_2:\text{Er}^{3+}$ thin film waveguides [37] and fibers [80].

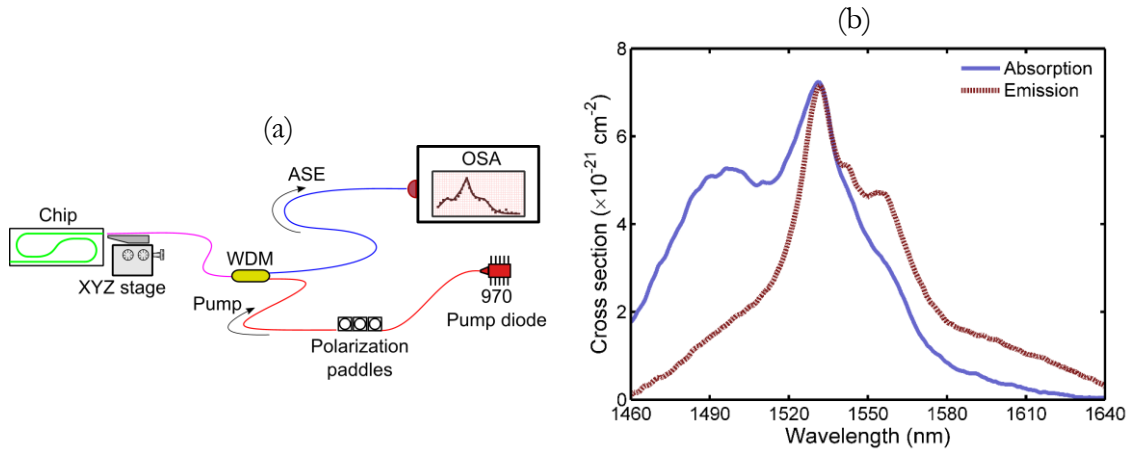


Fig. 4.7. (a) Setup used to measure the emission spectrum. (b) Emission cross section of $\text{TeO}_2:\text{Er}^{3+}$ around 1500 nm based on the back-collected ASE spectrum and scaled to match the measured absorption cross section.

4.2.4. Excited State Lifetimes

An electron in an excited state eventually experiences a decay event to the ground state, either through a radiative or non-radiative thermal process. From the Einstein relations' description of a medium at thermal equilibrium the spontaneous decay rate (γ_{Rad}), which is the inverse of the radiative lifetime (τ_{Rad}) can be related to the emission cross (σ_{em}) section through the Füchtbauer-Ladenburg equation [68] as follows,

$$\gamma_{\text{Rad}} = \frac{1}{\tau_{\text{Rad}}} = 8\pi n^2 c \int \frac{\sigma_{\text{em}}(\lambda)}{\lambda^4} d\lambda, \quad 4.12$$

where n is the refractive index of the medium, c is the speed of light in a vacuum and λ is the wavelength of light. While other oxide hosts exhibit ${}^4\text{I}_{13/2}$ radiative lifetimes of greater than 10 ms [81], TeO_2 has a relatively large refractive index and emission cross section, thus it is expected to have a much shorter radiative lifetime. Using a TeO_2 refractive index of 2.07 and the emission cross sections displayed in Fig. 4.6, a radiative lifetime of 4.5 ms is calculated, which is in agreement with values reported for tellurite fibers [82].

In addition to radiative decay events, excited electrons can also experience thermal decay to the ground state resulting in the release of a phonon into the lattice. While the 5d and 5p electron shells protect the valence 4f shell to preserve distinct atomic-like transition lines, they also act to protect excited electrons from non-radiative, thermal decay events. Additionally, the large energy gaps between certain energy levels reduces the ability of the host to support vibrational modes of sufficient energy to create non-radiative decay, typically requiring multiphonon relaxation [67]. Tellurite glass' relatively weak ionic bonds compared to other oxide glasses further reduces the strength of the ionic relations between the erbium dopants and the host with phonon energies of approximately $700\text{-}800\text{ cm}^{-1}$ [57], reducing the probability of phonon relaxation, which is expected to result in lower non-radiative recombination rates [83,84]. The total rate at which excited electrons experience decay events is then the sum of the radiative decay rate (γ_{Rad}) and non-radiative decay rate ($\gamma_{\text{Non Rad}}$), giving the luminescent decay rate ($\gamma_{\text{Luminescent}}$) as follows,

$$\gamma_{\text{Luminescent}} = \gamma_{\text{Rad}} + \gamma_{\text{Non Rad}} , \quad 4.13$$

whereby inverting the decay rates in Equation 4.13 can be used to describe the luminescent lifetime ($\tau_{\text{Luminescent}}$) of the state as follows,

$$\frac{1}{\tau_{\text{Luminescent}}} = \frac{1}{\tau_{\text{Rad}}} + \frac{1}{\tau_{\text{Non Rad}}} . \quad 4.14$$

Spontaneous radiative decay events result in the emission of a photon. From Equation 4.1 it is known that the rate of decay events, and equivalently photon emission, is proportional to the population of the excited state. The excited state ion population can then be directly tested by monitoring the intensity of radiative emission. Here we consider a system in which a large number of ions are initially excited to the ${}^4\text{I}_{13/2}$ state ($N_{2,\text{initial}}$), and then left to return to the thermal equilibrium. Assuming that spontaneous emissions are the only decay mechanism, the excited state population versus time ($N_2(t)$) can then be described by solving the differential equation of Equation 4.1, as shown below,

$$N_2(t) = N_{2,\text{initial}} e^{-t/\tau_{\text{Luminescent}}} , \quad 4.15$$

where the excited state ion population, and therefore emission events, are expected to exponentially decrease with a $1/e$ time constant equal to the luminescent lifetime. More complex models, such as Zubenko's [85] or a modified version of Zubenko's [86], also consider the effects of ETU on population decay. However, for smaller population densities and if any initial fast decay of the lifetime is neglected, the effects of ETU on the measurement are minimal and the excited state population decay time will approach that of Equation 4.15.

The luminescent lifetime of rare-earth doped waveguides was measured using the lifetime measurement setup displayed in Fig. 4.8. A 1470 nm diode that was modulated between 0 and 40 mW of output power, with an $5\text{ }\mu\text{s}$ turn off time, by a 40 Hz, 3 V peak-to-peak square wave

signal using a function generator and the output was launched onto the chip. When the pump diode was at its high output state erbium dopants were excited to the ${}^4I_{13/2}$ state until a steady state population of $N_{2,\text{initial}}$ was reached. When the pump source was turned off the erbium dopants returned to the ground state, through the radiative and non-radiative decay processes according to Equation 4.15. The radiative decay events generate an ASE signal that travels in both directions in the waveguide. Because the back-collected ASE is expected to be stronger than the forward ASE due to the greater population inversion near the pump source, the ASE was measured through the pump input fiber and routed to a photodetector. Once the pump source was turned off the intensity of the ASE decayed proportionally to the ${}^4I_{13/2}$ state lifetime, which was observed through monitoring the output signal of the photodetector on an oscilloscope.

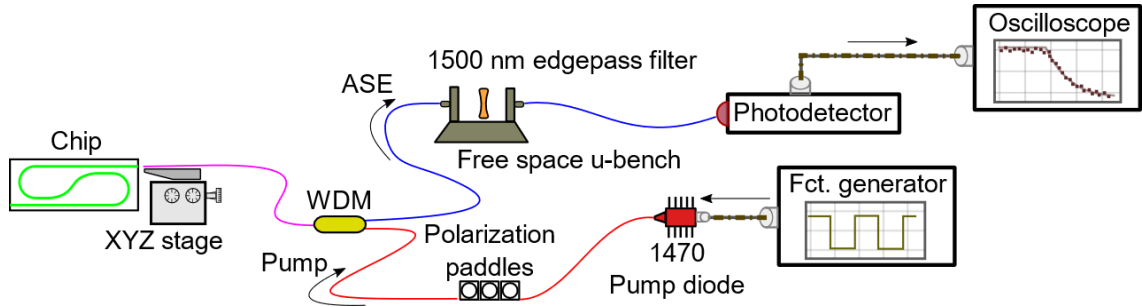


Fig. 4.8. Diagram of rare-earth luminescent lifetime measurement setup.

An example of the measured ASE intensity versus time for three different $\text{TeO}_2:\text{Er}^{3+}$ waveguide samples can be seen in Fig. 4.9. From the figure, samples with erbium dopant concentrations of 0.6 , 0.9 , and 1.5×10^{20} ions/ cm^3 were fit to have ${}^4I_{13/2}$ excited state lifetimes of 0.21 , 0.31 , and 0.26 ms respectively.

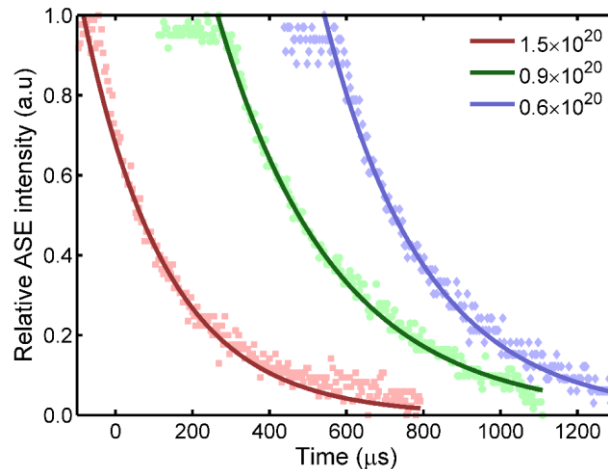


Fig. 4.9. Lifetime measurements of the ASE signal intensity versus time (with offset to distinguish between the data sets) carried out on $\text{TeO}_2:\text{Er}^{3+}-\text{Si}_3\text{N}_4$ waveguides with erbium concentrations of 0.6 , 0.9 , and 1.5×10^{20} ions/ cm^3 . The data is fit to have ${}^4I_{13/2}$ excited state lifetimes of 0.26 , 0.31 , and 0.21 ms, respectively.

It is clear from the results that the luminescent lifetimes are significantly less than the predicted radiative lifetimes, suggesting that non-radiative decay is the dominant decay process, even though tellurite glasses are predicted to have lower rates of non-radiative decay [83,84]. Previous work on $\text{TeO}_2:\text{Er}^{3+}$ amplifiers in fibers [87] and waveguides [36], has shown that excited state lifetimes in $\text{TeO}_2:\text{Er}^{3+}$ are strongly dependent on the concentration of OH^- molecule impurities in the glass. The work by Jha et. al. [88] demonstrated broadened OH^- absorption peaks in TeO_2 fibers as a result of alternative glass structural units, such as TeO_4 and TeO_3 , occurring in the TeO_2 glass matrix. They proposed that alternate structural units that bond with an OH^- group can free an H^+ proton which is able to freely roam through the glass and create fast relaxation events with erbium dopants. While bulk glass samples have shown excited state lifetimes on the order of 3 ms for erbium concentrations of approximately $1 \times 10^{20} \text{ cm}^{-3}$ [87], measurements in thin films have shown that excited state lifetimes can approach roughly 1.3 ms in the absence of OH^- molecules, with minimal dependence on dopant concentrations [36]. Figure 4.10 plots the measured luminescent lifetime of several samples with respect to their erbium ion concentration.

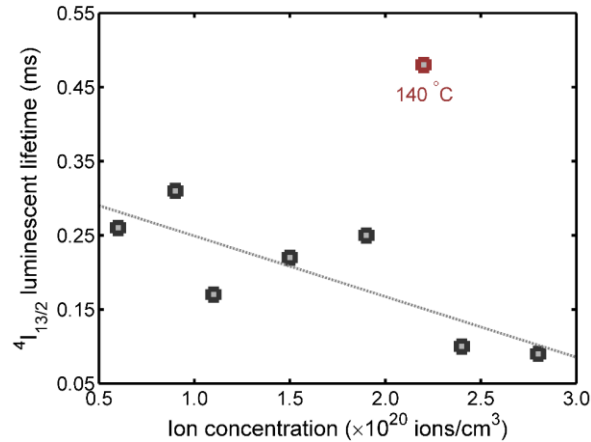


Fig. 4.10. Measured luminescent lifetimes in several different $\text{TeO}_2:\text{Er}^{3+}$ waveguides with erbium dopant concentrations of between 0.6×10^{20} and $2.8 \times 10^{20} \text{ ions/cm}^3$. Minimal correlation was found between dopant concentration and luminescent lifetime, as was also seen in other $\text{TeO}_2:\text{Er}^{3+}$ work [36], with an average measured lifetime of $200 \mu\text{s}$. A sample with a concentration of $2.2 \times 10^{20} \text{ ions/cm}^3$ deposited at a $140 \text{ }^\circ\text{C}$ temperature was seen to have a significant increase of luminescent lifetime up to 0.48 ms.

On average the samples had a measured lifetime of 0.20 ms, with a minimum measured value of 0.09 ms and maximum measured value of 0.31 ms for films with erbium dopant concentrations of 2.8 and $0.9 \times 10^{20} \text{ ions/cm}^3$, respectively. A small trend is observed in decreasing lifetime with increasing dopant concentration giving a linear fit of $-0.08 \text{ ms per every } 1 \times 10^{20} \text{ ions/cm}^3$, but they are only moderately correlated with an R^2 value of 0.6. The relatively small luminescent lifetimes measured here compared to other sources suggest that there is a reasonably strong OH^- concentration in the films. In an attempt to reduce OH^- impurities in the film and increase lifetime we deposited a sample at a substrate heater

temperature of 140 °C, which is hot enough to remove moisture, without crystalizing or introducing extra loss to the TeO₂ film [77]. This sample was measured to have an erbium ion concentration of 2.2×10^{20} ions/cm³, and demonstrated an excited state lifetime of 0.48 ms, which is significantly larger than the lifetimes measured on all samples fabricated at room temperature regardless of concentration. This suggests sample heating during deposition is a promising pathway towards reducing OH⁻ contamination and improving lifetimes in future studies. Additionally, higher purity sputtering targets and oxygen gas cylinders can also be explored in the future to reduce the potential for contaminating TeO₂:Er³⁺ films with OH⁻ molecules and other impurities.

4.2.5. Ion Quenching and Energy Transfer

In the previous discussions of transmission measurements and absorption cross sections it was assumed that the incident signal power into the waveguide was small enough such that it did not have a noticeable effect on the erbium ion population dynamics. Now, we consider the case in which the signal photon flux is sufficiently large to affect ion energy level population dynamics, up to the point that photon flux becomes large enough for stimulated transitions to become the dominant transition mechanism, such that spontaneous emission can be ignored to a reasonable approximation. With this assumption the spontaneous emission term is dropped from the population transition rates of Equations 4.7 and 4.8, and at steady state, when the transition rates are equal to 0, the following result is obtained:

$$\frac{dN_1}{dt} = -\frac{dN_2}{dt} \approx \sigma_{\text{em}}N_2\phi - \sigma_{\text{abs}}N_1\phi = 0. \quad 4.16$$

Substituting the relationship of Equation 4.16 in Equation 4.9, which describes the net change in photon flux with propagation distance, shows that for high signal powers travelling through a waveguide the net change in photon flux as a result of erbium absorption should also approach 0, through a process known as pump/signal absorption saturation [86].

This expectation assumes that all erbium ions in the waveguide act identically and share the same luminescent lifetime. However, some of the erbium ions in the material may be included in pairs/clusters, or near impurities, such as OH⁻ groups. Erbium ions in these states can experience increased decay rates through non-radiative processes, where the lifetimes are predicted to be on the order of 50 ns [89] to a few μs [90]. The erbium ions in the TeO₂:Er³⁺ film can then be considered in two distinct categories: independent ions with lifetimes described by the luminescent decay time, and fast-quenched ions, which experience optical absorption and then rapidly undergo a non-radiative decay back to the ground state. In the context of absorption saturation the population dynamics of the independent, unquenched, ions are still dominated by optical processes and tend towards no net erbium absorption at large optical powers. Meanwhile, the fast-quenched ions maintain spontaneous decay as the dominant factor in their population dynamics, such that a majority of the fast quenched ions remain in the ground state and are available to absorb incoming photons. These fast-quenched

dopants can be referred to as non-saturable absorbers (NSA). Therefore, by quantifying the optical absorption of a waveguide measured at large launched signal powers the fraction of quenched erbium dopants in the material can be estimated [86,91].

The quenched ion fractions were measured in the $\text{TeO}_2\text{:Er}^{3+}\text{-Si}_3\text{N}_4$ waveguides using the fiber-chip coupling setup shown in Fig. 4.11. Here, a 1530-nm laser signal was routed through a set of polarization paddles and into an erbium-doped fiber amplifier (EDFA) before being launched onto the chip via a tapered fiber. The EDFA gain was adjusted to control the signal output power that was coupled into the waveguide. The transmitted signal power was collected at the opposite side of the chip, where it was routed to a photodetector. While other absorption saturation measurements have been performed at a wavelength of 1480 nm [86,91], a 1530-nm signal wavelength was used here because it has the largest initial absorption in the waveguide which increases the resolution of the measurement, and it allows for maximizing the output signal power from the EDFA. The measurements were initially carried out with the EDFA set to a gain level such that the signal power incident on the waveguide was less than or equal to 0.01 mW, as characterized by measuring the output power of the input fiber on a free-space photodetector. Insertion loss measurements were then taken at this initial low incident power setting, which was assumed to have minimal absorption saturation, similar to the erbium absorption measured in passive waveguide transmission measurements (Fig. 4.4). The incident signal power was then incrementally increased up to 60 mW, which was the maximum output power of the EDFA, and any observed reduction in insertion loss was taken to be the result of absorption saturation.

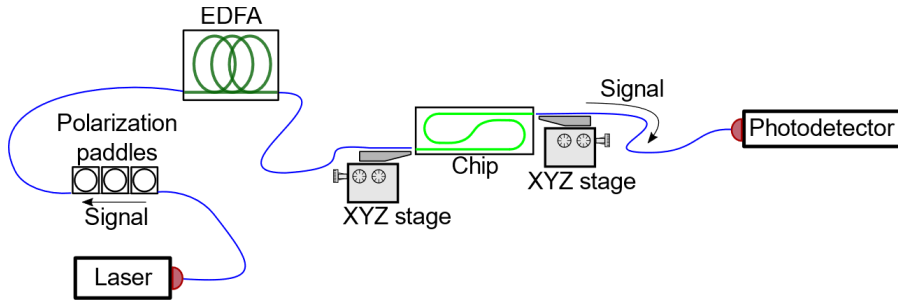


Fig. 4.11. Absorption saturation measurement setup diagram.

An example of the measured erbium absorption loss versus launched signal power, for the sample with a concentration of 1.5×10^{20} ions/cm³, in which example small-signal transmission measurements were also carried out as shown in Fig. 4.4, can be found in Fig. 4.12(a). At small signal powers the erbium ions contribute 6.9 dB of absorption loss at 1530 nm as measured earlier in Fig. 4.4. To a rough approximation the quenching fraction ratio can be estimated by the ratio of erbium related absorption measured at large signal powers where unquenched ions are expected to be saturated (A_{Sat}) compared to the peak absorption measured at small signal powers (A_{Peak}). For example, for a launched signal power of 20 mW, 2 dB of erbium-related signal absorption was measured compared to the 6.9 dB at small signal powers, which would suggest approximately 29 % of ions in this sample were fast-quenched.

However, higher order effects, such as erbium ions in regions of low intensity near the edge of the optical mode or farther along the waveguide not becoming saturated and a small quantity of quenched ions which are promoted to excited states, cause some deviation from this approximation. To accurately quantify the fraction of quenched ions in the sample more detailed rate equation models must be used. Here we used a three-level rate equation model, which is described in detail in Section 4.4, with a variable fraction of quenched ions to fit the absorption saturation versus launched signal power data. Firstly, a curve assuming no quenched ions was calculated, shown in Figure 4.12(a) to approach near total saturation of the erbium absorption at 20 mW of launched signal power. Several further simulations of the waveguide assuming different fractions of quenched ions in the sample were then performed. Based on these simulations a quenched-ion fraction of 27 % was found to best fit the experimental data. The relative erbium absorption ($A_{\text{Sat}}/A_{\text{Peak}}$) versus launched signal power curves for different samples with erbium dopant concentrations of 0.9, 1.5, and 2.4×10^{20} ions/cm³ can be seen in Fig. 4.12(b). The data sets are fit with estimated quenching fractions of 14, 27, and 38 %, respectively.

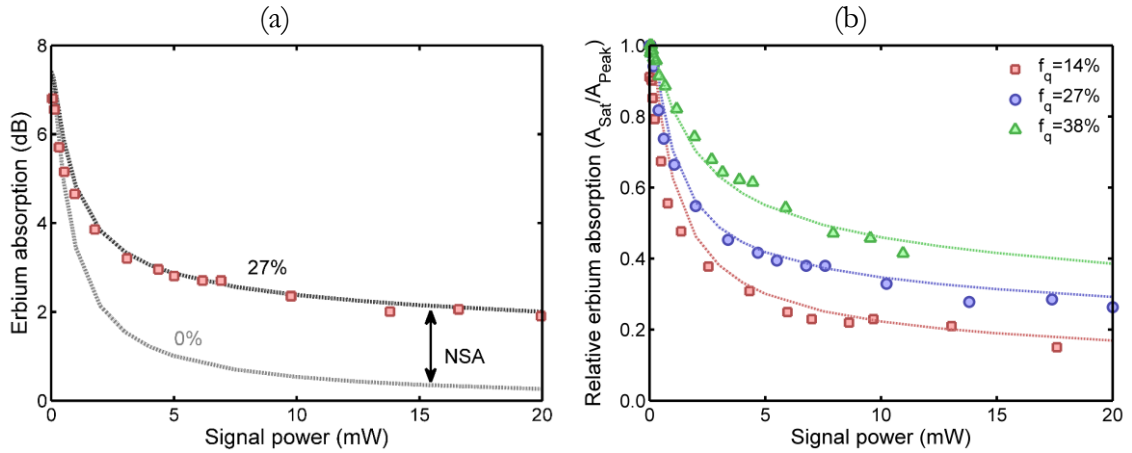


Fig. 4.12. (a) Measured erbium absorption loss at 1530 nm in a 2.93-cm-long waveguide coated in a 330-nm-thick $\text{TeO}_2\text{:Er}^{3+}$ film with an erbium concentration of 1.5×10^{20} ion/cm³ versus launched signal power into the waveguide. The results are compared to calculations based on a three-level rate equation model which assume that 0% and 27% of ions are quenched. (b) Measured erbium absorption loss relative to the peak absorption at 1530 nm versus signal power launched into the waveguide, for three different waveguides fit to have 14, 27 and 38 % ion quenching.

The quenching ratios measured here in several $\text{TeO}_2\text{:Er}^{3+}\text{-Si}_3\text{N}_4$ waveguides are plotted in Fig. 4.13(a). For larger erbium dopant concentrations, it is intuitive that the occurrence of ion pairs and clusters in the material will increase. This trend was observed in erbium-doped aluminum oxide waveguide amplifiers which showed quenching fractions on the order of 10 % for dopant concentrations of 1.0×10^{20} increasing up to 33 % for a 3.6×10^{20} dopant concentration [86]. For comparison, this data is reproduced in the black line of Fig. 4.13(a), where it can be seen that in general the fraction of quenched ions measured in our $\text{TeO}_2\text{:Er}^{3+}$

films were approximately 10 to 15 % larger than $\text{Al}_2\text{O}_3:\text{Er}^{3+}$ films with similar dopant concentrations. Additionally, while the $\text{Al}_2\text{O}_3:\text{Er}^{3+}$ results showed a very clear trend and fitted curve of quenching fraction versus dopant concentration, the results in $\text{TeO}_2:\text{Er}^{3+}$ are much more inconsistent and scattered with some relatively large variations from the trend. Plotting the measured quenching fraction of samples versus their luminescent lifetimes as shown in Fig. 4.13(b), demonstrates an additional trend of smaller quenching fractions with longer $^4\text{I}_{13/2}$ luminescent lifetimes. These results suggest that in addition to ion pairs and clusters the interaction of ions with impurities, such as OH^- groups, are a prevalent mechanism for quenching occurring in the $\text{TeO}_2:\text{Er}^{3+}$ films studied here.

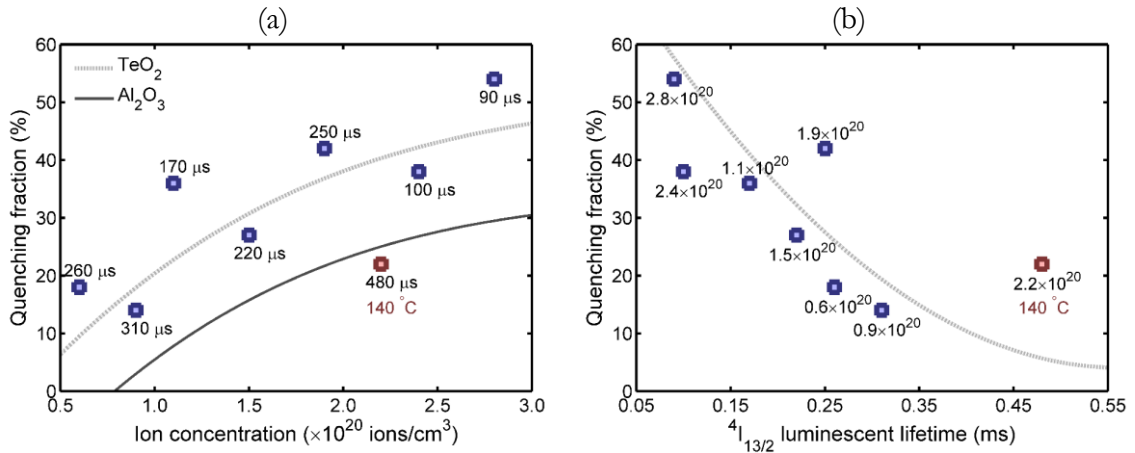


Fig. 4.13. Estimated quenching fraction of samples versus (a) erbium dopant concentration, and (b) $^4\text{I}_{13/2}$ luminescent lifetime. In general quenching fractions are larger than those seen in Al_2O_3 samples [86], with the exception of a sample deposited at a 140 °C temperature with a 2.2×10^{20} ions/cm³ erbium dopant concentration measured to have a 22 % quenching fraction. In general, longer excited state lifetimes are predicted to lead to reduced quenching fractions due to less pathways for quenching through OH^- impurity interactions [36].

The $\text{TeO}_2:\text{Er}^{3+}$ sample deposited at a 140 °C stage temperature with a measured excited state lifetime of 480 μs and dopant concentration of 2.2×10^{20} ions/cm³ was fit to have a 22 % fraction of quenched ions. This is roughly 20% lower than the quenching fraction measured in the $\text{TeO}_2:\text{Er}^{3+}$ samples fabricated at room temperature, and near what is expected in $\text{Al}_2\text{O}_3:\text{Er}^{3+}$ films of similar concentration. Therefore, in addition to improving luminescent lifetimes it is important to investigate reduced OH^- incorporation into films to reduce quenching fractions in the future. The work of Vu and Madden demonstrated a $\text{TeO}_2:\text{Er}^{3+}$ film with negligible OH^- incorporation with a luminescent lifetime of 1.3 ms [36]. This suggests that even for the sample with a 480 μs luminescent lifetime there is still some OH^- incorporation remaining in the $\text{TeO}_2:\text{Er}^{3+}$ film which is likely contributing towards quenching. Further removal of impurities could therefore lead to lower quenching fractions than those observed in $\text{Al}_2\text{O}_3:\text{Er}^{3+}$ waveguides, allowing for very large optical gain from $\text{TeO}_2:\text{Er}^{3+}$ - Si_3N_4 amplifier devices.

A relevant material parameter that is not thoroughly discussed in this thesis is ETU. As discussed in section 4.2.4, ETU parameters can be measured through modelling of high-resolution luminescent decay curves with specialized models [85,86]. However, due to the large fraction of quenched ions and relatively short luminescent lifetimes it becomes more difficult to resolve the effects of ETU in the measured luminescent decay curves, and these characteristics reduce the overall impact of ETU on amplifier performance. Therefore, in this thesis we simply take the ETU coefficient measured previously in TeO₂ fiber [92] of 2.8×10^{-18} cm³/s for an erbium concentration of 3.4×10^{20} ions/cm³ as the ETU coefficient of all films considered. Characterization of the ETU coefficient in the future on TeO₂:Er³⁺ thin films with less quenching and longer luminescent will become a more relevant.

4.2.6. Sample Comparison

In this section we summarize the spectroscopic properties of the various TeO:Er³⁺-Si₃N₄ waveguides that have been discussed in the preceding sections. The results are presented in Table 4.1. We summarize the samples based on their ion concentration, film thickness, background waveguide loss, ⁴I_{13/2} luminescent lifetime and ion quenching ratio, using the methods described in sections 4.2.3 to 4.2.5.

Table 4.1. Comparison of TeO₂:Er³⁺-coated Si₃N₄ waveguide samples' spectroscopic properties.

Deposition temperature (°C)	20							140
	0.6	0.9	1.1	1.5	1.9	2.4	2.8	2.2
Erbium concentration (ions/cm ³)								
TeO ₂ :Er ³⁺ film thickness (nm)	335	360	310	330	250	240	340	340
Background waveguide loss at 1550 nm (dB/cm)	0.8	0.7	0.8	0.8	0.6	0.9	1.2	0.25
I _{13/2} lifetime (ms)	0.26	0.31	0.17	0.22	0.25	0.10	0.09	0.48
Quenching percentage	18	14	36	27	42	38	54	23

Most samples were measured to have moderate background waveguide losses of <1 dB/cm, which are comparable to the losses measured in passive waveguides in Chapter 3. This suggests that the inclusion of erbium dopants within the concentration range studied has a minimal effect on optical propagation losses. Luminescent lifetimes of the ⁴I_{13/2} state were measured to be 0.20 ± 0.08 μs on average, with a small trend of decreased luminescent lifetime versus dopant concentration. The relatively short excited state lifetimes compared to the expected radiative decay time in TeO₂:Er³⁺ and concentration insensitivity was surmised to be result of OH⁻ impurities being the predominant decay mechanism. Similarly, the fraction of

quenched ions, while displaying some sensitivity to dopant concentration, as was observed in $\text{Al}_2\text{O}_3:\text{Er}^{3+}$ films [86], also displayed a strong trend of increased quenching with shorter excited state lifetimes. This shows that both ion pairs and impurities are prevalent quenching mechanisms in the $\text{TeO}_2:\text{Er}^{3+}$ films studied.

In comparison a sample deposited at a 140 °C temperature was characterized to have an erbium dopant concentration of 2.2×10^{20} ions/cm³, a larger $^4\text{I}_{13/2}$ luminescent lifetime than any of the samples deposited at room temperatures of 0.48 ms, and a quenched ion fraction of 22 %, much lower than what was measured for samples fabricated at room temperature with similar concentrations. Additionally, the background waveguide loss characterized for this sample was found to be 0.25 dB/cm, the lowest loss to be measured in undoped or doped waveguides on this platform. Based on these results, moderate increases to deposition temperatures in future investigations are expected to allow for improved passive and erbium related properties of devices. Due to this sample's promising properties, it was selected to undergo detailed gain characterization as outlined in the following section, in order to demonstrate amplification in the $\text{TeO}_2:\text{Er}^{3+}$ -coated Si_3N_4 waveguide platform.

4.3. Internal Net Gain in Erbium-Doped Waveguide Amplifiers

To operate as a gain medium for amplification/lasing, it is necessary for a large quantity of erbium ions to be excited to the $^4\text{I}_{13/2}$ energy states through an external mechanism in order to achieve population inversion. The most common excitation method for rare-earths is optical pumping through high power laser light launched into the waveguide. In the case of amplification the pump is multiplexed with a lower power signal which is amplified as it propagates in the waveguide, while in the case of lasing, an initial spontaneous emission event leads to stimulated emission and laser photons built up in a resonant cavity structure [62,61,93,94]. As discussed in the absorption saturation measurements in section 4.2.5, a single wavelength travelling through an erbium-doped waveguide will always experience a net absorption. Erbium amplifiers operating in the C-band (1530-1565 nm) can be pumped using either a ~970 or ~1470 nm source to excite ions to the $^4\text{I}_{11/2}$ or $^4\text{I}_{13/2}$ state, respectively. Pumping with a 970 nm source creates a 3-level energy system, where ground state electrons are excited into the $^4\text{I}_{11/2}$ state by optical absorption and then rapidly decay into the $^4\text{I}_{13/2}$ state. The use of a three-level system allows near total inversion of the ground state into the $^4\text{I}_{13/2}$ emission state, which allows the amplifier to reach its maximum possible gain. Alternatively, 1470 nm wavelength pumps operate as a 'quasi' three-level system, pumping ions into the upper Stark levels of the $^4\text{I}_{13/2}$ manifold followed by rapid thermal decay to the lower Stark levels in the same manifold before experiencing stimulated emission. However, in this case because the pump will also induce stimulated emissions from the $^4\text{I}_{13/2}$ state it prevents total inversion, instead limiting the inversion ratio to roughly 80 % depending on the exact pump wavelength and absorption/emission cross section ratio of the material. While this would suggest 970 nm pumps are preferable, the larger background optical propagation losses

expected for 970 nm wavelengths in the waveguide, reduced mode overlap and the energy lost when electrons decay from the $^4I_{11/2}$ to the $^4I_{13/2}$ states lead to lower efficiency compared to 1470 nm pumping. Here we study amplification in $\text{TeO}_2:\text{Er}^{3+}\text{-Si}_3\text{N}_4$ waveguides using both 970 and 1470 nm pump wavelengths.

The properties of the $\text{TeO}_2:\text{Er}^{3+}$ film for the gain sample are listed in Table 4.1, but are revisited and described in more detail here. Gain measurements were carried out in 2.2-cm-long straight and 6.7 paperclip waveguides with Si_3N_4 strip widths of $1.0\ \mu\text{m}$ (see design in Section 3.2, Chiplet B). The chip was coated in a 340-nm thick $\text{TeO}_2:\text{Er}^{3+}$ film with an erbium concentration of 2.2×10^{20} ions/ cm^3 . The chip was then top-cladded in a spin-on Cytop layer. Based on simulations, the waveguide supported a single, transverse-electric (TE) polarized mode at 1550 nm with a mode area of $1.1\ \mu\text{m}^2$ and 60 % optical overlap with the $\text{TeO}_2:\text{Er}^{3+}$ film. The background optical propagation loss of the waveguide was estimated using the ring resonators of a separate Si_3N_4 chip (see design in Section 3.2, Chiplet C) coated in the same $\text{TeO}_2:\text{Er}^{3+}$ film and Cytop cladding as the gain sample. A 400- μm -radius ring resonator with a nominal coupling gap of $2.6\ \mu\text{m}$ was fit using coupled mode theory to have an internal Q factor of 1.3×10^6 at 1637 nm as shown in Figure 4.14(a), corresponding to a propagation loss of approximately 0.25 dB/cm in the waveguide. This demonstrates an improvement over the waveguide losses of 0.8 dB/cm in cutback structures and 0.5 dB/cm in ring resonators coated in passive TeO_2 films for this platform. Low optical propagation losses such as this are important for achieving internal net gain and high performance amplifiers.

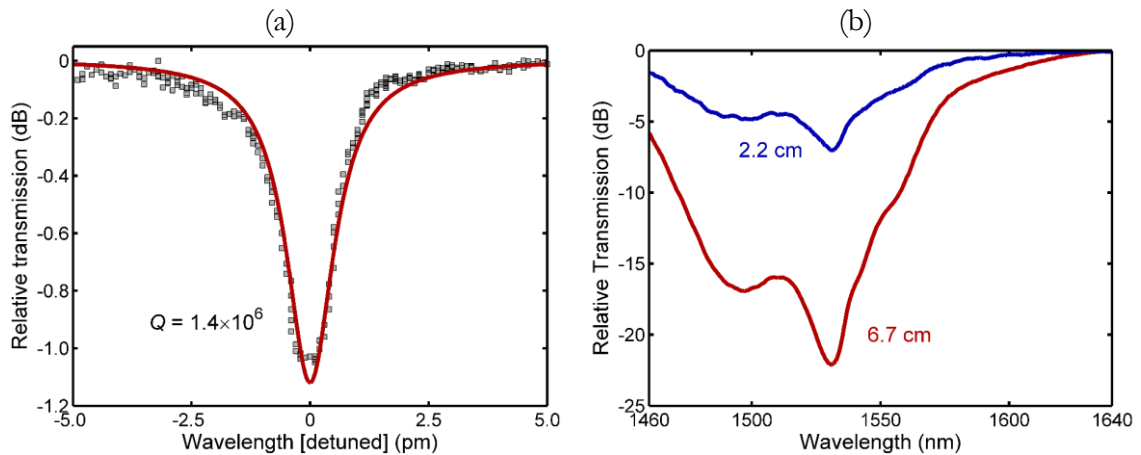


Fig. 4.14. (a) 1637 nm resonance mode measured on a $1.0\text{-}\mu\text{m}$ -wide, $400\text{-}\mu\text{m}$ -radius silicon nitride ring resonator with a gap of $2.6\ \mu\text{m}$, coated in the same $\text{TeO}_2:\text{Er}^{3+}$ film as the gain sample, fit to have a Q factor of 1.3×10^6 . (b) Measured erbium absorption losses from 1460 to 1640 nm across 2.2- and 6.7-cm-long waveguides, indicating a peak absorption of approximately 3.2 dB/cm at 1531 nm.

Transmission measurements were carried out using a passive fiber-chip coupling setup, to characterize losses from 1460 to 1640 nm. The insertion losses were found to be 12.1 and 20.1 dB for the 2.2- and 6.7-cm-long waveguides at 1640 nm, which correspond to an estimated 11.5 and 19.1 dB of total coupling loss after subtracting the expected 0.25 dB/cm of waveguide

propagation loss, respectively. The large variability in coupling loss between the different waveguide samples is a result of this chip having unpolished diced facets, which were shown in section 3.4.2 to have a large variation in coupling losses. Using the method described in section 4.2.3, where the background waveguide loss and coupling loss were assumed to be constant across the measured range, the erbium absorption loss was obtained. Figure 4.14(b) shows the calculated erbium absorption loss versus wavelength from 1460 to 1640 nm for the 2.2- and 6.7-cm-long waveguide samples, with a peak absorption of 3.2 dB/cm at 1531 nm, which was used to calculate an erbium concentration of 2.2×10^{20} ion/cm³.

The ⁴I_{13/2} luminescent lifetime was calculated by the method discussed earlier using the setup of Fig. 4.8. The measured ASE intensity versus time after the optical pump was turned off for this waveguide can be seen in Fig. 4.15(a), which was fit to have an excited state lifetime of 480 μs. Quenched ion measurements were also carried out using the setup of Fig. 4.11 to characterize absorption saturation of a high power signal input, with the measured relative erbium absorption versus signal power compared to the peak absorption at small signal powers for the 2.2-cm-long waveguide plotted in Fig. 4.15(b). The data was fit using the rate equation model described in Section 4.4 yielding a fast-quenched erbium ion fraction of 22%.

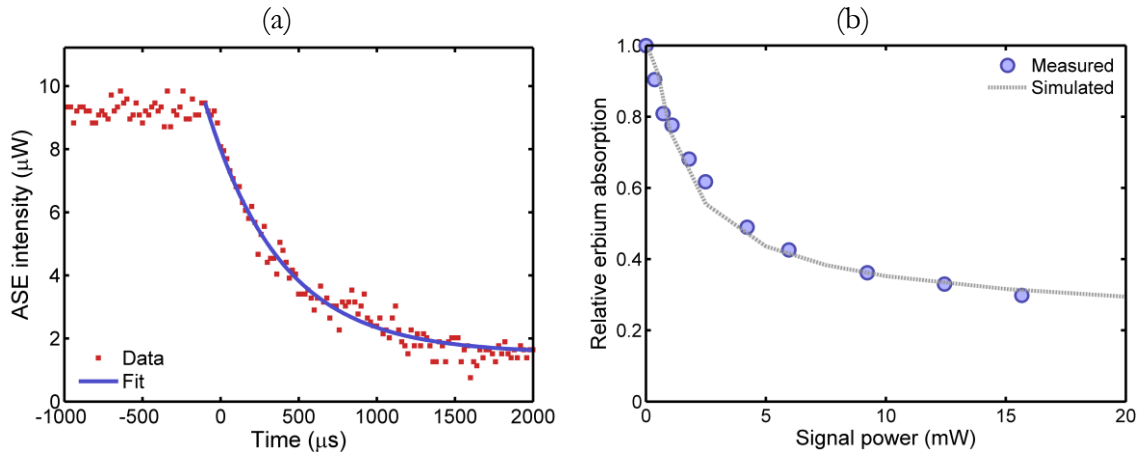


Fig. 4.15. (a) ASE intensity versus decay time measured on the sample selected for gain measurements using the luminescent lifetime setup, fit to give a lifetime of 048 ms. (b) Relative erbium absorption in a 2.2-cm-long waveguide versus launched signal power, fit to give a quenched ion fraction of 22%.

The optical properties of the waveguide around both the signal and pump wavelengths are of importance when considering the amplifier performance. For a 1470 nm pump the waveguide properties are generally considered to be the similar to the 1550 nm signal, with the background optical waveguide loss assumed to be equal, and absorption/emission cross sections of both characterized together as shown in Fig. 4.7. However, as observed in the cutback measurements in undoped TeO₂-Si₃N₄ waveguides in section 3.4.1, the waveguide loss in this platform is higher at 970 nm. To characterize the background waveguide loss a spectral measurement of a ring resonator with a radius and nominal coupling gap of 300 μm and 1.0

μm , respectively, and coated in the same $\text{TeO}_2\text{:Er}^{3+}$ film was taken around 940 nm, and the transmission data is plotted in Fig. 4.16. It is assumed that there is minimal erbium-related absorption loss at this wavelength, such that the ring loss represents the background optical propagation loss for 970 nm pump light. The resonance mode was fit with a Q factor of 2.5×10^5 which corresponds to a propagation loss of 2.5 dB/cm. This is slightly lower than the waveguide loss measured in cutback structures on passive TeO_2 -coated Si_3N_4 waveguides in Section 3.4.1. As well as different background losses, 970 nm pumping leads to a ground state absorption transition between the ${}^4\text{I}_{15/2}$ and ${}^4\text{I}_{11/2}$ states, which has a peak absorption cross section of $2.8 \times 10^{20} \text{ cm}^2$ at a 968 nm, as displayed in Fig. 4.6.

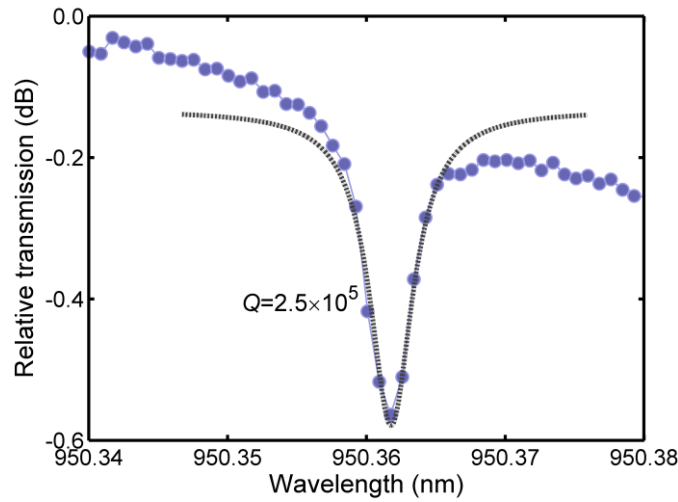


Fig. 4.16. 940 nm resonance mode measured in a 1- μm -wide, 300- μm -radius $\text{TeO}_2\text{:Er}^{3+}$ -coated silicon nitride ring resonator with a nominal coupling gap of 1.0 μm . The resonance is fit to have a Q factor of 2.5×10^5 , corresponding to an estimated optical propagation loss of 2.5 dB/cm at this wavelength.

Gain measurements were carried out using the double-side pumping setup shown in Fig. 4.17(a). The input side combines signal light from a tunable C-band laser, with pump light from either a 500-mW 970 or 300-mW 1470 nm pump diode using a wavelength-division multiplexor (WDM). Each arm on the input side of the WDM has its own set of polarization paddles, such that the polarization of each source can be independently orientated to the TE-polarized mode of the chip. To prevent the high powers of the pump from burning fiber connectors, the pump diode, polarization paddles and WDM connections were fused together using a splicer. The combined light sources on the multiplexed side of the WDM were then connected to a 2.5- μm -spot-size 1550 nm tapered fiber that was aligned to the input facet of the waveguide under test. Due to the losses through the polarization paddles and WDM the pump power for both pump wavelengths at this stage was typically below the threshold where damage to fiber connectors becomes likely ($\sim 300 \text{ mW}$). Therefore, the WDM-to-tapered fiber connection was made with FC/APC connectors rather than splicing, to allow the setup to more easily be switched between the 970 and 1470 nm pumps. However, the connectors had to be thoroughly cleaned with fiber cleaning cloth and checked before use to prevent potential

damage. At the chip output, the transmitted light was coupled to a similar tapered fiber, where it was routed to another WDM which was used to separate the residual pump light and signal light. The signal arm on the demultiplexed side of the WDM was then coupled through a fiber-to-free-space-to-fiber mount with a 1500 nm long pass filter to further prevent any pump light from reaching the detector and to reduce the ASE noise measured at the detector. A second 970 or 1470 nm pump diode, from the demultiplexed pump arm of the output facet WDM, was used to launch counter-propagating pump light onto the chip for double-sided pumping measurements. The incident pump power available from each side of the chip was characterized by launching the output power from the tapered fibers onto a free space optical power meter. The 970 nm pump diodes were found to provide maximum incident powers of up to 230 mW from each side, while the 1470 nm pump diodes were found to provide maximum incident powers of 200 mW. The maximum 970 or 1470 nm pump power that could be launched into the 2.2- and 6.7-cm-long samples was determined to be approximately 100 and 40 mW, respectively, after accounting the variable coupling losses in the two samples. An image of the 6.7-cm-long waveguide in the measurement setup as its excited by the 970 nm pump diodes is displayed in Fig. 4.17(b), where the green luminescence of radiative decays from the upper ${}^2\text{H}_{11/2}$ or ${}^4\text{S}_{3/2}$ state can be observed.

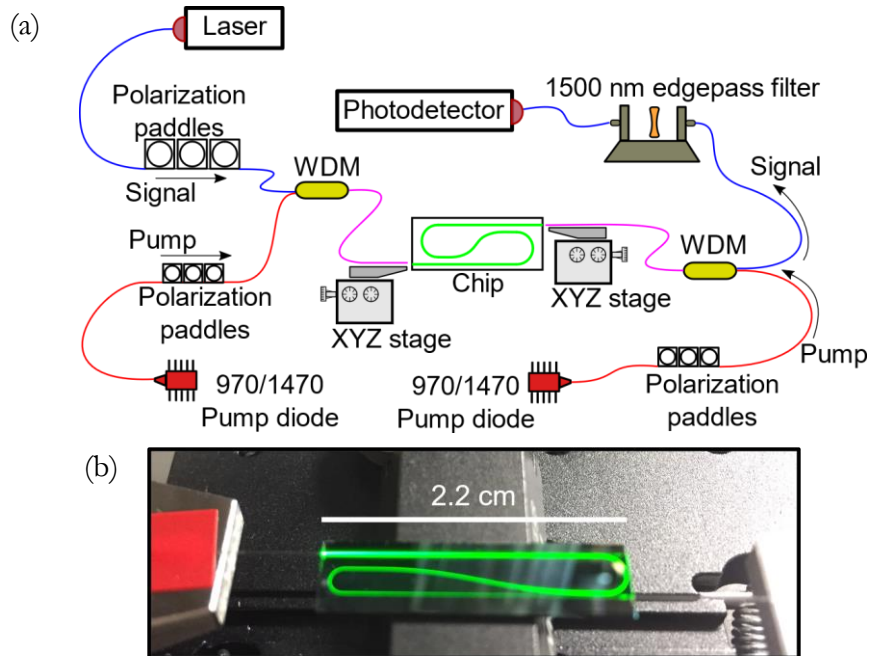


Fig. 4.17. (a) Diagram of double-side pump measurement setup used to measure gain in $\text{TeO}_2:\text{Er}^{3+}$ amplifiers. (b) Image of a $\text{TeO}_2:\text{Er}^{3+}$ paperclip amplifier pumped with a 970 nm diode laser exhibiting green luminescence from radiative decays from the ${}^4\text{F}_{7/2}$ state.

Due to the bandwidth of the WDMs, gain measurements were limited to between 1530 and 1570 nm to maintain measurable transmitted signal powers across the system. The transmitted signal power (in linear units) was initially measured in the gain setup with the pump diodes turned off ($P_{\text{unpumped}}(\lambda)$). The pumps were then turned on and the pump power was

gradually increased in several increments, equally between the forwards and backwards pump, such that a given total pump power P was launched into the waveguide, with a signal transmission measurement made at each increment by scanning the tunable laser from 1530–1570 nm ($P_{\text{pumped}}(\lambda, P)$). When pumped the waveguide produces an ASE output from spontaneous decays in addition to amplifying the signal through stimulated emissions. To avoid quantifying the ASE as signal gain before each measurement the signal laser was turned off and the ASE power was measured for each pump power ($P_{\text{ASE}}(P)$). The transmitted signal power for the pump-probe measurements was then taken as the measured power with the pump and signal on minus the measured power with just the pump on. The difference in transmission measured when the waveguide was pumped compared to the unpumped passive measurement was then taken as the optical signal enhancement ($SE(\lambda, P)$), calculated in the dB scale as shown in Equation 4.17,

$$SE(\lambda, P) = 10 \log_{10} \left(\frac{P_{\text{pumped}}(\lambda, P) - P_{\text{ASE}}(P)}{P_{\text{unpumped}}(\lambda)} \right). \quad 4.17$$

To achieve internal net gain, the signal launched into the chip must overcome both the erbium absorption losses and the background optical propagation losses of the waveguide. Therefore, to calculate the internal net gain ($g(\lambda, P)$) the erbium absorption and background waveguide losses were subtracted from the measured signal enhancement as shown in Equation 4.18,

$$g(\lambda, P) = SE(\lambda, P) - L_{\text{Er}}(\lambda) - L_{\text{WG}}. \quad 4.18$$

The internal net gain measured in the 2.2-cm-long waveguide sample is shown in Fig. 4.18. The gain is seen to reach a peak of 3.8 and 3.1 dB at 1533 nm which corresponds to a gain per unit length of 1.7 and 1.4 dB/cm, for 970 and 1470 nm pumps, respectively. Considering a calculated optical confinement factor of 60% in the $\text{TeO}_2:\text{Er}^{3+}$ film in this waveguide structure this corresponds well to the peak net gain of 2.8 dB/cm measured in $\text{TeO}_2:\text{Er}^{3+}$ ridge waveguides [25,26]. As seen in the internal net gain versus launched pump power plots of Fig. 4.18(a), the gain was observed to approach saturation at a launched pump power of approximately 60 mW. The slightly higher gain measured for the 970 versus 1470 nm pump is the result of the lower population inversion that can be obtained with a 1470 nm pump, which particularly limits peak gain at a signal wavelength of 1533 nm where the absorption and emission cross sections are approximately equal. This can be seen in the gain versus wavelength curve at maximum pump power for 1470 versus 970 nm wavelengths shown in Fig. 4.18(b), where the net gain achieved for the different pump wavelengths converges to similar values at longer wavelengths due to the significantly smaller absorption cross section compared to the emission cross section.

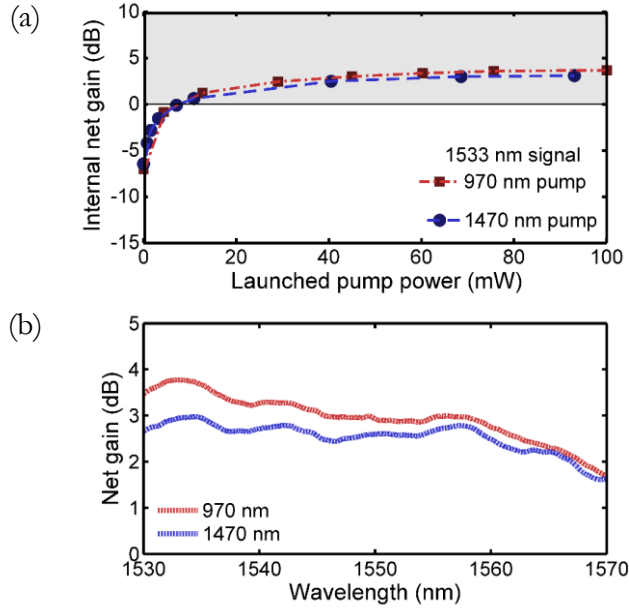


Fig. 4.18. Internal net gain measured in a 2.2-cm-long $\text{TeO}_2\text{:Er}^{3+}$ -coated Si_3N_4 waveguide amplifier versus (a) launched pump power at a 1533 nm signal wavelength, and (b) wavelength at maximum available pump power for both 970 and 1470 nm pump wavelengths.

The internal net gain versus launched pump power at 1558 nm and gain versus wavelength at maximum pump power measured in the 6.7-cm-long $\text{TeO}_2\text{:Er}^{3+}$ - Si_3N_4 waveguide are shown in Fig. 4.19(a) and 4.19(b), respectively. The internal net gain reached peak values of 1.1 and 5.0 dB at 1558 nm, corresponding to 0.2 and 0.8 dB/cm gain per unit length for the 970 and 1470 nm pumps, respectively. Because of its higher fiber-chip coupling loss, the maximum pump power launched onto this waveguide was limited to approximately 40 mW. The primary reason for the reduced gain per unit length in this sample was that the launched pump power did not approach the values required for gain saturation, which can be seen in the shape of the gain curves of Fig. 4.19(b), where the gain is not maximum at the emission peak around 1533 nm. For 1470 nm pumping > 3 dB gain was achieved across the C band in this sample. However, if enough pump power was launched such that the same gain per unit length gain as the 2.2-cm-long sample could be reached, the gain would have exceeded a peak of over 10 dB at 1533 nm and 7 dB across the C band. Pumping the waveguide at 970 nm was observed to be much less efficient than 1470 nm pumping, requiring launched pump powers of over 25 mW to reach the threshold for internal net gain. The large inefficiency was assumed to be a result of the relatively large background optical propagation loss at 970 nm of 2.5 dB/cm, which makes it difficult to invert erbium ions near the middle of the waveguide. In comparison, the low background waveguide loss expected around 1470 nm and the high pump-signal overlap makes pumping at this wavelength highly efficient, where only 7 mW of launched pump power was required to reach the threshold for internal net gain across the 6.7-cm-long waveguide sample.

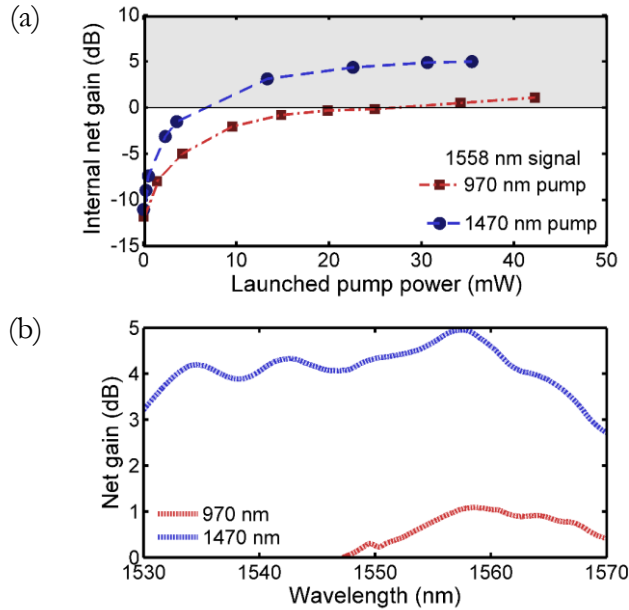


Fig. 4.19. Internal net gain measured in a 6.7-cm-long $\text{TeO}_2\text{:Er}^{3+}$ -coated Si_3N_4 waveguide amplifier versus (a) launched pump power at a 1533 nm signal wavelength, and (b) wavelength at maximum available pump power for both 970 and 1470 nm pump wavelengths.

The prior gain measurements were carried out in the small signal regime, with the output power of the tunable laser adjusted such that the power incident on the chip from the fiber was -10 dBm, resulting in estimated launched signal powers of -16 and -20 dBm for the 2.2- and 6.7-cm-long waveguides, respectively. This output power was used to maintain optical transmission values which were significantly greater than the ASE, which reached up to -33 dBm of ASE power measured at the detector when maximum pump powers were used, to reduce noise in the measured gain. While at maximum gain for the 1470 nm pump, the output power of the signal laser was also varied for each waveguide to characterize the gain versus signal power. The results are shown in Fig. 4.20, where the output power of the signal laser was increased to the maximum available 0 dBm incident from the fiber, corresponding to a launched signal power of -6 and -10 dBm in the 2.2- and 6.7-cm-long waveguide, respectively. No significant change in internal net gain is observed. This aligns well when compared to simulations, also shown in Fig. 4.20, using the model developed in the following section. The model predicts similar gain for launched signal powers of up to 0 dBm in the 2.2-cm-long waveguide amplifier. The 6.7-cm-long waveguide sample predicts an earlier roll-off, but it is believed that high levels of gain could be maintained up to launched signal powers > 0 dBm if enough pump power is launched onto the chip to fully invert the waveguide, as shown by the simulated curve for a pump power of 100 mW. The ability of the waveguide to maintain peak net gain up to reasonably large signal powers is predominantly attributed to the compact mode areas of the waveguide and low background propagation loss.

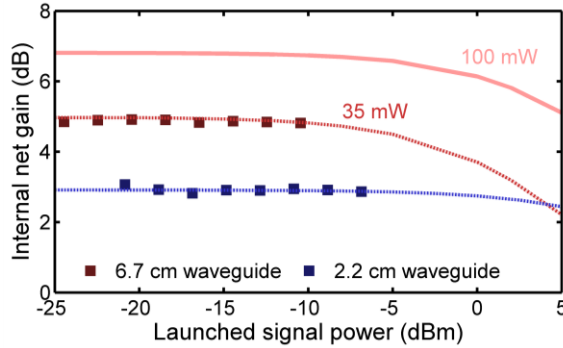


Fig. 4.20. Measured and simulated internal net gain at 1558 nm versus launched signal power for the 2.2- and 6.7-cm-long waveguide samples pumped at 1470 nm. Minimal change in net gain is measured up to launched signal powers of -6 and -10 dBm in the 2.2- and 6.7-cm-long waveguides respectively, in agreement with predictions from simulations.

4.4. Erbium-Doped Waveguide Rate Equation Modelling and Amplifier Optimization

To investigate the optimization and potential future performance metrics of the $\text{TeO}_2\text{:Er}^{3+}$ -coated Si_3N_4 waveguide amplifier platform a rate equation model was developed. Although the relatively long ${}^4\text{I}_{11/2}$ lifetimes measured in bulk glass TeO_2 of 0.26 ms [92] would typically necessitate a six-level rate equation model to properly account for excited-state absorption and energy transfer upconversion from the ${}^4\text{I}_{11/2}$ state, the lower ${}^4\text{I}_{13/2}$ luminescent lifetime than than the radiative lifetime measured in our thin films is expected to result in a similarly reduced ${}^4\text{I}_{11/2}$ lifetime. While the ${}^4\text{I}_{11/2}$ lifetime was not measured in our films, scaling its value by the same ratio of our ${}^4\text{I}_{13/2}$ lifetime compared to the fiber in reference [92] predicts a 0.04 ms ${}^4\text{I}_{11/2}$ lifetime. Therefore, the effects of excited state absorption and the upper energy levels on the erbium energy system are expected to be minimal, and a three-energy-level rate equation system was deemed sufficient to model our $\text{TeO}_2\text{:Er}^{3+}$ amplifiers, although the model was designed in a way such that it can easily be modified to a six-level system. The three-level energy system used here accounts for stimulated absorption and emission transitions between the ${}^4\text{I}_{15/2}$ ground state and the ${}^4\text{I}_{13/2}$ excited state, as well as stimulated transitions between the ground state and ${}^4\text{I}_{11/2}$ excited state. The model also accounts for spontaneous decay of the ${}^4\text{I}_{13/2}$ and ${}^4\text{I}_{11/2}$ states but makes no distinction between the different radiative and non-radiative decay mechanisms, referring just to the luminescent lifetime. It is also assumed that all ions in the ${}^4\text{I}_{11/2}$ state decay directly to the ${}^4\text{I}_{13/2}$ state. Lastly energy transfer upconversion (ETU) of electron pairs in the ${}^4\text{I}_{13/2}$ state into the ${}^4\text{I}_{15/2}$ and ${}^4\text{I}_{11/2}$ state are considered. Although, as seen in Fig. 4.3 one of the electrons in this ETU process is excited to the ${}^4\text{I}_{9/2}$ state, it is assumed that because of the short lifetime of this state the electron effectively instantly decays back to the ${}^4\text{I}_{11/2}$ state, as if it was initially promoted to this state. A summary of the relevant transitions used in this model can be seen in Fig. 4.21.

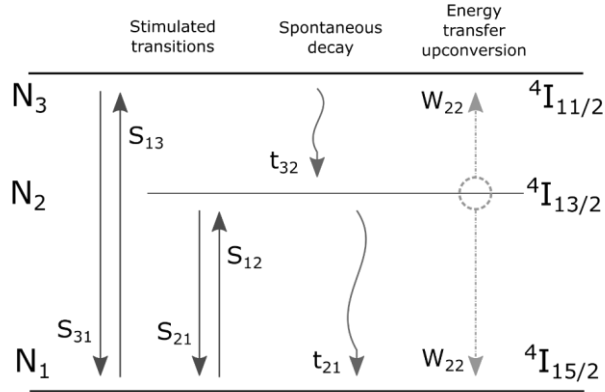


Fig. 4.21. Three-energy-level diagram for erbium-doped TeO₂ and relevant transitions used in device simulations, including: stimulated transitions between the ground state and the second or third energy levels, spontaneous decay of the third and second energy levels, and energy transfer upconversion of two second level electrons to the ground state and third energy level.

The use of rate equation models to simulate optical amplifiers can generally be broken down into a cyclic set of two calculations: 1) calculation of the time dependent change in the ion populations at the different energy levels based on the intensity of the light travelling through the medium, and 2) calculation of the propagation distance dependent changes to light intensity as it travels through the medium based on the ion populations of the different energy levels. While analytical solutions to the rate equation model at steady state can be developed, solutions for systems with a large number of energy-levels and higher order effects such as ion quenching are cumbersome to be derived analytically. Numerically solving the rate equations is a more versatile method, if, for example, one wishes to consider the influence of additional processes and/or extend the model beyond a three-level approximation. Therefore, a numerical solution method is implemented here, where the model recursively solves the ion energy level populations and optical intensity equations until a steady-state solution for both can be found.

4.4.1. Energy-Level Population Dynamics

To build a self-consistent energy level transition model that can be easily altered to systems with a greater or fewer number of energy levels, all electronic transitions of the system are described in an $n \times n$ transition matrix (T), where n is the number of energy levels of the system being modelled. The ground state of the energy system is considered energy level 1 with each successive excited state incremented by one. For the three-level erbium rate equation implemented here the ${}^4I_{15/2}$ state is considered the first energy level (1), while the ${}^4I_{13/2}$ and ${}^4I_{11/2}$ states are considered the second (2) and third (3) energy levels respectively. An electron transition from an initial energy level A to its destination energy level B, would then be described as a variable in the Ath row and Bth column of the transition matrix. As the transitions

resulting from each mechanism vary depending on different factors related to the photon flux and ion populations, an individual set of material parameter matrices for each transition mechanism are initially determined. Firstly, we consider spontaneous decay, which is described by the γ parameter matrix. Spontaneous decay occurs from the ${}^4I_{13/2}$ state (level 2) to the ${}^4I_{15/2}$ state (level 1) based on the ${}^4I_{13/2}$ luminescent lifetime (t_{21}), measured earlier to be 0.48 ms. As this is a transition from energy level 2 towards 1 it is described in the 2nd row and 1st column of the matrix. A similar parameter is included in the 3rd row and 2nd column of the matrix to represent the ${}^4I_{11/2}$ to ${}^4I_{13/2}$ spontaneous decay, estimated to have a lifetime (t_{32}) of 0.04 ms. The spontaneous decay rate parameter matrix can then be described using the inverse of the lifetimes as shown in Equation 4.19,

$$\gamma = \begin{bmatrix} 0 & 0 & 0 \\ 1/t_{21} & 0 & 0 \\ 0 & 1/t_{32} & 0 \end{bmatrix}. \quad 4.19$$

Next, we consider the influence of stimulated transitions on the rate equations. Stimulated transitions will occur as a result of both the pump (σ^p) and signal (σ^s), and are both treated with their own parameter matrices. Stimulated transition parameter matrices will have both an absorption (σ_{abs}) and emission (σ_{em}) component, equal to the cross sections determined for the exact wavelengths earlier in the chapter. For the pump parameter matrix, the position of the cross sections in the matrix will depend on whether a 970 nm pump, resulting in transitions between the 1st and 3rd energy levels, or a 1470 nm pump, resulting transitions between the 1st and 2nd energy levels, is used. An example of the pump transition parameter matrix for each wavelength can be found as follows:

$$\begin{aligned} \sigma^p(970) &= \begin{bmatrix} 0 & 0 & \sigma_{\text{abs}}^p \\ 0 & 0 & 0 \\ \sigma_{\text{em}}^p & 0 & 0 \end{bmatrix}, \\ \sigma^p(1470) &= \begin{bmatrix} 0 & \sigma_{\text{abs}}^p & 0 \\ \sigma_{\text{em}}^p & 0 & 0 \\ 0 & 0 & 0 \end{bmatrix}, \end{aligned} \quad 4.20$$

while the signal stimulated transition parameter matrix is described similarly, using the cross section values for the signal wavelength under consideration as:

$$\sigma^s = \begin{bmatrix} 0 & \sigma_{\text{abs}}^s & 0 \\ \sigma_{\text{em}}^s & 0 & 0 \\ 0 & 0 & 0 \end{bmatrix}. \quad 4.21$$

The consideration of energy transfer upconversion is described by the upconversion parameter matrix W . The ETU process of interest for this model considers ion pairs in the 2nd energy level that result in the promotion of one ion to the 3rd level while the other decays to the 1st level. The resulting upconversion parameter matrix would then be described with an upconversion parameter $W_{2\text{ETU}}$ as follows in Equation 4.22,

$$W = \begin{bmatrix} 0 & 0 & 0 \\ W_{2\text{ETU}} & 0 & W_{2\text{ETU}} \\ 0 & 0 & 0 \end{bmatrix}. \quad 4.22$$

The parameter matrices seen in Equations 4.19 through 4.22 describe only the constant material parameters that affect electronic transitions of the erbium dopants. However, the electron transition rates depend on both the material parameters and the variable population density of ions in each energy state and, for the case of stimulated transitions, the photon flux. To account for this a population matrix (N) is filled during each loop through the solution algorithm, described by Equation 4.23 as follows,

$$N = \begin{bmatrix} N_1 & N_1 & N_1 \\ N_2 & N_2 & N_2 \\ N_3 & N_3 & N_3 \end{bmatrix}, \quad 4.23$$

where N_1 , N_2 and N_3 are the population densities of ions in each energy level for the time step under consideration, the sum of which is equal to the total dopant concentration (N_{Er}). The total transition matrix can then be found by combining the contribution from the four different transition mechanisms. As described earlier in Equations 4.3 and 4.5 stimulated transitions are proportional to the cross section and energy level population matrices, as well as the photon flux, which can be treated as a scalar quantity in this context and is found from the optical intensity solution part of the algorithm. Spontaneous decays, as described in Equation 4.1, are proportional only to the energy level population of the excited state and the spontaneous decay rate. Because ETU relies on ion pairs its occurrence rate is proportional to the square of the excited state population density and the ETU parameter [95]. The total transition matrix is then described as follows:

$$T = N \cdot \sigma^s \cdot \phi_s + N \cdot \sigma^p \cdot \phi_p + N \cdot \Gamma + N^2 \cdot W, \quad 4.24$$

where piecewise multiplication of the parameters in Equation 4.24 yields the net transition matrix of the system, describing all the modelled transitions of the system as T in the following equation, considering a 970 nm pump source:

$$T = \begin{bmatrix} 0 & N_1 \cdot \sigma_{abs}^s \cdot \phi_s & N_1 \cdot \sigma_{abs}^p \cdot \phi_p \\ N_2 \cdot \sigma_{em}^s \cdot \phi_s + \frac{N_2}{t_{21}} + N_2^2 \cdot W_{2ETU} & 0 & N_2^2 \cdot W_{2ETU} \\ N_3 \cdot \sigma_{em}^p \cdot \phi_p & \frac{N_3}{t_{32}} & 0 \end{bmatrix}. \quad 4.25$$

The total transition matrix can then be used to determine the rate of population change of the different levels of the system. Based on the way the individual matrices have been setup elements of the matrix along the j^{th} row describe transitions away from the j^{th} energy level, while elements of the matrix along the i^{th} column describe transitions towards the i^{th} energy level. The rate of population change for each energy level can then be found by summing transitions along the column and subtracting transitions along the row as shown in Equation 4.26 as follows:

$$\frac{dN_j}{dt} = \sum_{i=1}^n (T_{ij} - T_{ji}). \quad 4.26$$

As discussed throughout this Chapter ion quenching plays a significant role in the $\text{TeO}_2:\text{Er}^{3+}$ amplifiers. However, to this point the development of the model has assumed that all ions are active. To account for quenching the model is adjusted by dividing the total ion population into an active portion and a fast-quenched portions each of which have independently solved rate equations. The dopant concentration of active ($N_{\text{Er,Active}}$) and quenched ($N_{\text{Er,Quench}}$) ions are then found based on the total dopant concentration as shown below:

$$\begin{aligned} N_{\text{Er,Active}} &= (1 - f_q)N_{\text{Er}}, \\ N_{\text{Er,Quench}} &= (f_q)N_{\text{Er}}, \end{aligned} \quad 4.27$$

where f_q is the fraction of quenched ions in the sample. Active ions are then treated as just discussed in Equations 4.19 through 4.26, only using the active dopant concentration instead of the total dopant concentration. Quenched ions are also solved similarly, but in addition to using the quenched dopant concentration, use significantly reduced excited state lifetimes in a modified spontaneous decay parameter matrix, assumed here to be $1 \mu\text{s}$ [90] for all excited states.

4.4.2. Change in Optical Power

While it is important to determine the population densities of the different energy levels, the primary goal of the amplifier simulation is to analyze the effect on the power of the light travelling through the system. The net change in photon flux from Equation 4.9 describes the change in photon flux per unit distance as a result of absorption and emission events in the erbium dopants. In developing the model it makes sense to consider the spatially-dependent

optical intensity of the light, I , which can be proportionally related to the photon flux by Equation 4.28 as follows:

$$I = \frac{hc}{\lambda} \phi , \quad 4.28$$

where h is the Planck constant, c is the speed of light in a vacuum, and λ is the wavelength of light under consideration. The differential equation of Equation 4.9 for the photon flux can then also be solved for the optical intensity. In addition to the contribution of erbium dopants to the change in optical intensity through the waveguide, the background propagation loss must be accounted for. From the Beer-Lambert law, the background propagation loss can be converted to an optical attenuation coefficient μ_{WG} , related to the background waveguide loss per unit length (A) as described in Equation 2.14 and added to the intensity relationship. The change in optical intensity over a distance dz for an initial intensity at position z can then be described as follows,

$$I_s(z + dz) = I(z)e^{(N_2\sigma_{em}^s - N_1\sigma_{abs}^s - \mu_{\text{WG,Signal}})dz} . \quad 4.29$$

Therefore, given an initially launched signal power ($I(z = 0)$) in the waveguide, the change in intensity can be calculated based on the energy level population densities determined from the rate equations discussed in the previous subsection and known background loss. As well as the signal intensity the optical intensity of the pump travelling through the waveguide must be similarly found, which is determined based on the populations in ground state and the third energy level for a 970 nm pump, or the second level for a 1470 nm pump as follows in Equations 4.30 and 4.31 respectively:

$$I_p(z + dz) = I(z)e^{(N_3\sigma_{em}^p - N_1\sigma_{abs}^p - \mu_{\text{WG,Pump}})dz} , \quad 4.30$$

$$I_p(z + dz) = I(z)e^{(N_2\sigma_{em}^p - N_1\sigma_{abs}^p - \mu_{\text{WG,Pump}})dz} . \quad 4.31$$

While these equations refer to intensity, which can vary based on the shape and mode area of the signal under consideration, the experimental measurements of waveguides are made in regards to power (P), which is equal to the integral of the intensity distribution of the light over its cross sectional area, described as follows:

$$P = \int I \cdot dA . \quad 4.32$$

To a first order approximation the power can simply be integrated over the optical mode area found from simulation to approximate a uniform optical intensity. However, the unique shape of the optical mode profile results in the areas near the center of the mode experiencing much greater intensity than at the edges. Additionally, a non-negligible portion of the mode in our hybrid $\text{TeO}_2:\text{Er}^{3+}\text{-Si}_3\text{N}_4$ waveguide design will travel through the Si_3N_4 strip and cladding regions where it will experience no interaction with the erbium dopants. Therefore, to account

for these effects in these simulations the mode was separated into an XY grid of $0.25 \mu\text{m} \times 0.15 \mu\text{m}$ areal elements of area dA . This grid size was found to provide a good compromise between accurate mode modeling and an acceptable simulation time for running the rate equation model. Firstly, each element was evaluated based on whether it was positioned in the $\text{TeO}_2:\text{Er}^{3+}$ coating, deemed active elements, or outside this area, deemed passive elements. Each active element was then characterized based on the fractional element (F_k) of the optical mode intensity that resided in that areal element. An example of the simulated optical mode and the approximated optical mode for rate equation modeling when broken into its active areal elements can be seen in Fig. 4.22.

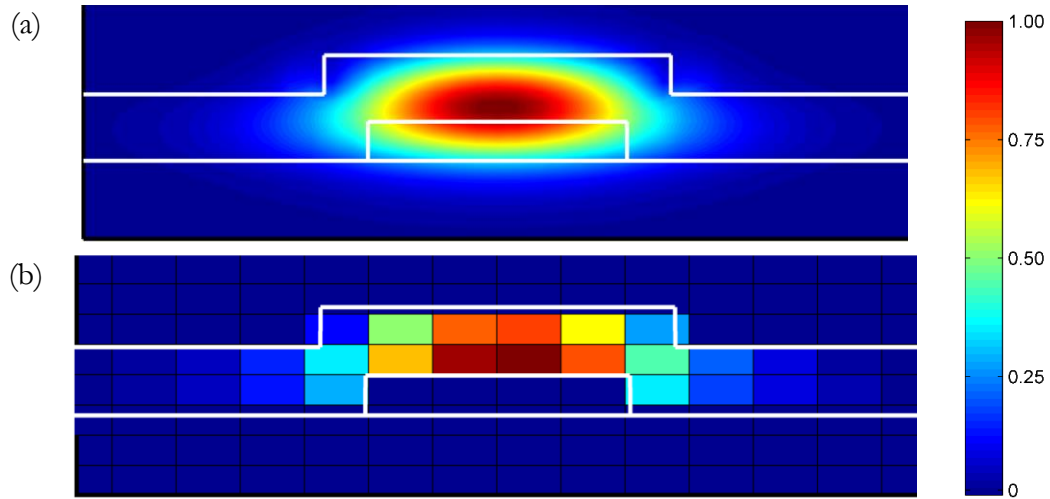


Fig. 4.22. (a) Optical mode profile determined by an eigenmode simulation, versus, (b) effective optical mode profile with 22 active areal elements representing the relative optical intensity in the gain medium applied in the rate equation solver.

The intensity in each active areal element can then be found as the total power multiplied by the fraction of power in the element and divided by the element area as shown in Equation 4.33 below:

$$I_k = \frac{P \cdot F_k}{dA}. \quad 4.33$$

A vector of all active areal elements with fractional elements of greater than 0.5 % of the total optical mode power is then made. Any remaining intensity that is not accounted for is then considered to be in a passive areal element with an intensity of I_L which can be found by Equation 4.34 as follows:

$$I_L = \frac{P}{dA} \left(1 - \sum F_k \right), \quad 4.34$$

where, as the passive elements do not interact with the erbium dopants, they experience only background waveguide loss and can be described as follows,

$$I_L(z + dz) = I_L(z)e^{(-\mu_{WG})dz} . \quad 4.35$$

The total power in the next step of the waveguide is then found from the sum of the fractional active areal elements and the passive element, as described by:

$$P(z + dz) = dA \left(\sum (I_k(z + dz)) + I_L(z + dz) \right) . \quad 4.36$$

where this method must be applied to both the pump and signal light travelling through the waveguide independently.

4.4.3. Rate Equation Model

The full rate equation model involves the cyclic solution of the time derivative ion population rate equations described in section 4.4.1 and the spatial intensity derivative described in section 4.4.2. The model starts with an initial ion population such that 98 % of total dopants (N_{Er}) are in the ground state (N_1), and 1% are in each of the other excited states (N_2 and N_3), with each active areal element having its own ion population. The small initial excited state population representing naturally thermally excited ions are required to prevent numerical errors in the simulation. Taking an initial launched pump and signal power at the input position of the waveguide, the total power is divided into the cross-sectional areal power and intensity elements of the waveguide determined from an optical mode simulation performed in RSoft. The population rate equations for each areal element at that z position are then determined by Equation 4.26 and updated in preparation for the next time step. For each element the optical intensity change is also calculated from Equation 4.29 for the signal and either Equation 4.30 or 4.31 for the pump depending on the pump wavelength. The powers of the active elements are then summed together with the passive power elements of Equation 4.35 to calculate the total optical power at the next z step based on Equation 4.36. This method is carried out along the length of the waveguide in L/dz steps. A dz value of 0.2 cm is typically used to optimize simulation time while maintain accurate solutions Once the end of the waveguide is reached, the simulation is rerun for the next time step, using the updated ion populations for each areal element. This process is iterated over multiple time steps of 250 ns until the calculated output power at the end of the waveguide returns a consistent solution in time. A demonstrative picture of the model operation and logic flow diagram can be found in Fig. 4.23.

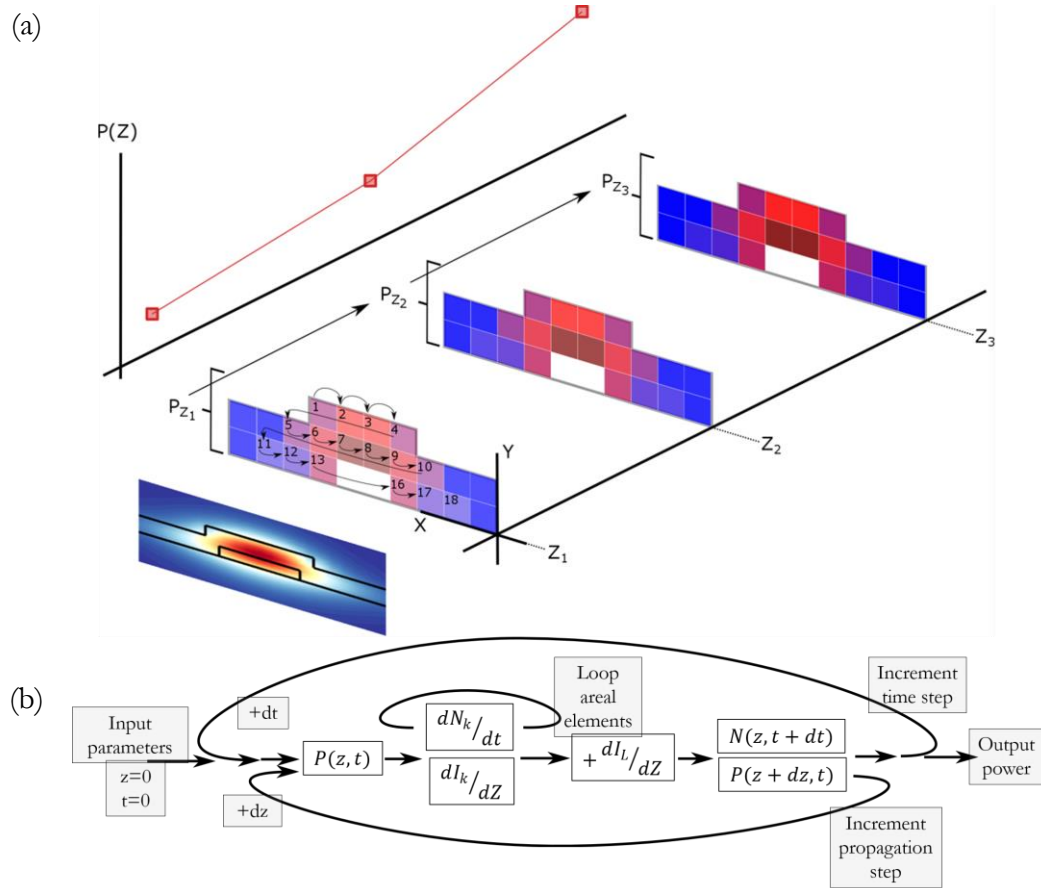


Fig. 4.23. (a) Diagram of operation method for rate equation model, where an initial optical power at a z position is broken down into areal elements based on the simulated mode profile. The population rate equations and intensity evolution are solved in each areal element, which then updates the initial power and intensities in the next z step along the length of the waveguide, where the process is repeated. (b) A more detailed logic flow diagram describing the rate equation model's calculation process.

As an example, Fig. 4.24(a) shows the simulated inversion ratio (N_2/N_1), averaged over each active element of the $\text{TeO}_2:\text{Er}^{3+}\text{-Si}_3\text{N}_4$ waveguide cross section versus propagation length, for launched 1470 pump powers of 1, 5 and 10 mW for the 140°C sample described in section 4.3. It can be seen that at larger pump powers the inversion ratio is larger, and as the pump propagates along the waveguide the level of inversion decreases due to the absorption and background loss. Figure 4.24(b) shows the simulated small-signal internal net gain at 1558 nm versus propagation length for the same system. It can be seen by comparing the two diagrams that when the inversion ratio is greater than 1 the internal net gain tends to increase, while when the inversion ratio is less than 1 the internal net gain tends to decrease. The simulations were run with dz set at 0.2 cm and dt set at 250 ns until the internal net gain measured at the end of the waveguide approached a constant value in time, which can be seen in the measured internal gain versus simulation time plots of Fig. 4.24(c). A full implementation of the model

as programmed in MATLAB that was used to analyze devices throughout this Chapter can be found in Appendix C.

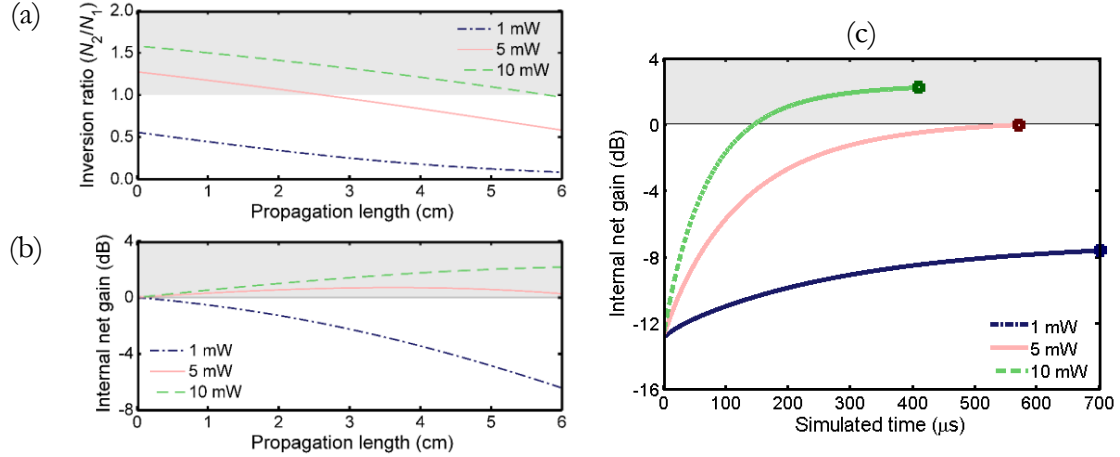


Fig. 4.24. Simulation results showing the (a) average inversion ratio versus propagation length, (b) internal net gain versus propagation length and (c) internal net gain at the end of the waveguide versus simulation time of the rate equation model for a launched 1558-nm signal power of -20 dBm and launched 1470-nm pump powers of 1, 5 and 10 mW.

4.4.4. Amplifier Optimization

The developed amplifier model was used to determine the optimized performance of $\text{TeO}_2:\text{Er}^{3+}-\text{Si}_3\text{N}_4$ waveguide amplifiers. In particular, we focus on the parameters determined for the sample with an erbium dopant concentration of 2.2×10^{20} ions/cm and deposited at a 140 °C, which underwent detailed gain investigations in Section 4.3. All relevant material parameters have been described at some point throughout this chapter, with the exception of the 970 nm emission cross section, which as it is near the peak of absorption is assumed to be equal to absorption cross section at the same wavelength of 2.8×10^{-21} cm². Table 4.2 summarizes the optical and spectroscopic parameters of the device.

Table 4.2. Default parameters used in the simulation and optimization of waveguide amplifiers.

Parameter	Symbol	Value
Er ³⁺ ion concentration	N_{Er}	2.2×10^{20} ions/cm ³
970 nm background propagation loss	$A_{\text{Back,Pump}}$	2.5 dB/cm
1470 nm background propagation loss	$A_{\text{Back,Pump}}$	0.25 dB/cm
1558 nm background propagation loss	$A_{\text{Back,Signal}}$	0.25 dB/cm
Launched signal power	P_{Signal}	-20 dBm
ETU parameter	$W_{2\text{ETU}}$	2.7×10^{-18} cm ³ /s
⁴ I _{13/2} / ⁴ I _{11/2} lifetime	t_{21} / t_{32}	0.48 / 0.04 ms
970 nm absorption / emission cross section	$\sigma_{\text{abs}}^p / \sigma_{\text{em}}^p$	2.8 / 2.8×10^{-21} cm ²
1470 nm absorption / emission cross section	$\sigma_{\text{abs}}^p / \sigma_{\text{em}}^p$	3.0 / 0.4×10^{-21} cm ²
1558 nm absorption / emission cross section	$\sigma_{\text{abs}}^s / \sigma_{\text{em}}^s$	3.5 / 4.4×10^{-21} cm ²

First the amplifier model was compared to the experimental devices under test to validate the model, using the gain measurements in the 6.7-cm-long waveguide sample pumped at 1470 nm. Fig. 4.24 shows the results of the simulated performance of the device from the model using 0, 22, and 40% quenched ions. The results for the model with 22% quenched ions match well to the measured data, and agree with the 22 % ion quenching estimated from absorption saturation measurements. From the results it is clear that ion quenching is a limiting factor in device performance, with the device modeled at 0% ion quenching simulated to achieve almost double the internal net gain at a launched pump power of 35 mW. Similarly, assuming a quenching fraction of 40 % predicts almost no net gain can be achieved at a pump power of 35 mW. This demonstrates the large influence quenching has on device performance and the importance of investing reducing quenching ratios in $\text{TeO}_2:\text{Er}^{3+}$ films in the future to achieve improved amplifier performance.

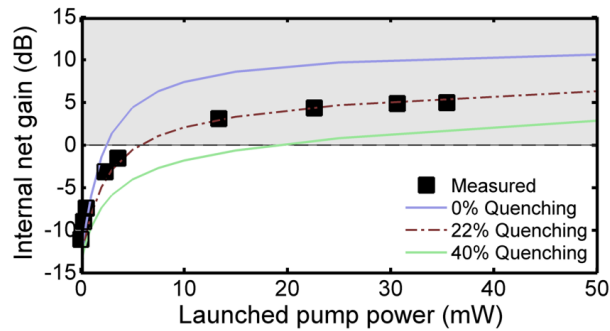


Fig. 4.25. Simulated internal net gain versus launched 1470 nm pump power for a 1558 nm signal with 0, 22, and 40% quenched ions compared to measured results, showing good agreement between simulation and measurement for a 22 % quenched ion fraction.

To investigate the potential for higher gain $\text{TeO}_2:\text{Er}^{3+}\text{-Si}_3\text{N}_4$ amplifiers, simulations were carried out using the same properties as described in Table 4.2 for varying waveguide length and launched pump power. The simulated net gain for a 1558 nm signal versus launched 1470 nm pump power for waveguide lengths of 5, 10 and 15 cm is shown in Fig. 4.25(a). The results demonstrate that by simply increasing the waveguide length and improving pump coupling efficiency to allow for 150 mW of launched pump power are expected to result in gain of > 10 dB and almost 20 dB for 10- and 15-cm-long amplifiers, respectively. Additionally, when investigating the gain versus wavelength at a launched pump power of 150 mW, as shown in Fig. 4.25(b), the 10-cm-long sample was calculated to achieve a gain of > 10 dB across the C-band. These results show the excellent potential for higher gain in $\text{TeO}_2:\text{Er}^{3+}\text{-Si}_3\text{N}_4$ waveguides, with further optimization possible by adjusting the waveguide dimensions and erbium doping concentration. As shown earlier hybrid $\text{TeO}_2\text{-Si}_3\text{N}_4$ devices can be bent down to radii of $\sim 300 \mu\text{m}$ with minimal loss, which would allow for patterning of a 10-cm-long spiral amplifier into a sub 2.5 mm^2 footprint area, a scale which is compatible with the integration of $\text{TeO}_2:\text{Er}^{3+}\text{-Si}_3\text{N}_4$ amplifiers in high performance Si_3N_4 photonic circuits.

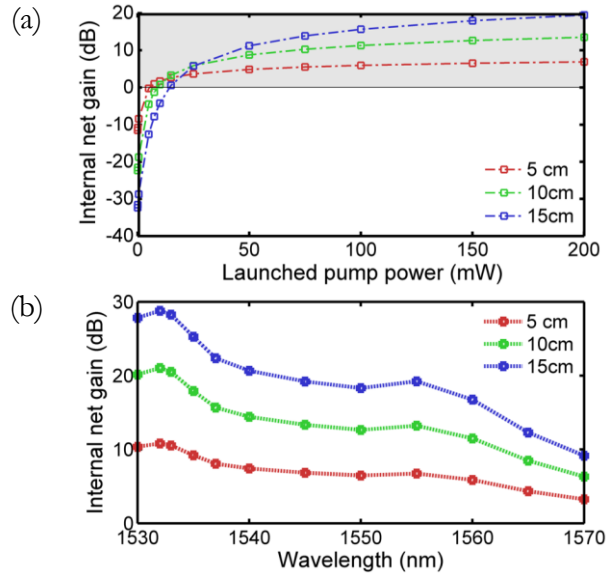


Fig. 4.26. Simulated internal net gain versus (a) launched 1470 nm pump power for a 1558 nm signal and (b) signal wavelength for 150 mW of launched pump power, for waveguide lengths of 5, 10, and 15 cm.

4.5. Conclusion

In summary, this chapter has demonstrated $\text{TeO}_2:\text{Er}^{3+}$ -coated Si_3N_4 waveguides to be a promising platform for integrated optical amplifiers on silicon. The general theory of optical process and the electronic energy diagram of erbium dopants was reviewed. Detailed experimental methods to characterize the properties of $\text{TeO}_2:\text{Er}^{3+}$ -coated Si_3N_4 waveguide amplifiers, including: background waveguide propagation loss, fiber-chip coupling loss, absorption cross sections, erbium-dopant concentration, emission cross sections, excited state lifetimes, and dopant quenching fractions were also developed. A set of samples with dopant concentrations between 0.6 and 2.8×10^{20} ions/cm³ were characterized, and revealed much lower luminescent lifetimes than the theoretical radiative lifetime, of 0.20 ms on average, as well as relatively large fractions of fast-quenched ions ranging from 14 to 54%. Based on previous results seen in fiber and ridge waveguide $\text{TeO}_2:\text{Er}^{3+}$ amplifiers, it was believed that the low lifetimes and large quenching ratios were primarily a result of OH impurity incorporation into the film. To attempt to reduce OH incorporation, we investigated depositing a film at an elevated temperature of 140 °C, large enough to drive out sources of OH contamination such as water, without crystallizing the TeO_2 . This sample was observed to have an erbium dopant concentration of 2.2×10^{20} ions/cm³, with an improved lifetime compared to samples fabricated at room temperatures of 0.48 ms, as well as a quenching ion fraction of 22 % and low waveguide background propagation loss of 0.25 dB/cm. This shows moderate annealing temperatures during deposition to be a promising pathway towards reducing OH incorporation into $\text{TeO}_2:\text{Er}^{3+}$ films. Detailed gain measurements of this sample demonstrated internal net gain of up to 1.7 and 1.4 dB/cm at a signal wavelength of 1533 nm

in a 2.2-cm-long waveguide when pumped at 970 and 1470 nm, respectively. A 6.7-cm-long waveguide sample was measured to have a peak internal net gain of 5 dB at a signal wavelength of 1558 nm and > 3 dB gain across the C-band when pumped at 1470 nm, limited by the available pump power. A numerical three-level rate equation model was developed to investigate the optimized performance of devices. The model predicts that by simply extending waveguide length to 10 cm and improving the fiber-chip coupling efficiency to allow for a launched pump power of 150 mW, > 10 dB gain can be achieved across the C-band in a similar device in a footprint of < 2.5 mm². These results present a promising approach towards fabricating ultra-compact and high performance hybrid TeO₂:Er³⁺ waveguide amplifiers and lasers as a part of advanced Si₃N₄ photonic integrated circuits.

References

- [1] A. Fernández Gavela, D. Grajales García, J. Ramirez, and L. Lechuga, “Last advances in silicon-based optical biosensors,” *Sensors* **16**(3), 285 (2016).
- [2] D. J. Moss, R. Morandotti, A. L. Gaeta, and M. Lipson, “New CMOS-compatible platforms based on silicon nitride and Hydex for nonlinear optics,” *Nat. Photonics* **7**(8), 597 (2013).
- [3] C. G. Roeloffzen, L. Zhuang, C. Taddei, A. Leinse, R. G. Heideman, P. W. van Dijk, R. M. Oldenbeuving, D. A. Marpaung, M. Burla, and K. J. Boller, “Silicon nitride microwave photonic circuits,” *Opt. Express* **21**(19), 22937–22961 (2013).
- [4] R. M. De Ridder, K. Warhoff, A. Driessen, P. V. Lambeck, and H. Albers, “Silicon oxynitride planar waveguiding structures for application in optical communication,” *IEEE J. Sel. Top. Quantum Electron.* **4**(6), 930–937 (1998).
- [5] J. F. Bauters, M. J. R. Heck, D. John, D. Dai, M.-C. Tien, J. S. Barton, A. Leinse, R. G. Heideman, D. J. Blumenthal, and J. E. Bowers, “Ultra-low-loss high-aspect-ratio Si₃N₄ waveguides,” *Opt. Express* **19**(4), 3163–3174 (2011).
- [6] J. F. Bauters, M. J. R. Heck, D. D. John, J. S. Barton, C. M. Bruinink, A. Leinse, R. G. Heideman, D. J. Blumenthal, and J. E. Bowers, “Planar waveguides with less than 0.1 dB/m propagation loss fabricated with wafer bonding,” *Opt. Express* **19**(24), 24090–24101 (2011).
- [7] D. J. Blumenthal, R. Heideman, D. Geuzebroek, A. Leinse, and C. Roeloffzen, “Silicon nitride in silicon photonics,” *Proc. IEEE* **106**(12), 2209–2231 (2018).
- [8] K. Wörhoff, R. G. Heideman, A. Leinse, and M. Hoekman, “TriPleX: A versatile dielectric photonic platform,” *Adv. Opt. Technol.* **4**(2), 189–207 (2015).
- [9] W. D. Sacher, J. C. Mikkelsen, Y. Huang, J. C. Mak, Z. Yong, X. Luo, Y. Li, P. Dumais, J. Jiang, D. Goodwill, E. Bernier, P. G. Q. Lo, and J. K. S. Poon, “Monolithically

- integrated multilayer silicon nitride-on-silicon waveguide platforms for 3-D photonic circuits and devices,” *Proc. IEEE* **106**(12), 2232–2245 (2018).
- [10] E. Timurdogan, Z. Su, C. V. Poulton, M. J. Byrd, S. Xin, R. J. Shiue, B. R. Moss, E. S. Hosseini, and M. R. Watts, “AIM process design kit (AIMPDKv2. 0): Silicon photonics passive and active component libraries on a 300mm wafer,” *Optical Fiber Communications Conference and Exposition*, 1–3 (2018).
- [11] Z. Fang, Q. Y. Chen, and C. Z. Zhao, “A review of recent progress in lasers on silicon,” *Opt. Laser Technol.* **46**, 103–110 (2013).
- [12] R. M. Oldenbeuving, E. J. Klein, H. L. Offerhaus, C. J. Lee, H. Song, and K. J. Boller, “25 kHz narrow spectral bandwidth of a wavelength tunable diode laser with a short waveguide-based external cavity,” *Laser Phys. Lett.* **10**(1), 015804 (2013).
- [13] Y. Fan, R. M. Oldenbeuving, E. J. Klein, C. J. Lee, H. Song, M. R. Khan, H. L. Offerhaus, P. J. van der Slot, and K. J. Boller, “A hybrid semiconductor-glass waveguide laser,” *Proc. SPIE* **9135**, 91351B (2014).
- [14] Y. Fan, J. P. Epping, R. M. Oldenbeuving, C. G. H. Roeloffzen, M. Hoekman, R. Dekker, R. G. Heideman, P. J. M. van der Slot, and K. J. Boller, “Optically integrated InP-Si₃N₄ hybrid laser,” *IEEE Photon. J.* **8**(6), 1505111 (2016).
- [15] A. W. Fang, H. Park, O. Cohen, R. Jones, M. J. Paniccia, and J. E. Bowers, “Electrically pumped hybrid AlGaInAs-silicon evanescent laser,” *Opt. Express* **14**(20), 9203–9210 (2006).
- [16] D. Liang and J. E. Bowers, “Recent progress in lasers on silicon,” *Nat. Photonics* **4**(8), 511–517 (2010).
- [17] G. Roelkens, L. Liu, D. Liang, R. Jones, A. Fang, B. Koch, and J. E. Bowers, “III-V/silicon photonics for on-chip and intra-chip optical interconnects,” *Laser Photonics Rev.* **4**(6), 751–779 (2010).
- [18] M. J. Heck, J. F. Bauters, M. L. Davenport, J. K. Doylend, S. Jain, G. Kurczveil, S. Srinivasan, Y. Tang, and J. E. Bowers, “Hybrid silicon photonic integrated circuit technology,” *IEEE J. Sel. Top. Quantum Electron.* **19**(4), 6100117 (2012).
- [19] R. J. Mears, L. Reekie, I. M. Jauncey, and D. N. Payne, “Low-noise erbium-doped fibre amplifier operating at 1.54 μm ,” *Electron. Lett.* **23**(19), 1026–1028 (1987).
- [20] A. J. Kenyon, “Recent developments in rare-earth doped materials for optoelectronics,” *Prog. Quantum Electron.* **26**(4-5), 225–284 (2002).
- [21] A. J. Kenyon, “Erbium in silicon,” *Semicond. Sci. and Technol.* **20**(12), R65 (2005).
- [22] S. E. Yerci, R. Li, and L. Dal Negro, “Electroluminescence from Er-doped Si-rich silicon nitride light emitting diodes,” *Appl. Phys. Lett.* **97**(8), 081109 (2010).

- [23] C. G. Atkins, J. F. Massicott, J. R. Armitage, R. Wyatt, B. J. Ainslie, and S. P. Craig-Ryan, "High-gain broad spectral bandwidth erbium-doped fibre amplifier pumped near 1.5 μm ," *Electron. Lett.* **25**(14), 910–911 (1989).
- [24] Y. Sun, J. W. Sulhoff, A. K. Srivastava, J. L. Zyskind, T. A. Strasser, J. R. Pedrazzani, C. Wolf, J. Zhou, J. B. Judkins, R. P. Espindola, and A. M. Vengsarkar, "80 nm ultra-wideband erbium-doped silica fibre amplifier," *Electron. Lett.* **33**(23), 1965–1967 (1997).
- [25] T. Kitagawa, K. Hattori, M. Shimizu, Y. Ohmori, and M. Kobayashi, "Guided-wave laser based on erbium-doped silica planar lightwave circuit," *Electron. Lett.* **27**(4), 334–335 (1991).
- [26] T. Kitagawa, K. Hattori, K. Shuto, M. Yasu, M. Kobayashi, and M. Horiguchi, "Amplification in erbium-doped silica-based planar lightwave circuits," *Electron. Lett.* **28**(19), 1818–1819 (1992).
- [27] K. Shuto, K. Hattori, T. Kitagawa, Y. Ohmori, and M. Horiguchi, "Erbium-doped phosphosilicate glass waveguide amplifier fabricated by PECVD," *Electron. Lett.* **29**(2), 139–141 (1993).
- [28] R. Brinkmann, W. Sohler, and H. Suche, "Continuous-wave erbium-diffused LiNbO_3 waveguide laser," *Electron. Lett.* **27**(5), 415–417 (1991).
- [29] R. Brinkmann, I. Baumann, M. Dinand, W. Sohler, and H. Suche, "Erbium-doped single-and double-pass Ti: LiNbO_3 waveguide amplifiers," *IEEE J. Quantum Electron.* **30**(10), 2356–2360 (1994).
- [30] H. Suche, I. Baumann, D. Hiller, and W. Sohler, "Modelocked Er: Ti: LiNbO_3 -waveguide laser," *Electron. Lett.* **29**(12), 1111–1112 (1993).
- [31] Y. C. Yan, A. D. Faber, H. De Waal, P. G. Kik, and A. Polman, "Erbium-doped phosphate glass waveguide on silicon with 4.1 dB/cm gain at 1.535 μm ," *Appl. Phys. Lett.* **71**(20), 2922–2924 (1997).
- [32] S. Blaize, L. Bastard, C. Cassagnetes, and J. E. Broquin, "Multiwavelengths DFB waveguide laser arrays in Yb-Er codoped phosphate glass substrate," *IEEE Photon. Technol. Lett.* **15**(4), 516–518 (2003).
- [33] G. Della Valle, S. Taccheo, P. Laporta, G. Sorbello, E. Cianci, and V. Foglietti, "Compact high gain erbium-ytterbium doped waveguide amplifier fabricated by Ag-Na ion exchange," *Electron. Lett.* **42**(11), 632–633 (2006).
- [34] G. Della Valle, A. Festa, G. Sorbello, K. Ennser, C. Cassagnetes, D. Barbier, and S. Taccheo, "Single-mode and high power waveguide lasers fabricated by ion-exchange," *Opt. Express* **16**(16), 12334–12341 (2008).

- [35] J. Shmulovich, A. J. Bruce, G. Lenz, P. B. Hansen, T. N. Nielsen, D. J. Muehler, G. A. Bogert, I. Brener, E. J. Laskowski, A. Paunescu, and I. Ryazansky, "Integrated planar waveguide amplifier with 15 dB net gain at 1550 nm," in Optical Fiber Communication Conference, San Diego, CA, 1999, OSA Technical Digest (online) (Optical Society of America, 1999), paper PD42.
- [36] K. Vu and S. Madden, "Tellurium dioxide Erbium doped planar rib waveguide amplifiers with net gain and 2.8dB/cm internal gain," *Opt. Express* **18**(18), 19192–19200 (2010).
- [37] K. Vu, S. Farahani, and S. Madden, "980nm pumped erbium doped tellurium oxide planar rib waveguide laser and amplifier with gain in S, C and L band," *Opt. Express* **23**(2), 747–755 (2015).
- [38] S. A. Vázquez-Córdova, M. Dijkstra, E. H. Bernhardt, F. Ay, K. Wörhoff, J. L. Herek, S. M. García-Blanco, and M. Pollnau, "Erbium-doped spiral amplifiers with 20 dB of net gain on silicon," *Opt. Express* **22**(21), 25993–26004 (2014).
- [39] A. Z. Subramanian, G. S. Murugan, M. N. Zervas, and J. S. Wilkinson, "Spectroscopy, Modeling, and Performance of Erbium-Doped Ta₂O₅ Waveguide Amplifiers," *J. Light Technol.* **30**(10), 1455–1462 (2012).
- [40] Purnawirman, J. Sun, T. N. Adam, G. Leake, D. Coolbaugh, J. D. B. Bradley, E. Shah Hosseini, and M. R. Watts, "C- and L-band erbium-doped waveguide lasers with wafer-scale silicon nitride cavities," *Opt. Lett.* **38**(11), 1760–1762 (2013).
- [41] M. Belt, T. Huffman, M. L. Davenport, W. Li, J. S. Barton, and D. J. Blumenthal, "Arrayed narrow linewidth erbium-doped waveguide-distributed feedback lasers on an ultra-low-loss silicon-nitride platform," *Opt. Lett.* **38**(22), 4825–4828 (2013).
- [42] M. Belt and D. J. Blumenthal, "Erbium-doped waveguide DBR and DFB laser arrays integrated within an ultra-low-loss Si₃N₄ platform," *Opt. Express* **22**(9), 10655–10660 (2014).
- [43] E. S. Hosseini, Purnawirman, J. D. B. Bradley, J. Sun, G. Leake, T. N. Adam, D. D. Coolbaugh, and M. R. Watts, "CMOS-compatible 75 mW erbium-doped distributed feedback laser," *Opt. Lett.* **39**(11), 3106–3109 (2014).
- [44] Purnawirman, N. Li, E. S. Magden, G. Singh, N. Singh, A. Baldycheva, E. S. Hosseini, J. Sun, M. Moresco, T. N. Adam, G. Leake, D. Coolbaugh, J. D. B. Bradley, and M. R. Watts, "Ultra-narrow-linewidth Al₂O₃Er³⁺ lasers with a wavelength-insensitive waveguide design on a wafer-scale silicon nitride platform," *Opt. Express* **25**(12), 13705–13713 (2017).
- [45] E. S. Magden, N. Li, Purnawirman, J. D. B. Bradley, N. Singh, A. Ruocco, G. S. Petrich, G. Leake, D. D. Coolbaugh, E. P. Ippen, M. R. Watts, and L. A. Kolodziejski,

- "Monolithically-integrated distributed feedback laser compatible with CMOS processing," *Opt. Express* **25**(15), 18058–18065 (2017).
- [46] N. Li, E. S. Magden, Z. Su, N. Singh, A. Ruocco, M. Xin, M. Byrd, P. T. Callahan, J. D. B. Bradley, C. Baiocco, D. Vermeulen, and M. R. Watts, "Broadband 2- μm emission on silicon chips: monolithically integrated Holmium lasers," *Opt. Express* **26**(3), 2220–2230 (2018).
- [47] J. D. B. Bradley, E. S. Hosseini, Purnawirman, Z. Su, T. N. Adam, G. Leake, D. Coolbaugh, and M. R. Watts, "Monolithic erbium-and ytterbium-doped microring lasers on silicon chips," *Opt. Express* **22**(10), 12226–12237 (2014).
- [48] Z. Su, N. Li, E. S. Magden, M. Byrd, Purnawirman, T. N. Adam, G. Leake, D. Coolbaugh, J. D. B. Bradley, and M. R. Watts, "Ultra-compact and low-threshold thulium microcavity laser monolithically integrated on silicon," *Opt. Lett.* **41**(24), 5708–5711 (2016).
- [49] N. Li, D. Vermeulen, Z. Su, E. S. Magden, M. Xin, N. Singh, A. Ruocco, J. Notaros, C. V. Poulton, E. Timurdogan, C. Baiocco, and M. R. Watts, "Monolithically integrated erbium-doped tunable laser on a CMOS-compatible silicon photonics platform," *Opt. Express* **26**(13), 16200–16211 (2018).
- [50] J. Mu, M. Dijkstra, J. Korterik, H. Offerhaus, and S. M. García-Blanco, "High-gain waveguide amplifiers in Si_3N_4 technology via double-layer monolithic integration," *Photonics Res.* **8**(10), 1634-1641 (2020).
- [51] J. Mu, M. Dijkstra, and S. M. García-Blanco, "Resonant Coupling for Active–passive monolithic integration of Al_2O_3 and Si_3N_4 ," *IEEE Photonic Tech. L.* **31**(10), 771–774 (2019).
- [52] J. Mu, M. Dijkstra, Y. Yong, M. de Goede, L. Chang, and S. M. García-Blanco, "Monolithic integration of Al_2O_3 and Si_3N_4 toward double-layer active-passive platform," *IEEE J. Sel. Top. Quantum Electron.* **25**(5), 8200911 (2019).
- [53] J. Rönn, W. Zhang, A. Autere, X. Leroux, L. Pakarinen, C. Alonso-Ramos, A. Säynätjoki, H. Lipsanen, L. Vivien, E. Cassan, and Z. Sun, "Ultra-high on-chip optical gain in erbium-based hybrid slot waveguides," *Nat. Commun.* **10**(1), 432 (2019).
- [54] J. Rönn, J. Zhang, W. Zhang, Z. Tu, A. Matikainen, X. Leroux, E. Durán-Valdeiglesias, N. Vulliet, F. Boeuf, C. Alonso-Ramos, and H. Lipsanen, "Erbium-doped hybrid waveguide amplifiers with net optical gain on a fully industrial 300 mm silicon nitride photonic platform," *Opt. Express* **28**(19), 27919–27926 (2020).
- [55] S. J. Madden and K. T. Vu, "Very low loss reactively ion etched Tellurium Dioxide planar rib waveguides for linear and non-linear optics," *Opt. Express* **17**(20), 17645–17651 (2009).

- [56] J. S. Wang, E. M. Vogel, and E. Snitzer, “Tellurite glass: a new candidate for fiber devices,” *Opt. Mater.* **3**(3), 187–203 (1994).
- [57] A. Jha, B. Richards, G. Jose, T. Teddy-Fernandez, P. Joshi, X. Jiang, and J. Lousteau, “Rare-earth ion doped TeO₂ and GeO₂ glasses as laser materials,” *Prog. Mater. Sci.* **57**(8), 1426–1491 (2012).
- [58] R. C. Hilborn, “Einstein coefficients, cross sections, f values, dipole moments, and all that,” *Am. J. Phys.* **50**(11), 982–986 (1982).
- [59] A. Yariv and P. Yeh, *Optical Electronics in Modern Communications* (Oxford University, 2006).
- [60] B. G. Wybourne, *Spectroscopic Properties of Rare Earths* (Interscience, 1965).
- [61] S. Hüfner, *Optical Spectra of Rare Earth Compounds* (Academic Press, 1978).
- [62] P. M. Becker, A.A. Olsson, and J. R. Simpson, *Erbium-doped fiber amplifiers: fundamentals and technology* (Elsevier, 1999).
- [63] M. J. Digonnet, *Rare-earth-doped fiber lasers and amplifiers, revised and expanded* (CRC press, 2001).
- [64] H. N. Russell and F. A. Saunders, “New Regularities in the Spectra of the Alkaline Earths,” *Atomic Spectra: The Commonwealth and International Library: Selected Readings in Physics* **206**, (2013).
- [65] F. E. Auzel, “Materials and devices using double-pumped-phosphors with energy transfer,” *Proc. IEEE* **61**(6), 758–786 (1973).
- [66] P. S. Golding, S. D. Jackson, T. A. King, and M. Pollnau, “Energy transfer processes in Er³⁺-doped and Er³⁺, Pr³⁺-codoped ZBLAN glasses,” *Phys. Rev. B* **62**(2), 856–864 (2000).
- [67] C. B. Layne, W. H. Lowdermilk, and M. J. Weber, “Multiphonon relaxation of rare earth ions in oxide glasses,” *Phys. Rev. B* **16**(1), 10–20, 1977.
- [68] P W. Milonni and J. H. Eberly, *Lasers* (Wiley, 1998).
- [69] G. H. Dieke, *Spectra and Energy Levels of Rare Earths Ions in Crystals* (Interscience, 1968).
- [70] B. R. Judd, “Optical absorption intensities of rare-earth ions,” *Phys. Rev.* **127**(3), 750 (1962).
- [71] G. S. Ofelt, “Intensities of crystal spectra of rare-earth ions,” *J. Chem. Phys.* **37**(3), 511–520 (1962).

- [72] H. Steinkemper, S. Fischer, M. Hermle, and J. C. Goldschmidt, “Stark level analysis of the spectral line shape of electronic transitions in rare earth ions embedded in host crystals,” *New J. Phys.* **15**(5), 053033 (2013).
- [73] C. H. Huang, L. McCaughan, and D. M. Gill, “Evaluation of absorption and emission cross sections of Er-doped LiNbO₃ for application to integrated optic amplifiers,” *J. Light. Technol.* **12**(5), 803–809 (1994).
- [74] X. Tang, Q. Han, X. Zhao, H. Song, K. Ren, and T. Liu, “Method for estimating the Stark splitting of rare-earth ions from the measured cross-section spectra,” *Appl. Opt.* **57**(29), 8573–8577 (2018).
- [75] E. Desurvire and J. R. Simpson, “Evaluation of ⁴I_{15/2} and ⁴I_{13/2} Stark-level energies in erbium-doped aluminosilicate glass fibers,” *Opt. Lett.* **15**(10), 547–549 (1990).
- [76] https://www.thorlabs.com/newgrouppage9.cfm?objectgroup_id=1504#.
- [77] R. Nayak, V. Gupta, A. L. Dawar, and K. Sreenivas, “Optical waveguiding in amorphous tellurium oxide thin films,” *Thin Solid Films* **445**(1), 118–126 (2003).
- [78] R. Paschotta, article on 'doping concentration' in the Encyclopedia of Laser Physics and Technology, 1. edition October 2008, Wiley-VCH, ISBN 978-3-527-40828-3.
- [79] D. E. McCumber, “Einstein relations connecting broadband emission and absorption spectra,” *Phys. Rev.* **136**(4A), A954 (1964).
- [80] A. Mori, “Tellurite-based fibers and their applications to optical communication networks,” *J. Ceram. Soc. Japan* **116**(1358), 1040–1051 (2008).
- [81] W. J. Miniscalco, “Erbium-doped glasses for fiber amplifiers at 1500 nm,” *J. Light. Technol.* **9**(2), 234–2350 (1991).
- [82] Y. Ohishi, A. Mori, M. Yamada, H. Ono, Y. Nishida, and K. Oikawa, “Gain characteristics of tellurite-based erbium-doped fiber amplifiers for 1.5- μ m broadband amplification,” *Opt. Lett.* **23**(4), 274–276 (1998).
- [83] R. Reisfeld and Y. Eckstein, “Radiative and non-radiative transition probabilities and Quantum yields for excited states of Er³⁺ in germanate and tellurite glasses,” *J. Non. Cryst. Solids* **15**(1), 125–140 (1974).
- [84] R. Reisfeld and C. K. Jørgensen, *Excited State Phenomena in Vitreous Materials* (Elsevier, 1987).
- [85] D. A. Zubenko, M. A. Noginov, V. A. Smirnov, and I. A. Shcherbakov, “Different mechanisms of nonlinear quenching of luminescence,” *Phys. Rev. B* **55**(14), 8881 (1997).

- [86] L. Agazzi, Spectroscopic excitation and quenching processes in rare-earth-ion-doped Al_2O_3 and their impact on amplifier and laser performance (Doctoral dissertation, University of Twente).
- [87] S. Dai, C. Yu, G. Zhou, J. Zhang, and G. Wang, "Effect of OH-content on emission properties in Er^{3+} -doped tellurite glasses," *J. Non-Cryst. Solids* **354**(12-13), 1357–1360 (2008).
- [88] A. Jha, S. Shen, and M. Naftaly, "Structural origin of spectral broadening of 1.5- μm emission in Er^{3+} -doped tellurite glasses," *Phys. Rev. B* **62**(10), 6215 (2000).
- [89] P. Myslinski, J. Fraser, and J. Chrostowski, "Nanosecond kinetics of upconversion process in EDF and its effect on EDFA performance," in *Optical Amplifiers and Their Applications*, Proc. OAA'95, 1995 (Optical Society of America, Washington DC, 1995), paper ThE3, pp. 100–103.
- [90] R. Wyatt, "Spectroscopy of rare earth doped fibers," *Proc. Soc. Photo-Opt. Instrum. Eng.* **1171**, 54–64 (1990).
- [91] L. Agazzi, E. H. Bernhardt, K. Wörhoff, and M. Pollnau, "Impact of luminescence quenching on relaxation-oscillation frequency in solid-state lasers," *Appl. Phys. Lett.* **100**(1), 011109 (2012).
- [92] Y. Hu, S. Jiang, G. Sorbello, T. Luo, Y. Ding, B. Hwang, J. Kim, H. Seo, and N. Peyghambarian, "Numerical analyses of the population dynamics and determination of the upconversion coefficients in a new high erbium-doped tellurite glass," *J. Opt. Soc. Am. B* **18**(12), 1928–1934 (2001).
- [93] E. Desurvire, J. R. Simpson, and P. C. Becker, "High-gain erbium-doped traveling-wave fiber amplifier," *Opt. Lett.* **12**(11), 888–890 (1987).
- [94] G. A. Ball and W. W. Morey, "Continuously tunable single-mode erbium fiber laser," *Opt. Lett.* **17**(6), 420–422 (1992).
- [95] G. N. van den Hoven, E. Snoeks, A. Polman, C. van Dam, J. W. M. van Uffelen, and M. K. Smit, "Upconversion in Er-implanted Al_2O_3 waveguides," *J. Appl. Phys.* **79**(3), 1258–1266 (1996).

CHAPTER 5

Tellurium Oxide Microcavities Integrated on a Silicon Photonics Platform

This chapter focuses on the integration of tellurium oxide (TeO_2) microcavities onto silicon photonic chips. The microcavities are fabricated by filling a circular trench etched into the silicon dioxide top-cladding with a TeO_2 coating in post-processing. It is shown that aligning such a structure next to a silicon bus waveguide allows for evanescent coupling from the silicon waveguide to a high confinement TeO_2 microresonator. This approach enables a photonic platform that can combine tellurium oxide's promising passive, active and nonlinear optical material properties with high performance silicon optoelectronic microsystems. Two iterative chip designs were fabricated and studied. The optical properties of the microtrench cavities are found to depend strongly on the trench structure, prepared in the foundry, and the TeO_2 thin film, deposited in our lab. The microtrench structure was investigated by focused ion beam milling and scanning electron microscopy to reveal its shape including the etch angle, the conformal TeO_2 film with varying thickness on the bottom and sidewalls of the trench and location of the silicon waveguide. Both designs exhibited significantly over-etched microtrenches due to the timed SiO_2 etch and an approximately 80 degree sidewall angle, such that the microtrench is vertically and laterally offset from the silicon waveguide, respectively, which influenced the waveguide-microcavity coupling. A model of the microcavity structure is used to predict the optical properties of the device. TeO_2 confinement of over 80% can be realized for TeO_2 film thicknesses greater than 500 nm. However, the optical mode of the microcavity is seen to vary significantly with bend radius due to its effect on lateral confinement. Smaller bending radii improve lateral confinement, allowing for the microcavity to maintain a smaller mode in the corner. Negligible bending radiation losses are calculated for radii down $\sim 40 \mu\text{m}$, even with 1100-nm-thick TeO_2 films. A model for the optical power coupled between the silicon waveguide and TeO_2 microtrench was developed based on coupled mode theory. It predicts that coupling Q factors can reach as low as 0.2×10^5 , representing strong coupling, for pulley coupled structures with nominal coupling gaps of between 0.10 and 0.35 μm depending on the TeO_2 film thickness. An initial set of microcavity devices fabricated via the AMF silicon photonics foundry were coated in 300–1100-nm-thick TeO_2 layers. The measured intrinsic Q factors of the devices peaked at 1.6×10^5 for a 1110-nm-thick TeO_2 coated device. This is an order of magnitude lower than the expected material limited Q factor of $> 1 \times 10^6$ and believed to be a result of light scattering at microtrench interface roughness as opposed to substrate leakage. The over-etched microtrenches were also seen to result in very high

external Q factors, representing weak coupling, with all measuring greater than 2.0×10^5 . A second design run with a less severe over-etch has improved coupling efficiency, with external Q factors reaching down to 0.4×10^5 in one case, close to the external Q factors predicted by simulation. However, the internal Q factors of devices was observed to be less than 1×10^5 for all measured devices, suggesting a rougher interface than the initial run. Thin spin-coated polymer coatings were subsequently used to smooth the microtrench surface before TeO_2 film depositions and were found to improve device performance up to an intrinsic Q factor of 2.1×10^5 , approaching the values necessary for laser operation in rare-earth-doped TeO_2 cavities. Environmental sensing is one of the highly promising application areas for these microcavities, as the potential for narrow linewidths via high Q factors and rare-earth lasing would allow for low limits of detection. The thermal sensitivity of the microcavities was measured and found to cause an approximately $30 \text{ pm}/^\circ\text{C}$ shift in resonance wavelengths. Evanescent field sensing was tested by coating chips in solutions containing water and varying concentrations of glycerol. Resonance shift sensitivities of up to $15.4 \text{ nm}/\text{refractive index unit (RIU)}$ and limit of detections (LODs) of $2.2 \times 10^{-3} \text{ RIU}$ were observed, which are comparable to many other silicon-on-insulator (SOI) sensing alternatives. These results demonstrate a promising pathway towards SOI-based high Q dielectric resonator and laser sensor devices, as well as a potential platform for on-chip non-linear optics, quantum information processing, and acousto-optics through TeO_2 coated microcavities.

The results of this chapter have contributed to the following journal publications:

- H. C. Frankis, D. Su, D. B. Bonneville, and J. D. B. Bradley, “A tellurium oxide microcavity resonator sensor integrated on-chip with a silicon waveguide,” *Sensors* **18**(11), 4061 (2018).
- H. C. Frankis, D. B. Bonneville, and J. D. B. Bradley, “Tellurite glass microcavity resonators integrated on a silicon photonics platform,” *J. Opt. Microsyst.* **1**(2), 024002 (2021).

5.1. Introduction

The deposition of tellurium oxide (TeO_2) films using a versatile, low-temperature sputtering method enables their integration on a wide variety of substrates and standard wafer-scale platforms. The previous chapters of this thesis have focused on the integration of TeO_2 thin films onto silicon-nitride (Si_3N_4) photonic systems. Although Si_3N_4 waveguide technologies are becoming increasingly relevant in photonic devices [1-3], the silicon-on-insulator (SOI) waveguide platform currently offers a significantly larger library of optoelectronic components. In particular, optoelectronic devices necessary for fully integrated communication systems, such as high speed Si modulators [4,5] and Ge photodetectors [6-8],

have demonstrated high performance on SOI platforms, but there currently exists no standardized processes to fabricate these devices directly on silicon-nitride photonic circuits. Advanced photonic platforms could use multilayer approaches to integrate TeO₂ coated passive silicon-nitride waveguides with optoelectronic silicon devices for a complete photonic system [9,10], but are complex and costly to fabricate. For certain applications, such as biological sensors, low cost fabrication techniques using a single waveguiding layer with optoelectronic functionality is preferable. Therefore, it is desirable to develop methods of monolithically integrating TeO₂ or other thin film dielectric devices onto silicon photonic chips. Although direct deposition of the TeO₂ thin film onto a silicon waveguide [11] as done previously with silicon-nitride could be used, several difficulties arise from this, including: the high refractive index of silicon limiting the optical overlap in the TeO₂ layer and the larger optical propagation losses of typical single-mode silicon waveguides reducing device efficiencies. An alternative integration method is to use microtrench structures, where the top SiO₂ cladding of fabricated chips is etched down and can then be coated in TeO₂ films in post-processing, creating a TeO₂ waveguiding layer on the same level as the silicon waveguide. Aligning the microtrench to a silicon waveguide allows for both material systems to be implemented onto the same platform, with no changes to the existing foundry processing steps. This method allows devices enabled by the unique material properties of TeO₂ [12-15], such as rare-earth lasers and nonlinear optical devices, to be monolithically integrated with silicon photonic systems.

Microtrench structures coated in aluminum oxide thin films and coupled to silicon-nitride bus waveguides have been studied previously [16–19]. This platform has demonstrated high Q factor resonators ($Q > 10^6$) [16], which have been used in the fabrication of erbium, ytterbium [17], and thulium [18] lasers, and nonlinear photonic devices [19]. Aluminum oxide coated microtrenches coupled to resonant structures in silicon nitride photonic circuitry have also been used to demonstrate single-mode and tunable wavelength rare-earth lasers [20], and full-link communication systems in a multilayer Si₃N₄/Si photonic platform [21]. However, integration of aluminum oxide microcavities directly with silicon waveguides has never been demonstrated, largely because aluminum oxide's relatively low refractive index (1.65) makes it difficult to phase match to high refractive index silicon waveguides. In comparison tellurium oxide's refractive index of 2.08 can be reasonably phase matched to a silicon bus waveguide. Additionally, the ability to deposit high-quality TeO₂ thin films at low temperatures makes it an ideal candidate for back-end integration without the potential to damage the metal layers of optoelectronic silicon devices [22]. Recently a silicon waveguide coupled to a chalcogenide film coated into a microtrench and smoothed with a heating/dewetting process has demonstrated high Q factors [23]. Although highly promising, the low thermal and photostability of chalcogenide glasses could make the practical implementation of these devices challenging.

In this chapter microtrench resonator structures, coupled to silicon bus waveguides and coated in TeO₂ thin films in post-processing were designed, fabricated and tested. TeO₂

microcavities with Q factors of up to 2.1×10^5 and evanescent field sensing where a refractive index sensitivity of 15.4 nm/RIU and limit of detection of 2.2×10^{-3} RIU were demonstrated. These TeO_2 microtrench resonators provide a promising platform for rare-earth devices [17,18], biological sensors [24,25], non-linear optical devices [26-28], quantum information processing [29] and acousto-optic cavities [30] in combination with silicon photonic circuits.

5.2. Silicon-Integrated TeO_2 Microcavity Fabrication

In this work, silicon photonic chips were fabricated at the IME/AMF (Institute of Microelectronics/Advanced Micro Foundry) foundry in Singapore. The chips were designed as part of a multi-project wafer run, for full active-passive optoelectronic technology, offered through CMC (Canadian Microsystems Corporation) Microsystems. The foundry fabrication process began by initially forming a 0.22- μm -thick silicon layer onto a 2- μm -thick thermally oxidized 200-mm-diameter silicon substrate handle wafer by a wafer bonding and smart cut SOI process [31]. Silicon waveguides were patterned by a deep-UV stepper lithography process capable of defining features down to 0.15- μm -wide. Three waveguide etch steps that can etch down to silicon layer heights of 0.15- μm , 0.09- μm , or no remaining silicon for both strip or ridge waveguide designs were available. Following waveguide fabrication several dopant implant steps with various concentrations were masked and carried out to form pn-junctions for modulators and photodiodes. Germanium layers could also be epitaxially grown onto silicon waveguides, and then doped in another set of implantation steps to form germanium detectors. A top-cladding silicon dioxide layer was then grown in 3 stages, during the formation of 2 metal trace layers and a set of vias running between the trace layers and from the lower metal layer to optoelectronic devices on the silicon/germanium layer. The cladding oxide can then be etched down to the silicon layer, in a process step typically used to expose silicon waveguides. To complete the process, a deep trench etch step is used to form optical facets along chip edges, after which the individual chips are diced from the wafer.

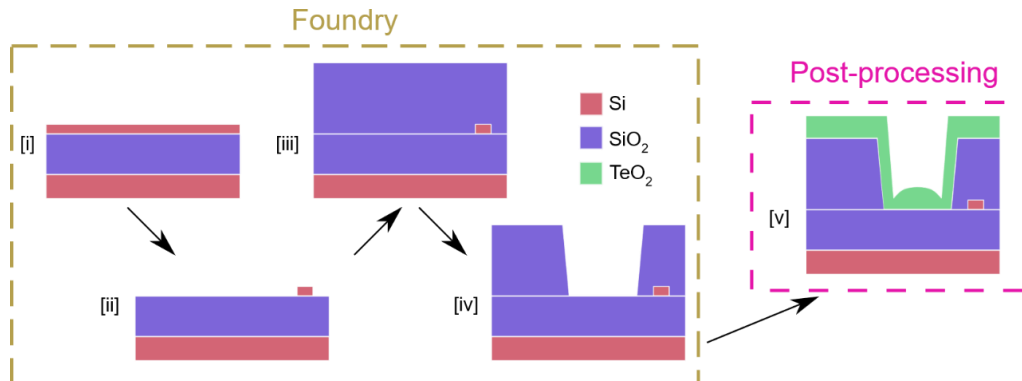


Fig. 5.1. Diagram of microcavity fabrication procedure. The foundry began fabrication with, [i] a 0.22- μm thick silicon layer on a 2- μm BOX [ii] which was patterned and etched to form the bus waveguides, [iii] after which a 3 μm thick silicon dioxide top cladding is deposited, [iv] which was patterned and etched into a circular microtrench structure. Chips were then sent out of the foundry where [v] a tellurite coating was deposited in post-processing, forming the resonator layer.

For the TeO₂ microcavity device design only a few steps of the total process available from IME/AMF were used. Starting with the initial 0.22- μm -thick smart cut SOI wafer strip silicon waveguides were patterned, followed by a 3- μm -thick cladding oxide being grown in a PECVD process. Microtrench rings were then patterned into the cladding oxide using a timed etch intended to reach the buried oxide (BOX). After the wafer was diced into chips, they were sent from the foundry to CMC Microsystems and then to McMaster University, where tellurium oxide coatings were deposited in post-processing via reactive sputtering in the Centre for Emerging Device Technologies (CEDT). The full microcavity fabrication procedure is detailed in Fig. 5.1. Although in the devices studied here the entirety of the chip was coated in TeO₂, in future work incorporating optoelectronic functionality the metal contact pads can be protected using either a lift-off or shadow masking process [32].

Two separate design runs were submitted to the foundry for fabrication and characterized, including an initial design (Design A) followed by a secondary design (Design B) with some minor parameter variations, although the general layout between each design remains the same. The mask design for the microtrenches included ring shapes, with trench widths (w_{Trench}) of 10 μm , and ring radii (R), defined along the outer wall of the trench, of either 40 or 100 μm depending on the design run. The silicon waveguide is patterned around the microcavity such that a straight waveguide from one edge facet of the chip meets the microcavity at a minimum coupling distance of G . The silicon waveguide then maintains this coupling distance as it pulley couples around the ring over a 60 degree angle. This creates an effective coupling length of either 62 or 104 μm for a 40- or 100- μm radius cavity, respectively. The bus waveguide then transitions away from the ring with a diagonally mirrored 60 degree radial bend to continue towards the other edge facet. The mask design and an SEM image of the fabricated device around the microcavity can be seen in Fig. 5.2(a) and Fig. 5.2(b), respectively. Near the coupling region between the microtrench and the bus waveguide a reduced silicon waveguide strip width (w_{Si}) is used to improve the phase matching and optical coupling into the microcavity. In the initial design a 0.35- μm strip width was used, while in the following design it was reduced to 0.30- μm to improve phase matching and coupling strength. Away from the microtrench device, 0.5- μm -wide waveguides are standard to maintain minimal optical propagation loss and stay within the single mode cutoff. Therefore, on each side of the microcavity there is a 10- μm long taper, 10- μm away from the minimum coupling gap that linearly tapers the waveguide width between the standard single-mode silicon waveguide width and the designed waveguide width for the microcavity coupler. Fig. 5.2(c) shows a diagram of the dimensions for the silicon bus waveguide around the microcavity. Near the edge facets waveguides are similarly nano-tapered to 0.18- μm -wide over a length of 100 μm to better match the fiber mode and improve coupling losses [33].

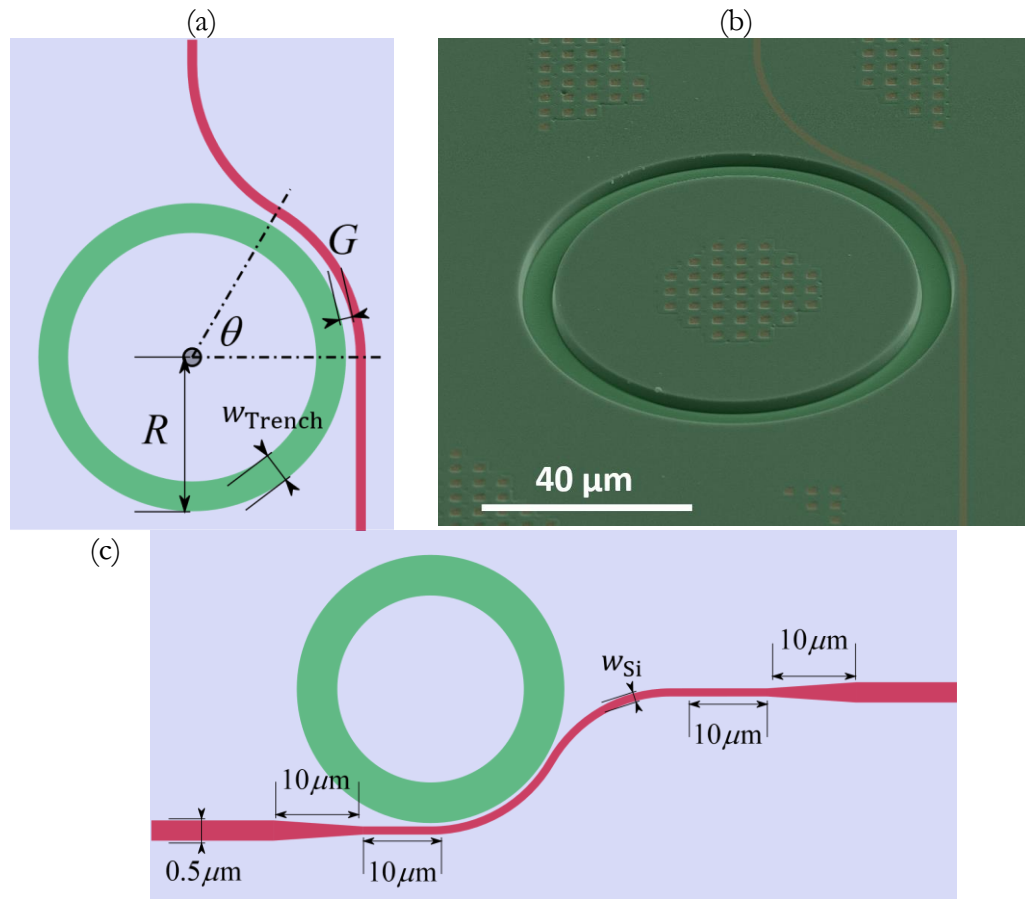


Fig. 5.2. (a) Layout and dimensions of microtrench mask design, (b) SEM image of fabricated microtrench and (c) dimensions of silicon bus waveguide and width tapers.

The mask design for the microtrench cavity defines the dimensions of the device at the chip surface. However, the oxide etch process is not perfectly anisotropic as it etches down which results in slanted sidewalls that narrow the width of the microtrench at the bottom of the cavity compared to the designed width. A diagram demonstrating the cross section of the device near the microtrench is shown in Fig. 5.3(a). While a reduced trench width only has a minor effect on the properties of the microcavity, as the optical mode of the microcavity is primarily confined in the corner of the device, the sidewall angle results in increasing the mask designed (nominal) coupling gap G by an additional lateral offset of Δ , which can have a significant effect on the coupling efficiency of the system. As seen in the SEM image of a microcavity fabricated in the initial design in Fig. 5.3(b), the external angle of the microtrench sidewall (ϕ) is approximately 80 degrees. From Fig. 5.3(b) it can also be seen that in the fabricated microtrench the silica top-cladding etch has extended approximately $1 \mu\text{m}$ below the BOX underneath the silicon waveguide layer (T_{BOX}). The over-etched microtrench adds a vertical offset (δ) between the silicon waveguide and microcavity, which further increases the effective coupling gap and reduces the effective BOX thickness (t_{BOX}) separating the microtrench from the silicon substrate, making the microcavity waveguiding layer more

susceptible to substrate radiation leakage. For a 3- μm -thick SiO_2 top cladding and a sidewall angle of 80 degrees the bottom corner of the microtrench is laterally offset by an additional 0.7 μm ($\Delta = 0.7 \mu\text{m}$), accounting for the additional 1- μm overetch ($\delta = 1.0 \mu\text{m}$). The combination of the lateral and vertical offsets is then calculated to create an effective 1.3- μm coupling gap between the silicon waveguide and the bottom corner of the microtrench for the minimum nominal coupling gap of 0.2 μm on Design A. Thus, it is expected that coupling gaps of this size will lead to very weak coupling between the microcavity and waveguide.

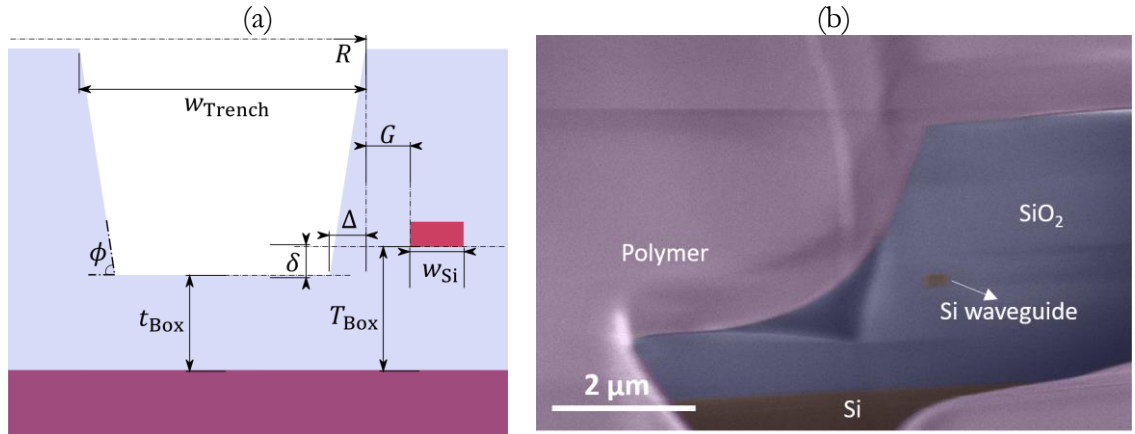


Fig. 5.3. (a) Relevant dimensions of the fabricated microtrench cross section. (b) Cross sectional SEM image of a microtrench after a focused-ion beam cut. The trench was coated in a polymer to improve image quality.

In the second design run nominal coupling gaps ranging between 0.3 μm within the cavity wall to account for the lateral offset, to 0.3 μm outside the cavity wall were used. In this design run a 100 $\mu\text{m} \times 100 \mu\text{m}$ square oxide etch test structure was included to characterize the magnitude of the overetch more precisely by surface profilometry measurements. By measuring several samples an average overetch of 0.25 μm , with a standard deviation of 0.09 μm was estimated for this design run. This is a significantly less severe overetch than what was characterized for the initial run, likely because of modifications to the timed etch process made by the foundry between the different tape-outs. However, from Fig. 5.3(b), it can be seen that the microtrench etch is deeper near the cavity sidewall than near the center of the etch window, by an estimated 0.3 μm . As the surface profilometer has a 10- μm -diameter probe tip it is unable to resolve the etch depth near the etch sidewall, instead measuring the value near the center of the etch pattern. Based on this it was estimated that the overetch on the second design run was approximately 0.5 μm near the cavity sidewall. The minimum designed coupling gap of – 0.3 μm on this design run is then expected to have an effective coupling gap of 0.6 μm accounting for the lateral and vertical offsets, increasing to a 0.8 μm effective gap for a nominal 0.3 μm coupling gap. Table 5.1 summarizes the relevant layout parameters of the microtrench devices in the two different design runs studied.

Table 5.1. Layout parameters for microtrench devices in Design A and B

	Design A	Design B
Si waveguide width, w_{Si} (μm)	0.35	0.30
Microtrench width, w_{Trench} (μm)	10	10
Microtrench radius, R (μm)	40	100
Coupling gaps, G (μm)	0.2 to 1.0	-0.3 to 0.3
Effective coupling length (μm)	62	104
Estimated overetch, δ (μm)	1.0	0.5

Following reception of the chips from the foundry tellurium oxide films were coated onto samples using the deposition process described in Chapter 2. The silicon photonic chips received from the foundry were mounted onto the deposition stage using carbon tape, along with bare silicon and unpatterned thermal oxide test pieces to characterize the refractive index, thickness, and optical propagation loss of the deposited film. A cross-sectional image of a microcavity after the deposition of a TeO_2 thin film can be seen in Fig. 5.4. The following sections of this chapter will discuss the optical design and experimental characterization of the TeO_2 microcavities.

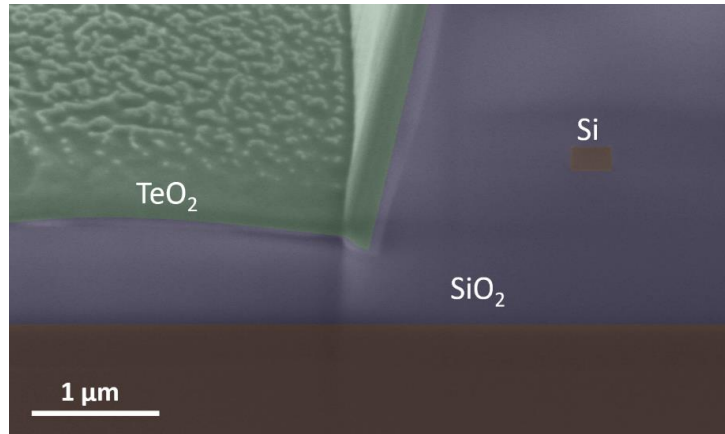


Fig. 5.4. Cross-sectional SEM image of microcavity resonator exposed with a focused-ion-beam cut, showing a microtrench coated in a TeO_2 film next to a silicon bus waveguide.

5.3. TeO_2 Microcavity Design

To simulate the properties of the TeO_2 coated microtrench devices an appropriate cross sectional model of the microcavity system must be developed. In general, this requires two distinct waveguide models, one for the silicon bus waveguide and another for the microcavity resonator.

The silicon strip waveguide is modelled as a $t_{Si} \times w_{Si}$ tall-by-wide box, with a material refractive index of 3.473 at a wavelength of 1550 nm [34]. The foundry process defines a standard thickness for the silicon layer (t_{Si}) of 0.22 μm , which lies on a thermal SiO_2 layer and is clad in a PECVD SiO_2 layer. For simplicity, our silicon waveguide model assumes it is

cladded in a uniform SiO₂ layer in all directions with a material refractive index of 1.444 at a wavelength of 1550 nm [35]. The properties of the silicon bus waveguide can then be tuned by adjusting the width of the waveguide used in the mask design.

With regards to the microcavity, the previous section discussed several design and fabrication details that affect the cross section of the microtrench device. The mask design determines the radius (R) of the microcavity and the width of the microtrench (w_{Trench}). Because of the curvature of the microcavity, the optical mode profile of the structure is shifted towards the outer corner of the device, such that it is assumed that the inner wall of the microtrench has minimal effect on the device properties for a microtrench width of 10 μm . The cross-sectional model can therefore be simplified to only include the exterior sidewall and an etched down SiO₂ layer extending infinitely away from the corner. As seen in the SEM images of devices earlier, the etch process creates a small curve towards the corner of the trench, however, the trench bottom is assumed to be flat in simulations for simplicity. The SEM images also show that although the etch process is designed to land on the BOX layer it consistently over etches, such that the bottom of the microtrench extends below the nominal BOX. The microcavity is then considered to have a variable effective BOX layer of t_{Box} separating the microtrench from the substrate. The etch process also induces a slight angular offset between the bottom and sidewall of the trench, which is assumed to be 80 degrees in all cases as discussed earlier. With the shape of the etch step described, the profile of the microcavity resonator is lastly dependent on the TeO₂ coating thickness (t_{TeO_2}), which is controlled by the length of the TeO₂ deposition performed in postprocessing, where t_{TeO_2} is the deposition thickness as measured on a bare silicon wafer witness sample. The use of a confocal sputtering gun arrangement and rotating substrate holder in the TeO₂ deposition process results in a deposition profile within the cavity similar to that reported in [16] for aluminum oxide coated microtrenches. The standard unpatterned TeO₂ film thickness coats the majority of the surface of the chip and the bottom of the microtrench structure. Near the cavity sidewall, approximately half the deposited thickness ($t_{\text{TeO}_2}/2$) grows along the sidewall while the TeO₂ layer along the bottom of the cavity thins into the corner where it meets the sidewall. For modeling purposes, the TeO₂ layer thinning near the cavity sidewall is assumed to take the shape of an ellipse, with a minor (vertical) axis of half the deposited film thickness aligned to the bottom of the trench, and a major (horizontal) axis aligned to the bottom corner of the trench. For all simulations a major axis width for the ellipse (w_{Corner}) of 2 μm is used, as little variation is seen in simulation results with major axis widths varying from 0.5 to 4 μm .

The shape of the microtrench and silicon waveguide models with relevant device dimensions are shown in Fig. 5.5(a), and sample simulated optical mode profiles for both devices are shown in Fig. 5.5(b). As there is limited confinement on the interior side of the microcavity resonator, several higher order optical modes are generally found in simulations. To simplify the upcoming design and analysis of the microcavity, only the fundamental TE-polarized mode of the device is considered, as it should be the mode with the lowest loss and strongest optical coupling to the silicon waveguide.

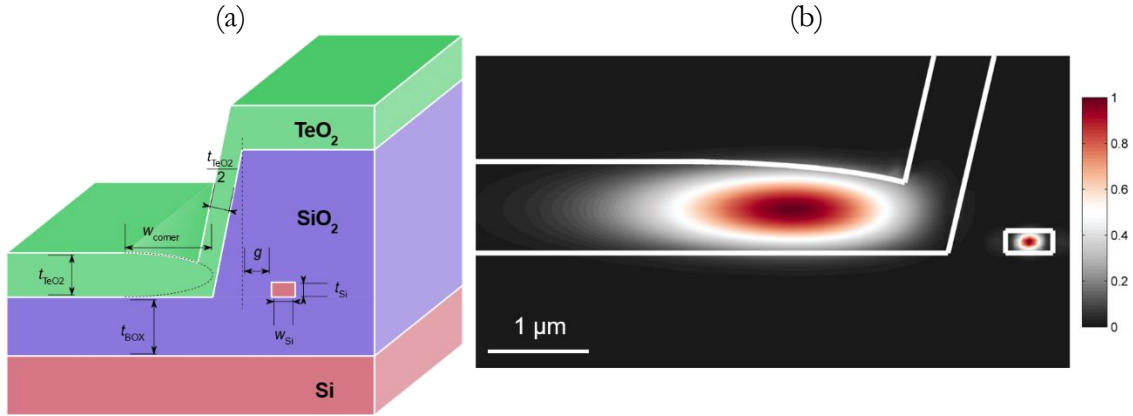


Fig. 5.5. (a) Cross-sectional profile of TeO₂ coated microcavity and silicon waveguide, with relevant device dimensions used in simulations. (b) Simulated fundamental TE-polarized electric-field profiles for the fundamental mode of a TeO₂ cavity with a 900-nm-thick TeO₂ coating at a 100 μm bend radius, next to the simulated mode of a 0.22×0.30 μm² silicon waveguide.

5.3.1 Microcavity Mode Properties

From Fig. 5.5(b) it can be seen that the optical mode of the TeO₂-coated microtrench is primarily confined in the corner of the cavity. Although the mode could also be confined closer to the center of the trench by the ellipsoidal pinch points on each side of the microtrench the curvature along the radial bend path of the microcavity causes the optical mode to shift away from the center of the microtrench. This results in the mode instead being confined between the ellipsoidal pinch point of the TeO₂ coating and microtrench sidewall. The bending radius of the microcavity is therefore very influential on the shape of the optical mode and optical properties of the microcavity, in contrast to the silicon strip waveguide, which is relatively insensitive to the bending radius of the device except at very small radii (< 10 μm). The fundamental TE-polarized mode of a microcavity coated in a 900-nm-thick TeO₂ film simulated at bending radii of 40, 100, and 200 μm can be seen in Fig. 5.6.

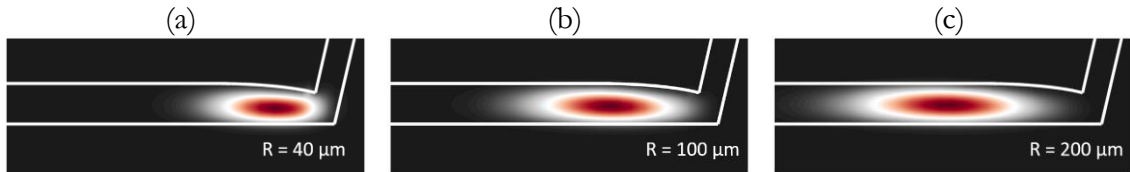


Fig. 5.6. Simulated electric-field mode profiles for a microcavity coated in a 900-nm-thick TeO₂ film at bending radii of (a) 40 μm, (b) 100 μm and (c) 200 μm.

From Fig. 5.6, it is evident that the optical mode of the microcavity resonator can be greatly influenced by changes to the bending radius. The most obvious visible effect of increasing the bending radius is the expansion of the optical mode's effective area. The optical mode area of the resonator versus TeO₂ coating thickness for microcavities with 40-, 100- and 200-μm bending radii was simulated, with the results shown in Fig. 5.7(a). While thicker TeO₂ coatings result in increasing the mode size due to increasing the diameter of the mode along

the vertical axis, the mode area is seen to almost double for all TeO₂ thicknesses when increasing from a 40- to 200- μm bend radius due to the decreased lateral confinement in the corner of the cavity. Large optical mode areas in TeO₂ devices can in some cases be less ideal as it decreases the intensity and efficiency of non-linear and rare-earth doped devices. This would suggest that tighter bending radii are better for TeO₂ devices. However, shifting the mode away from the microcavity sidewall can provide the added benefit of reducing mode overlap with the cavity sidewall, potentially reducing losses [16]. Thinner trench widths could be used to more strongly confine the optical mode near the center of the trench for larger radii, but this approach risks potentially introducing additional roughness from the sidewall on the opposite side of the trench. The centralization of the mode at larger radii might also reduce the optical power that can be coupled into the cavity, as its evanescent tail will be further from the silicon waveguide. An elliptical cavity that couples to the silicon waveguide at a small radius, and then expands to a larger radius to reduce losses could potentially be used. This type of cavity has also been used to promote unidirectional lasing [36,37]. For the simulated modes of Fig. 5.6 they can all be seen to be strongly confined within the TeO₂ film, with optical confinement predominantly determined by the vertical axis of the device, making it much less affected by bending radius. Fig. 5.7(b) shows the simulated optical confinement of the mode for TeO₂ coating thicknesses from 500 to 1100-nm at bending radii of 40, 100 and 200 μm . The optical confinement within the TeO₂ for the 100- and 200- μm bending radii modes are almost identical despite their different mode sizes, predicting approximately 82% confinement for a 500-nm-thick TeO₂ coating, increasing up to 95% confinement for a 1100-nm-thick TeO₂ coating. At a 40- μm bending radius there is a small decrease of the optical confinement in the TeO₂ ($\sim 3\%$) at all TeO₂ thicknesses, because the evanescent tail of the optical mode begins to leak out of the exterior sidewall of the microcavity. These confinement values demonstrate sufficient TeO₂ material interaction in the microcavity to realize novel TeO₂ devices in silicon photonic systems.

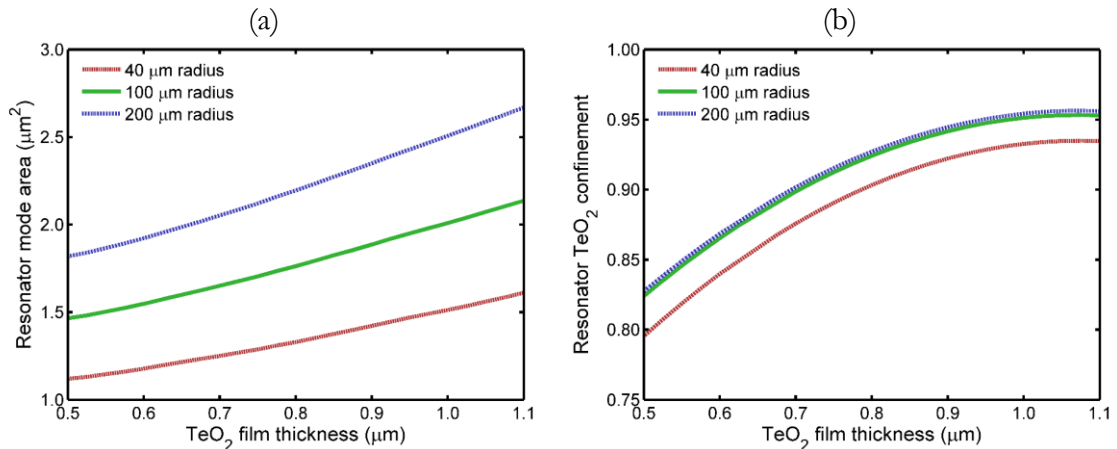


Fig. 5.7. Simulated (a) mode area and (b) optical confinement of the fundamental TE-polarized mode of microcavity resonator coated in TeO₂ film thicknesses of 0.5 to 1.1 μm at bending radii of 40, 100, and 200 μm .

5.3.2 Radiation Loss Minimization

Although the bending radius of the microcavity can affect many properties as just discussed, a primary consideration of the choice of bending radius is related to the optical propagation loss. To allow for the fabrication of effective nonlinear and rare-earth-doped microcavity devices, it is essential to achieve low waveguide loss or, equivalently, high Q factor resonators. There are several pathways for losses to occur in the microcavity, including: losses due to scattering at rough interfaces, material-related absorption, bend-related radiation losses and mode radiation into the silicon substrate. TeO₂ thin films exhibit some optical absorption and create some scattering due to surface roughness of the deposited film, but for high quality films these sources should be minimal, as demonstrated by the low loss planar film modes measured in Chapter 2. Surface roughness can be induced along the SiO₂-TeO₂ interface along the bottom and sidewall of the microtrench from the etch process, however, and this can also translate into TeO₂-Air interface roughness due to the conformal coating. This can be partially minimized in the design by using thicker TeO₂ coatings and larger radii to reduce sidewall interaction [16], but has the negative trade-offs just discussed. The radiation related pathways of loss can be effectively minimized in the device by appropriately designing the cavity to limit bending and substrate leakage. The radiation losses were found by calculating the imaginary index of the microcavity through eigenmode simulations in Synopsys RSoft, which are then converted to the radiation limited Q factor using Equation 3.28. The bending radiation losses were calculated for cavities with TeO₂ film thicknesses ranging from 500 to 1100 nm and a BOX thickness of 2 μm at microcavity bending radii ranging from 200 down to 5 μm , with the results shown in Fig. 5.8(a). The data show that thinner TeO₂ films can allow for smaller bending radii before the radiation loss becomes significant, but in general devices demonstrate the ability to be tightly bent on the scale necessary for silicon photonic systems ($\sim 10\text{s}$ of μm). TeO₂ coatings with thickness of 500 and 700 nm are shown to maintain bending radiation limited intrinsic Q factors of $>10^9$ at bending radii of $< 20 \mu\text{m}$, while an 1100-nm-thick coating is able to maintain high intrinsic Q factors at radii of 40 μm and above. Therefore, to effectively minimize bending radiation devices were fabricated at bending radii of either 40 or 100 μm , which should minimize loss without unnecessary expansion of the mode. The other pathway for radiation loss in the device is for light to leak into the silicon substrate, through optical overlap with the microcavity mode's lower evanescent tail. To prevent substrate leakage the t_{Box} distance between the substrate and microcavity must be sufficiently large. The silicon substrate radiation losses were calculated for microcavities with TeO₂ coating thicknesses of 500 to 1100 nm for a bending radius of 40 μm , which as seen in Fig. 5.8(a) should have minimal bending radiation losses, and BOX separations from 2 μm down to 0.2 μm . The calculated substrate-radiation limited Q factor results are shown in Fig. 5.8(b). The simulations show that substrate radiation is negligible, with internal Q factors of $>10^9$, at a 2- μm separation between resonator and substrate for all film thicknesses. However, in fabricated devices the microtrench was found to be significantly over etched beyond the designed BOX, such that the microcavity experiences an estimate separation of roughly only 1 or 1.5- μm for design A

and B, respectively. At a 1.5 μm separation Q factors should still be able to exceed 10^8 for the TeO_2 coating thicknesses under consideration, but quickly drops to Q factor limits of roughly $\sim 10^6$ at a 1- μm substrate separation. Therefore, to maintain the potential of high Q factor devices in this platform it is essential to ensure that the thermal oxide layer under the microcavity remains above at least 1 μm . Increasing the bending radius of the cavity to greater than 40 μm is seen to result in a minor decrease in the substrate radiation limited Q factor as the mode becomes less strongly confined in the corner of the cavity and experiences slightly more overlap with the substrate.

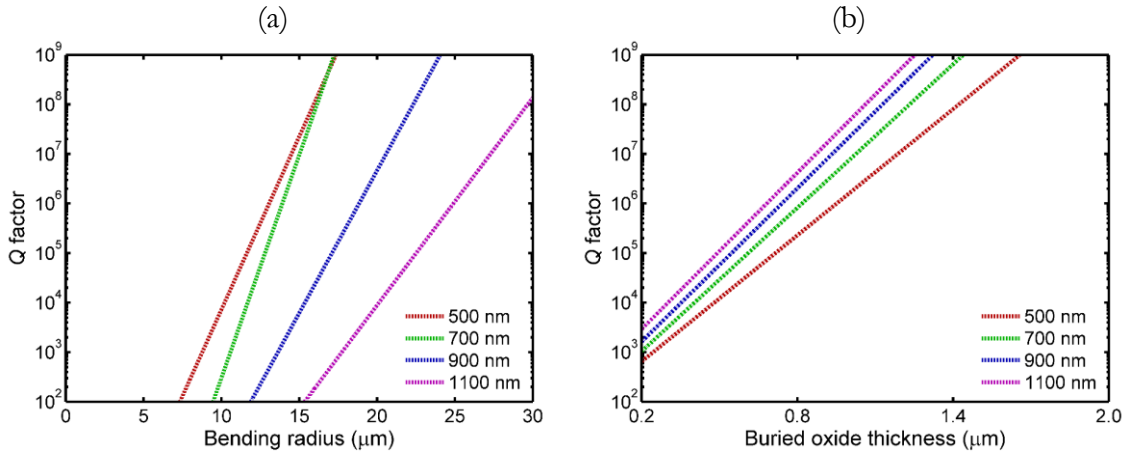


Fig. 5.8. Simulated radiation limited internal Q factors of microcavities coated in 500-, 700-, 900-, and 1100-nm-thick TeO_2 coatings considering the effects of (a) bending radiation losses and (c) substrate radiation losses.

5.3.3 Optical Coupling Between Silicon Waveguide and TeO_2 Microcavity

To access the TeO_2 microcavity on the SOI platform light must be able to be efficiently coupled to/from the silicon bus waveguide. To achieve this the bus waveguide and cavity must be closely phase matched, with similar effective indices, because differences in phase will limit the total amount of light from the bus waveguide that can be coupled into the microcavity resonator [38]. The effective index of the silicon strip waveguide, for a 0.22- μm -thick strip height was calculated versus strip width using eigenmode simulations. Thinner waveguide widths cause the evanescent tail of the mode to expand out of the silicon core. This causes the mode to experience greater interaction with the SiO_2 cladding which reduces the effective index. The simulated effective indices versus waveguide width are shown in Fig. 5.9(a). This data can be used to match the effective index of the silicon waveguide to the TeO_2 microcavity. The simulated effective index of the microcavity for TeO_2 coating thicknesses of 500 to 1100 nm and 40, 100 and 200- μm bending radii are shown in Fig. 5.9(b). It can be seen that thicker TeO_2 coatings increase the effective index of the microcavity due to the higher optical confinement in the TeO_2 film, from 1.80 with a 500-nm-thick TeO_2 coating up to 1.96 with a 1100-nm-thick coating for a 100- μm bending radius. Decreasing the bending radius results in

a small reduction in effective index, as the evanescent mode extending beyond the sidewall grows larger, as discussed earlier. This makes it difficult to design ideal phase matching between the silicon waveguide and microcavity resonator, because the effective index of the microcavity is highly dependent on the thickness of the TeO_2 coating, which will be varied between chips when fabricating devices. In the initial design run a $0.35\text{-}\mu\text{m}$ wide silicon bus waveguide was used, which is expected to have an effective refractive index of 2.037. Although this is a slightly higher index than the expected refractive index from the microcavity, it was chosen to reduce fabrication variations, where $0.3\text{-}\mu\text{m}$ wide silicon bus waveguides can experience refractive index variations of greater than ± 0.045 for a $\pm 10\text{-nm}$ fabrication tolerance in waveguide width. This can lead to significant chip-to-chip and even device-to-device variability in the fabricated circuits. However, this bus width was seen to result in low coupling strengths in the initial design, therefore $0.3\text{-}\mu\text{m}$ wide silicon bus waveguides with an effective index of 1.821 were selected in the second design run for improved coupling strength despite the higher fabrication tolerance.

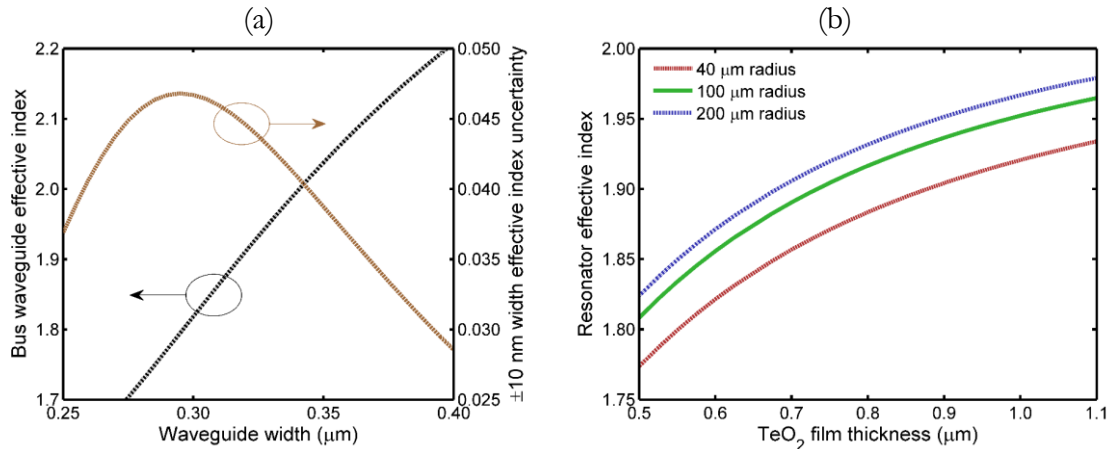


Fig. 5.9. Simulated (a) effective index of silicon bus waveguide versus waveguide width, and variation in effective index for a ± 10 nm waveguide width variation, (b) effective index versus TeO_2 coating thickness for microcavities with 40, 100 and 200 μm bending radii.

Because of the large permittivity, mode size, and phase differences between the silicon waveguide and TeO_2 microcavity the cross-over ratio (x), describing the ratio of power coupled between the two structures cannot be effectively modelled using the eigenmode expansion method described earlier in Section 3.4.3. Additionally, due to the large vertical differences between the mode shapes confined by each waveguide finite-difference-time-domain (FDTD) simulations of the coupler would have to be performed in 3 dimensions, making modelling computationally intensive and time consuming. An alternative method to determine the cross-over ratio is by using coupled mode theory analysis. The theory is presented here, and closely follows the derivations provided in [39-41] with some minor modifications. For simplicity, the coupler is modelled only along the region of the coupler that maintains the minimum coupling distance G between the resonator and waveguide, shown in the shaded region of Fig. 5.10(a). The coupled mode theory models described in references.

39-41 discuss coupling between a point coupled bus waveguide and a circular ring resonator, which requires the ring resonator to be translated from cylindrical to cartesian coordinates. In this work however both the resonator and pulley-coupled bus waveguide bend together in the simulated region. Therefore, the coupler can be modelled in an equivalent cartesian coordinate system, assuming that the waveguides propagate straight along the z axis as shown in Fig. 5.10(b) with the optical modes described by the bent structure.

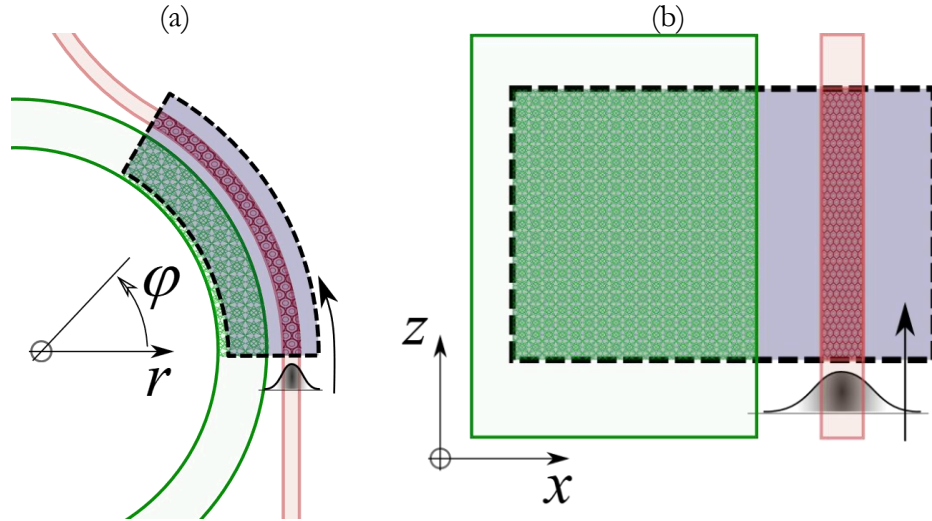


Fig. 5.10. Shaded box shows the simulation region for the silicon waveguide and microcavity resonator in (a) cylindrical coordinates and (b) mapped to Cartesian coordinates.

The cross-over ratio is then determined by defining a permittivity/refractive index profile and electric- and magnetic-field mode profiles of each independent waveguide structure. The first waveguide structure is defined as the TeO_2 coated microcavity, with dimensions described earlier in Fig. 5.5(a), with the bottom right corner of the cavity defined as the 0,0 point of the xy plane. This profile defines the permittivity matrix of the microcavity (ϵ_1), with an example in Fig. 5.11(a), and is used to calculate the electric- (\vec{E}_1) and magnetic-field (\vec{H}_1) vector profiles of the microcavity. The electric- and magnetic field vectors contain an \hat{x} and \hat{y} polarized field matrix in the xy cross section of the device, with amplitudes found by eigenmode simulations ($E_{1x}^0, E_{1y}^0, H_{1x}^0, H_{1y}^0$). Although there will be a small \hat{z} polarized component of the fields it is assumed that the light propagates directly along the \hat{z} axis, such that there will be no \hat{z} polarized component of the electric- and magnetic-field vector. For the microcavity resonator Fig 5.11(b) and (c) show the simulated x component of the electric field and y component of the magnetic field respectively, with normalized values. These polarization components were chosen to be shown as they are the dominant field components for a TE-polarized mode. A corresponding y and x component of each field exists and is used in the calculation, but are of a much smaller value when normalized to the dominant mode component.

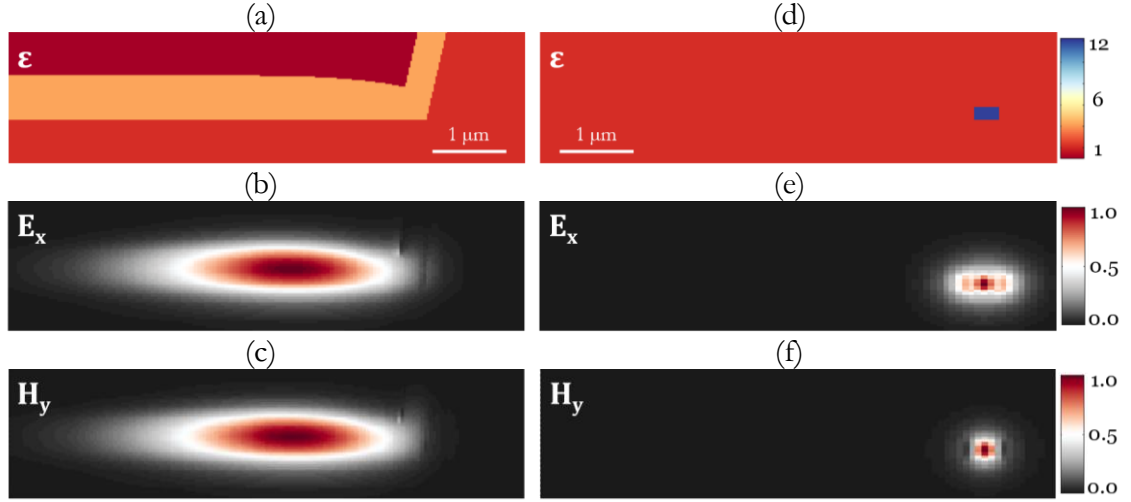


Fig. 5.11. Permittivity profile and normalized x polarized electric-field component and y polarized magnetic-field component of the optical mode profiles for the (a-c) microcavity resonator and (d-f) silicon bus waveguide.

Each field component oscillates along the propagation distance (z) of the microcavity waveguide with periodicity determined by the propagation constant (β_1) of the waveguide, which is found from the simulated effective refractive index of the waveguide mode ($n_{\text{Eff},1}$) at a wavelength of λ by the following,

$$\beta_1 = \frac{2\pi n_{\text{Eff},1}}{\lambda}. \quad (5.1)$$

The general equation for the electric- and magnetic- field equations for the microcavity at any point of the simulated structure can be described by the Equations 5.2 and 5.3 respectively,

$$\vec{E}_1(x, y, z) = (E_{1x}^0(x, y) \cdot \hat{x} + E_{1y}^0(x, y) \cdot \hat{y})e^{-i\beta_1 z}, \quad (5.2)$$

$$\vec{H}_1(x, y, z) = (H_{1x}^0(x, y) \cdot \hat{x} + H_{1y}^0(x, y) \cdot \hat{y})e^{-i\beta_1 z}. \quad (5.3)$$

This can be similarly calculated for the silicon bus waveguide, with a permittivity matrix (ϵ_2) described by the silicon waveguide surrounded by an SiO_2 cladding, with the inner sidewall of the silicon waveguide separated from the bottom corner of the microtrench by the nominal coupling gap. Example permittivity and mode profiles for the silicon waveguide are shown in Fig. 5.11 (d-f). From coupled mode theory the electric- and magnetic field- mode profile of the combined waveguide structure (\vec{E}_C, \vec{H}_C) should be a linear combination of the modes confined by the microcavity (\vec{E}_1, \vec{H}_1) and bus waveguide (\vec{E}_2, \vec{H}_2), as described in Equation 5.4:

$$\begin{aligned} \vec{E}_C(x, y, z) &= A_{(z)}\vec{E}_1(x, y, z) + B_{(z)}\vec{E}_2(x, y, z), \\ \vec{H}_C(x, y, z) &= A_{(z)}\vec{H}_1(x, y, z) + B_{(z)}\vec{H}_2(x, y, z), \end{aligned} \quad (5.4)$$

where A and B are the ratio of the electric- and magnetic- fields of the microcavity and silicon waveguide contributing to the combined fields respectively, referred to as the field coefficients. The values of A and B vary as a function of the propagation distance along the waveguide z . Considering a unit power launched into the silicon bus waveguide ($A_{(0)} = 0, B_{(0)} = 1$), the squared amplitudes of A and B after propagating the length L of the coupler could then be considered the cross-over (α) and transmission (β) ratios respectively. Therefore, to find the cross-over ratio of the device Equation 5.4 must be rearranged to solve for the constants A and B . The Lorentz Reciprocity Theorem states that for any two electromagnetic modes a and b with electric and magnetic field profiles \vec{E}_a and \vec{H}_a and \vec{E}_b and \vec{H}_b , respectively, the following relationship can be derived,

$$\iint \nabla \cdot (\vec{E}_a \times \vec{H}_b^* + \vec{E}_b^* \times \vec{H}_a) dx dy = -i\omega \iint (\epsilon_a - \epsilon_b) \vec{E}_a \cdot \vec{E}_b dx dy, \quad (5.5)$$

where ϵ_a and ϵ_b are the permittivity distributions describing the two modes under consideration. To simplify the notation in future equations the vector expression on the left-hand side of Equation 5.5 is simplified to the variable $\vec{\Phi}_{ab}$ as follows:

$$\vec{\Phi}_{ab} = (\vec{E}_a \times \vec{H}_b^* + \vec{E}_b^* \times \vec{H}_a). \quad (5.6)$$

Equation 5.5 is then applied twice, between the combined structure (C) with each of the independent waveguide structures describing the individual microcavity and silicon waveguide (1 and 2, respectively). This results in Equations 5.7 and 5.8 below, using the notation of Equation 5.6,

$$\iint \nabla \cdot \vec{\Phi}_{C1} dx dy = -i\omega \iint (\epsilon_C - \epsilon_1) \vec{E}_C \cdot \vec{E}_1 dx dy, \quad (5.7)$$

$$\iint \nabla \cdot \vec{\Phi}_{C2} dx dy = -i\omega \iint (\epsilon_C - \epsilon_2) \vec{E}_C \cdot \vec{E}_2 dx dy. \quad (5.8)$$

Equations 5.7 and 5.8 can then be simplified by rewriting the combined field variables in terms of the independent fields using the definitions of Equation 5.4. The simplification process is carried out here on Equation 5.7 as an example, but will be similar for both Equations 5.7 and 5.8. The first step of the process is to take the left-hand side of Equation 5.7 outside the double integral, and redefine the combined electric-field profile as shown below in Equation 5.9:

$$\begin{aligned} \nabla \cdot \vec{\Phi}_{C1} &= \nabla \cdot (A_{(z)} \vec{E}_1 \times \vec{H}_1^* + A_{(z)} \vec{E}_1^* \times \vec{H}_1 + B_{(z)} \vec{E}_2 \times \vec{E}_1^* + \vec{E}_1^* \times B_{(z)} \vec{H}_2) \\ &= \nabla \cdot (A_{(z)} (\vec{E}_1 \times \vec{H}_1^* + \vec{E}_1^* \times \vec{H}_1)) + \nabla \cdot (B_{(z)} (\vec{E}_2 \times \vec{E}_1^* + \vec{E}_1^* \times \vec{H}_2)) \\ &= \nabla \cdot A_{(z)} \cdot \vec{\Phi}_{11} + \nabla \cdot B_{(z)} \vec{\Phi}_{21}. \end{aligned} \quad (5.9)$$

The expression of Equation 5.9 is now described totally in terms of the two independent mode profiles. The two terms on the right-hand side of Equation 5.9 can be simplified further using the following general identity between a scalar (ρ) and vector (\vec{V}),

$$\nabla \cdot (\rho \vec{V}) = (\rho \nabla \cdot \vec{V}) + (\vec{V} \cdot \nabla \rho), \quad (5.10)$$

which is used to expand the right-hand side of Equation 5.9 as follows,

$$\nabla \cdot \overrightarrow{\Phi_{C1}} = (A_{(z)} \nabla \cdot \overrightarrow{\Phi_{11}}) + (\overrightarrow{\Phi_{11}} \cdot \nabla A_{(z)}) + (B_{(z)} \nabla \cdot \overrightarrow{\Phi_{21}}) + (\overrightarrow{\Phi_{21}} \cdot \nabla B_{(z)}). \quad (5.11)$$

The Lorentz Reciprocity Theorem (Equation 5.5) can then be reapplied to the first term on the right-hand side of Equation 5.11, which is reduced to 0 as the permittivity distribution profiles of a structure with itself cancel out,

$$\iint (\nabla \cdot \overrightarrow{\Phi_{11}}) dx dy = 0. \quad (5.12)$$

This can also be used to describe the third term of Equation 5.11 as follows,

$$\iint B_{(z)} \nabla \cdot \overrightarrow{\Phi_{21}} dx dy = -i\omega B_{(z)} \iint (\epsilon_2 - \epsilon_1) \overrightarrow{E}_2 \cdot \overrightarrow{E}_1 dx dy. \quad (5.13)$$

The second and fourth terms of Equation 5.11 take the gradient of the field coefficients, which are transformed into vectors along the \hat{z} direction, as the field coefficients are a parameter of only the propagation distance along the device,

$$\begin{aligned} \nabla A_{(z)} &= \frac{dA_{(z)}}{dz} \hat{z}, \\ \nabla B_{(z)} &= \frac{dB_{(z)}}{dz} \hat{z}. \end{aligned} \quad (5.14)$$

The integral addition rule then allows each term of Equation 5.11 to be individually returned to the double integral on the left hand side of Equation 5.7, which by using Equations 5.12-5.14 can now be described as Equation 5.15,

$$\iint \nabla \cdot \overrightarrow{\Phi_{C1}} = \frac{dA_{(z)}}{dz} \iint \overrightarrow{\Phi_{11}} \cdot \hat{z} + \frac{dB_{(z)}}{dz} \iint \overrightarrow{\Phi_{21}} \cdot \hat{z} - i\omega B_{(z)} \iint (\epsilon_2 - \epsilon_1) \overrightarrow{E}_2 \cdot \overrightarrow{E}_1. \quad (5.15)$$

As the third term of Equation 5.15 is of the same form as the right-hand side of Equation 5.7 it is transferred to the right-hand side. By using this new term and expanding the combined electric field term (\overrightarrow{E}_C), the right-hand side of Equation 5.7 can be similarly rewritten only in terms of the two independent mode profiles, as shown in Equation 5.16.

$$\begin{aligned}
 & -i\omega \iint (\epsilon_C - \epsilon_1) \vec{E}_C \cdot \vec{E}_1 + i\omega \iint B_{(z)} (\epsilon_2 - \epsilon_1) \vec{E}_2 \cdot \vec{E}_1 \\
 & = -i\omega \iint (\epsilon_C - \epsilon_1) (\vec{E}_C \cdot \vec{E}_1) - B_{(z)} (\epsilon_2 - \epsilon_1) (\vec{E}_2 \cdot \vec{E}_1) \\
 & = -i\omega \iint (\epsilon_C - \epsilon_1) (A_{(z)} \vec{E}_1 \cdot \vec{E}_1 + B_{(z)} \vec{E}_2 \cdot \vec{E}_1) - (\epsilon_2 - \epsilon_1) (B_{(z)} \vec{E}_2 \cdot \vec{E}_1) \quad (5.16) \\
 & = -i\omega \iint A_{(z)} (\epsilon_C - \epsilon_1) (\vec{E}_1 \cdot \vec{E}_1) + B_{(z)} ((\epsilon_C - \epsilon_1) - (\epsilon_2 - \epsilon_1)) (\vec{E}_2 \cdot \vec{E}_1) \\
 & = -i\omega \iint A_{(z)} (\epsilon_C - \epsilon_1) (\vec{E}_1 \cdot \vec{E}_1) + B_{(z)} (\epsilon_C - \epsilon_2) (\vec{E}_2 \cdot \vec{E}_1).
 \end{aligned}$$

Equation 5.7 now takes the form of a differential equation for the field coefficients A and B , which depend only on the known permittivity distributions of the device and the independent field profiles found from eigenmode simulation. By similarly simplifying Equation 5.8 as just carried out in Equations 5.9 to 5.16, a system of differential equations for the variables of A and B can be developed, as shown in Equation 5.17:

$$\begin{aligned}
 & \begin{bmatrix} \iint \hat{z} \cdot \Phi_{11} & \iint \hat{z} \cdot \Phi_{21} \\ \iint \hat{z} \cdot \Phi_{12} & \iint \hat{z} \cdot \Phi_{22} \end{bmatrix} \begin{bmatrix} \frac{dA_{(z)}}{dz} \\ \frac{dB_{(z)}}{dz} \end{bmatrix} \\
 & = -i\omega \begin{bmatrix} \iint (\epsilon_C - \epsilon_1) \vec{E}_1 \cdot \vec{E}_1 & \iint (\epsilon_C - \epsilon_2) \vec{E}_2 \cdot \vec{E}_1 \\ \iint (\epsilon_C - \epsilon_1) \vec{E}_1 \cdot \vec{E}_2 & \iint (\epsilon_C - \epsilon_2) \vec{E}_2 \cdot \vec{E}_2 \end{bmatrix} \begin{bmatrix} A \\ B \end{bmatrix}. \quad (5.17)
 \end{aligned}$$

To simplify notation, the values of the 2×2 matrix on the left- and right-hand side of Equation 5.17 are simplified to σ_{ii} and C_{ii} respectively. These two matrices are used to determine the Transfer matrix T as follows:

$$\begin{bmatrix} T_{11} & T_{21} \\ T_{12} & T_{22} \end{bmatrix} = \begin{bmatrix} \sigma_{11} & \sigma_{21} \\ \sigma_{12} & \sigma_{22} \end{bmatrix}^{-1} \begin{bmatrix} C_{11} & C_{21} \\ C_{12} & C_{22} \end{bmatrix}, \quad (5.18)$$

where the transfer matrix can be used to simplify Equation 5.17 as follows:

$$\begin{bmatrix} \frac{dA_{(z)}}{dz} \\ \frac{dB_{(z)}}{dz} \end{bmatrix} = -i\omega \begin{bmatrix} T_{11} & T_{21} \\ T_{12} & T_{22} \end{bmatrix} \begin{bmatrix} A_{(z)} \\ B_{(z)} \end{bmatrix}. \quad (5.19)$$

Because the transfer matrix T is dependent only on the electric and magnetic-field profiles of the individual modes and the permittivity distributions and not on the field coefficients (A and

B), the transfer matrix can be solved at all z points of the structure before solving for the field coefficients. The simulation is then run considering a set of initial field coefficients, normalized such that the sum of their squared amplitudes is equal to one, and applying Equation 5.19 along the length of the coupler. To estimate the cross-over ratio of the system the initial boundary value conditions assume a unit pulse of light entering the silicon bus waveguide and no initial light in the microcavity resonator as follows,

$$\begin{bmatrix} A_{(0)} \\ B_{(0)} \end{bmatrix} = \begin{bmatrix} 0 \\ 1 \end{bmatrix}. \quad (5.20)$$

The cross-over ratio κ at any point along the coupler is then found from the squared amplitude of the field coefficient A as follows,

$$\kappa_{(z)} = |A_{(z)}|^2. \quad (5.21)$$

Simulations to find the cross-over ratio were carried out using the RSoft data files and Matlab code presented in Appendix D for a 0.3- μm -wide by 0.22- μm -thick silicon waveguide, with an effective waveguide index of 1.821. The silicon waveguide was coupled to 100 μm radius microcavities with 500-, 700-, 900-, and 1100-nm-thick TeO_2 coatings and effective waveguide indices of 1.838, 1.922, 1.969, and 1.999, respectively, at coupling gaps of 0.1 to 0.45 μm . The coupling gap is referenced between the bottom right corner of the resonator cavity and the interior wall of the bus waveguide, not accounting for any lateral offset introduced during fabrication. For simplicity, it was assumed that the bottom of the resonator and waveguide are aligned such that there is no overetch of the oxide into BOX. Each simulation was run in steps of 0.5- μm over a 120- μm distance. Examples of the calculated cross-over ratios for a 700-nm-thick TeO_2 cavity and gaps of 0.14, 0.18 and 0.25 μm are shown in Fig. 5.12.

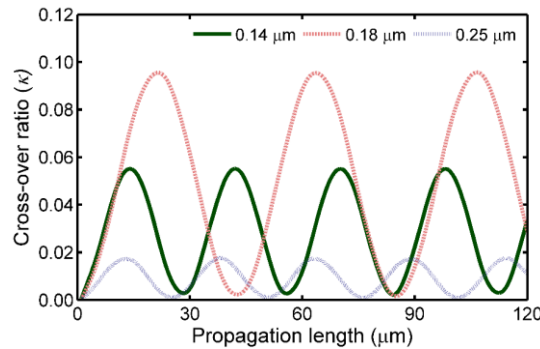


Fig. 5.12. Cross-over ratio versus propagation length along the coupler for a 700-nm-thick TeO_2 microcavity with a 0.30- μm -wide silicon bus waveguide at simulated coupling gaps of 0.14, 0.18 and 0.25 μm .

As can be seen from the results the light couples from the bus waveguide to the microcavity and back in a sinusoid shape along the coupler length as described earlier (Section

3.4.3). Here however, due to the large phase and permittivity distribution differences between waveguides not all of the light is coupled from the microcavity into the waveguide, instead peaking at a smaller value based on the coupling gap. Although the directional couplers in devices have specified length values that could be used to determine precise cross-over ratios, additional coupling occurs in the transition sections near the coupler, and the various uncertainties in the device dimensions affect exactly where on the sinusoidal coupling curve the measured value lies for a given wavelength. Therefore, the peak cross-over ratio value that was found over the simulated range was taken as the maximum possible cross-over ratio for the cross-sectional geometry under consideration. The maximum cross-over ratio can then be converted into the minimum attainable external Q factor (Q_e) for that microcavity geometry using the following relationship [42],

$$Q_e = -\frac{\pi \cdot l_{RT} \cdot n_g}{\lambda \cdot \log(1 - \kappa)}, \quad (5.22)$$

where l_{RT} is the round-trip length and n_g is the group index of the microcavity.

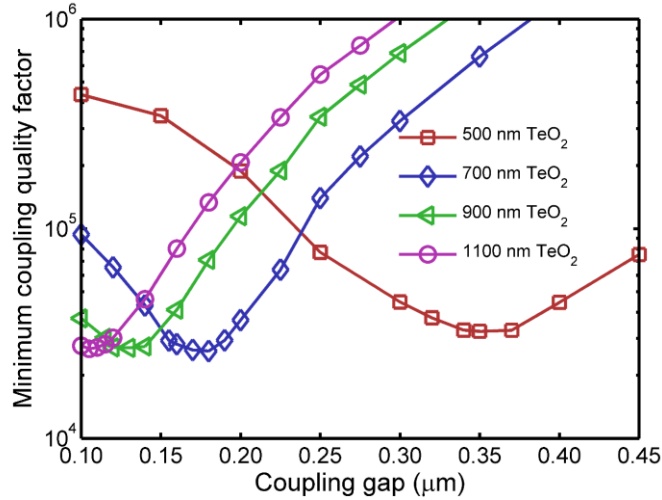


Fig. 5.13. Minimum calculated external Q factors between a 0.30- μm -wide silicon bus waveguide and TeO_2 microtrench cavities with a 100 μm bend radius coated in 500-, 700-, 900- and 1100-nm thick TeO_2 layers at coupling gaps between 0.10 and 0.45 μm .

The calculated minimum external Q factors for the microcavity geometries under consideration are plotted in Fig. 5.13. The results demonstrate that for each of the microcavity dimensions studied the minimum attainable coupling Q factor is around 0.2×10^5 . The measured coupling Q factors of devices would be expected to fall at or above these values depending on which phase of the sinusoidal coupling relationship they fall within. In general, each curve demonstrates a peak in coupling strength at a particular coupling gap, with significantly reduced coupling efficiency for relatively small variations in gap. Although it is expected to observe reduced coupling efficiency at larger gaps, it is unusual for the coupling efficiency to also decrease at smaller gaps, as observed here. This is potentially a result of the

phase difference between devices, as well as the vertical offset between the peak electric field of the bus waveguide and resonator modes. For applications of microcavities in lasers, high coupling Q factors, typically of $\sim 1 \times 10^6$ and greater, are generally of interest to minimize total losses and achieve roundtrip optical gain. This generally requires coupling gaps of $0.4 \mu\text{m}$ and above based on these results. The fabricated devices would generally be expected to have significantly larger external Q factors than what is calculated here because of the large effective coupling gaps created by the over etched microtrenches.

5.4. TeO₂ Microcavity Characterization

The TeO₂ coated optical microcavities were tested by characterization of their resonance spectra using a passive fiber-chip transmission setup with a tunable 1550 nm wavelength laser. Because the microcavity is a self-contained element on the chip, its properties can be simply analyzed from the relative spectral transmission data (T), without the need to characterize the fiber (F) or coupling losses (M), although the nano-tapered silicon waveguides were typically found to have coupling losses of 4 to 5 dB using tapered ($2.5 \mu\text{m}$ spot size) input and output fibers. The fabricated chips were characterized at wavelengths from 1510 to 1640 nm. On each chip the measurements started with the microcavity with the smallest available coupling gap and were carried out on devices in order of increasing gaps. The polarization was initially set to maximize the transmission across the chip at 1550 nm wavelength, after which a first wavelength sweep was taken. If any resonance modes were observed the wavelength was tuned onto one of the resonance dips and the polarization paddles were adjusted to maximize the extinction ratio. This was assumed to be the TE-polarized mode of the device and confirmed by measuring transmission on TeO₂ coated Si₃N₄ waveguide samples that support only a TE-polarized mode (see section 3.3) using the same polarization state. If no resonance modes were found several random polarization states were attempted, after which if resonance modes were still not found it was assumed that the microcavity under test did not have any measurable resonant modes.

5.4.1 Design A Results

The initial design run (Design A) was tested with five different tellurium oxide thin film coatings, with nominal thicknesses of 310, 480, 570, 900, and 1100 nm, as measured by ellipsometry on the bare silicon witness sample mounted on the sample stage during deposition. The thin film propagation losses were measured on unpatterned thermally oxidized wafers, with each film observed to have 0.3 dB/cm of loss or less at a 1550 nm wavelength. This demonstrates that the films have high optical quality, with low absorption and smooth surfaces, such that if the film losses were the only source of propagation loss in the microcavity internal Q factors could be expected to exceed 10^6 . For the five chips studied only the chips coated in 480-, 900- and 1100-nm-thick TeO₂ films were observed to have identifiable resonances, with the other samples not displaying any noticeable resonance modes. Furthermore, resonances were only measured at small coupling gaps, with no resonances

observed on any sample at nominal coupling gaps of greater than $0.4\ \mu\text{m}$. This is likely a result of the large effective coupling gaps due to the deep over etching of the micro trench on this chip set creating very weak coupling between the bus waveguide and resonator. The devices that did have observable resonances were characterized by identifying the resonance wavelengths using a peak finding algorithm. Each resonance mode was then fit using the Q fitting algorithm (Appendix B), to determine an internal (Q_i) and external (Q_e) Q factor. The resonance spectrum measured from 1590 to 1640 nm for the chip coated in 1100-nm of TeO_2 and a coupling gap of $0.2\ \mu\text{m}$ is shown in Fig. 5.14(a).

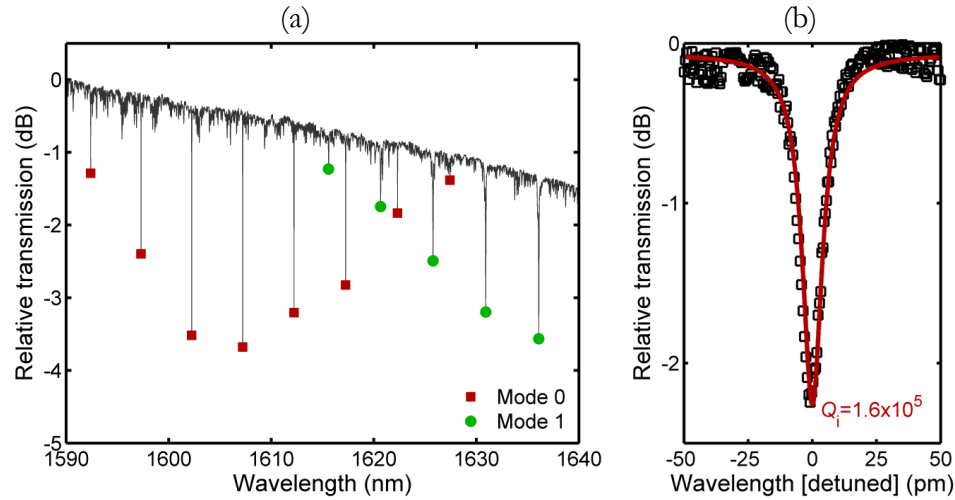


Fig. 5.14. (a) Transmission spectrum of microtrench cavity from design A, with a 1100-nm-thick TeO_2 coating. (b) A fundamental mode of the device fit using the Q factor fitting code to have an internal Q factor of 1.6×10^5 at a wavelength of 1597 nm.

Two resonant modes can be observed in this range, with the first set of modes (marked by squares) assumed to be the fundamental mode due to their higher measured internal Q factor and larger FSR, which suggests a greater group index. One of the fundamental modes of the device is fit with an internal Q factor of 1.6×10^5 , using the Q factor fitting code and assuming the cavity is undercoupled, which corresponds to approximately 2.2 dB/cm of waveguide loss in the microcavity. This is significantly higher than the optical propagation loss measured in the thin films, while simulations predict that the bending radiation loss should be minimal for microcavity radii of $40\ \mu\text{m}$ and the substrate-radiation-limited Q should exceed 10^6 . Therefore, it is assumed that the dominant source of loss in the microcavity comes from surface roughness along the bottom and sidewall of the microtrench, introduced during the oxide etch step. The internal Q factors measured for the other chips, summarized in Table 5.2, are 0.4×10^5 and 0.7×10^5 for the 480- and 900-nm-thick TeO_2 coated microcavities, respectively. In general, thicker films are seen to have larger internal Q factors, due to the reduced optical overlap with the roughness along the microtrench interface. The fundamental mode of this device is observed to have a maximum extinction ratio of 3.2 dB, which is fit with an external Q factor of 4.4×10^5 , assuming that the device is undercoupled. The measured

coupling Q factors of all devices are relatively large, mainly as a result of the $\sim 1 \mu\text{m}$ overetch creating effective coupling gaps that are greater than $1 \mu\text{m}$. Modifications in the second design run (Design B) were largely targeted towards improving the optical coupling efficiency through smaller coupling gaps, longer pulley lengths, and thinner silicon bus waveguides.

Table 5.2. Measured properties of TeO_2 coated microcavities characterized on chip design A.

TeO_2 coating thickness (nm)	TeO_2 film loss (dB/cm)	Minimum external Q factor	Maximum extinction ratio (dB)	Maximum internal Q factor	Microcavity propagation loss (dB/cm)
305	0.2 ± 0.2	---	---	---	---
480	0.1 ± 0.1	2.3×10^5	3.0	0.4×10^5	8.7
570	0.1 ± 0.1	---	---	---	---
900	0.3 ± 0.3	2.0×10^5	6.6	0.7×10^5	5.1
1100	0.2 ± 0.2	4.4×10^5	3.2	1.6×10^5	2.2

5.4.2 Design B Results

Chips from the second design run were tested in the same method as the initial run, beginning with a set of three chips coated in 495-, 775-, and 1115-nm-thick layers of TeO_2 respectively. Fig. 5.15(a) shows the transmission spectrum measured for the 1115-nm TeO_2 device at a nominal coupling gap of $0.2 \mu\text{m}$. From this figure two resonance modes can be observed, with the squares representing what was determined as the fundamental mode. It is found to have a maximum internal Q factor of 0.9×10^5 , as shown in Fig 5.15(b), corresponding to 4.0 dB/cm of waveguide propagation loss.

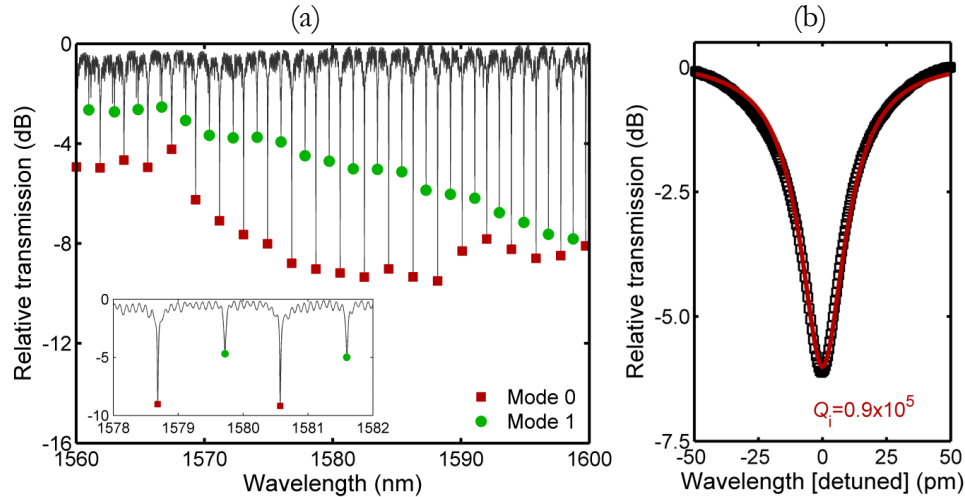


Fig. 5.15. (a) Transmission spectrum of microtrench cavity from design B, coated in 1115-nm of TeO_2 , with inset showing a close-up view of two resonant free spectral ranges. (b) A fundamental mode of the device fit using the Q factor fitting code to have an internal Q factor of 0.9×10^5 at a wavelength of 1627 nm.

In general, the chips in the second design run, summarized in Table 5.3, are found to have lower internal Q factors than the initial design run, despite similar TeO₂ film optical propagation losses and what is expected to be less radiation loss through bending and substrate leakage. It is assumed that modifications to the foundry fabrication procedure, despite reducing the over etching of the trenches, resulted in a rougher SiO₂ etch wall interface, which translated to increased losses in the microcavity. However, the reduced over etching was seen to improve external Q factors. The devices had much larger extinction ratios and the 775-nm-thick TeO₂ coated sample was fit with a minimum external Q factor of 0.4×10^5 . This approaches the minimum external Q factor that would be expected for a device with this film thickness, as shown in the simulation results in Fig. 5.13.

Table 5.3. Measured properties of TeO₂ coated microcavities characterized on chip design B.

Cytop coating thickness (nm)	TeO ₂ coating thickness (nm)	TeO ₂ film loss (dB/cm)	Minimum external Q factor	Maximum extinction ratio (dB)	Maximum internal Q factor	Microcavity propagation loss (dB/cm)
0	495	0.1 ± 0.1	1.2×10^5	4.8	0.2×10^5	18.0
0	775	0.3 ± 0.2	0.4×10^5	16.1	0.3×10^5	12.0
0	1115	0.2 ± 0.2	1.1×10^5	8.9	0.9×10^5	4.0
100	335	0.3 ± 0.2	3.3×10^5	4.8	1.2×10^5	3.0
100	630	0.2 ± 0.2	4.8×10^5	2.5	2.1×10^5	1.7
100	840	0.1 ± 0.1	1.7×10^5	5.0	1.5×10^5	2.4
50	970	0.4 ± 0.2	2.0×10^5	3.5	1.8×10^5	2.0

To reduce the roughness of the trench interface, coating the chips in a thin fluoropolymer layer using a spin-on and baking technique before TeO₂ depositions was investigated. This step was carried out using a diluted version of the Cytop top cladding applied to the TeO₂ coated Si₃N₄ waveguides studied earlier. Because the polymer layer is spun on it is more likely create a smooth top surface, rather than conform around the roughness of the SiO₂ etch interface as is expected for the TeO₂ deposition. The devices studied using this technique are also summarized in the last four entries of Table 5.3 and demonstrate a significant general improvement in the measured internal Q factors, with all devices demonstrating internal Q factors of greater than 10^5 . In particular, a device with a 100-nm-thick polymer coating and 630-nm-thick TeO₂ film, with resonance spectrum and Q factor fit displayed in Fig. 5.16, was observed to have an internal Q factor of 2.1×10^5 . This corresponds to a waveguide loss of 1.7 dB/cm and begins to approach the values needed to demonstrate efficient nonlinear and rare-earth optical devices ($< \sim 1$ dB/cm). However, the improvement in internal Q factor is accompanied by an increase in the external Q factor, likely as a result of the polymer coating increasing the lateral offset between the bus waveguide and the microcavity resonator.

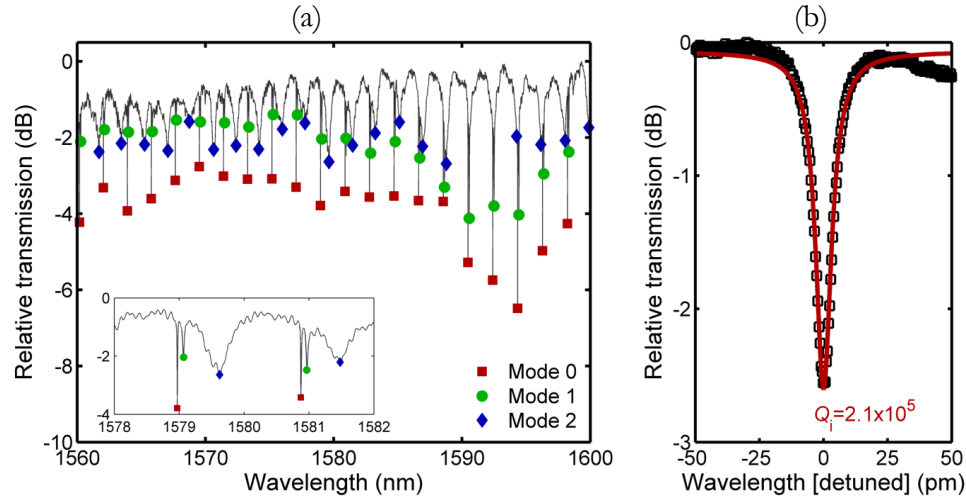


Fig. 5.16. (a) Transmission spectrum of microtrench cavity from design B, with a 100-nm-thick Cytop layer under a 630-nm-thick coating of TeO_2 , with inset showing a close-up view of two resonant free spectral ranges. (b) A fundamental mode of the device at a wavelength of 1566 nm fit to have an internal Q factor of 2.1×10^5 .

These results strongly suggest that the surface roughness of the SiO_2 interface is currently the limiting factor in the internal Q factors measured for the devices. Future efforts in the development of this platform should focus on optimizing the Cytop coating process, and implementing more smoothing techniques, such as HF etching or using a silicon etch stop which can be removed in post-processing before TeO_2 coatings to realize high Q factor devices.

5.5. Application of TeO_2 Microcavity as an Environmental Sensor

Integrated optical devices are able to provide a platform of compact, cheap, and portable devices for the emerging market of biological and environmental sensing devices. Most on-chip optical sensors operate based on the principle of refractive index changes in a sensing medium on an exposed waveguide creating a change in the optical path length of an interferometric device, which can be detected as a change in the interference wavelength. An effective optical sensor requires a distinct interference pattern and strong optical interactions between the waveguide and sensing medium through its evanescent tail. Optical microcavities therefore provide an ideal architecture for sensing devices, as they can achieve very narrow resonance linewidths through high Q factor devices, and optical interaction with a sensing medium through their exposed surface. Sensing through optical methods provides advantages compared to fully electrical counterparts, including improved electromagnetic insensitivity and assessment speed. However, this comes with an increased sensitivity to thermal fluctuations, which are able to modify the optical path length of the device through both the thermo-optic

effect and thermal expansion of the materials. Therefore, it is important to characterize the thermal sensitivity of the device.

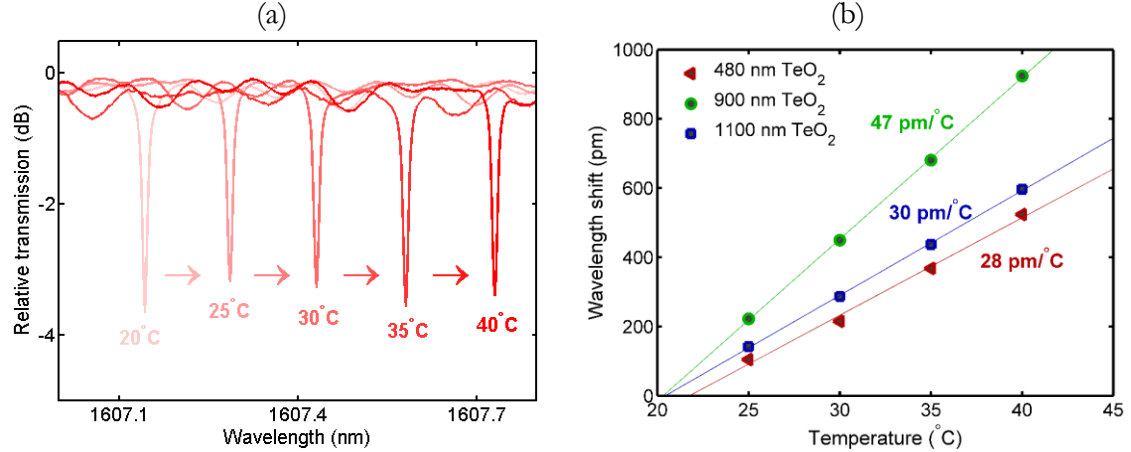


Fig. 5.17. (a) Resonance spectra of a microcavity coated in 1100-nm of TeO₂ at temperatures from 20 to 40 °C. (b) Thermal shift of resonances versus temperature for 480-, 900- and 1100-nm-thick TeO₂ coated cavities fit with thermal sensitivities of 28, 47 and 30 pm/°C respectively.

The thermal sensitivity of the TeO₂ coated microcavities was characterized using the resonant devices from chip design A. The temperature was controlled by mounting the chips on a thermoelectric Peltier cooler stage with a temperature probe, which adjusts the current applied to the Peltier cooler in order to achieve a desired temperature setpoint through a feedback control loop. To measure the thermal shift, the stage was initially set to 20 °C and a spectral transmission measurement of the device was taken with the tunable wavelength laser. The temperature setpoint of the Peltier cooler was then increased in increments of 5 °C up to a maximum temperature of 40 °C. At each increment a transmission measurement was taken 5 minutes after the temperature setpoint change so that the chip can reach thermal equilibrium. An example of the resonance spectra for the 1100-nm-thick TeO₂ coated cavity around 1607 nm at the different temperature setpoints is shown in Fig. 5.17(a). A prominent change in the resonance wavelength is seen, shifting from 1607.14 nm at 20 °C to 1607.73 at 40 °C. This process was carried out to measure the thermally induced resonance shift for the 480-, 900- and 1100-nm-thick TeO₂ coated cavities, with the resonant wavelength shift at each temperature interval relative to the 20 °C measurement recorded and plotted in Fig. 5.17(b). The resonance wavelength shift versus temperature was fit with a line to extract thermal shifts of 28, 47, and 30 pm/°C, with correlation coefficients greater than 0.99. As seen earlier, the light is highly confined within the TeO₂ film, with over 80 % confinement for the 480-nm-thick TeO₂ film and over 90 % for the other two film thicknesses. Because of the high confinement it is assumed that any changes due to thermal expansion will have minimal effect on the optical path length, such that the shift is dominated by the thermo-optic effect. This assumption is supported by the highly linear temperature sensitivity relationship over the range measured. Therefore, the thermally induced resonance shifts can be used to estimate the thermo-optic coefficient (ν) of tellurium oxide from the thermal sensitivity ($\Delta\lambda/\Delta T$) group

index (n_g) and initial resonance wavelength. A sample calculation for the 1100-nm-thick TeO₂ coated sample, with a thermal sensitivity of 30 pm/°C at an original 1602.2 nm wavelength with a group index of 2.05 and a free spectral range of 4.97 nm, is shown in Equation 5.23,

$$\begin{aligned}
 \nu &= \frac{\Delta\lambda}{\Delta T} \cdot \frac{n_g}{\lambda_0} \\
 &= 30 \frac{\text{pm}}{^\circ\text{C}} \cdot \frac{2.05 \text{ RIU}}{1602.2 \text{ nm}} \\
 &= 3.8 \times 10^{-5} \frac{\text{RIU}}{^\circ\text{C}}.
 \end{aligned} \tag{5.23}$$

The thermo optic coefficient is then estimated to be 3.8×10^{-5} RIU/°C. Similar calculations for the 480- and 900-nm-thick TeO₂ coated devices estimate thermo-optic coefficients of 3.6 and 5.9×10^{-5} RIU/°C for TeO₂ respectively, which agree reasonably well with the previously reported values for tellurite glass [43]. The variations between devices likely arises from small stoichiometric differences between the different films, and inconsistencies in etch processes between the chips. This thermo-optic coefficient is approximately 3-5 times the thermo-optic coefficient of silica, and 0.3-0.5 times the value of silicon. Because of silicon's much larger thermo-optic coefficient SOI waveguides have been shown to reach thermal sensitivities of 83 pm/°C [44], approximately two to three times the sensitivity demonstrated here.

In the case of a temperature sensing instrument, having a large thermal sensitivity is preferable. However, most optical sensors are targeted at fluidic or gas sensing applications, in which a large thermal sensitivity can result in noisy or spurious measurement results, thus external cooling is required. Although the TeO₂ microcavity sensor has demonstrated lower thermal sensitivity than a silicon waveguide, an evanescent sensor would still require thermal stabilization in a practical device. However, a TeO₂ based microcavity provides an advantage in that it could potentially be doped with rare earth ions, such as erbium, which would allow for laser-based sensing. Previous implementations of lasing sensors using non-monolithically integrated platforms have been able to detect single nano-particle attachments to the surface of resonators [45] and can be operated in a beat frequency detection mode which is insensitive to thermal changes [46]. TeO₂ coated microcavities therefore provide an excellent pathway towards integrating lasing sensors monolithically onto silicon photonic microsystems.

The evanescent field sensing capabilities of the resonator were characterized by measuring the transmission spectrum of the devices, before and after coating chips in deionized (DI) water, with the temperature control stage held at 20 °C. Plots of the resonance spectra measured before and during DI water exposure for the 900- and 1100-nm-thick TeO₂ coated cavities are shown in Figures 5.18(a) and (b), respectively. The 900-nm-thick coated cavity is found to have a resonant wavelength shift of 4.81 nm for a resonance at an initial wavelength of 1608.00 nm, increasing to a 4.87 nm shift for an initial resonance wavelength of 1618.16 nm. The 1100-nm-thick coated device is seen to have resonance wavelength shifts of 3.28 to

3.34 nm. As these results show, longer wavelengths and thinner TeO₂ film coatings tend to result in an increased evanescent field sensitivity, as a result of the evanescent tail of the waveguide extending further into the DI water medium. Assuming the refractive index of air is 1.000 and DI water is 1.316, the cladding refractive index unit sensitivity (S) of the device can be found by comparing the resonant wavelength shift ($\Delta\lambda$) to the change in cladding index ($\Delta n_{\text{Cladding}}$) as shown for the 900-nm-thick coated device below:

$$\begin{aligned}
 S &= \frac{\Delta\lambda}{\Delta n_{\text{Cladding}}} \\
 &= \frac{4.87 \text{ nm}}{1.316 - 1.000} \\
 &= 15.4 \frac{\text{nm}}{\text{RIU}}.
 \end{aligned} \tag{5.24}$$

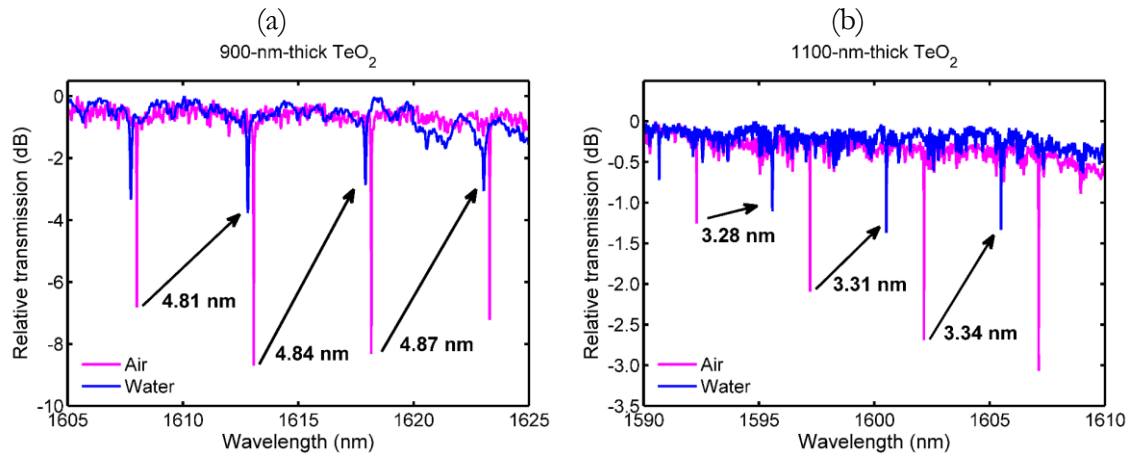


Fig. 5.18. Resonance spectra measured for optical microcavities coated in (a) 900- and (b) 1100-nm-thick TeO₂ films before and after the chips were coated in a layer of DI water.

A 15.4 and 10.6 nm/RIU maximum sensitivity is then found for the 900- and 1100-nm-thick coated devices, respectively. For the 900-nm-thick coated device we also measured resonance shift as a function of various glycerol concentration in water to characterize the local sensitivity for indices ranging from 1.316–1.371. The measured shifts, plotted in Figure 5.19, demonstrate a local sensitivity of 19.6 ± 1.3 around this refractive index.

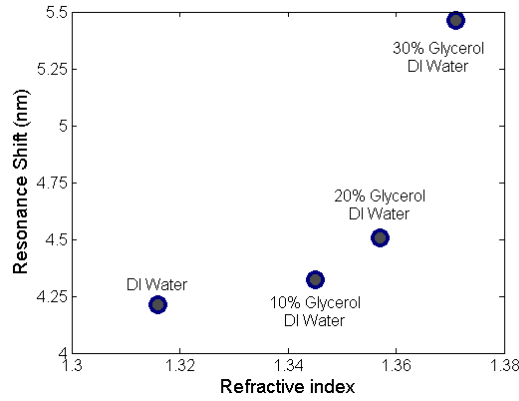


Fig. 5.19. Measured resonance shift versus cladding refractive index for a 900-nm-thick TeO_2 microcavity coated in solutions with various concentrations of glycerol and DI water.

Based on the greater sensitivity it would be assumed that thinner coatings are preferable for sensors, however, the addition of water is also seen to result in a decrease in the Q factor of the resonator as a result of the optical absorption of water causing increased attenuation within the cavity. Fig. 5.20 shows the fitted internal Q factor of resonances on each device before and during exposure to water. The internal Q factor of the 900-nm-thick TeO_2 coated device was observed to decrease from 0.7×10^5 to 0.2×10^5 , corresponding to an additional 12.9 dB/cm of optical propagation loss in the cavity. Because the 1100-nm coated microcavity has less optical overlap with the water coating, its Q factor only decreased from 1.6×10^5 to 0.7×10^5 , corresponding to a 2.9 dB/cm increase in loss. When the 480-nm-thick TeO_2 coated chip was measured under DI water the resonance modes were found to disappear completely, which is likely because the additional loss from the water resulted in a large internal/external Q mismatch and prevented coupling.

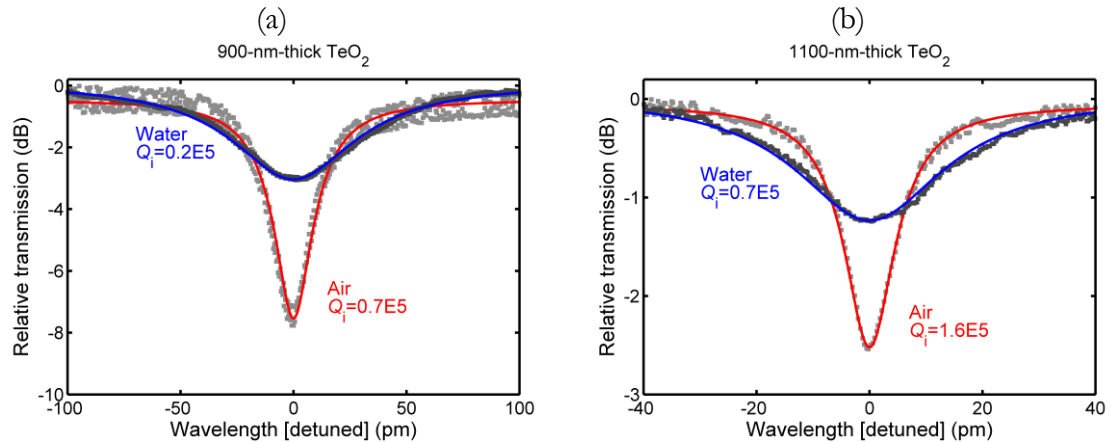


Fig. 5.20. Resonance modes of (a) 900- and (b) 1100-nm-thick TeO_2 coated optical microcavities before and after being coated in a layer of DI water showing reduced Q factors.

The resonance wavelength shift of the TeO_2 microtrenches can be modelled in eigenmode simulations using the device cross section developed in Fig. 5.5(a), with variations to the air

cladding refractive index. For each cladding refractive index (n_{Clad}) the effective index of the waveguide mode can be simulated (n_{Eff}). The resulting resonant wavelength shift ($\Delta\lambda$) can then be found for an initial resonance wavelength (λ_0) and effective index for an air cladding ($n_{\text{Eff},0}$) as follows.

$$\Delta\lambda = n_{\text{Eff}} \frac{\lambda_0}{n_{\text{Eff},0}}. \quad (5.25)$$

The simulated wavelength shift for 500-, 700-, 900- and 1100-nm thick TeO_2 coated cavities at cladding indices from 1.0 to 1.5 are shown in Fig. 5.21(a). The simulated results for a DI water cladding on the 900- and 1100-nm-thick TeO_2 devices predict wavelength shifts of 4.81 and 3.32 nm, respectively, agreeing very well with the measured results. From these plots the 480-nm-thick TeO_2 sample would have been expected to exhibit a wavelength shift of 14.8 nm under the water coating. It can also be seen from the figure that the wavelength shift versus cladding refractive index is not a linear relationship, becoming increasingly sensitive as the cladding refractive index increases. This relationship is a result of the decreased refractive index contrast between the TeO_2 microcavity and the cladding at larger cladding refractive indices, which causes the evanescent tail of the waveguide mode to leak exponentially more into the cladding, increasing the sensitivity. This effect is more pronounced in the TeO_2 microcavity than it is in a silicon waveguide, where the refractive index contrast between the waveguide and cladding is larger. This effect also results in a discrepancy between the measured and simulated RIU sensitivity. The measured RIU sensitivity determined earlier based on the experimental data assumed a perfectly linear shift with refractive index, however because the true relationship is non-linear the actual local RIU sensitivity of the device around the cladding index of water is larger. Fig. 5.21(b) shows the simulated local sensitivity of the 900-nm thick coated sample to be 19.9 nm/RIU, while the 1100-nm-thick coated sample has a local sensitivity of 14.3 nm/RIU.

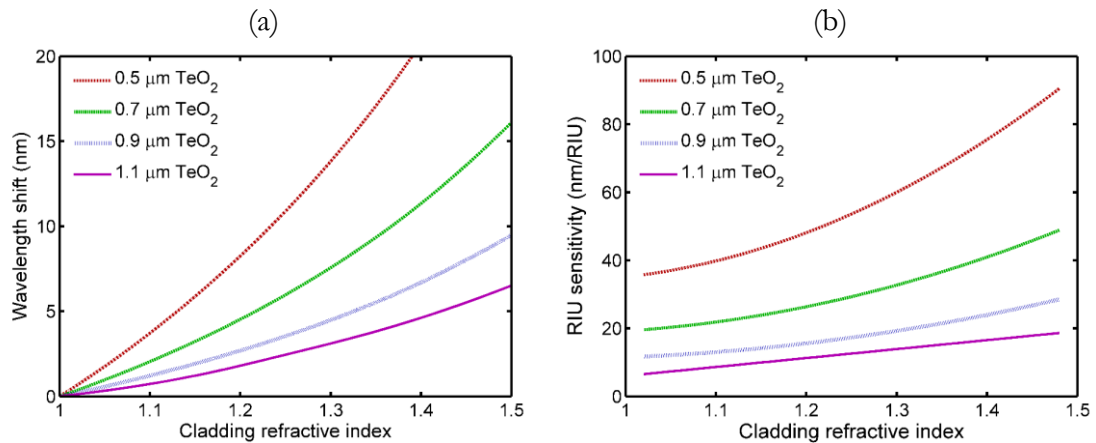


Fig. 5.21. Simulated (a) wavelength shift and (b) RIU sensitivity versus evanescent medium refractive index for cavities with 500 to 1100-nm-thick TeO_2 coatings.

The sensitivities demonstrated here compare relatively poorly to the sensitivities that have been achieved in SOI waveguides, where devices have approached sensitivities of almost 250 nm/RIU [46]. Although the sensitivity of the TeO₂ microcavity could be improved by using thinner films, this has been shown to result in a large decrease in the Q factors of devices. In extreme cases this can lead to the disappearance of resonance modes as seen earlier, but also causes the resonance bandwidth to widen, which reduces the ability to distinguish resonance wavelength shifts. Therefore, a more relevant metric to quantify the detection ability of sensors is to determine the change in refractive index of the cladding necessary to create a resonance wavelength shift of one bandwidth, referred to as the limit of detection (LOD), which is ideally as small as possible. The LOD can be determined by the sensing wavelength (λ_0), Q factor while coated in water (Q_{water}) and evanescent field sensitivity (S) of the device. This is calculated for the 900-nm-thick coated microcavity as follows,

$$\begin{aligned} \text{LOD} &= \frac{\lambda_0}{Q_{\text{water}} \cdot S} \\ &= \frac{1600 \text{ nm}}{(20000) \cdot \left(15.4 \frac{\text{nm}}{\text{RIU}}\right)} \\ &= 5.2 \times 10^{-3} \text{ RIU}. \end{aligned} \tag{5.26}$$

The LOD for the 1100-nm-thick coated cavity is similarly found to be 2.2×10^{-3} RIU, which is higher than the thinner film's LOD despite its lower sensitivity. These LODs compare reasonably well to some of the high sensitivity devices mentioned earlier [47], but still remain an order of magnitude higher than the state-of-the-art LODs [48,49] that have been demonstrated on SOI platforms. However, the potential for improved Q factors and to integrate lasing functionality into these microcavities makes them of great interest for future platform development.

5.6. Conclusion

In summary, this chapter has presented on TeO₂ microresonators compatible with silicon photonic waveguides for a combined TeO₂-Si platform, which can leverage both tellurium oxide's promising material properties and silicon's low-cost, high-performance optoelectronic devices. Microtrenches were fabricated using standard silicon waveguide processing steps for active silicon photonic circuits from the IME/AMF foundry, and coated in a TeO₂ thin film during post-processing to form TeO₂ microresonators. High optical confinements of 80 to 95% in the tellurite can be achieved in the microcavity for film thicknesses of 500 to 1100 nm. Simulations of bending radiation loss predict that a microcavity coated in a 500-nm-thick TeO₂ film can maintain negligible radiation loss at bending radii down to 20- μm , while cavities coated in a 1100-nm-thick TeO₂ film require 40- μm bending radii and larger to maintain negligible radiation losses. To model the coupling between the TeO₂ microresonator and silicon waveguide a fast and accurate method based on coupled mode theory was developed.

Taking into account the structure of the fabricated devices, the simulations predict that external Q factors of approximately 0.2×10^5 can be obtained for pulley coupled resonators at an optimum gap. In an initial design run, 40- μm radius microtrenches with 0.35- μm -wide silicon bus waveguides at nominal coupling gaps of 0.2 to 1.0 μm were fabricated. SEM images revealed a trench sidewall angle and that the microtrench had been overetched by an estimated 1- μm below the level of the silicon waveguide. This significantly reduced the coupling strength between the silicon waveguide and microresonator compared to the designed coupling strength. Characterization of the devices showed low coupling strengths and moderate intrinsic Q factors, up to 1.6×10^5 for a device coated in 1100-nm-thick TeO_2 film. A follow up design run used 100- μm radius microtrenches and 0.30- μm -wide silicon bus waveguides in an attempt to improve losses in the microcavity and coupling strengths. Surface profilometry of the chips revealed a reduced overetch on this design run, of 0.5 ± 0.1 - μm . This led to much higher coupling Q factors and extinction ratios overall, with a microcavity coated in an 775-nm-thick TeO_2 film measured to have a 0.4×10^5 external Q factor, approaching the calculated limit. However lower internal Q factors were measured overall, peaking at 0.9×10^5 internal Q factor for a microtrench coated in an 1115-nm-thick TeO_2 film. Spin-on polymer coatings before TeO_2 depositions were studied as a method to reduce optical propagation losses as a result of roughness along the SiO_2 microtrench surface. This was seen to improve the intrinsic Q factor of several devices, up to 2.1×10^5 for a device with a 100-nm-thick polymer coating under a 630-nm-thick TeO_2 coating. This corresponds to a waveguide loss of 1.7 dB/cm, which approaches the values required to make rare-earth and nonlinear optical TeO_2 devices feasible. Investigations of the devices' sensing properties revealed a thermal shift of up to 47 pm/ $^\circ\text{C}$ for a microcavity coated in a 900-nm-thick TeO_2 film, and evanescent field sensitivities of 15.4 and 10.6 nm/RIU for microcavities with 900 and 1100-nm-thick TeO_2 coatings respectively. These results demonstrate a promising platform for the monolithic integration of rare-earth doped and nonlinear TeO_2 devices within silicon photonic optoelectronic circuits.

References

- [1] K. Wörhoff, R. G. Heideman, A. Leinse, and M. Hoekman, "TriPleX: A versatile dielectric photonic platform," *Adv. Opt. Technol.* **4**(2), 189–207 (2015).
- [2] C. G. H. Roeloffzen, M. Hoekman, E. J. Klein, L. S. Wevers, R. B. Timens, D. Marchenko, D. Geskus, R. Dekker, A. Alippi, R. Grootjans, A. van Rees, R. M. Oldenbeuving, J. P. Epping, R. G. Heideman, K. Wörhoff, A. Leinse, D. Geuzebroek, E. Schreuder, P. W. L. van Dijk, I. Visscher, C. Taddei, Y. Fan, C. Taballione, and Y. Liu, D. Marpaung, L. Zhuang, M. Benelajla and K. Boller, "Low Loss Si_3N_4 TriPleX optical waveguides: technology and applications overview," *IEEE J. Sel. Top. Quantum Electron.* **24**(4), 1–21 (2018).
- [3] D. J. Blumenthal, R. Heideman, D. Geuzebroek, A. Leinse, and C. Roeloffzen, "Silicon nitride in silicon photonics," *Proc. IEEE* **106**(12), 2209–2231 (2018).

- [4] G. Li, A. V. Krishnamoorthy, I. Shubin, J. Yao, Y. Luo, H. Thacker, X. Zheng, K. Raj, and J. E. Cunningham, “Ring resonator modulators in silicon for interchip photonic links,” *IEEE J. Sel. Top. Quantum Electron.* **19**(6), 95–113 (2013).
- [5] D. Patel, S. Ghosh, M. Chagnon, A. Samani, V. Veerasubramanian, M. Osman, and D. V. Plant, “Design, analysis, and transmission system performance of a 41 GHz silicon photonic modulator,” *Opt. Express* **23**(11), 14263–14287 (2015).
- [6] J. J. Ackert, A. S. Karar, J. C. Cartledge, P. E. Jessop, and A. P. Knights, “Monolithic silicon waveguide photodiode utilizing surface-state absorption and operating at 10 Gb/s,” *Opt. Express* **22**(9), 10710–10715 (2014).
- [7] J. J. Ackert, D. J. Thomson, L. Shen, A. C. Peacock, P. E. Jessop, G. T. Reed, G. Z. Mashanovich, and A. P. Knights, “High-speed detection at two micrometres with monolithic silicon photodiodes,” *Nat. Photonics* **9**(6), 393–396 (2015).
- [8] L. Vivien, A. Polzer, D. Marris-Morini, J. Osmond, J. M. Hartmann, P. Crozat, E. Cassan, C. Kopp, H. Zimmermann, and J. M. Fédéli, “Zero-bias 40 Gbit/s germanium waveguide photodetector on silicon,” *Opt. Express* **20**(2), 1096–1101 (2012).
- [9] W. D. Sacher, J. C. Mikkelsen, Y. Huang, J. C. Mak, Z. Yong, X. Luo, Y. Li, P. Dumais, J. Jiang, D. Goodwill, E. Bernier, P. G. Q. Lo, and J. K. S. Poon, “Monolithically integrated multilayer silicon nitride-on-silicon waveguide platforms for 3-D photonic circuits and devices,” *Proc. IEEE*, **106**(12), 2232–2245 (2018).
- [10] E. Timurdogan, Z. Su, C. V. Poulton, M. J. Byrd, S. Xin, R. J. Shiue, B. R. Moss, E. S. Hosseini, and M. R. Watts, “AIM process design kit (AIMPDKv2. 0): Silicon photonics passive and active component libraries on a 300mm wafer,” *Optical Fiber Communications Conference and Exposition*, 1–3 (2018).
- [11] C. M. Naraine, J. W. Miller, H. C. Frankis, D. E. Hagan, P. Mascher, J. H. Schmid, P. Cheben, A. P. Knights, and J. D. B. Bradley, “Subwavelength grating metamaterial waveguides functionalized with tellurium oxide cladding,” *Opt. Express* **28**(12), 18538–18547 (2020).
- [12] R. A. H. El-Mallawany, *Tellurite Glasses Handbook: Physical Properties and Data*, Second Edition (CRC Press, 2012).
- [13] V. A. G. Rivera and D. Manzani, *Technological Advances in Tellurite Glasses: Properties, Processing, and Applications* (Springer, 2017).
- [14] A. Jha, B. D. O Richards, G. Jose, T. T. Fernandez, C. J. Hill, J. Lousteau, and P. Joshi, “Review on structural, thermal, optical and spectroscopic properties of tellurium oxide based glasses for fibre optic and waveguide applications,” *Int. Mater. Rev.* **57**(6), 357–382 (2012).

- [15] J. S. Wang, E. M. Vogel, and E. Snitzer, “Tellurite glass: a new candidate for fiber devices,” *Opt. Mater.* **3**, 187–203 (1994).
- [16] Z. Su, N. Li, H. C. Frankis, E. S. Magden, T. N. Adam, G. Leake, D. Coolbaugh, J. D. B. Bradley, and M. R. Watts, “High-Q-factor Al₂O₃ micro-trench cavities integrated with silicon nitride waveguides on silicon,” *Opt. Express* **26**(9), 11161–11170 (2018).
- [17] J. D. B. Bradley, E. Shah Hosseini, Purnawirman, Z. Su, T. N. Adam, G. Leake, D. Coolbaugh, and M. R. Watts, “Monolithic erbium- and ytterbium-doped microring lasers on silicon chips,” *Opt. Express* **22**(10), 12226–12237 (2014).
- [18] Z. Su, N. Li, E. S. Magden, M. Byrd, Purnawirman, T. N. Adam, G. Leake, D. Coolbaugh, J. D. B. Bradley, and M. R. Watts, “Ultra-compact and low-threshold thulium microcavity laser monolithically integrated on silicon,” *Opt. Lett.* **41**(24), 5708–5711 (2016).
- [19] H. C. Frankis, Z. Su, N. Li, E. S. Magden, M. Ye, M. R. Watts, and J. D. B. Bradley, “Four-wave mixing in a high-Q aluminum oxide microcavity on silicon,” in *Conference on Lasers and Electro-Optics, San Jose, CA, 2018, OSA Technical Digest (online) (Optical Society of America, 2018)*, paper STh3I.3.
- [20] N. Li, D. Vermeulen, Z. Su, E. S. Magden, M. Xin, N. Singh, A. Ruocco, J. Notaros, C. V. Poulton, E. Timurdogan, C. Baiocco, and M. R. Watts, “Monolithically integrated erbium-doped tunable laser on a CMOS-compatible silicon photonics platform,” *Opt. Express* **26**(13), 16200–16211 (2018).
- [21] N. Li, M. Xin, Z. Su, E. S. Magden, N. Singh, J. Notaros, E. Timurdogan, Purnawirman, J. D. B. Bradley, and M. R. Watts, “A silicon photonic data link with a monolithic erbium-doped laser,” *Sci. Rep.* **10**, 1114 (2020).
- [22] S. J. Madden and K. T. Vu, “Very low loss reactively ion etched tellurium dioxide planar rib waveguides for linear and non-linear optics,” *Opt. Express* **17**(20), 17645–17651 (2009).
- [23] P. Jean, A. Douaud, V. Michaud-Belleau, S. H. Messaddeq, J. Genest, S. LaRochelle, Y. Messaddeq, and W. Shi, “Etchless chalcogenide microresonators monolithically coupled to silicon photonic waveguides,” *Opt. Lett.* **45**(10), 2830–2833 (2020).
- [24] E. P. Ostby and K. J. Vahala, “Yb-doped glass microcavity laser operation in water,” *Opt. Lett.* **34**(8), 1153–1155 (2009).
- [25] L. He, S. K. Ozdemir, J. Zhu, W. Kim, and L. Yang, “Detecting single viruses and nanoparticles using whispering gallery microlasers,” *Nat. Nanotechnol.* **6**(7), 428–432 (2011).
- [26] S. M. Spillane, T. J. Kippenberg, and K. J. Vahala, “Ultralow-threshold Raman laser using a spherical dielectric microcavity,” *Nature* **415**(6872), 621–623 (2002).

- [27] I. H. Agha, Y. Okawachi, and A. L. Gaeta, “Theoretical and experimental investigation of broadband cascaded four-wave mixing in high-Q microspheres,” *Opt. Express* **17**(18), 1620–16215 (2009).
- [28] T. J. Kippenberg, R. Holzwarth, and S. A. Diddams, “Microresonator-based optical frequency combs,” *Science* **332**(6209), 555–559 (2011).
- [29] T. Aoki, B. Dayan, E. Wilcut, W. P. Bowen, A. S. Parkins, T. J. Kippenberg, K. J. Vahala, and H. J. Kimble, “Observation of strong coupling between one atom and a monolithic microresonator,” *Nature* **443**(7112), 671–674 (2006).
- [30] T. J. Kippenberg and K. J. Vahala, “Cavity opto-mechanics,” *Opt. Express* **15**(25):17172–17205 (2007).
- [31] M. Bruel, 1994, “Process for the production of thin semiconductor material films,” US5374564A.
- [32] C. I. van Emmerik, M. Dijkstra, M. de Goede, L. Chang, J. Mu, and S. M. Garcia-Blanco, “Single-layer active-passive Al_2O_3 photonic integration platform,” *Opt. Mater. Express* **8**(10), 3049–3054 (2018)
- [33] N. Fang, Z. Yang, A. Wu, J. Chen, M. Zhang, S. Zou, and X. Wang, “Three-dimensional tapered spot-size converter based on (111) silicon-on-insulator,” *IEEE Photon Technol. Lett.* **21**(12), 820–822 (2009).
- [34] H. H. Li, “Refractive index of silicon and germanium and its wavelength and temperature derivatives,” *J. Phys. Chem. Ref. Data* **9**(3), 561–658 (1993).
- [35] I. H. Malitson, “Interspecimen comparison of the refractive index of fused silica,” *JOSA* **55**(10), 1205–1209 (1965).
- [36] J. U. Nöckel, and A. D. Stone, “Ray and wave chaos in asymmetric resonant optical cavities,” *Nature* **385**(6611), 45–47 (1997).
- [37] X. F. Jiang, C. L. Zou, L. Wang, Q. Gong, and Y. F. Xiao, “Whispering-gallery microcavities with unidirectional laser emission,” *Laser Photonics Rev.* **10**(1), 40–61 (2016).
- [38] A. Yariv, “Coupled-mode theory for guided-wave optics,” *IEEE J. Quantum Electron.* **9**(9), 919–933 (1973).
- [39] K. R. Hiremath and M. Hammer, Modeling of 2D cylindrical integrated optical microresonators (Master’s Report, University of Twente).
- [40] R. Stoffer, K. R. Hiremath, and M. Hammer, “Comparison of coupled mode theory and FDTD simulations of coupling between bent and straight optical waveguides,” *AIP Conf. Proc.* **709**(1), 366–377 (2004).

- [41] W. P. Huang and J. Mu, “Complex coupled-mode theory for optical waveguides,” *Opt. Express* **17**(21), 19134–19152 (2009).
- [42] M. Soltani, Novel integrated silicon nanophotonic structures using ultra-high Q resonators (Doctoral dissertation, Georgia Institute of Technology).
- [43] T. Komatsu, N. Ito, T. Honma, and V. Dimitrov, “Temperature dependence of refractive index and electronic polarizability of RO–TeO₂ glasses (R= Mg, Ba, Zn),” *Solid State Sci.* **14**(10), 1419–1425 (2012).
- [44] G. Kim, H. Lee, C. Park, S. Lee, B. Lim, H. Bae, and W. Lee, “Silicon photonic temperature sensor employing a ring resonator manufactures using a standard CMOS process,” *Opt. Express* **18**(21), 22215–22221 (2010).
- [45] L. He, Ş. K. Özdemir, J. Zhu, W. Kim, and L. Yang, “Detecting single viruses and nanoparticles using whispering gallery microlasers,” *Nat. Nanotechnol.* **6**(7), 428–432 (2011).
- [46] E. P. Ostby and K. J. Vahala, “Yb-doped glass microcavity laser operation in water,” *Opt. Lett.* **34**(8), 1153–1155 (2009).
- [47] S. M. Lo, S. Hu, G. Gaur, Y. Kostoulas, S. M. Weiss, and P. M. Fauchet, “Photonic crystal microring resonator for label-free biosensing,” *Opt. Express* **25**(6), 7046–7054 (2017).
- [48] D. X. Xu, M. Vachon, A. Densmore, R. Ma, S. Janz, A. Delâge, J. Lapointe, P. Cheben, J. H. Schmid, E. Post, and S. Messaoudène, “Real-time cancellation of temperature induced resonance shifts in SOI wire waveguide ring resonator label-free biosensor arrays,” *Opt. Express* **18**(22), 22867–22879 (2010).

CHAPTER 6

Conclusion

6.1. Major Results

The aim of this thesis was to develop tellurium oxide (TeO_2) thin film photonic structures compatible with the current state of the art, foundry level, waveguide processing techniques for silicon (Si) and silicon nitride (Si_3N_4) based photonic platforms.

Through this undertaking we have demonstrated the development of a high-quality RF reactive sputtering TeO_2 thin film deposition process capable of achieving low planar film losses from the visible (<0.5 dB/cm at 638 nm), through to the infrared (<0.1 dB/cm at 1550 nm). Importantly, the process is low temperature and highly versatile, allowing for dopant incorporation via co-sputtering and post-processing deposition on a variety of photonic substrates, including full wafers or individual chips.

Integration of TeO_2 on Si_3N_4 waveguides fabricated at the LioniX foundry was investigated using a conformally coated hybrid waveguide structure. We developed a thorough design guide for TeO_2 -coated Si_3N_4 waveguides with regard to device properties to optimize optical overlap in the TeO_2 while maintaining small mode areas and compact bends. We show approximately 60% optical confinement in the TeO_2 , a mode area of $1.20 \mu\text{m}^2$ and a bend radius of $200 \mu\text{m}$ with minimal loss in $1.2\text{-}\mu\text{m}$ -wide by $0.2\text{-}\mu\text{m}$ -thick Si_3N_4 strips with a 400-nm -thick TeO_2 -coating at 1550 nm. The TeO_2 -coated Si_3N_4 waveguide platform demonstrated low optical propagation losses in the infrared (<1 dB/cm), and moderate propagation losses in the visible regime (< 8 dB/cm). Additionally, the first integrated passive photonic circuit elements using TeO_2 were demonstrated, including directional couplers and microring resonators, which were observed to achieve high device Q factors of 7.3×10^5 .

Erbium-doped tellurium oxide ($\text{TeO}_2:\text{Er}^{3+}$) thin films conformally coated on Si_3N_4 waveguides in a similar manner were investigated for on-chip optical amplifiers. A $\text{TeO}_2:\text{Er}^{3+}$ film with an erbium-dopant concentration of 2.2×10^{20} ions/ cm^3 deposited at a moderate temperature of 140°C was seen to greatly improve the spectroscopic properties compared to films deposited at room temperature, with an improved excited state lifetime of 0.48 ms, reduced quenching ratios of down to 22 % and lower background waveguide losses of 0.25 dB/cm. Detailed gain investigations of this sample showed peak gains per unit length of 1.7 and 1.4 dB/cm in a 2.2-cm-long waveguide for 970 and 1470 nm pump wavelengths, respectively. A 6.7-cm-long sample demonstrated 5 dB of total gain at a wavelength of 1558 nm wavelength and > 3 dB across the C-band when pumped at 1470 nm. It was shown that the low fiber-chip coupling efficiency, which can be improved in future designs, limited the launched pump power and the total gain that could be achieved. Rate equation modelling of the waveguides predicted that if a 10-cm-long waveguide with the same device properties was

pumped with 150 mW of 1470 nm pump power, > 10 dB of gain cross the C-band could be realized.

To integrate TeO₂ films on a silicon photonics platform, a lateral multilayer integration technique utilizing TeO₂-coated microtrenches was investigated with silicon-on-insulator (SOI) chips which were fabricated through the IME/AMF foundry. A design guide was developed which predicts that optical confinements of > 80 % in the TeO₂ can be achieved for a 500-nm-thick TeO₂ thin film while maintaining negligible radiation losses at a bending radius of 20 μm, which increases up to 40 μm for a 1100-nm-thick TeO₂ film. TeO₂-coatings on devices as received from the foundry were found to have waveguide losses predominantly limited by the sidewall roughness of the oxide etch process to be < 1 × 10⁵. Filling the microtrenches in a spin-on Cytop fluoropolymer layer prior to TeO₂ deposition was found to smooth the microcavity sidewalls. Consistently improved device *Q* factors of > 1 × 10⁵ were observed, with a microcavity with a 100-nm-thick Cytop coating under a 630-nm-thick TeO₂-coating demonstrating an internal *Q* factor of 2.1 × 10⁵, corresponding to 1.7 dB/cm of waveguide loss. Explorations of TeO₂ microcavities as a sensing device exhibit evanescent field sensors with moderate sensitivities of 15.4 nm/RIU and a limit of detection of up to 2.2 × 10⁻³ RIU.

Overall, the results presented in this thesis provide a promising platform towards the realization of TeO₂ devices monolithically integrated on Si and Si₃N₄ photonic circuits for wafer scale design and fabrication of passive, nonlinear and rare-earth active TeO₂ devices.

6.2. Suggested Future Work

The results demonstrated in this thesis provide several interesting avenues for future work to expand upon.

For the TeO₂-Si₃N₄ waveguide platform one of the primary challenges encountered with regard to experimentally characterizing devices throughout this thesis and ultimately limiting the performance of TeO₂:Er³⁺ amplifiers was the relatively large fiber-chip coupling loss. While focused-ion-beam (FIB) milling was proven to allow for the demonstration of reasonably low coupling loss, the serial nature of the process limits its potential use for volume production, adds significant costs and requires extensive extra handling. To address this issue in future Si₃N₄ layout designs two primary methods should be utilized: Si₃N₄ waveguide nano-tapers and TeO₂ deposition shadow masking. Appropriate nano-taper designs achieved through simulation can be used to optimize the expected fiber-chip coupling losses based on mode profiles. However as seen in the simulations of section 3.4.2, for TeO₂-Si₃N₄ waveguides even optimized taper designs still predict nearly 3 dB of coupling loss for TeO₂ coating thicknesses appropriate for other device designs. Shadow masking allows for the TeO₂ to be locally deposited in the regions of interest with adiabatic transitions to uncoated Si₃N₄ waveguides elsewhere and low-loss Si₃N₄ fiber-chip edge couplers. More generally, it can allow for active-passive photonic integrated circuits with passive Si₃N₄ and active doped TeO₂-Si₃N₄

regions. Currently, some initial shadow masking experiments have been explored with promising results estimated to approach ~ 3 dB of loss per facet, but further experimental validation and a formal fabrication methodology must still be worked upon.

Experimental demonstrations of the $\text{TeO}_2\text{-Si}_3\text{N}_4$ waveguide platform in this thesis were investigated using 0.2- μm -thick Si_3N_4 strip waveguides, to provide a tradeoff between obtaining large optical confinement in the TeO_2 layer while maintaining small bending radii. However, future investigations into thinner Si_3N_4 layers could potentially lead to improved waveguide losses due to less sidewall scattering and greater TeO_2 optical confinement, while thicker Si_3N_4 layers of up to 0.4- μm -thick would be needed for appropriate dispersion engineering of nonlinear TeO_2 devices.

With regard to the $\text{TeO}_2\text{:Er}^{3+}$ films and waveguide amplifiers, while the initial results have already demonstrated net internal gain, the potential for the experimental demonstration of gains >10 dB across the C-band should be readily achievable. Additionally, there are still many details about the properties of $\text{TeO}_2\text{:Er}^{3+}$ films to be explored. The primary factor limiting devices was seen to be quenching, strongly believed to be through OH^- groups based on prior TeO_2 work in literature, however this was never directly proven experimentally in our devices. In the future, characterization of absorption losses around 1310 nm can be used to confirm the expected link between OH^- contamination and increased quenching. We demonstrated that moderate temperature elevations during the deposition process can provide a pathway to decreased quenching. A more thorough and systematic study of the effects of deposition temperature on the luminescent lifetime and quenching properties of $\text{TeO}_2\text{:Er}^{3+}$ films and waveguides should be undertaken in an attempt to reduce OH^- incorporation and quenching ratios as much as possible. With the potential for reduced quenching ratios and increased excited state lifetimes, exploring the spectroscopy of the upper energy levels of TeO_2 and deeper investigations into energy transfer upconversion parameters will become more relevant as a next step to modeling and optimizing the amplifier performance.

With the demonstration of on-chip gain the potential for the realization of integrated on-chip lasers becomes a possibility. $\text{TeO}_2\text{:Er}^{3+}$ films in combination with the high Q microring resonators discussed in section 3.4.4 are a promising pathway towards lasers. However, some difficulties arise with regard to the simple microring design used here, namely achieving large pump powers in the ring while maintaining low outcoupling losses for efficient pumping and roundtrip net gain, respectively, can be difficult. Modified microring designs with extended couplers (pulley couplers) can be appropriately designed using the results of section 3.4.3 to simultaneously achieve large pump powers in the resonator with low outcoupling losses for the signal. Additionally, more advanced resonator designs such as cavities with Vernier filters or feedback loops can be explored to promote single mode and unidirectional lasing. Implementation of heaters either on $\text{TeO}_2\text{-Si}_3\text{N}_4$ waveguides or Si_3N_4 waveguides in combination with shadow masking the gain cavity could further allow for the realization of tunable lasers and integration of light sources with tunable passive and nonlinear PICs.

Currently the potential of the TeO₂-coated microcavities on an SOI platform developed here are largely limited by the surface roughness of the microtrench introduced during the oxide etch step. While Cytop coatings have shown some promise towards smoothing devices and improving Q factors, the measured waveguide losses are still on the high end of what would be necessary to demonstrate rare-earth or nonlinear light emission. Investigations into chemically etching or smoothing microtrenches in combination with Cytop smoothing layers should be explored to investigate improved device performance. Additionally, a more varied study of the effects of the microtrench design, including trench width and bending radius should be explored. If high Q factor microcavities can be achieved, the potential for many interesting passive, rare earth light-emitting and nonlinear applications can be realized. These devices could then be integrated with various SOI passive and optoelectronic functionalities for complex circuit designs with various applications.

While the work demonstrated in this thesis has focused in particular upon undoped TeO₂ and erbium-doped TeO₂ as materials of interest, the conformal coating and microtrench filling integration methods can be more broadly applied to a wide variety of thin film coatings, of which the design considerations and results measured throughout this thesis can provide a guideline for. Alternative glass hosts, such as aluminum oxide (Al₂O₃) or tantalum pentoxide (Ta₂O₅) could be similarly studied for promising rare-earth dopant applications. Furthermore, different materials could be studied for various other functions such as aluminum nitride (AlN) as a material with promising electro-optic modulation capabilities, or polycrystalline silicon for applications in integrated photodetection.

In summary, building on this work, undoped TeO₂ layers and TeO₂ films with various dopants and co-dopants can be explored for a wide variety of passive, active and nonlinear optical properties and new devices and functionalities in Si and Si₃N₄ PICs.

Appendices

Appendix A – List of Silicon Nitride Structures

This appendix summarizes the full list of Si_3N_4 structures which were designed for $\text{TeO}_2\text{-Si}_3\text{N}_4$ waveguides and devices and included in the Si_3N_4 layout which was fabricated at the LioniX foundry.

Chip Design A

Structure type	Variations			
Straight waveguides	# of sets	Waveguide widths (μm)		
	2	0.5, 0.6, 0.7, 0.8, 0.9, 1.0, 1.2, 1.4, 1.6, 1.8, 2.0		
Paperclip waveguides	Waveguide lengths (cm)	Waveguide width (μm)	First bend radius (μm)	Second bend radius (μm)
	2.54,	0.6	900	720
	2.93,		870	750
	3.54,		840	780
	3.93	0.8	810	810
			720	900
			750	870
			780	840
		1.0	810	810
			1020	600
			990	630
			960	660
		1.2	930	690
	600		1020	
	630		990	
	660		960	
		690	930	
Spiral waveguides	Waveguide width (μm)	Min bend radius (μm)	Spiral length (cm)	
	0.8	100	5	
	0.8	500	5	
	0.8	500	10	
	1.0	500	10	
	1.0	100	5	
	1.0	200	5	
	1.0	300	5	
	1.0	400	5	
1.0	500	5		

Chip Design B

Structure type	Variations			
Straight waveguides	# of sets	Waveguide widths (μm)		
	4	0.5, 0.6, 0.7, 0.8, 0.9, 1.0, 1.2, 1.4, 1.6, 1.8, 2.0		
Paperclip waveguides	Waveguide lengths (cm)	Waveguide width (μm)	First bend radius (μm)	Second bend radius (μm)
	6.7 cm	0.6	1240	1330
			1270	1300
			1300	1270
			1330	1240
		0.8	1210	1360
			1180	1390
			1150	1420
			1120	1450
		1.0	1360	1210
			1390	1180
			1420	1150
			1450	1120
		1.2	1090	1480
			1060	1510
			1030	1540
			1000	1570
		1.4	1480	1090
			1510	1060
			1540	1030
		1570	1000	

Chip Design C

Structure type	Variations		
Straight waveguides	# of sets	Waveguide widths (μm)	
	8	0.5, 0.6, 0.7, 0.8, 0.9, 1.0, 1.2, 1.4, 1.6, 1.8, 2.0	
Ring resonators	Waveguide width (μm)	Radius (μm)	Gaps (μm)
	0.8	600	1.0, 1.5, 2.0, 2.5, 3.0
	1.0	600	1.0, 1.5, 2.0, 2.5, 3.0
		400	0.7, 1.0, 1.2, 1.4, 1.6, 1.8, 2.0, 2.3, 2.6
		300	0.6, 0.7, 0.9, 1.0, 1.1, 1.3, 1.4, 1.5, 1.6, 1.7, 1.8, 2.0, 2.2
		200	0.5, 0.7, 0.8, 1.0, 1.2, 1.4, 1.6, 1.8, 2.0, 2.2, 2.3, 2.5
100	0.5, 0.6, 0.7, 0.8, 0.9, 1.0, 1.2, 1.4, 1.5, 1.6, 1.8, 2.0, 2.2		
1.2	600	1.0, 1.8, 2.0, 2.5, 3.0	
Directional couplers	Waveguide width (μm)	Coupling gap (μm)	Coupling length (μm)
	1.0	0.8	1, 5, 8, 10, 12, 14, 15, 18, 20, 25, 30, 35, 40, 45, 50, 60, 70, 80, 90, 100, 110
Sagnac interferometers	Waveguide width (μm)	Coupling gap (μm)	Coupler length (μm)
	1.0	0.8	5.0, 7.5, 10.0, 12.5, 13.5, 15.0, 17.5, 20.0, 25.0
Multimode interferometers	Waveguide width (μm)	MMI width (μm)	MMI length (μm)
	0.8	5	295, 325, 345, 350, 355, 360, 365, 385, 415, 550, 580, 600, 605, 610, 615, 620, 640, 670
			295, 325, 345, 350, 355, 360, 365, 385, 415, 550, 580, 600, 605, 610, 615, 620, 640, 670
1.0	5	295, 325, 345, 350, 355, 360, 365, 385, 415, 550, 580, 600, 605, 610, 615, 620, 640, 670	

Appendix B – Q Factor Fitting Code

This appendix provides the MATLAB code used for the Q factor fitting of resonances in both single and split mode microring resonators.

Single resonance

```
function SingleResonanceQFit
clear all; close all; clc;

lam0List = 1550.1254; %(nm) Initial guess of resonance wavelength

span_fit = 120; %(pm) span around resonance wavelength for fitting
span_fit = span_fit/1000; %(nm)

% IMPORT DATA -----
----
str = 'W10R300G22.csv'; % Transmission v Wavelength data file
f1 = importdata(str); % import data
wavelength = f1(:,1) * 1E9; %(nm) Import wavelength -> convert to nm
transmission = real(f1(:,2)); %(mW) Measured transmission (in mW)
transmission_dBm = ...
    real(10*log10(transmission/0.001));% Convert transmission to dBm

% Plot Transmission v Wavelength data
figure;
plot(wavelength, transmission_dBm, 'sk', 'markerSize', 7, ...
    'lineWidth', 0.5, 'markerFaceColor', [0.2 0.2 0.8]);
hold on;

% SET WAVELENGTH LIMITS FOR FITTING
% -----
----
l1 = find(wavelength > (lam0-span_fit)); l1 = l1(1); % lower limit
l2 = find(wavelength < (lam0+span_fit)); l2 = l2(end); % upper limit
wavelengthSelect_zhan = wavelength(l1:l2); % select wavelength data
transmissionSelect_zhan = transmission_dBm(l1:l2);% select transmission
data
transmissionSelect_zhan_norm = ...
    max(transmissionSelect_zhan); % normalize transmission data
transmissionSelect_zhan = transmissionSelect_zhan - ...
    max(transmissionSelect_zhan); % normalize transmission data

% INITIAL FITTING GUESSES
% If Qi < Qe (Assume undercoupled)
Qi = 3E5; % initial intrinsic Q-factor (Assuming undercoupled)
Qe = 4E5; % initial extrinsic Q-factor (Assuming undercoupled)
C = max(transmissionSelect_zhan); % power level adjustment (dB)
paramStart = [Qi Qe lam0 C]'; % Initial guesses
```

```

lb = [1e3 1e3 min(wavelengthSelect_zhan) -5]; % lower bounds
ub = [1e8 1e8 max(wavelengthSelect_zhan) 2]; % upper bounds

% Options for native MATLAB fitting algorithm
options = optimset('lsqcurvefit');
options = optimset(options, 'TolX', 1e-15, 'TolFun', 1e-13);
options.MaxFunEvals = 50000;
options.MaxIter = 50000;

%% FIT DATA TO EQUATION -----
----
[paramEndlsq, ~] = lsqcurvefit(@lorFitSingleLog, paramStart, ...
    wavelengthSelect_zhan, transmissionSelect_zhan, lb, ub, options);
%% -----
----

QFit_i = paramEndlsq(1) % Calculated intrinsic Q factor
QFit_e = paramEndlsq(2) % Calculated extrinsic Q factor

% Plot resonance fit over data -----
----
wavelengthFit = min(wavelengthSelect_zhan):0.05e-
3:max(wavelengthSelect_zhan); % 0.5pm resolution
transmissionFit = lorFitSingleLog(paramEndlsq, wavelengthFit);
plot(wavelengthFit, transmissionFit + transmissionSelect_zhan_norm, '-
r', 'LineWidth', 3);
hold on;
end

%% SINGLE RESONANCE LORENTZIAN LINESHAPE FUNCTION -----
----
% Soln to Eq 3.22 in Thesis

function [y] = lorFitSingleLog(param,x)
% % param = [Qi Qe lam0(nm) C]
% % Qi = initial guess of intrinsic Q-factor
% % Qe = initial guess of coupling (extrinsic) Q-factor
% % lam0 = initial guess of resonant wavelength
% % C = initial guess of off resonance insertion loss
% % x is wavelength in nm
imj = -sqrt(-1); % imaginary number
c0 = 2.99792458e17; % nm/s speed of light

Qi = param(1); % intrinsic Q - Initial guess
Qe = param(2); % coupling (extrinsic) Q - Initial guess
lam0 = param(3); % Resonance wavelength (nm) - Initial guess
C = param(4); % Off resonance insertion loss - Initial guess
w0 = 2*pi*c0/lam0; % 1/s - Central frequency of light
w = 2*pi*c0./x; % 1/s - Frequency of light

dividend = imj*2*(w-w0)/w0+1/Qi-1/Qe;
divisor = imj*2*(w-w0)/w0+1/Qi+1/Qe;

```

```
T = (abs(dividend).^2)./(abs(divisor).^2); % transmission calculated
from CMT
y = 10*log10(T)+C; % transform into dB scale + level adjustment
end
```

Split resonance

```
function SplitResonanceQFit
clear all; close all; clc;

lam0List = 1550.1254; % (nm) Initial guess of resonance wavelength

span_fit = 120; % (pm) span around resonance wavelength for fitting
span_fit = span_fit/1000; % (nm)

% IMPORT DATA -----
----
str = 'W10R300G22.csv'; % Transmission v Wavelength data file
f1 = importdata(str); % import data
wavelength = f1(:,1) * 1E9; % (nm) Import wavelength -> convert to nm
transmission = real(f1(:,2)); % (mW) Measured transmission (in mW)
transmission_dBm = ...
    real(10*log10(transmission/0.001)); % Convert transmission to dBm

% Plot Transmission v Wavelength data
figure;
plot(wavelength, transmission_dBm, 'sk', 'markerSize', 7, ...
    'lineWidth', 0.5, 'markerFaceColor', [0.2 0.2 0.8]);
hold on;

% SET WAVELENGTH LIMITS FOR FITTING
% -----
----
l1 = find(wavelength > (lam0-span_fit)); l1 = l1(1); % lower limit
l2 = find(wavelength < (lam0+span_fit)); l2 = l2(end); % upper limit
wavelengthSelect_zhan = wavelength(l1:l2); % select wavelength data
transmissionSelect_zhan = transmission_dBm(l1:l2); % select transmission
data
transmissionSelect_zhan_norm = ...
    max(transmissionSelect_zhan); % normalize transmission data
transmissionSelect_zhan = transmissionSelect_zhan - ...
    max(transmissionSelect_zhan); % normalize transmission data

% INITIAL FITTING GUESSES
Qi1 = 8e5; % intrinsic Q-factor for resonance 1 - Initial guess
Qi2 = 5e5; % intrinsic Q-factor for resonance 2 - Initial guess
Qe = 2.9e6; % extrinsic Q-factor - Initial guess
Qb = 8e5; % CW to CCW mode coupling Q
C = max(transmissionSelect_cmt_split); % power level adjustment (dB)
paramStart = [Qi1 Qi2 Qe Qb lam0 C]'; % guess value (fitting starting
point)
```

```

lb = [1e4 1e4 1e5 1e4 min(wavelengthSelect_cmt_split) -5]; % lower
bounds
ub = [1e7 1e7 1e9 1e7 max(wavelengthSelect_cmt_split) +2]; % upper
bounds

% Options for native MATLAB fitting algorithm
options = optimset('lsqcurvefit');
options = optimset(options, 'TolX',1e-15 , 'TolFun',1e-13);
options.MaxFunEvals = 50000;
options.MaxIter = 50000;

%% FIT DATA TO EQUATION -----
----
[paramEndlsq, ~] = lsqcurvefit(@lorFitDoubleLogCorrelated,
paramStart,...
    wavelengthSelect_zhan, transmissionSelect_zhan, lb, ub, options);
%% -----
----

Qfit_i1 = paramEndlsq(1); % Calculated intrinsic Q factor (first mode)
Qfit_i2 = paramEndlsq(2); % Calculated intrinsic Q factor (second mode)
Qfit_e = paramEndlsq(3); % Calculated extrinsic Q factor

% Plot resonance fit over data -----
----
wavelengthFit = min(wavelengthSelect_zhan):0.05e-
3:max(wavelengthSelect_zhan); % 0.5pm resolution
transmissionFit = lorFitSingleLog(paramEndlsq, wavelengthFit);
plot(wavelengthFit, transmissionFit + transmissionSelect_zhan_norm, '-
r', 'LineWidth', 3);
hold on;
end

%% SPLIT RESONANCE LORENTZIAN LINESHAPE FUNCTION -----
----
function [y] = lorFitDoubleLogCorrelated(param,x)
% % param = [Qi1 Qi2 Qe Qb lam0(nm) C]
% % Qi1 = initial guess of intrinsic Q-factor for first resonance
% % Qi2 = initial guess of intrinsic Q-factor for second resonance
% % Qe = initial guess of coupling (extrinsic) Q-factor
% % lam0 = initial guess of resonant wavelength
% % Qb: first to second resonance mode coupling Q
% % C = initial guess of off resonance insertion loss
% % x is wavelength in nm

imj = -sqrt(-1); % j imaginary number
c0 = 2.99792458e17; % nm/s speed of light

Qi1 = param(1); % intrinsic Q for resonance 1 - Initial Guess
Qi2 = param(2); % intrinsic Q for resonance 2 - Initial Guess

```

```
Qe = param(3); % coupling (extrinsic) Q - Initial Guess
Qb = param(4); % first to second mode coupling Q - Initial Guess
lam0 = param(5); % center wavelength (nm) - Initial Guess
C = param(6); % power level adjustment - Initial Guess

lam1 = lam0+0.5*lam0/Qb;
lam2 = lam0-0.5*lam0/Qb;
w1 = 2*pi*c0/lam1;
w2 = 2*pi*c0/lam2;
w0 = 0.5*(w1+w2);
w = 2*pi*c0./x;
deltaW = w-w0;

ge = w0/(Qe);
g1 = w1/(Qi1);
g2 = w2/(Qi2);
gb = w0/Qb;

ac = sqrt(ge/2)./((g1+ge)/2+imj*(deltaW+gb/2));
as = sqrt(ge/2)./((g2+ge)/2+imj*(deltaW-gb/2));

t = -1+sqrt(ge/2)*(ac+as); % transmission amplitude
T = abs(t).^2; % transmission calculated from CMT

y = 10*log10(T)+C; % transform into dB scale + level adjustment
end
```

Appendix C – Rate Equation Solver Code

This appendix provides the MATLAB code used for implementation of the erbium-doped waveguide rate equation solver.

Rate equation solver

```
function [netGain_ZMatrix, Ppump_time, Psignal_time, N_MeanVec] = ...
    IntegratedWaveguideAmplifierRateEqnsSolver_VThesis(InputParams)
%% -----
----
% Integrated waveguide rare earth amplifier rate equation model
% - Generalized to operate with any # of energy levels
% - discretized mode profile for signal and pump
% - includes affects of ion quenching
% - forwards and reverse pump source
%
% OUTPUT VARIABLES -----
%
% netGain_ZMatrix
%   -> 2 rows | N columns based on number of z pts
%   Row 1 -> steady state net gain to signal versus z
%   Row 2 -> steady state net gain to pump versus z
%
% Ppump_time
%   -> 1 rows | N columns based on number of simulation time steps
%   -> Pump power at end of waveguide for each simulation time loop
%
% Psignal_time
%   -> 1 rows | N columns based on number of simulation time steps
%   -> Signal power at end of waveguide for each simulation time loop
%
% N_MeanVec
%   -> X rows = to number of energy levels
%   -> Y columns based on number of z pts
%   -> Population at each energy level averaged over active areal
elements
%       versus z pts
%
% Henry C. Frankis
% -----
----

%% INPUT PARAMETERS - Values given by InputParams object -----
----
%% -----
----

% SIGNAL LIGHT PARAMETERS -----
----
% Wavelength of signal light (nm)
wlSignal = InputParams.wlSignal;
% Launched signal light power (mW)
```

```

PSignal = InputParams.PSignal;
% Background (non rare earth absorption) waveguide loss of signal (dB)
lossSignal = InputParams.lossSignal;

% PUMP LIGHT PARAMETERS -----
----
% Wavelength of signal light (nm)
wlPump = InputParams.wlPump;
% Launched forward pump light power (mW)
PPumpforward = InputParams.PPumpforward;
% Launched reverse pump light power (mW)
PPumpreverse = InputParams.PPumpreverse;
% Background (non rare earth absorption) waveguide loss of pump (dB)
lossPump = InputParams.lossPump;

% background loss of waveguide | [signal pump]
Params.BGLoss = (1/4.34294482)*[lossSignal, lossPump];

% WAVEGUIDE PARAMETERS -----
----
% Rare earth dopant concentration (ions / cm3)
N = InputParams.N;
% Fraction of rare earth ions that are quenched
fracQuench = InputParams.fracQuench;
% length of waveguide (cm)
Length = InputParams.Length;

% SIMULATION PARAMETERS -----
----
Params.dT = InputParams.dT; % time step (us)
TimeSegmentsMin = InputParams.TimeSegmentsMin; % (# of time steps to
take)
TimeSegmentsMax = InputParams.TimeSegmentsMax; % (# of time steps to
take)
Zsegments = InputParams.Zsegments; % (# of z segments for waveguide)
Params.dZ = Length/Zsegments; % Z increment step (cm)

% Ground level energy level (Typically 1)
Params.GroundLevel = InputParams.GroundLevel;
% Emission level energy level (Typically 2)
Params.EmissionLevel = InputParams.EmissionLevel;
% Pump level energy level (2 for 1480 pump | 3 for 980 pump)
Params.PumpLevel = InputParams.PumpLevel;

% MODE PROFILES -----
----
fNameSignal = InputParams.fNameSignal; % File name of signal mode
profile
fNamePump = InputParams.fNamePump; % File name of pump mode profile
%% -----
----

```

```

%% -----
% -----
% XY DISCRETIZATION OF MODE
[PassiveElements, ActiveElementVector, dA] = ...
    ModeDiscretization_V4(fNameSignal, fNamePump);
% ActiveElementVector = Fractional ratio for active areal elements
% PassiveElements = Total fractional ratio of passive elements
% dA = Areal element area

% -----
% LIGHT INTENSITY VECTOR
PSignal0 = 0.001 * PSignal; % Launched signal power
PPumpforward0 = 0.001 * PPumpforward; % Launched pump power (forward)
PPumpreverse0 = 0.001 * PPumpreverse; % Launched pump power (reverse)
PVec0 = [PSignal0, PPumpforward0, PPumpreverse0];
netGain_ZMatrix = zeros(3, Zsegments);

% -----
% MATERIAL PARAMETER MATRIX

% Regular (active) ion lifetimes
Tau = [inf, inf, inf; 0.5, inf, inf; inf, 0.04, inf]; % (ms)
Params.GammaMatrix = 1 ./ (0.001 * Tau); % spontaneous decay matrix

% Quenched ion lifetimes
Tau = [inf, inf, inf; 1E-3, inf, inf; inf, 1E-3, inf]; % (ms)
Params.GammaMatrix_Quench = 1 ./ (0.001 * Tau); % spontaneous decay
matrix

%(cm^3)/(s) energy transfer up conversion matrix
Params.WMatrix = [0, 0, 0; 2.7E-18, 0, 2.7E-18; 0, 0, 0];

% (cm^2) Absorption cross section matrices
Params.SigmaMatrix_Signal = [0, 7.0E-21, 0; 7.0E-21, 0, 0; 0, 0, 0];
Params.SigmaMatrix_Pump = [0, 2.0E-21, 0; 2.0E-21, 0, 0; 0, 0, 0];
% signal wavelength (1/J)
Params.lambda_Signal = ((1)/(h*c))*(wlSignal * 1E-9);
% pump wavelength (1/J)
Params.lambda_Pump = ((1)/(h*c))*(wlPump * 1E-9);

% -----
% ION CONCENTRATIONS

% Active Ions -----
NumLevels = length(Params.GammaMatrix); % number of energy levels
ThermExcite = 0.01; % Initial thermally excited population fraction

```

```

NVec0_Active = (N * (1-fracQuench)) ... % Initial popn of levels
* [(1-(NumLevels-1)*ThermExcite); ThermExcite*ones(NumLevels-1,
1)];
N_ZMatrix_Active = NVec0_Active * ... % Popn levels @ each z position
ones(1, Zsegments); % of waveguide | (ions)/(cm^3)
N_Cell_Active = cell(1, length(ActiveElementVector));
% Popn levels @ each z position of waveguide for
% each active elemnt of waveguide | (ions)/(cm^3)
for xx = 1 : length(ActiveElementVector)
    N_Cell_Active{xx} = N_ZMatrix_Active;
end

% Fast Quenched Ions -----
NVec0_Quench = (N * (fracQuench)) * [0.98; 0.01; 0.01]; % Initial popn
N_ZMatrix_Quench = NVec0_Quench * ones(1, Zsegments); % Popn @ each z
pst
N_Cell_Quench = cell(1, length(ActiveElementVector));
% Quenched Popn levels @ each z position of waveguide for
% each active areal element of waveguide | (ions)/(cm^3)
for xx = 1 : length(ActiveElementVector)
    N_Cell_Quench{xx} = N_ZMatrix_Quench;
end

%% -----
%% AMPLIFIER MODEL
%% -----

Ppump_time = zeros(1,TimeSegmentsMin);
Psignal_time = zeros(1,TimeSegmentsMin);

% Loop through time segments
cc = 1;
Eps = 1; EpsTarget = 0.0001;

while (cc <= TimeSegmentsMin) || (Eps > EpsTarget && cc <=
TimeSegmentsMax)

    % Z STEPS -----
    % Solve rate eqns along z steps
    [netGain_ZMatrix, N_Cell_Active, N_Cell_Quench, ...
    N_MeanVec] = RateEqns_Zstep (PVec0, netGain_ZMatrix,
N_Cell_Active, ...
    N_Cell_Quench, ActiveElementVector, PassiveElements, Zsegments, dA,
Params);

    Psignal2 = PSignal0 * 10^(netGain_ZMatrix(1,end)/10);
    Psignal_time(cc) = Psignal2;
    Ppump2 = PPumpforward0 * 10^(netGain_ZMatrix(2,end)/10);

```

```

Ppump_time(cc) = Ppump2;

if cc > 1
    Eps = abs(Psignal2 / Psignal_time(cc-1)) - 1;
end

cc = cc+1;

end

end

%% -----
%% Z STEPS
%% -----

function [netGain_ZMatrix, N_Cell_Active, N_Cell_Quench, ...
    N_MeanVec] = RateEqns_Zstep (Pvec0, netGain_ZMatrix,
N_Cell_Active, ...
    N_Cell_Quench, ActiveElementVector, PassiveElements, Zsegments,
dA, ...
    Params)

BGLoss = Params.BGLoss;
dZ = Params.dZ;

% loop through Z segments - forwards
for bb = 1:Zsegments
    % Bins for total amount of intensity @ next z step
    Intensity_signal_total = 0;
    Intensity_pump_forward_total = 0;
    Intensity_pump_reverse_total = 0;

    N_MeanSum = zeros(3,1);

    % loop through active xy discretization elements
    % -----
    % -----
    % -----
    for cc = 1 : 1
        % SOLVE RATE EQNS + UPDATE INTENSITY
        if Pvec0(3) > 0
            % REVERSE -----
            % Calculate optical intensity of active element cc @ z-bb

```

```

Intensity_signal_element = ... % Signal intensity
| (W)/(cm^2)
    ( 10^(netGain_ZMatrix(1,end+1-bb)/10)* Pvec0(1) ) * ...
    ActiveElementVector(1,cc) / (dA*1E-8);
Intensity_pump_forward_element = ... % Forward pump
intensity
    ( (10^(netGain_ZMatrix(2,end+1-bb)/10)*Pvec0(2)) )
* ...
    ActiveElementVector(2,cc) / (dA*1E-8);
Intensity_pump_reverse_element = ... % Reverse pump
intensity
    ( (10^(netGain_ZMatrix(3,end+1-bb)/10)*Pvec0(3)) )
* ...
    ActiveElementVector(2,cc) / (dA*1E-8);

Intensity_elements = [Intensity_signal_element, ...
    Intensity_pump_forward_element, ...
    Intensity_pump_reverse_element];

% Select population vector for element cc @ z-bb location
NVec_Active_reverse = N_Cell_Active{cc}(:,end+1-bb);
NVec_Quench_reverse = N_Cell_Quench{cc}(:,end+1-bb);

[Intensity_element_plus_reverse, ~, ~] = ...
    RateEqns_IStep (Intensity_elements,
NVec_Active_reverse, ...
    NVec_Quench_reverse, Params);

% Bin optical intensities @ next step into total vector
Intensity_pump_reverse_total =
Intensity_pump_reverse_total ...
    + Intensity_element_plus_reverse(2);
end

% FORWARDS -----
-----

% Calculate optical intensity of active element cc @ bb
Intensity_signal_element = ... % Signal intensity | (W)/(cm^2)
    ( 10^(netGain_ZMatrix(1,bb)/10) * Pvec0(1) ) * ...
    ActiveElementVector(1,cc) / (dA*1E-8);
Intensity_pump_forward_element = ... % Forward pump intensity
    ( (10^(netGain_ZMatrix(2,bb)/10)*Pvec0(2)) ) * ...
    ActiveElementVector(2,cc) / (dA*1E-8);
Intensity_pump_reverse_element = ... % Reverse pump intensity
    ( (10^(netGain_ZMatrix(3,bb)/10)*Pvec0(3)) ) * ...
    ActiveElementVector(2,cc) / (dA*1E-8);

Intensity_elements = [Intensity_signal_element, ...
    Intensity_pump_forward_element,
Intensity_pump_reverse_element];

% Select population vector for element cc @ bb location

```

```

NVec_Active_forward = N_Cell_Active{cc}(:,bb);
NVec_Quench_forward = N_Cell_Quench{cc}(:,bb);

[Intensity_element_plus_forward, NVec_Active_forward, ...
 NVec_Quench_forward] = ...
RateEqns_IStep (Intensity_elements,
NVec_Active_forward, ...
 NVec_Quench_forward, Params);

% Update population matrix
N_Cell_Active{cc}(:,bb) = NVec_Active_forward;
N_Cell_Quench{cc}(:,bb) = NVec_Quench_forward;
N_MeanSum = N_MeanSum + ((NVec_Active_forward) + ...
 (NVec_Quench_forward))*ActiveElementVector(1,cc);

% Bin optical intensities @ next step into total vector
Intensity_signal_total = Intensity_signal_total + ...
 Intensity_element_plus_forward(1);
Intensity_pump_forward_total = Intensity_pump_forward_total
+ ...
 Intensity_element_plus_forward(2);
end

N_MeanVec(:,bb) = (N_MeanSum) / sum(ActiveElementVector(1,:));

% passive intensity element
% -----
% -----
% -----

% Signal - Update intensity at next step
Intensity_signal_element = (10^(netGain_ZMatrix(1,bb)/10) * ...
 PassiveElements(1) * Pvec0(1)) / (dA*1E-8); % Signal intensity
% Bin optical intensities @ next step into total vector
Intensity_signal_total = Intensity_signal_total + ...
 Intensity_signal_element * exp(-BGLoss(1)*dZ);

% Pump - forwards element - Update intensity at next step
Intensity_pump_forward_element = (10^(netGain_ZMatrix(2,bb)/10)
* ...
 PassiveElements(2) * Pvec0(2)) / (dA*1E-8); % Pump intensity
% Bin optical intensities @ next step into total vector
Intensity_pump_forward_total = Intensity_pump_forward_total + ...
 Intensity_pump_forward_element * exp(-BGLoss(2)*dZ);

% Pump - reverse element - Update passive intensity at next step
Intensity_pump_reverse_element = (10^(netGain_ZMatrix(3,end+1-
bb)/10)...
 * PassiveElements(2) * Pvec0(3)) / (dA*1E-8); % Pump intensity
% Bin optical intensities @ next step into total vector
Intensity_pump_reverse_total = Intensity_pump_reverse_total + ...
 Intensity_pump_reverse_element * exp(-BGLoss(2)*dZ);

```

```

if bb < Zsegments
    % Calculate net gain for signal compared to z=0
    netGain_ZMatrix(1,bb+1) = ...
        10*log10((Intensity_signal_total*dA*1E-8)/Pvec0(1));
    % Calculate net gain for forward pump compared to z=0
    netGain_ZMatrix(2,bb+1) = ...
        10*log10((Intensity_pump_forward_total*dA*1E-8)/Pvec0(2));
    % Calculate net gain for reverse pump compared to z=L
    netGain_ZMatrix(3,end-bb) = ...
        10*log10((Intensity_pump_reverse_total*dA*1E-8)/Pvec0(3));

    % If no reverse pump
    if Pvec0(3) == 0
        % Calculate net gain for pump compared to z=L
        netGain_ZMatrix(3,end-bb) = 0;
    end
end
end
end
%% -----
%% -----
%% -----
%% -----
%% INTENSITY STEP
%% -----
function [Iout, NVec_Active_out, NVec_Quench_out] = ...
    RateEqns_IStep (IVec, NVec_Active, NVec_Quench, Params)

%% PARAMETERS
% take static parameters from Params structure
GammaMatrix_Active = Params.GammaMatrix; % spontaneous decay matrix
GammaMatrix_Quench = Params.GammaMatrix_Quench; % spontaneous decay
matrix
WMatrix = Params.WMatrix; % energy transfer up conversion matrix
SigmaMatrix_Pump = Params.SigmaMatrix_Pump; % stimulated transition
matrix
SigmaMatrix_Signal = Params.SigmaMatrix_Signal; % stimulated transition
lambda_Pump = Params.lambda_Pump; % pump wavelength (1/J)
lambda_Signal = Params.lambda_Signal; % signal wavelength (1/J)
dZ = Params.dZ; % Z increment step (cm)
dT = Params.dT;
BGLoss = Params.BGLoss; % background loss of waveguide | [signal pump]
GroundLevel = Params.GroundLevel;
EmissionLevel = Params.EmissionLevel;
PumpLevel = Params.PumpLevel;

```

```

I_Signal = IVec(1);
I_Pump = IVec(2) + IVec(3);

%% RATE EQNS
% Solve for population change of levels
% -----
----
%% Active
NVec_Active_out = RateEqns(NVec_Active, I_Signal, I_Pump, ...
    lambda_Pump, lambda_Signal, GammaMatrix_Active, WMatrix, ...
    SigmaMatrix_Pump, SigmaMatrix_Signal, dT);

%% Quench
NVec_Quench_out = RateEqns(NVec_Quench, I_Signal, I_Pump, ...
    lambda_Pump, lambda_Signal, GammaMatrix_Quench, WMatrix, ...
    SigmaMatrix_Pump, SigmaMatrix_Signal, dT);

%% INTENSITY UPDATE
% update intensity vectors
% -----
Ntotal = (NVec_Active + NVec_Quench);
NMatrix = Ntotal * ones(1,length(Ntotal)); % (ions/cm^3)
SigmaPrime_Signal = NMatrix .* SigmaMatrix_Signal; % (ions)/(cm^3 s)
SigmaPrime_Pump = NMatrix .* SigmaMatrix_Pump; % (ions)/(cm^3 s)
% -----

Iout = zeros(1,2);
% SIGNAL
% Signal amplification/attenuation coefficient | (unitless)
dI = (sum(SigmaPrime_Signal(EmissionLevel, GroundLevel)) - ...
    sum(SigmaPrime_Signal(GroundLevel, EmissionLevel)) - ...
    BGLoss(1)) * IVec(1) * dZ;
Iout(1) = IVec(1) + dI; % Update intensity at next z step | (W)/(cm^2)

% PUMP
% Pump amplification/attenuation coefficient | (unitless)
dI = (sum(SigmaPrime_Pump(PumpLevel, GroundLevel)) - ...
    sum(SigmaPrime_Signal(GroundLevel, PumpLevel)) - ...
    BGLoss(2)) * IVec(2) * dZ;
Iout(2) = IVec(2) + dI; % Update intensity at next z step | (W)/(cm^2)

end
%% -----
----
%% -----
----

%% -----
----
%% RATE EQNS

```

```

%% -----
function [NVec] = RateEqns(NVec, I_Signal, I_Pump, ...
    lambda_Pump, lambda_Signal, GammaMatrix, ...
    WMatrix, SigmaMatrix_Pump, SigmaMatrix_Signal, dT)

%% MATRIX CALCULATION
% popn matrix
NMatrix = NVec * ones(1,length(NVec)); % (ions/cm^3)
% spontaneous transitions matrix
GammaPrime = NMatrix .* GammaMatrix; % (ions)/(cm^3 s)
% energy transfer upconversion / cross relaxation matrix
WPrime = (NMatrix.^2) .* WMatrix; % (ions)/(cm^3 s)
% stimulated transitions matrix - pump and signal
SigmaPrime_Signal = NMatrix .* SigmaMatrix_Signal .* ...
    I_Signal .* lambda_Signal; % (ions)/(cm^3 s)
SigmaPrime_Pump = NMatrix .* SigmaMatrix_Pump .* ...
    I_Pump .* lambda_Pump; % (ions)/(cm^3 s)

% -----
%% TRANSITION MATRIX
TransitionMatrix = GammaPrime + WPrime + SigmaPrime_Signal +
SigmaPrime_Pump;
% -----

%% RATE EQUATIONS
for aa = 1:length(NVec)
    delta = sum(TransitionMatrix(:,aa)) - sum(TransitionMatrix(aa,:));
    % Update in new popn matrix | (ions)/(cm^3 s)
    NVec(aa) = NVec(aa) + dT*delta;
end
end

%% -----
%% -----
%% -----
%% -----
%% MODE DISCRETIZATION
%% -----

function [PassiveElements, ActiveElementVector, dA] = ...
    ModeDiscretization_V4(fName1, fName2, tFilm, wSiN)
xSplit = 3;
ySplit = 3;

% SIGNAL MODE FILE INPUT

```

```

% -----
----
dat = importdata(fName1, ' ', 4);
dat = dat.data;
I_XY_signal = transpose(dat); % E field | (0 -> 1)
I_XY_signal = I_XY_signal(1:ySplit:end, 1:xSplit:end); % reduce # of
points
I_XY_signal = I_XY_signal.^2; % Power (E^2)
% normalize to ratio of total power | (%)
I_XY_signal = (I_XY_signal) / (sum(sum(I_XY_signal)));

% PUMP MODE FILE INPUT
% -----
----
dat = importdata(fName2, ' ', 4);
dat = dat.data;
I_XY_pump = transpose(dat); % E field | (0 -> 1)
I_XY_pump = I_XY_pump(1:ySplit:end, 1:xSplit:end); % reduce # of points
I_XY_pump = I_XY_pump.^2; % Power (E^2)
% normalize to ratio of total power | (%)
I_XY_pump = (I_XY_pump) / (sum(sum(I_XY_pump)));

% DISCRETIZE AREAL ELEMENTS
% -----
----
[Ydivs, Xdivs] = size(I_XY_signal);
xmin = -4; xmax = 4; X = linspace(xmin, xmax, Xdivs); % (um)
ymin = 4; ymax = 9; Y = linspace(ymin, ymax, Ydivs); % (um)
dAx = (xmax - xmin) / Xdivs % (um)
dAy = (ymax - ymin) / Ydivs % (um)
dA = dAx * dAy; % (um2)

% Find if elements are in active or passive region - sort into matrix
% -----
----
[ActiveMatrix, ~, ~] = YLims_Lionix(X, Y, tFilm, wSiN);
A = size(ActiveMatrix);
ActiveMatrixPlot = zeros(length(Y), length(X));

%% OUTPUT VECTORS
% SORT PASSIVE ACTIVE X/Y ELEMENTS INTO VECTOR
% -----
----
peak = max(max(I_XY_signal)); % Peak signal ratio | (%)
% Percentage of peak signal in element necessary to consider element
cutoff = 0.01;
% ratio of total signal power for each passive element | [Pump Signal]
| (%)
PassiveElementVector = [];

```

```

% ratio of total signal power for each active element | [Pump Signal] |
(%)
ActiveElementVector = [];
dA_passive = 0;
dA_active = 0;

for aa = 1 : A(1)
    for bb = 1 : A(2)
        % Is element in active or passive region?
        if ActiveMatrix(aa,bb) == 0 % In passive region
            ActiveMatrixPlot(aa,bb) = 0;
            % Index to passive signal vector
            PassiveElementVector = [PassiveElementVector ...
                [I_XY_signal(aa,bb) ; I_XY_pump(aa,bb)]];
        else % In active region
            % Check if element signal power is above cutoff
            if I_XY_signal(aa,bb) > cutoff * peak
                ActiveMatrixPlot(aa,bb) = I_XY_signal(aa,bb);
                % Index to passive signal vector
                ActiveElementVector = [ActiveElementVector ...
                    [I_XY_signal(aa,bb) ; I_XY_pump(aa,bb)]];
            end
        end
    end
end

% Recorrect to 1 intensity
totalSignal = sum(PassiveElementVector(1,:)) +
sum(ActiveElementVector(1,:));
totalPump = sum(PassiveElementVector(2,:)) +
sum(ActiveElementVector(2,:));

ActiveElementVector(1,:) = ActiveElementVector(1,:) / totalSignal;
ActiveElementVector(2,:) = ActiveElementVector(2,:) / totalPump;
PassiveElements = zeros(2,1);
PassiveElements(1) = sum(PassiveElementVector(1,:)) / totalSignal;
PassiveElements(2) = sum(PassiveElementVector(2,:)) / totalPump;

end

function [ActiveMatrix, y_lowLim, y_upLim] = YLims_Lionix(X, Y, tFilm,
wSiN)
tBox = 6; % thickness of box (um)
% tFilm = 0.34; % thickness of film (um)
tSiN = 0.2; % thickness of SiN (um)
% wSiN = 1; % width of SiN (um)
eps = 0.001;

% Initialize active region xy matrix
ActiveMatrix = zeros(length(Y), length(X));

% Vector for lower and upper y limit of active region

```

```

y_lowLim = zeros(1, length(X)); y_upLim = zeros(1, length(X));
for aa = 1 : length(X)
    x = X(aa);

    % -----
    % LOWER LIMIT
    if (abs(x)) > (wSiN/2)
        % upper limit = film height - etch depth | away from waveguide
        lowLim = (tBox) - eps;
    else
        % upper limit defined by circular etch profile | at etch
sidewall
        lowLim = (tBox + tSiN) - eps;
    end
    % -----
    % UPPER LIMIT
    if (abs(x)) > ((wSiN+tFilm)/2)
        % upper limit = film height - etch depth | away from waveguide
        upLim = (tBox+tFilm) + eps;
    else
        % upper limit defined by circular etch profile | at etch
sidewall
        upLim = (tBox+tSiN+tFilm) + eps;
    end

    y_lowLim(aa) = lowLim; y_upLim(aa) = upLim;
    for bb = 1 : length(Y)
        if (Y(bb) > lowLim) && (Y(bb) < upLim) % If element in active
region
            ActiveMatrix(bb,aa) = 1; % Set active region matrix element
= 1
        end
    end
end
end
end

```

Appendix D – Coupled Mode Theory Solver Code

This appendix provides the MATLAB code used for the coupled mode theory simulation of coupled power between a silicon bus waveguide and TeO₂ microcavity resonator.

Three sub functions: “**CMT_ModeImport.m**”, “**DoubleIntSum.m**”, and “**ZCross.m**” are used in combination with the primary coupled mode theory solver code. The sub functions are responsible for importing mode profiles from RSoft simulations of the optical mode, calculating the value of double integrals, and calculating the cross product of two vectors with no z polarized component, respectively. The code also requires the use of RSoft generated mode profiles, with 4 files (x polarized electric field, y polarized electric field, x polarized magnetic field, and y polarized magnetic field) for each independent waveguide structure for a total of 8 files.

CMT_ModeImport.m

```
function [E_XY] = CMT_ModeImport(XVec, YVec, XBound, YBound, XYOffset,
fName)
% XVec = vector of x mesh points
% YVec = vector of y mesh points
% XBound = [2x1] vector of left and right x boundary of RSoft sim
% YBound = [2x1] vector of bottom and top y boundary of RSoft sim
% XYOffset = [2x1] vector of x and y offsets between RSoft and CMT
%           waveguide cross sections
% fName = RSoft import file name

% E_XY = Value of mode profile at x/y mesh points

% MODEFILEINPUT
% -----
----
dat = importdata(fName, ' ', 4);
dat = dat.data;
dat = transpose(dat); %E field | (0 -> 1)

% DISCRETIZE AREA ELEMENTS
% -----
----
[Ydivs, Xdivs] = size(dat);
Xspace = XYOffset(1) + linspace(XBound(1), XBound(2), Xdivs); % (um)
Yspace = XYOffset(2) + linspace(YBound(1), YBound(2), Ydivs); % (um)

E_XY = zeros(length(YVec), length(XVec));
for bb = 1 : length(YVec)
    indY = find(Yspace > YVec(bb),1);
    for aa = 1 : length(XVec)
        ind1 = find(Xspace > XVec(aa),1);
        if isempty(ind1) || ind1 == length(dat)
```

```

        ind1 = length(dat)-1;
    end

    x1 = Xspace(ind1); y1 = dat(indY,ind1);
    x2 = Yspace(ind1+1); y2 = dat(indY,ind1+1);

    Val = (y1) + (XVec(aa) - x1) * ((y2-y1)/(x2-x1)); % lin interp
    E_XY(bb,aa) = Val;
end
end
end

```

DoubleIntSum.m

```

%% DOUBLE INTEGRAL CALCULATOR
function [Sum] = DoubleIntSum(XVec, YVec, Z)
% XVec = vector of x mesh points
% YVec = vector of y mesh points
% Z = Value at xy mesh points

IntX = zeros(1, length(YVec));
for i = 1 : length(YVec) % Perform Reimann Sum along columns (Y)
    IntX(i) = ReimSum(XVec, Z(i,:));
end
Sum = ReimSum(YVec, IntX); % Perform Reimann Sum along sum of columns
end

% REIMANN SUM ALGORITHM<
function [Sum] = ReimSum(x, V)
Sum = 0;
for aa = 1: length(x) - 1
    Sum = Sum + (V(aa) + V(aa+1))/(2) * (x(aa+1)-x(aa));
end
end

```

ZCross.m

```

function [Out] = ZCross(AX, AY, BX, BY)
Out = AX.*BY - AY.*BX;
end

```

Coupled mode theory solver

```

clear all; close all; clc;

Gap = 0.2; % (um) % Set coupling gap between bus / ring
lambda = 1.55; % (um) % Set wavelength for simulation

fileprint = 1; % Output simulation results to file (1 = Yes | 0 = No)
filename = 'T1100G0200Si35.dat'; % RSoft Simulation output file name

% Constants %

```

```

c = 299792458; %(m/s) % Speed of light
omega = (2*pi*c)/(lambda*1E-6); % (1/s) % Frequency of light
u0 = 1.256E-6; %(H/m) % Vacuum permeability
eps0 = 8.854E-12; %(F/m) % Vacuum permittivity

%% -----
%%
%% Set XY refractive index profile
%% -----

dZ = 0.5; % (um) % Z step for simulations
dX = 0.02; % (um) % X Discretization for simulation
dY = 0.02; % (um) % Y Discretization for simulation

% WINDOW BOUNDARIES -----
----
Boundary_left = -5; % (um) % Left sided simulation boundary
Boundary_right = 1.2; % (um) % Right sided simulation boundary
Boundary_bottom = 2.3; % (um) % Left sided simulation boundary
Boundary_top = 4.4; % (um) % Right sided simulation boundary
Boundary_length = 120; % (um) % Simulation length (z)

AR = (Boundary_top - Boundary_bottom) / ...
     (Boundary_right - Boundary_left); % XY Aspect ratio

XPoints = (Boundary_right - Boundary_left) / (dX); % Num of x mesh
points
YPoints = (Boundary_top - Boundary_bottom) / (dY); % Num of y mesh
points
ZPoints = (Boundary_length) / (dZ); % Num of z steps
XVec = (Boundary_left) : (dX) : ...
       (Boundary_left)+(dX*XPoints); % Vector of x points
YVec = (Boundary_bottom) : (dY) : ...
       (Boundary_bottom)+(dY*YPoints); % Vector of y points
ZVec = (0) : (dZ) : (dZ*ZPoints); % Vector of z points

% REFRACTIVE INDICES -----
----
N_Background = 1.444; % Background refractive index

N_WGA = 2.08; %(WG A (TeO2) - material index)
EffIndex_WGA = 1.998981; % WG A - Effective waveguide index
Beta_WGA = (2*pi*EffIndex_WGA) / (lambda*1E-6); % Propagation vector
(1/m)

N_WGB = 3.473; %(WG B (Si) - material index)
EffIndex_WGB = 1.821354; % WG B - Effective waveguide index
Beta_WGB = (2*pi*EffIndex_WGB) / (lambda*1E-6); % Propagation vector
(1/m)

```

```

% MATERIAL OUTLINES -----
-----
TBox = 3; % Thickness of BOX in Mode simulation

% Waveguide A -----
T_WGA = 1.1; % (um) % Thickness of TeO2
E_X = 2; % (um) % Major axis of ellipse (Wcorner)
E_X0 = 0; % (um) % X position of bottom corner of microcavity

% Waveguide A (TeO2) - lower y axis cross section boundary
WGA_bottomBoundary = (TBox) * ones(1,length(XVec));
for aa = 1 : length(XVec)
    if XVec(aa) > 0
        WGA_bottomBoundary(aa) = TBox + XVec(aa)*tand(80);
    end
end

% Waveguide A (TeO2) - Upper y axis cross section boundary
WGA_topBoundary = (TBox + T_WGA) * ones(1,length(XVec));
Xint = cosd(10) * (T_WGA/2);
for aa = length(XVec) : -1 : 1
    if XVec(aa) > 0
        Y_Arm = TBox + (XVec(aa) + Xint) *tand(80);
        WGA_topBoundary(aa) = TBox + (XVec(aa) + Xint) *tand(80);
    end

    if XVec(aa) > -E_X
        Y_Ellipse = (TBox) + (T_WGA/2) * ...
            (1 + sqrt(1 - ((XVec(aa)+E_X)/(E_X))^2));
        Y_Arm = TBox + (XVec(aa) + Xint) *tand(80);
        WGA_topBoundary(aa) = max([Y_Ellipse, Y_Arm]);
    end
end

% Waveguide B -----
W_WGB = 0.30; % (um) % (Width of waveguide B (Si))
T_WGB = 0.22; % (um) % (Width of waveguide B (Si))
X_WGB = Gap + W_WGB/2; % (um) % (Center position of waveguide B (Si))
Y_WGB = TBox + T_WGB/2; % (um) % (Center position of waveguide B (Si))
WGB_leftBoundary = (X_WGB - W_WGB/2);
WGB_rightBoundary = (X_WGB + W_WGB/2);
WGB_bottomBoundary = (Y_WGB - T_WGB/2);
WGB_topBoundary = (Y_WGB + T_WGB/2);

% BUILD PERMITIVITY DISTRIBUTION MATRIX -----
-----
NMat0 = (N_Background) * (ones(length(YVec), length(XVec))); %
Background
EpsMat = NMat0.^2; % Combined Permittivity matrix
EpsMatA = NMat0.^2; % WG A (TeO2) Permittivity matrix
EpsMatB = NMat0.^2; % WG B (Si) Permittivity matrix

```

```

% Waveguide A permittivity -----
for bb = 1:length(XVec)
    for cc = 1:length(YVec)
        if YVec(cc) > WGA_bottomBoundary(bb) && XVec(cc) <
WGA_topBoundary(bb)
            EpsMat(cc,bb) = N_WGA^2;
            EpsMatA(cc,bb) = N_WGA^2;
        end
        if YVec(cc) > WGA_topBoundary(bb)
            EpsMat(cc,bb) = 1^2;
            EpsMatA(cc,bb) = 1^2;
        end
    end
end
end

% Waveguide B permittivity -----
for bb = 1:length(YVec)
    if YVec(bb) > WGB_bottomBoundary && YVec(bb) < WGB_topBoundary
        for cc = 1:length(XVec)
            if XVec(cc) > WGB_leftBoundary && XVec(cc) <
WGB_rightBoundary
                EpsMat(bb,cc) = N_WGB^2;
                EpsMatB(bb,cc) = N_WGB^2;
            end
        end
    end
end
end

clear NMat WGA_leftBoundary_Vec WGA_rightBoundary_Vec ...
WGB_leftBoundary_Vec WGB_rightBoundary_Vec

%% -----
%%
%% Import Waveguide Mode Profiles from RSoft
%% -----

% Waveguide A mode profile import -----
-----
XBound = [-3, 4]; YBound = [-3, 4]; XYOffset = [-E_X, TBox];
fname='T1100Coupler_er.m02';
Ex0_WGA = CMT_ModeImport(XVec, YVec, XBound, YBound, XYOffset, fname);
fname='T1100Coupler_ey.m02';
Ey0_WGA = CMT_ModeImport(XVec, YVec, XBound, YBound, XYOffset, fname);
fname='T1100Coupler_hx.m02';
Hx0_WGA = CMT_ModeImport(XVec, YVec, XBound, YBound, XYOffset, fname);
fname='T1100Coupler_hy.m02';
Hy0_WGA = CMT_ModeImport(XVec, YVec, XBound, YBound, XYOffset, fname);

% Find maximum electric field value
[Val_A, ~] = max(Ex0_WGA, [], 2);

```

```
[~, Ind_WGA] = max(Val_A);

% Waveguide B mode profile import -----
-----
XBound = [-7.5, 7.5]; YBound = [-2, 8]; XYOffset = [X_WGB, 0];
fname='SiStripW30_ex.m00';
Ex0_WGB = CMT_ModeImport(XVec, YVec, XBound, YBound, XYOffset, fname);
fname='SiStripW30_ey.m00';
Ey0_WGB = CMT_ModeImport(XVec, YVec, XBound, YBound, XYOffset, fname);
fname='SiStripW30_hx.m00';
Hx0_WGB = CMT_ModeImport(XVec, YVec, XBound, YBound, XYOffset, fname);
fname='SiStripW30_hy.m00';
Hy0_WGB = CMT_ModeImport(XVec, YVec, XBound, YBound, XYOffset, fname);

[Val_B, ~] = max(Ex0_WGB, [], 2);
[~, Ind_WGB] = max(Val_B); % Find maximum electric field value

% normalize mode profiles
ENormA = max([max(Ex0_WGA), max(Ey0_WGA)]);
ENormB = max([max(Ex0_WGB), max(Ey0_WGB)]);
HNormA = max([max(abs(Hx0_WGA)), max(abs(Hy0_WGA))]);
HNormB = max([max(abs(Hx0_WGB)), max(abs(Hy0_WGB))]);

Ex0_WGA = Ex0_WGA/ENormA; % (WG A (TeO2)) x polarized electric field
matrix
Ey0_WGA = Ey0_WGA/ENormA; % (WG A (TeO2)) y polarized electric field
matrix
Ex0_WGB = Ex0_WGB/ENormB; % (WG B (Si)) y polarized electric field
matrix
Ey0_WGB = Ey0_WGB/ENormB; % (WG B (Si)) y polarized electric field
matrix

% Magnetic field matrices
Hx0_WGA = (Beta_WGA)/(u0*omega) * Hx0_WGA/HNormA;
Hy0_WGA = (Beta_WGA)/(u0*omega) * Hy0_WGA/HNormA;
Hx0_WGB = (Beta_WGB)/(u0*omega) * Hx0_WGB/HNormB;
Hy0_WGB = (Beta_WGB)/(u0*omega) * Hy0_WGB/HNormB;

%% -----
-----
%% Z STEPS
%% -----
-----

% Transfer Matrix (T) -----
-----
MCell = cell(1, length(ZVec)); % Transfer matrix at z positions
MCellHalf = cell(1, length(ZVec)); % Transfer matrix at half z
positions

% Sweep through z vector
```

```

for ii = 1:2*length(ZVec)
    % Update electric field at z position
    WGA_ExZ = (Ex0_WGA) * exp(-1i*Beta_WGA*(dZ*(ii-1)/2)*1E-6);
    WGB_ExZ = (Ex0_WGB) * exp(-1i*Beta_WGB*(dZ*(ii-1)/2)*1E-6);
    WGA_EyZ = (Ey0_WGA) * exp(-1i*Beta_WGA*(dZ*(ii-1)/2)*1E-6);
    WGB_EyZ = (Ey0_WGB) * exp(-1i*Beta_WGB*(dZ*(ii-1)/2)*1E-6);
    % Update magnetic field at z position
    WGA_HxZ = (Hx0_WGA) * exp(-1i*Beta_WGA*(dZ*(ii-1)/2)*1E-6);
    WGB_HxZ = (Hx0_WGB) * exp(-1i*Beta_WGB*(dZ*(ii-1)/2)*1E-6);
    WGA_HyZ = (Hy0_WGA) * exp(-1i*Beta_WGA*(dZ*(ii-1)/2)*1E-6);
    WGB_HyZ = (Hy0_WGB) * exp(-1i*Beta_WGB*(dZ*(ii-1)/2)*1E-6);

    % Calculate Sigma matrix values at z position -----
    -----
    Sigma_11 = DoubleIntSum(XVec*1E-6, YVec*1E-6,
    ZCross(conj(WGA_ExZ), ...
        conj(WGA_EyZ), WGA_HxZ, WGA_HyZ) + ZCross(WGA_ExZ, WGA_EyZ, ...
        conj(WGA_HxZ), conj(WGA_HyZ)) );
    Sigma_12 = DoubleIntSum(XVec*1E-6, YVec*1E-6,
    ZCross(conj(WGB_ExZ), ...
        conj(WGB_EyZ), WGA_HxZ, WGA_HyZ) + ZCross(WGA_ExZ, WGA_EyZ, ...
        conj(WGB_HxZ), conj(WGB_HyZ)) );
    Sigma_21 = DoubleIntSum(XVec*1E-6, YVec*1E-6,
    ZCross(conj(WGA_ExZ), ...
        conj(WGA_EyZ), WGB_HxZ, WGB_HyZ) + ZCross(WGB_ExZ, WGB_EyZ, ...
        conj(WGA_HxZ), conj(WGA_HyZ)) );
    Sigma_22 = DoubleIntSum(XVec*1E-6, YVec*1E-6,
    ZCross(conj(WGB_ExZ), ...
        conj(WGB_EyZ), WGB_HxZ, WGB_HyZ) + ZCross(WGB_ExZ, WGB_EyZ, ...
        conj(WGB_HxZ), conj(WGB_HyZ)) );

    % Populate Sigma matrix
    SigmaMat = [Sigma_11, Sigma_12; Sigma_21, Sigma_22];

    % Calculate C matrix values at z position -----
    -----
    C_11 = DoubleIntSum(XVec*1E-6, YVec*1E-6, ...
        (EpsMat-EpsMatA).* (conj(WGA_ExZ) .* (WGA_ExZ) ...
        + conj(WGA_EyZ) .* (WGA_EyZ)));
    C_12 = DoubleIntSum(XVec*1E-6, YVec*1E-6, ...
        (EpsMat-EpsMatB).* (conj(WGA_ExZ) .* (WGB_ExZ) + ...
        conj(WGA_EyZ) .* (WGB_EyZ)));
    C_21 = DoubleIntSum(XVec*1E-6, YVec*1E-6, ...
        (EpsMat-EpsMatA).* (conj(WGB_ExZ) .* (WGA_ExZ) + ...
        conj(WGB_EyZ) .* (WGA_EyZ)));
    C_22 = DoubleIntSum(XVec*1E-6, YVec*1E-6, ...
        (EpsMat-EpsMatB).* (conj(WGB_ExZ) .* (WGB_ExZ) + ...
        conj(WGB_EyZ) .* (WGB_EyZ)));

    % Populate C Matrix
    CMat = -1i*omega*eps0*[C_11, C_12; C_21, C_22];

    % Populate vector (M) of transfer matrices (T)

```

```

T = (SigmaMat^-1) * CMat;
if mod(ii,2) == 1
    MCell{(ii+1)/2} = T;
else
    MCellHalf{(ii)/2} = T;
end
end

% COUPLING COEFFICIENTS -----
-----
A = 0; B=1; % (A/B Coupling coefficients, Assume all initial power in
WG B)

% AMat -> A and B values versus z steps
% Row 1 = A values
% Row 2 = B values
% Column = Z position vector
AMat = zeros(2,length(ZVec));
AMat(:,1) = [A; B];

% Calculate A/B values versus propagation length
for ii = 2:length(ZVec)
    deltaZ = dZ * 1E-6; % Z step

    % Perform 4th order Runge Kutta on Transfer Matrices
    dA1 = (MCell{ii-1})*(AMat(:,ii-1));
    dA2= (MCellHalf{ii-1})*(AMat(:,ii-1) + deltaZ/2*dA1);
    dA3= (MCellHalf{ii-1})*(AMat(:,ii-1) + deltaZ/2*dA2);
    dA4= (MCellHalf{ii})*(AMat(:,ii-1) + deltaZ*dA3);

    % Calculate A/B values at next z position
    AMat(:,ii) = AMat(:,ii-1) + (deltaZ/6)*(dA1+2*dA2+2*dA3+dA4);
end

C = abs(AMat(1,:)).^2; % (Cross over ratio (Kappa) versus length)

% Output data)
if fileprint
    OUTPUTDATA = [ZVec', C'];
    dlmwrite(filename,OUTPUTDATA,'delimiter',' ','precision','%0.8f');
end

```